



#### This is to certify that the

#### dissertation entitled

## INTERACTION OF ELECTROMAGNETIC FIELDS WITH A MATERIAL SAMPLE PLACED WITHIN AN ENERGIZED CAVITY

presented by

JIANPING ZHANG

has been accepted towards fulfillment of the requirements for

Ph.D degree in ELECTRICAL ENGINEERING

kun-mu Chen

Major professor

Date July 14,1998

MSU is an Affirmative Action/Equal Opportunity Institution

0-12771

### LIBRARY Michigan State University

# PLACE IN RETURN BOX to remove this checkout from your record. TO AVOID FINES return on or before date due.

DATE DUE	DATE DUE	DATE DUE

1/98 c:/CIRC/DateDue.p65-p.14

## INTERACTION OF ELECTROMAGNETIC FIELDS WITH A MATERIAL SAMPLE PLACED WITHIN AN ENERGIZED CAVITY

By

Jianping Zhang

#### A DISSERTATION

Submitted to
Michigan State University
in partial fulfilment of the requirements
for the degree of

**DOCTOR OF PHILOSOPHY** 

Department of Electrical Engineering

1998

#### **ABSTRACT**

## INTERACTION OF ELECTROMAGNETIC FIELDS WITH A MATERIAL SAMPLE PLACED WITHIN AN ENERGIZED CAVITY

By

#### Jianping Zhang

The investigation of the heating of a material sample in an energized electromagnetic cavity requires the understanding of the interaction of the electromagnetic fields with the material sample in a cavity. The key factor for this understanding is to quantify the distribution of the induced electric field inside the material sample placed in the cavity.

The goal of this research is to solve Maxwell's equations in an electromagnetic cavity in the presence of a material sample based on an Electric Field Integral Equation (EFIE) or a Magnetic Field Integral Equation (MFIE) and the dyadic Green's function in an electromagnetic cavity. In this study, a complete set of vector wave functions which include both solenoidal and irrotational functions are employed and the electric field (and magnetic field) integral equation is derived based on the expansion of these vector wave functions.

When solving the integral equation, due to the slow convergence rate of the dyadic Green's function, the infinite triple summation over the cavity eigenfunctions is reduced to the infinite double summation, and the infinite double summation is then estimated by a finite double summation plus an infinite single summation using the Poisson summation

formula. For some material samples with specific geometries, a scheme of separating the material sample into the boundary layer region and the interior region is proposed. This scheme tends to improve the convergence of numerical results and also to save computation time. Numerical results agree well with the theoretical estimation using these methods.

The mode-matching method is also employed to analyze the induced electric field distribution in homogeneous material samples with simple cylindrical geometries placed in an energized cylindrical cavity. In this method, the whole cavity is divided into three waveguide regions and the eigenmodes in the inhomogeneously filled waveguide which contains the material sample are derived. Numerical calculation shows that the resultant matrix is sparse and the number of eigenmodes needed in the summation is reduced considerably compared with the integral equation method. The numerical results of the mode-matching method are found to be consistent with the corresponding results of the integral equation method.

To my husband Yong Wan and our son Moquan Wan

#### **ACKNOWLEDGMENTS**

First and foremost, I would like to express my deep gratitude to my major professor, Dr. Kun-Mu Chen, for introducing me to Electromagnetics, and his invaluable help and patience. I owe him no less gratitude for the congenial manner in which he has overseen my career as a graduate student. In addition, his editorial, technical, and thematic comments on the rough drafts of this dissertation have improved it more than I would care to admit. Without his guidance and expert knowledge in Electromagnetics, this dissertation would not have been possible. I am grateful for the opportunity to learn from his example as both a researcher and an educator. I would like to thank the other members of my committee, Dr. Dennis Nyquist, Dr. Edward Rothwell, and Dr. Byron Drachman, for many helpful comments on this research.

Finally if it were not for the generous and patient nature of my husband, Yong Wan, our son and family, no one would be reading this today. Grateful acknowledgement is also due to my former professors, Yong Huang and Dongguang He from Shandong University, for their continuous concerns during my stay at Michigan State University. I must also extend thanks to my fellow students for their friendship and valuable discussions throughout the duration of my program.

This research was supported by the National Science Foundation under Grant NO. CTS 9526038 and The State of Michigan under a Research Excellence Fund.

#### TABLE OF CONTENTS

LIST	OF TA	ABLES ix	
LIST	OF FI	GURESx	
CHA	CHAPTER 1 INTRODUCTION		
CHA)	MAT	2 CRACTION OF ELECTROMAGNETIC FIELDS WITH A ERIAL SAMPLE PLACED WITHIN A RECTANGULAR ITY	
	2.1	Vector Wave Functions in Rectangular Cavities 9	
		2.1.1 Definitions for Vector Wave Functions $\vec{L}_{nml}$ , $\vec{M}_{nml}$ and $\vec{N}_{nml}$ in Rectangular Cavities	
		2.1.2 Expressions for Vector Wave Functions $\vec{L}_{nml}$ , $\vec{M}_{nml}$ and $\vec{N}_{nml}$ in Rectangular Cavities	
		2.1.3 Vector Wave Functions $\vec{L}_{nml}$ , $\vec{M}_{nml}$ and $\vec{N}_{nml}$ Satisfy Vector Helmholtz Equation	
		2.1.4 Orthogonality of the Vector Wave Functions $\overrightarrow{L}_{nml}$ , $\overrightarrow{M}_{nml}$ and $N_{nml}$	
		2.1.5 Normalization of the Vector Wave Functions $\overrightarrow{L}_{nml}$ , $\overrightarrow{M}_{nml}$ and $\overrightarrow{N}_{nml}$	
		2.1.6 Completeness of the Vector Wave Functions $\overrightarrow{L}_{nml}$ , $\overrightarrow{M}_{nml}$ and $N_{nml}$	
	2.2	Derivation of Dyadic Green's Function and Electric Field Integral Equation (EFIE) in Rectangular Cavities	
		2.2.1 Maxwell's Equations in the Material Sample	
		2.2.2 Expansion of $\overrightarrow{E}^s(\dot{r})$ and Derivation of the Electric Dyadic	

	Green's Function46
	2.2.3 Derivation of the Integral Equation in the Material Sample48
	2.2.4 Expression of the Dyadic Green's Function
	2.2.5 Detailed Expression of $\overline{G}_{eo}(\hat{r}',\hat{r})$ and Comparison with the Results of Y. Rahmat-Samii [11]
	2.2.6 Derivation of the Electrical Field Outside the Material Sample .51
2.3	Derivation of the Magnetic Dyadic Green's Function and Magnetic Field Integral Equation (MFIE)53
2.4	Comparison of EFIE with MFIE and Explanation of the Result 57
СНАРТЕ	R 3
EL	MERICAL TECHNIQUES AND RESULTS ON THE INDUCED ECTRIC FIELD IN A MATERIAL SAMPLE PLACED THIN A RECTANGULAR CAVITY
3.1 3.2	Applying Galerkin's Method to EFIE
3.2	
3.4	
СНАРТЕ	D A
	JANTIFICATION OF THE INDUCED ELECTRIC FIELD IN A
MA	ATERIAL SAMPLE PLACED WITHIN A CYLINDRICAL
CA	<b>.VITY</b> 125
4.1	Expressions for Vector Wave Functions $\overrightarrow{L}_{nml}$ , $\overrightarrow{M}_{nml}$ and $\overrightarrow{N}_{nml}$ in Cylindrical Cavities
	4.1.1 Expression for Vector Wave Function $\vec{L}_{nml}$
	4.1.2 Expression for Vector Wave Function $\overrightarrow{M}_{nml}$
	4.1.1 Expression for Vector Wave Function $\vec{N}_{nml}$
4.2	Normalization of Vector Wave Functions $\vec{L}_{nml}$ , $\vec{M}_{nml}$ and $\vec{N}_{nml}$ in Cylindrical Cavities
	4.2.1 Normalization of Vector Wave Function $\hat{L}_{nml}$
	4.2.2 Normalization of Vector Wave Function $\overrightarrow{M}_{nml}$
	4.2.3 Normalization of Vector Wave Function $\vec{N}_{nml}$
	4.2.4 Some Field Structures of Vector Wave Functions in Cylindrical Cavities
4.3	_
4.4	

CHAPTER 5 QUANTIFICATION OF THE INDUCED ELECTRIC FIELD IN A MATERIAL SAMPLE PLACED INSIDE AN EM CAVITY USING MODE MATCHING METHOD	
5.1	Eigenmodes in Different Waveguide Regions
	5.1.1 Eigenmodes in a Homogeneously Filled Wavguide
5.2 5.3	Electromagnetic Fields in the Three Regions
CHAPTER CON	6 NCLUSIONS
	X A MPUTATION OF DYADIC GREEN'S FUNCTION IN CAVITIES Y. RAHMAT-SAMII [11]
$\sum_{n}$	E IDENTITY OF $\sum_{m} \sum_{l} \left[ \vec{L}_{nml}(\vec{r}') \vec{L}_{nml}(\vec{r}') + \vec{N}_{nml}(\vec{r}') \vec{N}_{nml}(\vec{r}') + \vec{M}_{nml}(\vec{r}') \vec{M}_{nml}(\vec{r}') \right] = \bar{I}\delta(\vec{r} - \vec{r}')$ RECTANGUALR CAVITIES
	K C ALTERNATIVE REPRESENTATION OF THE ELECTRIC ADIC GREEN'S FUNCTION
	K D OMOGENEOUS DIELECTRIC SPHERE IN UNIFORMELY PLIED STATIC FIELD243
BIBLIOGI	<b>RAPHY</b> 252

#### LIST OF TABLES

Table 3.1	Induced electric field inside the 4-mm cubic material sample and its ratio to the initial electric field for different values of N, where the relative permittivity of the sample is assumed to be $\varepsilon_r = 2.5$ , the resonant frequency shift is 5% and the initial electric field is $E_y^i = 321.5729$ . The geometry of the rectangular cavity is shown in Figure 3.7 90
Table 3.2	Induced electric field inside the 4-mm cubic material sample and its ratio to the initial electric field for different relative permittivities of the material sample, where the resonant frequency shift is 5% and the initial electric field is $E_y^i = 321.5729$ . The geometry of the rectangular cavity is shown in Figure 3.7
Table 3.3	Induced electric field and the ratio vs. the resonant frequency shift. The relative permittivity of the 4-mm cubic material sample is assumed to be $\varepsilon_r = 2.5$ and the initial electric field is $E_y^i = 321.5729$ . The geometry of the rectangular cavity is shown in Figure 3.7
Table 5.1	Significant modes in the mode-matching method when the dimensions of the cavity are: a=0.0762m, c=0.15458m and that of the material sample are: r0=0.004m and h0=0.008m. The operating frequency is 2.45 GHz and the excitation probe is located at c/4 from the bottom
Table 5.2	Number of eigenmodes used in the mode-matching method for the different geometris of the material sample

#### **LIST OF FIGURES**

Figure 2.1	A rectangular cavity and the designation of the coordinate system 13
Figure 2.2	E-field structure of $L_{III}$ in the x-y plane with $z=c/4$
Figure 2.3	E-field structure of $L_{III}$ in the x-z plane with $y=b/4$
Figure 2.4	E-field structure of $L_{III}$ in the y-z plane with $x=a/4$
Figure 2.5	E-field structure of $M_{221}$ in the x-y plane with $z=c/4$
Figure 2.6	E-field structure of $M_{221}$ in the x-z plane with $y=b/4$
Figure 2.7	E-field structure of $M_{221}$ in the y-z plane with $x=a/4$
Figure 2.8	E-field structure of $N_{221}$ in the x-y plane with $z=c/44$
Figure 2.9	E-field structure of $N_{221}$ in the x-z plane with $y=b/4$
Figure 2.10	E-field structure of $N_{221}$ in the y-z plane with $x=a/4$
Figure 2.11	E-field structure of $L_{221}$ in the x-y plane with $z=c/4$
Figure 2.12	E-field structure of $L_{221}$ in the x-z plane with $y=b/4$
Figure 2.13	E-field structure of $L_{221}$ in the y-z plane with $x=a/4$
Figure 3.1	Integration of the triple summation format $G_{eoxx}(\hat{r}', \hat{r})$ vs. the number of summation modes when $\hat{r} = \hat{r}'$ , $\hat{r} = [0.033m, 0.014m, 0.0551m]$ and $\Delta x = \Delta y = \Delta z = 0.002m$ . The dimensions of the rectangular cavity are: $a = 0.072m$ , $b = 0.034m$ and $c = 0.1163m$ 70
Figure 3.2	Integration of the triple summation format $G_{eoxx}(\mathring{r}',\mathring{r})$ vs. the number of summation modes when $\mathring{r}=[0.035m, 0.014m, 0.0551m]$ , $\mathring{r}'=[0.033m, 0.014m, 0.0551m]$ and $\Delta x=\Delta y=\Delta z=0.002m$ . The dimensions of the rectangular cavity are: $a=0.072m$ , $b=0.034m$ and $c=0.1163m$

Figure 3.3	Integration of the triple summation format $G_{eoxx}(\hat{r}, \hat{r})$ vs. the number of summation modes when $\hat{r} = [0.035m, 0.016m, 0.0553m]$ , $\hat{r} = [0.033m, 0.014m, 0.0551m]$ and $\Delta x = \Delta y = \Delta z = 0.002m$ . The dimensions of the rectangular cavity are: $a = 0.072m$ , $b = 0.034m$ and $c = 0.1163m$
Figure 3.4	Integration of the double summation format $G_{eox}(\hat{r}', \hat{r})$ vs. the number of summation modes when $\hat{r} = \hat{r}'$ , $\hat{r} = [0.033m, 0.014m, 0.0551m]$ and $\Delta x = \Delta y = \Delta z = 0.002m$ . The dimensions of the rectangular cavity are: $a = 0.072m$ , $b = 0.034m$ and $c = 0.1163m$
Figure 3.5	Integration of the double summation format $G_{eox}(\hat{r}, \hat{r})$ vs. the number of summation modes when $\hat{r} = [0.035m, 0.014m, 0.0551m]$ , $\hat{r} = [0.033m, 0.014m, 0.0551m]$ and $\Delta x = \Delta y = \Delta z = 0.002m$ . The dimensions of the rectangular cavity are: $a = 0.072m$ , $b = 0.034m$ and $c = 0.1163m$
Figure 3.6	Integration of the double summation format $G_{eox}(\hat{r}', \hat{r})$ vs. the number of summation modes when $\hat{r} = [0.035m, 0.016m, 0.0553m]$ , $\hat{r}' = [0.033m, 0.014m, 0.0551m]$ and $\Delta x = \Delta y = \Delta z = 0.002m$ . The dimensions of the rectangular cavity are: $a = 0.072m$ , $b = 0.034m$ and $c = 0.1163m$ .
Figure 3.7	Dimensions of the rectangular cavity and the material sample. The center of the material sample is consistent with the center of the cavity
Figure 3.8	Ratios of $E_y/E_y^i$ at different volume cells in the 4-mm cubic material sample, where the relative permittivity of the material sample is assumed to be $\varepsilon_r = 2.5$ . The geometry of the rectangular cavity is shown in Figure 3.7. The resonant frequency shift is assumed to be 5%.
Figure 3.9a	The ratios of $E_y/E_y^i$ at different volume cells in the 6-mm cubic material sample, where the relative permittivity of the material sample is assumed to be $\varepsilon_r = 2.5$ . The geometry of the rectangular cavity is shown in Figure 3.7. The resonant frequency shift is assumed to be $5\% \dots 96$
Figure3.9b	The x component of the induced electric field at different volume cells of the 6-mm cubic material sample, where the relative permittivity of the material sample is assumed to be $\varepsilon_r = 2.5$ . The geometry of the rectangular cavity is shown in Figure 3.7. The resonant frequency shift is assumed to be $5\%$

Figure 3.9c	the z component of the induced electric field at different volume cells of the 6-mm cubic material sample, where the relative permittivity of the material sample is assumed to be $\varepsilon_r = 2.5$ . The geometry of the rectangular cavity is shown in Figure 3.7. The resonant frequency shift is assumed to be 5%98
Figure 3.10	Ratios of $E_y/E_y^i$ varies in the x-direction. Each curve represents this ratio as a function of x for different locations of y and z. The relative permittivity of the 2-cm cubic material sample is $\varepsilon_r = 2.5$ . The geometry of the rectangular cavity is shown in Figure 3.7. The resonant frequency shift is assumed to be 8%
Figure 3.11	Ratios of $E_y/E_y^i$ varies in the x-direction. Each curve represents this ratio as a function of x for different locations of z. The highest one is for $z=z_1$ and the lowest one for $z=z_5$ . The relative permittivity of the thin square plate material sample is $\varepsilon_r = 2.5$ and the geometry of the cavity is shown in Figure 3.7. The resonant frequency shift is assumed to be $1\%101$
Figure 3.12	Ratios of $E_y/E_y^i$ varies as a function of y. The dimensions of the material sample are: $x_0=0.002m$ , $y_0=0.02m$ , $z_0=0.002m$ and the geometry of the cavity is shown in Figure 3.7. The resonant frequency shift is assumed to be 1%. The upper limit in the double summation is chosen to be $N=200$ .
Figure 3.13	Ratios of $E_y/E_y^i$ varies as a function of y for different N. The dimensions of the material sample are: $x_0=0.002m$ , $y_0=0.02m$ , $z_0=0.002m$ and the geometry of the cavity is shown in Figure 3.7. The resonant frequency shift is assumed to be 1%
Figure 3.14	Integration of $G_{esxx}(\overset{\bullet}{r},\overset{\bullet}{r})$ vs. number of summation modes when $\overset{\bullet}{r}=\overset{\bullet}{r},\overset{\bullet}{r}=[0.033m,0.014m,0.0551m]$ and $\Delta x=\Delta y=\Delta z=0.002m$ .
Figure 3.15	Integration of $G_{esxx}(\hat{r}', \hat{r})$ vs. number of summation modes when $\hat{r} = [0.035m, 0.014m, 0.0551m]$ , $\hat{r}' = [0.033m, 0.014m, 0.0551m]$ and $\Delta x = \Delta y = \Delta z = 0.002m$
Figure 3.16	Integration of $G_{esxx}(\hat{r}', \hat{r})$ vs. number of summation modes when $\hat{r} = [0.035m, 0.016m, 0.0553m]$ , $\hat{r}' = [0.033m, 0.014m, 0.0551m]$ and $\Delta x = \Delta y = \Delta z = 0.002m$
Figure 3.17	Numerical results obtained with the scheme of dividing the sample volume into boundary layer region and interior region. The ratio of $E_y/E_y^i$ varies as a function of y coordinate. The sample dimensions are: $x_0=0.003m$ , $y_0=0.021m$ , $z_0=0.003m$ and the geometry of the cavity is shown in Figure 3.7. The resonant frequency shift is assumed to be 1%

Figure 4.1	A cylindrical cavity and the designation of the coordinate system127
Figure 4.2	E-field structure of $N_{012}$ in the $r$ - $z$ plane with $\varphi = 121^{\circ}$ . The dimensions of the cylindrical cavity are $a=0.0762m$ , $c=0.15458m$ 145
Figure 4.3	E-field structure of $N_{012}$ in the r- $\phi$ plane with $z=0.0271m$ . The dimensions of the cylindrical cavity are $a=0.0762m$ , $c=0.15458m$ 146
Figure 4.4	E-field structure of $M_{III}$ in the r-z plane with $\varphi = 121^{\circ}$ . The dimensions of the cylindrical cavity are $a=0.0762m$ , $c=0.15458m$
Figure 4.5	E-field structure of $M_{III}$ in the $r$ - $\phi$ plane with $z$ =0.0271 $m$ . The dimensions of the cylindrical cavity are $a$ =0.0762 $m$ , $c$ =0.15458 $m$
Figure 4.6	E-field structure of $L_{112}$ in the $r$ - $z$ plane with $\varphi = 121^{\circ}$ . The dimensions of the cylindrical cavity are $a=0.0762m$ , $c=0.15458m$
Figure 4.7	E-field structure of $L_{112}$ in the $r$ - $\phi$ plane with $z$ =0.0271 $m$ . The dimensions of the cylindrical cavity are $a$ =0.0762 $m$ , $c$ =0.15458 $m$
Figure 4.8	Dimensions of the cylindrical cavity and the material sample. The center of the material sample is consistent with the center of the cavity 162
Figure 4.9	Ratio of $E_z/E_z^i$ varies in the r direction at the different locations of z. The dimensions of the material sample are $d_0=0.02m$ and $h_0=0.02m$ with the relative permittivity of $\varepsilon_r=2.5$ . The dimensions of the cylindrical cavity are shown in Figure 4.8
Figure 4.10	Ratio of $E_z/E_z^i$ varies in the r direction. The dimensions of the material sample are $d_0=0.04m$ and $h_0=0.002m$ with the relative permittivity of $\varepsilon_r=2.5$ . The dimensions of the cylindrical cavity are shown in Figure 4.8.
Figure 4.11	Ratio of $E_z/E_z^i$ varies in the z direction at the different locations of r. The dimensions of the material sample are $d_0=0.008m$ and $h_0=0.044m$ with the relative permittivity of $\varepsilon_r=2.5$ . The dimensions of the cylindrical cavity are shown in Figure 4.8
Figure 4.12	Ratio of $E_z/E_z^i$ varies in the z direction with the scheme of the separation of the boundary layer and interior regions. The dimensions of the material sample are $d_0=0.008m$ and $h_0=0.044m$ with the relative permittivity of $\varepsilon_r=2.5$ . The dimensions of the cylindrical cavity are shown in Figure 4.8.
Figure 4.13	Ratios of $E_z/E_z^i$ varies in the r direction. Each curve represents this ratio as

	dimensions of the material sample are: radius $r_0 = 0.004m$ and height $h_0 = 0.008m$ . The upper graphs are for the real parts of the ratios and the lower ones are for the imaginary parts of the ratios
Figure 4.14	Ratios of $E_z/E_z^i$ varies in the $r$ direction. Each curve represents this ratio as a function of $r$ for different locations of $z$ in a material sample when the material sample has a complex permittivity of $\varepsilon_r = 2.5 - j1.5$ . The dimensions of the material sample are: radius $r_0 = 0.004m$ and height $h_0 = 0.008m$ . The upper graphs are for the real parts of the ratios and the lower ones are for the imaginary parts of the ratios
Figure 4.15	An inhomogeneous material sample is placed in the center of a cylindrical cavity
Figure 4.16	Ratios of $E_z/E_z^i$ in an inhomogeneous material sample with the dimensions of $r_1 = 0.004m$ , $h_1 = 0.008m$ , $r_2 = 0.008m$ and $h_2 = 0.016m$ , where the relative permittivity in the shadowed region is $\varepsilon_1 = 2.5$ and that in the non-shadowed region is $\varepsilon_2 = 4.0$ . The electrostatic estimations of the ratios are $R_1 = 0.5818$ and $R_2 = 0.5091177$
Figure 4.17	Ratios of $E_z/E_z^i$ in the inhomogeneous material sample with the dimensions of $r_1 = 0.002m$ , $h_1 = 0.004m$ , $r_2 = 0.004m$ and $h_2 = 0.008m$ , where the relative permittivity in the shadowed region is $\varepsilon_1 = 2.5$ and that in the non-shadowed region is $\varepsilon_2 = 4.0$ . The electrostatic estimations of the ratios are $R_1 = 0.5818$ and $R_2 = 0.5091$ 178
Figure 4.18	Geometry of an irregularly shaped material sample placed in the cylindrical cavity. The material sample is azimuthally symmetrical and the center of the material sample is consistent with the center of the cylindrical cavity
Figure 4.19	Ratios of $E_z/E_z^i$ in an irregularly shaped material sample
Figure 5.1	Geometry of the material sample placed in a cylindrical cavity driven by an excitation probe
Figure 5.2	Geometry of the inhomogeneously filled waveguide187
Figure 5.3	Ratio of $E_z/E_z^i$ varies in the z direction at $r=0.0004m$ . The dimensions of the material sample are $r_0=0.004m$ and $h_0=0.008m$ with the relative permittivity of $\varepsilon_r=2.5$ . The dimensions of the cylindrical waveguide are: $a=0.0762m$ and $c=0.15458m$ . The operating frequency is 2.45 GHz
Figure 5.4	Ratio of $E/F^{i}$ varies in the r direction at the different locations of z. The

	dimensions of the material sample are $r_0=0.01m$ and $h_0=0.02m$ with the relative permittivity of $\varepsilon_r=2.5$ . The dimensions of the cylindrical waveguide are: $a=0.0762m$ and $c=0.15458m$ The operating frequency is 2.45 $GH_Z$
Figure 5.5	Ratio of $E_z/E_z^i$ varies in the $r$ direction. The dimensions of the material sample are $r_0=0.02m$ and $h_0=0.001m$ with the relative permittivity of $\varepsilon_r=2.5$ . The dimensions of the cylindrical waveguide are: $a=0.0762m$ and $c=0.15458m$ . The operating frequency is 2.45 GHz
Figure 5.6	Ratio of $E_z/E_z^i$ varies in the z direction at $r=0.0004m$ . The dimensions of the material sample are $r_0=0.004m$ and $h_0=0.044m$ with the relative permittivity of $\varepsilon_r=2.5$ . The dimensions of the cylindrical waveguide are: $a=0.0762m$ and $c=0.15458m$ . The operating frequency is 2.45 GHz
Figure D.1	Geometry of an inhomogeneous dielectric sphere

#### **CHAPTER 1**

#### INTRODUCTION

The research reported in this dissertation was motivated by the investigation of microwave heating of material samples. Microwave heating techniques have been widely utilized in many industrial process [1]. However, the question of why the microwave heating is much faster and more efficient than the conventional thermal heating in promoting the chemical reaction and the heating of materials is still unanswered. Since the microwave heating of material samples is usually conducted within an energized electromagnetic cavity, to provide an answer to this question it is essential to study the interaction of the microwave field with a material sample in an electromagnetic cavity.

To understand the coupling of the microwave energy into molecules of a material sample, it is necessary to determine the microwave (EM) energy absorption rate (or dissipated microwave power density) P at any point inside the material sample. To determine this P, it is essential to quantify accurately the distribution of the induced electric field at any point inside the material sample. Therefore, the key factor to understand the heating of a material sample in an energized electromagnetic cavity is to quantify the induced electric field inside the material sample.

Recently, some studies [3]-[8] on this subject based on the finite difference-time domain method, the finite element method, or the method of lines have been reported.

However, numerical results of these methods can not provide physical pictures of how the microwave field interacts with a material sample. The method which gives more physical pictures is to solve Maxwell's equations in an electromagnetic cavity in the presence of a material sample based on an Electric Field Integral Equation (EFIE) or a Magnetic Field Integral Equation (MFIE) and the dyadic Green's function in an electromagnetic cavity, Tai [9]. However, in many studies involving this type of problem [9], [15]-[21], the unknown induced electric field inside the material sample is expanded in terms of the normal cavity electric modes which are completely solenoidal. This is not correct for the following reason. When a material sample is placed in the cavity, the initial cavity electric field will induce electric charges on the surface of the material sample if it is of finite size or at the heterogeneity boundaries if it is heterogeneous. Thus, the divergence of the electric field will not be zero at the location of the induced charges, or the divergence of the electric field will not vanish at all points in the cavity. Therefore, the normal cavity electric modes which are solenoidal are not sufficient to represent the unknown induced electric field inside the material sample. Additional eigenfunctions which are irrotational will be needed.

In this dissertation, a complete set of vector wave functions which include both solenoidal and irrotational functions are employed and the electric field (and magnetic field) integral equation is derived based on the expansion of these vector wave functions. In the solving of the integral equation, the convergence property of the derived dyadic Green's function plays a vital role, thus several mathematical methods are explored to increase the convergence rate of the dyadic Green's function. The same problem was also solved by the mode-matching method when the material sample is homogeneous and of

simple cylindrical geometry. The results of this method provide a check for the validity of that generated by the integral equation method.

In Chapter 2, the properties of the three vector wave functions  $\vec{L}_{nml}$ ,  $\vec{M}_{nml}$  and  $\vec{N}_{nml}$  in a rectangular cavity are introduced. The orthogonality and completeness of these three vector wave functions are proved. Using these three vector wave functions as a complete set of eigenfunctions to expand the unknown electric field, we derive the Electric Field Integral Equation (EFIE). On the other hand, based on the expansion for the unknown magnetic field, we obtain the Magnetic Field Integral Equation (MFIE). The EFIE and the MFIE are shown to be consistent even though different approaches for deriving them are employed.

In Chapter 3, Galerkin's method is applied to solve the EFIE derived in Chapter 2 and the convergence property of the dyadic Green's function in the EFIE is studied. Due to the slow convergence rate of the dyadic Green's function, the infinite triple summation over the cavity eigenfunctions is reduced to the infinite double summation, and the infinite double summation is then estimated by a finite double summation plus an infinite single summation using the Poisson summation formula. Numerical results show that the electromagnetic fields distribution in the material sample are strongly dependent on the geometry and the dielectric parameters of the material sample. For some material samples with specific geometries, a scheme of separating the material sample into the boundary layer region and the interior region is proposed. This scheme tends to improve the convergence of numerical results and also to save computation time.

In Chapter 4, the microwave heating of a material sample in a cylindrical cavity is

studied. Theoretical analysis of the induced electric field inside a material sample placed within an energized cylindrical cavity is more involved than that of a rectangular cavity case as studied in Chapter 2 and Chapter 3. The vector wave functions  $\vec{L}_{nml}$ ,  $\vec{M}_{nml}$  and  $\vec{N}_{nml}$  in a cylindrical cavity are derived and normalized. The infinite triple and double summation formats of the dyadic Green's function in terms of these vector wave functions are provided. The numerical calculation is conducted for material samples with simple or complex geometry and homogeneous or heterogeneous composition. Numerical results agree well with the theoretical estimation.

In Chapter 5, the mode-matching method is employed to analyze the induced electric field distribution in homogeneous material samples with simple cylindrical geometries placed in an energized cylindrical cavity. In this method, the whole cavity is divided into three waveguide regions and the eigenmodes in the inhomogeneously filled waveguide which contains the material sample are derived. The electromagnetic fields in each region are then expressed as infinite sums of the eigenmodes, and their tangential components are matched at the junction surfaces between different regions. Numerical calculation shows that the resultant matrix is sparse and the number of eigenmodes needed in the summation is reduced compared with the integral equation method while the convergence rate is improved. The numerical results of the mode-matching method are found to be consistent with the corresponding results of the integral equation method reported in Chapter 4.

Some derivations and proofs that are useful in this dissertation are provided in Appendices. Appendix A compares the derivation of the dyadic Green's function with that

of Rahmat-Samii [11] and explains the discrepancy of the expression in [11]. Appendix B proves the identity of

$$\sum_{n}\sum_{m}\sum_{l}\left[\vec{L}_{nml}(\vec{r}_{0})\vec{L}_{nml}(\vec{r}) + \vec{N}_{nml}(\vec{r}_{0})\vec{N}_{nml}(\vec{r}) + \vec{M}_{nml}(\vec{r}_{0})\vec{M}_{nml}(\vec{r})\right] = \bar{I}\delta(\vec{r} - \vec{r}_{0}) \quad (1.1)$$

which is essential in the proof of the completeness of the vector wave functions  $\vec{L}_{nml}$ ,  $\vec{M}_{nml}$  and  $\vec{N}_{nml}$ . Appendix C provides a detailed derivation of the infinite double summation reduced from the infinite triple summation and this reduction is important in the numerical calculation. Appendix D gives the electric field in an inhomogeneous dielectric sphere which includes two regions of different dielectric materials induced by a uniform static electric field and this result is used as a theoretical estimation in Chapter 4.

#### **CHAPTER 2**

# INTERACTON OF ELECTROMAGNETIC FIELDS WITH A MATERIAL SAMPLE PLACED WITHIN A RECTANGUALR CAVITY

In this chapter, the interaction of the electromagnetic field with a material sample placed in a rectangular cavity is studied. We will consider a material sample of finite dimensions with dielectric parameters of relative permittivity  $\varepsilon = \varepsilon' + j\varepsilon''$ , permeability  $\mu$ , and conductivity  $\sigma$ , and assume that a certain electromagnetic mode of a rectangular cavity has been maintained before a material sample is introduced. Our goal is to determine the total electromagnetic fields inside the material sample induced by the initial cavity electromagnetic fields, and the perturbed electromagnetic fields in the vicinity of the material sample as well.

In many studies involving this type of problem[9], [15]-[20], the unknown induced electric field inside the material sample is expanded in terms of the normal cavity electric eigenmodes which are completely solenoidal. This is not correct for the following reason. When a material sample is placed in the cavity, the initial cavity electric field will induce electric charges on the surface of the material sample if it is of finite size or at the heterogeneity boundaries if it is heterogeneous. Thus, the divergence of the electric field

will not be zero at the location of the induced charges, or the divergence of the electric field will not vanish at all points in the cavity. Therefore, the normal cavity electric eigenmodes which are solenoidal are not sufficient to represent the unknown induced electric field inside the material sample. Additional eigenmodes which are irrotational will be needed. In our study, a complete set of vector wave functions which include both solenoidal and irrotational functions are employed.

The vector wave functions are the building blocks of the eigenfunction expansions of various kinds of dyadic Green's functions [9]. These functions were first introduced by Hansen [60], [61] and [62] in formulating certain electromagnetic problems. The effectiveness of these functions was recognized by Stratton [23] who, for example, reformulated Mie's theory of the diffraction of a plane electromagnetic wave by a sphere using the spherical vector wave functions. In his original work [60] Hansen introduced three kinds of vector wave functions, denoted by  $\vec{L}$ ,  $\vec{M}$  and  $\vec{N}$ , which are the solutions of the homogeneous vector Helmholtz equations. Such a presentation was followed by Stratton [23] and by Morse and Feshbach [42].

In this study, we use the three vector wave functions  $\vec{L}_{nml}$ ,  $\vec{M}_{nml}$  and  $\vec{N}_{nml}$  as the basis functions to expand the unknown induced electric field inside the cavity. We will show that the vector wave function  $\vec{M}_{nml}$  are the normal TE modes,  $\vec{N}_{nml}$  are the normal TM modes and  $\vec{L}_{nml}$  are the so-called zero frequency modes which are irrotational. Also the orthogonality and completeness of the vector wave functions  $\vec{L}_{nml}$ ,  $\vec{M}_{nml}$  and  $\vec{N}_{nml}$  will be proved to assure that they form a complete and orthogonal set of basis functions.

An Electric Field Integral Equation (*EFIE*) is constructed when the electric dyadic Green's function is derived based on these vector wave functions  $\vec{L}_{nml}$ ,  $\vec{M}_{nml}$  and  $\vec{N}_{nml}$ .

Although there is a material sample inside the rectangular cavity, the divergence of the magnetic field vanishes at all points inside the cavity. The solenoidal eigenfunctions can form a complete set of basis functions within the space of solenoidal vector fields but not within the space of all vector fields [28]. Thus, we can use the simple cavity magnetic eigenfunctions which are solenoidal to expand the unknown magnetic field inside the cavity and the Magnetic Field Integral Equation (MFIE) is obtained after the magnetic dyadic Green's function is derived. We will show that the EFIE is equivalent to the MFIE and we will compare our results with those of Rahmat-Samii [11]. They are almost identical except a minus sign. After carefully examining the derivation and the results of [11], we have found an error of a minus sign in [11].

The outline of this chapter is as follows: Vector wave functions  $\vec{L}_{nml}$ ,  $\vec{M}_{nml}$ ,  $\vec{N}_{nml}$  and their properties are introduced in Section 2.1. Based on Maxwell's equations, we obtain the electric dyadic Green's function and EFIE in Section 2.2. In Section 2.3, a MFIE is derived based on the magnetic field expansion and a magnetic dyadic Green's function. The results of EFIE and MFIE are compared and the explanation is given in Section 2.4.

#### 2.1 Vector Wave Functions in Rectangular Cavities

# 2.1.1 Definitions for Vector Wave Functions $\vec{L}_{nml}$ , $\vec{M}_{nml}$ and $\vec{N}_{nml}$ in Rectangular Cavities

The definitions of vector wave functions  $\vec{L}_{nml}$ ,  $\vec{M}_{nml}$  and  $\vec{N}_{nml}$  in rectangular cavities can be found in [2], [9] and [23] as

$$\hat{L}_{nml} = \frac{1}{k_{nml}} (\nabla \phi_{nml}^L) \tag{2.1}$$

$$\vec{M}_{nml} = \nabla \times (\hat{z} \phi_{nml}^M) \tag{2.2}$$

$$\vec{N}_{nml} = \frac{1}{k_{nml}} \nabla \times \nabla \times (\hat{z} \phi_{nml}^{N})$$
 (2.3)

where all the scalar wave functions  $\phi_{nml}$  which yield the vector wave functions  $\vec{L}_{nml}$ ,  $\vec{M}_{nml}$  and  $\vec{N}_{nml}$  satisfy the scalar Helmholtz equation  $(\nabla^2 + k_{nml}^2)\phi_{nml} = 0$  and the subscripts n, m, and l are used to identify the eigenmodes in a cavity. The vector wave functions  $\vec{L}_{nml}$ ,  $\vec{M}_{nml}$  and  $\vec{N}_{nml}$  also need to satisfy the boundary conditions on the perfectly conducting walls of the cavity as:

$$\hat{n} \times \hat{L}_{nml} = 0 \tag{2.4}$$

$$\hat{n} \times \overrightarrow{M}_{nml} = 0 \tag{2.5}$$

$$\hat{n} \times \vec{N}_{nml} = 0 \tag{2.6}$$

Based on the definitions of the vector wave functions  $\vec{L}_{nml}$ ,  $\vec{M}_{nml}$  and  $\vec{N}_{nml}$ , it is easy to show that these vector wave functions have the following properties:

$$\nabla \cdot \overrightarrow{M}_{nml} = 0 \tag{2.7}$$

$$\nabla \cdot \vec{N}_{nml} = 0 \tag{2.8}$$

$$\nabla \times \dot{L}_{nml} = 0 \tag{2.9}$$

That is, the vector wave functions  $\overrightarrow{M}_{nml}$  and  $\overrightarrow{N}_{nml}$  are solenoidal and  $\overrightarrow{L}_{nml}$  is irrotational.

The first complete theory for the spectrum of modes in a cavity was presented by Kurokawa [12]. Helmholtz's theorem states that a general vector field has both a solenoidal and an irrotational part and may be derived from a vector and a scalar potential. According to Helmholtz's theorem, the electric field in the interior of a volume V bounded by a closed surface S can be expressed in the form [2], [12] of

$$\vec{E}(\hat{r}) = -\nabla \left[ \int_{V} \frac{\nabla_{0} \cdot \vec{E}(\hat{r}_{0})}{4\pi R} dV_{0} + \oint_{S} \frac{\hat{n} \cdot \vec{E}(\hat{r}_{0})}{4\pi R} dS_{0} \right] 
+ \nabla \times \left[ \int_{V} \frac{\nabla_{0} \times \vec{E}(\hat{r}_{0})}{4\pi R} dV_{0} + \oint_{S} \frac{\hat{n} \times \vec{E}(\hat{r}_{0})}{4\pi R} dS_{0} \right]$$
(2.10)

where  $R = |\vec{r} - \vec{r}_0|$  and  $\hat{n}$  is the unit inward normal to the surface S. This theorem gives the conditions for which the electric field is a pure solenoidal or a pure irrotational field.

The pure solenoidal field must satisfy the conditions  $\nabla \cdot \vec{E} = 0$  in volume V and  $\hat{n} \cdot \vec{E} = 0$  on the closed surface S, in which case there is no volume or surface charge associated with the field. In a similar way there are two conditions that must be met in

order for a field to be a pure irrotational or lamellar field, namely,  $\nabla \times \vec{E} = 0$  in volume V and  $\hat{n} \times \vec{E} = 0$  on the closed surface S.

For a cavity with perfectly conducting walls the boundary condition  $\hat{n} \times \vec{E} = 0$  must hold on the cavity surface S. In general,  $\hat{n} \cdot \vec{E}$  does not vanish, and is not required to vanish, on S. Hence the electric field in a cavity with perfectly conducting walls is generally not a pure solenoidal nor a lamellar field. In other words, pure solenoidal and pure irrotational vector eigenmodes are difficult to find analytically.

In the integral equation method or the moment method, the basis expansion for the unknown electric field is necessary. That is, we need a set of complete orthogonal basis functions to expand the unknown electric field and the basis expansion for the unknown electric field will converge much better if we use the basis functions that satisfy the same boundary conditions as the unknown electric field we are expanding [1]. From a mathematical point of view, it really does not matter whether the basis functions are pure solenoidal or pure irrotational as long as they form a complete set of basis functions. Based on the definitions and properties of the vector wave functions  $\vec{L}_{nml}$ ,  $\vec{M}_{nml}$  and  $\overrightarrow{N}_{nml}$ , we can choose the vector wave functions  $\overrightarrow{L}_{nml}$ ,  $\overrightarrow{M}_{nml}$  and  $\overrightarrow{N}_{nml}$  as a set of expansion basis functions after we prove that they are orthogonal and complete, where  $\vec{L}_{nml}$  will be referred to as pure irrotational modes, while  $\vec{M}_{nml}$  and  $\vec{N}_{nml}$  will be referred to as solenoidal modes but will not be pure solenoidal modes. All these vector wave functions can be called the short-circuit modes because they satisfy the boundary conditions

$$\hat{n} \times \vec{E} = 0$$

on S. In spite of the lack of purity in the short-circuit modes, in many instances non-pure solenoidal modes turn out to be sufficient to express certain electric field distributions for which  $\hat{n} \cdot \hat{E}$  is not zero on S.

# 2.1.2 Expressions for Vector Wave Functions $\vec{L}_{nml}$ , $\vec{M}_{nml}$ and $\vec{N}_{nml}$ in Rectangular Cavities

In order to obtain the numerical solution of the unknown induced electric field, we need to know the expressions for the vector wave functions  $\vec{L}_{nml}$ ,  $\vec{M}_{nml}$  and  $\vec{N}_{nml}$  based on their definitions given by eqs. (2.1) to (2.6).

The rectangular cavity under consideration has the geometry shown in Figure 2.1.

#### 1. Expression for vector wave function $\hat{L}_{nml}$ .

Based on the definition of the vector wave function  $\vec{L}_{nml}$ , we have

$$\hat{L}_{nml} = \frac{1}{k_{nml}} (\nabla \phi_{nml}^L) \tag{2.11}$$

$$(\nabla^2 + k_{nml}^2) \phi_{nml}^L = 0 (2.12)$$

Applying the variables separation method to eq. (2.12), we obtain the solution of the scalar function  $\phi_{nml}^{L}$  as

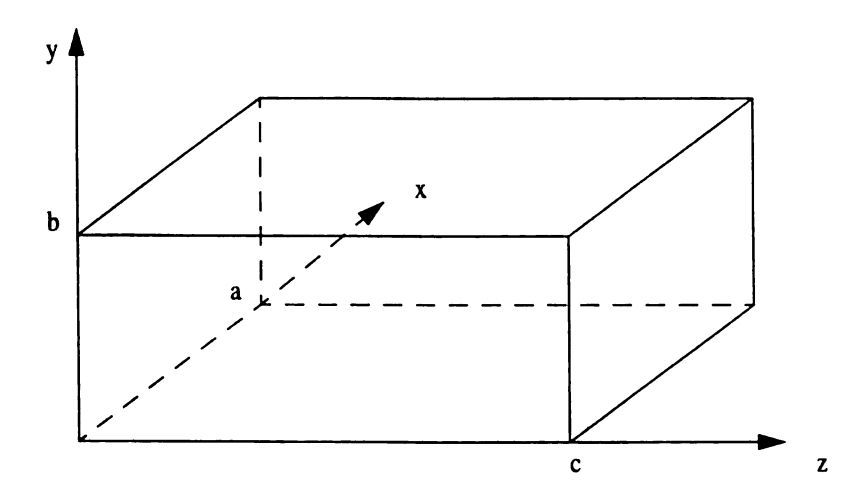


Figure 2.1 A rectangular cavity and the designation of the coordinate system

$$\phi_{nml}^{L} = A_{nml} \begin{cases} \cos(k_x x) \\ \sin(k_x x) \end{cases} \begin{cases} \cos(k_y y) \\ \sin(k_y y) \end{cases} \begin{cases} \cos(k_z z) \\ \sin(k_z z) \end{cases}$$
 (2.13)

where  $A_{nml}$  is an unknown constant which will be determined by the normalization of the

vector wave function  $\hat{L}_{nml}$  and  $k_x^2 + k_y^2 + k_z^2 = k_{nml}^2$ . Then the three components of the

vector wave function  $\hat{L}_{nml}$  can be expressed as

$$L_{nmlx} = \frac{A_{nml}}{k_{nml}} k_x \begin{cases} -\sin(k_x x) \\ \cos(k_x x) \end{cases} \begin{cases} \cos(k_y y) \\ \sin(k_y y) \end{cases} \begin{cases} \cos(k_z z) \\ \sin(k_z z) \end{cases}$$
(2.14)

$$L_{nmly} = \frac{A_{nml}}{k_{nml}} k_y \begin{cases} \cos(k_x x) \\ \sin(k_x x) \end{cases} \begin{cases} -\sin(k_y y) \\ \cos(k_z z) \\ \cos(k_z z) \end{cases}$$
(2.15)

$$L_{nmlz} = \frac{A_{nml}}{k_{nml}} k_z \begin{cases} \cos(k_x x) \\ \sin(k_x x) \end{cases} \begin{cases} \cos(k_y y) \\ \sin(k_y y) \end{cases} \begin{cases} -\sin(k_z z) \\ \cos(k_z z) \end{cases}$$
(2.16)

Based on boundary conditions given by eq. (2.4), the vector wave function  $\hat{L}_{nml}$  is derived as

$$\hat{L}_{nml} = \frac{A_{nml}}{k_{nml}} \left[ \hat{x} \frac{n\pi}{a} \cos\left(\frac{n\pi}{a}x\right) \sin\left(\frac{m\pi}{b}y\right) \sin\left(\frac{l\pi}{c}z\right) + \hat{y} \frac{m\pi}{b} \sin\left(\frac{n\pi}{a}x\right) \cos\left(\frac{m\pi}{b}y\right) \\
\sin\left(\frac{l\pi}{c}z\right) + \hat{z} \frac{l\pi}{c} \sin\left(\frac{n\pi}{a}x\right) \sin\left(\frac{m\pi}{b}y\right) \cos\left(\frac{l\pi}{c}z\right) \right]$$
(2.17)

where  $k_{nml}^2 = \left(\frac{n\pi}{a}\right)^2 + \left(\frac{m\pi}{b}\right)^2 + \left(\frac{l\pi}{c}\right)^2$  and the expression for the scalar function  $\phi_{nml}^L$  is given by

$$\phi_{nml}^{L} = A_{nml} \sin\left(\frac{n\pi}{a}x\right) \sin\left(\frac{m\pi}{b}y\right) \sin\left(\frac{l\pi}{c}z\right)$$
 (2.18)

#### 2. Expression for vector wave function $\overrightarrow{M}_{nml}$

Based on the definition of the vector wave function  $\overrightarrow{M}_{nml}$ , we have

$$\overrightarrow{M}_{nml} = \nabla \times (\widehat{z} \phi_{nml}^{M}) \tag{2.19}$$

$$(\nabla^2 + k_{nml}^2)\phi_{nml}^M = 0 (2.20)$$

Using the variables separation method, the solution of the scalar function  $\phi_{nml}^{M}$  is given by

$$\phi_{nml}^{M} = B_{nml} \begin{cases} \cos(k_x x) \\ \sin(k_x x) \end{cases} \begin{cases} \cos(k_y y) \\ \sin(k_y y) \end{cases} \begin{cases} \cos(k_z z) \\ \sin(k_z z) \end{cases}$$
 (2.21)

where  $B_{nml}$  is an unknown constant which will be determined by the normalization of the vector wave function  $\overrightarrow{M}_{nml}$  and  $k_x^2 + k_y^2 + k_z^2 = k_{nml}^2$ . The two components of the vector wave function  $\overrightarrow{M}_{nml}$  can then be expressed as

$$M_{nmlx} = B_{nml}k_y \begin{cases} \cos(k_x x) \\ \sin(k_x x) \end{cases} \begin{cases} -\sin(k_y y) \\ \cos(k_y y) \end{cases} \begin{cases} \cos(k_z z) \\ \sin(k_z z) \end{cases}$$
(2.22)

$$M_{nmly} = -B_{nml}k_x \begin{cases} -\sin(k_x x) \\ \cos(k_x x) \end{cases} \begin{cases} \cos(k_y y) \\ \sin(k_y y) \end{cases} \begin{cases} \cos(k_z z) \\ \sin(k_z z) \end{cases}$$
(2.23)

Based on boundary conditions given by eq. (2.5), the vector wave function  $\vec{M}_{nml}$  is derived as

$$\overrightarrow{M}_{nml} = B_{nml} \left[ -\hat{x} \frac{m\pi}{b} \cos\left(\frac{n\pi}{a}x\right) \sin\left(\frac{m\pi}{b}y\right) \sin\left(\frac{l\pi}{c}z\right) + \hat{y} \frac{n\pi}{a} \sin\left(\frac{n\pi}{a}x\right) \right]$$

$$\cos\left(\frac{m\pi}{b}y\right) \sin\left(\frac{l\pi}{c}z\right)$$
(2.24)

where  $k_{nml}^2 = \left(\frac{n\pi}{a}\right)^2 + \left(\frac{m\pi}{b}\right)^2 + \left(\frac{l\pi}{c}\right)^2$  and the expression for the scalar function  $\phi_{nml}^M$  is given by

$$\phi_{nml}^{M} = B_{nml} \cos\left(\frac{n\pi}{a}x\right) \cos\left(\frac{m\pi}{b}y\right) \sin\left(\frac{l\pi}{c}z\right)$$
 (2.25)

#### 3. Expression for vector wave function $\vec{N}_{nml}$

Based on the definition of the vector wave function  $\vec{N}_{nml}$ , we have

$$\vec{N}_{nml} = \frac{1}{k_{nml}} \nabla \times \nabla \times (\hat{z} \phi_{nml}^{N})$$
 (2.26)

$$(\nabla^2 + k_{nml}^2) \phi_{nml}^N = 0 (2.27)$$

In a similar way as before, the variables separation method is applied to eq. (2.27), and the solution of the scalar function  $\phi_{nml}^{N}$  becomes

$$\phi_{nml}^{N} = C_{nml} \begin{cases} \cos(k_x x) \\ \sin(k_x x) \end{cases} \begin{cases} \cos(k_y y) \\ \sin(k_z z) \end{cases} \begin{cases} \cos(k_z z) \\ \sin(k_z z) \end{cases}$$
 (2.28)

where  $C_{nml}$  is an unknown constant which will be determined by the normalization of the vector wave function  $\vec{N}_{nml}$  and  $k_x^2 + k_y^2 + k_z^2 = k_{nml}^2$ . The three components of the vector wave function  $\vec{N}_{nml}$  can then be expressed as

$$N_{nmlx} = \frac{C_{nml}}{k_{nml}} k_x k_z \begin{cases} -\sin(k_x x) \\ \cos(k_x x) \end{cases} \begin{cases} \cos(k_y y) \\ \sin(k_y y) \end{cases} \begin{cases} -\sin(k_z z) \\ \cos(k_z z) \end{cases}$$
(2.29)

$$N_{nmly} = \frac{C_{nml}}{k_{nml}} k_y k_z \begin{cases} \cos(k_x x) \\ \sin(k_x x) \end{cases} \begin{cases} -\sin(k_y y) \\ \cos(k_y y) \end{cases} \begin{cases} -\sin(k_z z) \\ \cos(k_z z) \end{cases}$$
(2.30)

$$N_{nmlz} = \frac{C_{nml}}{k_{nml}} (k_x^2 + k_y^2) \begin{cases} \cos(k_x x) \\ \sin(k_x x) \end{cases} \begin{cases} \cos(k_y y) \\ \sin(k_y y) \end{cases} \begin{cases} \cos(k_z z) \\ \sin(k_z z) \end{cases}$$
(2.31)

Based on boundary conditions given by eq. (2.6), the vector wave function  $\vec{N}_{nml}$  is derived as

$$\vec{N}_{nml} = \frac{C_{nml}}{k_{nml}} \left[ -\hat{x} \frac{n\pi}{a} \frac{l\pi}{c} \cos\left(\frac{n\pi}{a}x\right) \sin\left(\frac{m\pi}{b}y\right) \sin\left(\frac{l\pi}{c}z\right) - \hat{y} \frac{m\pi}{b} \frac{l\pi}{c} \sin\left(\frac{n\pi}{a}x\right) \right] \\
\cos\left(\frac{m\pi}{b}y\right) \sin\left(\frac{l\pi}{c}z\right) + \hat{z} \left(\left(\frac{n\pi}{a}\right)^2 + \left(\frac{m\pi}{b}\right)^2\right) \sin\left(\frac{n\pi}{a}x\right) \sin\left(\frac{m\pi}{b}y\right) \cos\left(\frac{l\pi}{c}z\right) \right]$$
(2.32)

where  $k_{nml}^2 = \left(\frac{n\pi}{a}\right)^2 + \left(\frac{m\pi}{b}\right)^2 + \left(\frac{l\pi}{c}\right)^2$  and the expression for the scalar function  $\phi_{nml}^N$  is given by

$$\phi_{nml}^{N} = C_{nml} \sin\left(\frac{n\pi}{a}x\right) \sin\left(\frac{m\pi}{b}y\right) \cos\left(\frac{l\pi}{c}z\right)$$
 (2.33)

From all of these expressions for the vector wave functions (2.17), (2.24), and (2.32), we can identify that  $\overrightarrow{M}_{nml}$  are the normal TE modes and  $\overrightarrow{N}_{nml}$  are the normal TM modes in a rectangular cavity [10]. We can also identify  $\overrightarrow{L}_{nml}$  as the so-called zero-frequency modes. It is noted that for these three vector eigenfunctions, the eigenvalues

$$k_{nml}^2 = \left(\frac{n\pi}{a}\right)^2 + \left(\frac{m\pi}{b}\right)^2 + \left(\frac{l\pi}{c}\right)^2$$

are the same for the same indices. This will cause some degenerate modes.

Some field structures of the vector wave functions  $\vec{L}_{nml}$ ,  $\vec{M}_{nml}$  and  $\vec{N}_{nml}$  which represent electric fields have been plotted in Figure 2.2 to Figure 2.13.

Figure 2.2 to Figure 2.4 show the electric field structures for the eigenfunction  $L_{III}$ , where Figure 2.2 depicts for  $L_{IIIx}$  and  $L_{IIIy}$  in the x-y plane with z=c/4, Figure 2.3 depicts  $L_{IIIx}$  and  $L_{IIIz}$  in the x-z plane with y=b/4 and Figure 2.4 depicts  $L_{IIIy}$  and  $L_{IIIz}$  in the y-z plane with x=a/4. From Figure 2.2 to Figure 2.4, we observe that the normal components of the electric field decrease as the field point moves from the walls of the cavity towards the center of the cavity. There is a sink point at the center of the cavity for the eigenfunction  $L_{III}$ . Since the eigenfunction  $L_{III}$  is irrotational, and

$$\nabla \cdot \hat{L}_{111} = -k_{111} A_{111} \sin\left(\frac{\pi}{a}x\right) \sin\left(\frac{\pi}{b}y\right) \sin\left(\frac{\pi}{c}z\right)$$

where  $x \in [0, a]$ ,  $y \in [0, b]$  and  $z \in [0, c]$ . It is obvious that the minimum value of the divergence of the eigenfunction  $L_{III}$  occurs at the center of the cavity and the divergence of the eigenfunction  $L_{III}$  does not vanish at any point inside the cavity.

Figure 2.5-Figure 2.7 show the electric field structures for the eigenfunction  $M_{221}$ , where  $M_{221x}$  and  $M_{221y}$  in the x-y plane with z=c/4,  $M_{221x}$  and  $M_{221z}$  in the x-z plane with y=b/4, and  $M_{221y}$  and  $M_{221z}$  in the y-z plane with x=a/4 are plotted orderly in Figure 2.5 to Figure 2.7. Since  $M_{221z}$  is zero, there is only  $M_{221x}$  in Figure 2.6 and  $M_{221y}$  in Figure 2.7. Also we can observe that  $M_{221x}$  and  $M_{221y}$  form a rotational field in Figure 2.5.

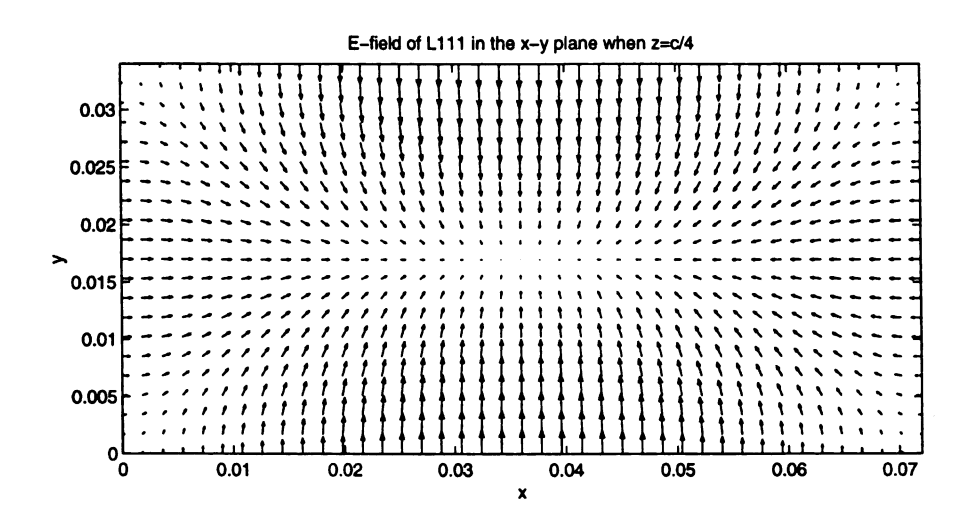


Figure 2.2 E-field structure of  $L_{111}$  in the x-y plane with z=c/4. The dimensions of the rectangular cavity are: a=0.072m, b=0.034m, and c=0.1163m.

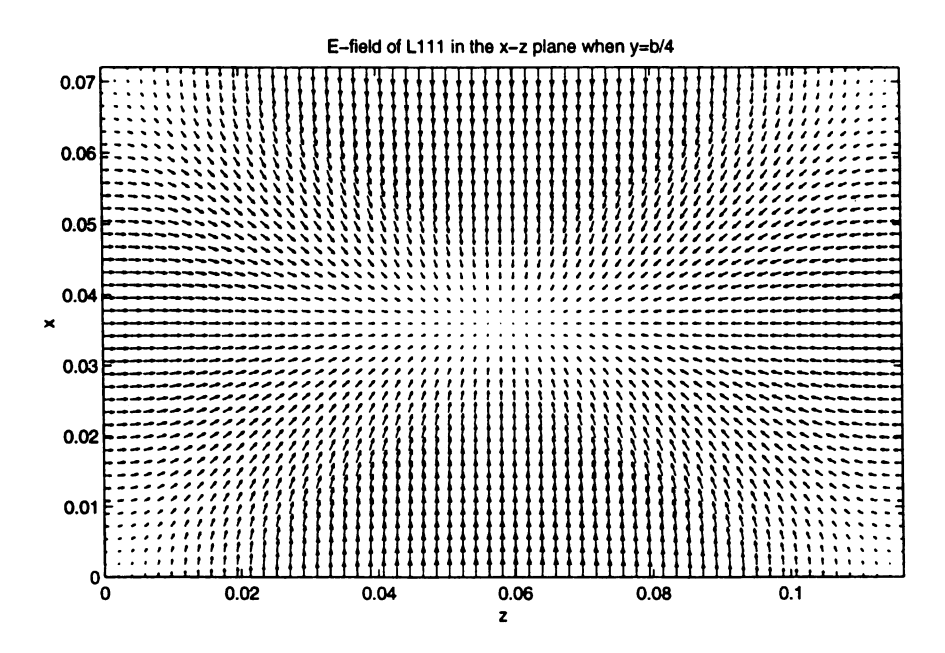


Figure 2.3 E-field structure of  $L_{111}$  in the x-z plane with y=b/4. The dimensions of the rectangular cavity are: a=0.072m, b=0.034m, and c=0.1163m.

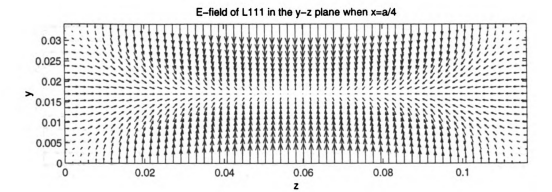


Figure 2.4 E-field structure of  $L_{111}$  in the y-z plane with x=a/4. The dimensions of the rectangular cavity are: a=0.072m, b=0.034m, and c=0.1163m.

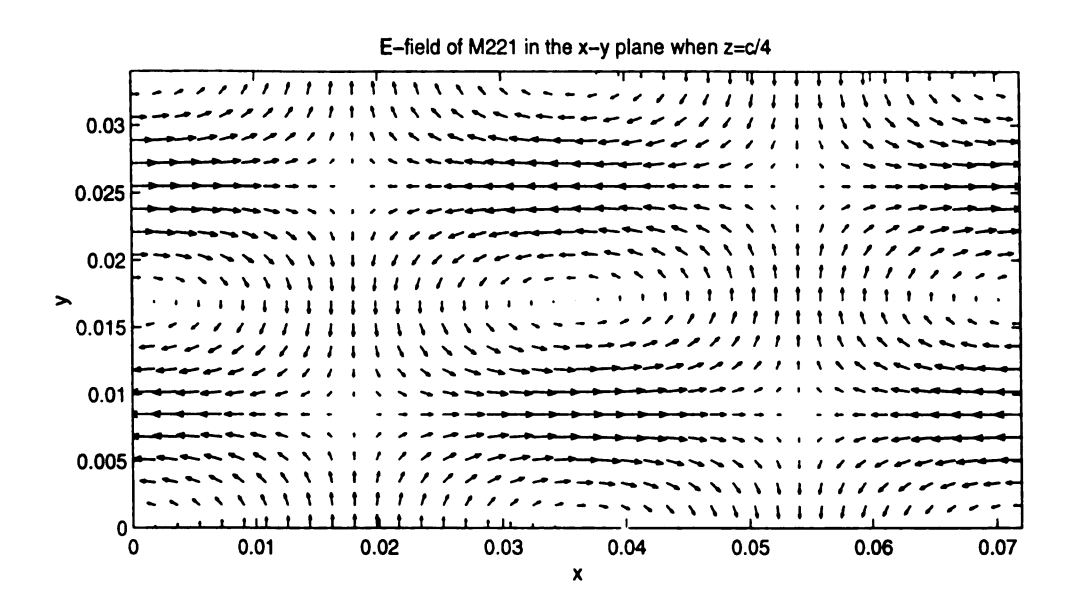


Figure 2.5 E-field structure of  $M_{221}$  in the x-y plane with z=c/4. The dimensions of the rectangular cavity are: a=0.072m, b=0.034m, and c=0.1163m.

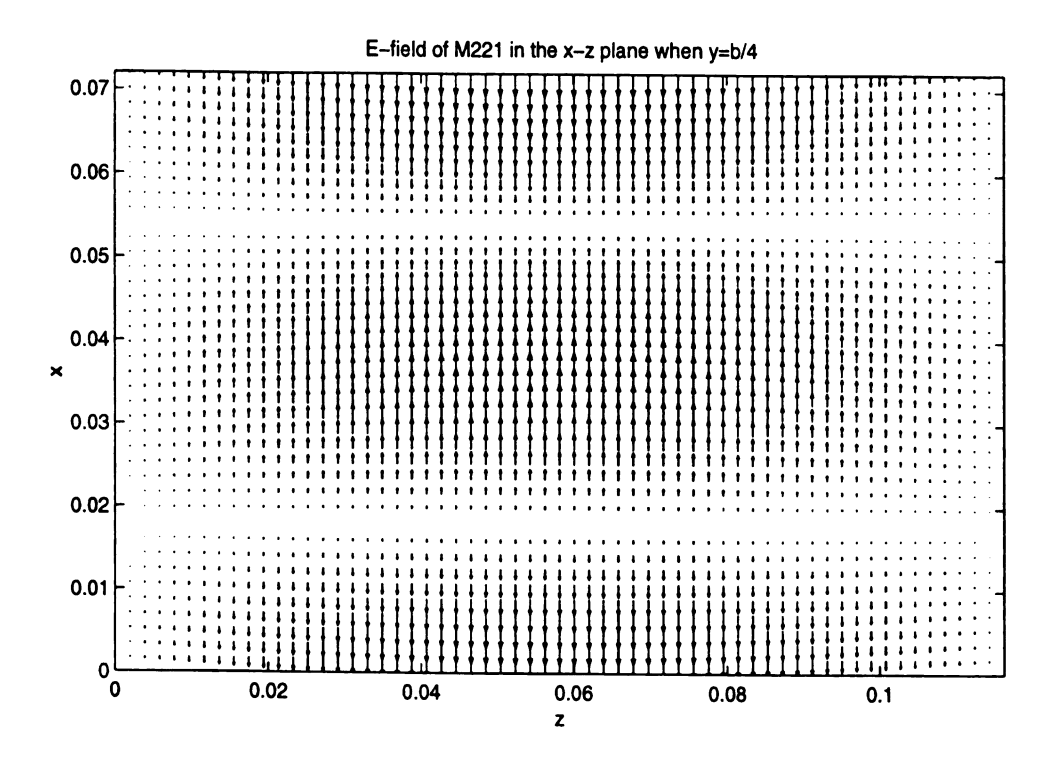


Figure 2.6 E-field structure of  $M_{221}$  in the x-z plane with y=b/4. The dimensions of the rectangular cavity are: a=0.072m, b=0.034m, and c=0.1163m.

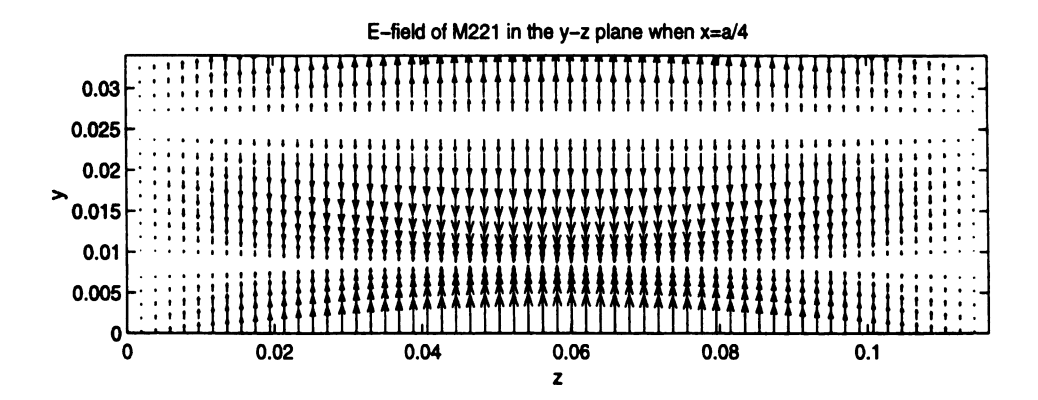


Figure 2.7 E-field structure of  $M_{221}$  in the y-z plane with x=a/4. The dimensions of the rectangular cavity are: a=0.072m, b=0.034m, and c=0.1163m.

Figure 2.8 to Figure 2.10 show the electric field structures for the eigenfunction  $N_{22I_1}$  where  $N_{22I_2}$  and  $N_{22I_2}$  in the x-y plane with z=c/4,  $N_{22I_2}$  and  $N_{22I_2}$  in the x-z plane with y=b/4, and  $N_{22I_2}$  and  $N_{22I_2}$  in the y-z plane with x=a/4 are plotted orderly in Figure 2.8 to Figure 2.10. For the eigenfunction  $N_{22I_1}$ ,  $N_{22I_2} = 0$  at x = a/4 and  $N_{22I_2} = 0$  at y = b/4. Because Figure 2.10 is plotted for  $N_{22I_2}$  and  $N_{22I_2}$  at the x = a/4 plane, there are only  $N_{22I_2}$  and  $N_{22I_2}$  and they form a rotational field, no sink or source points exist. Also Figure 2.9 is plotted at the y = b/4 plane,  $N_{22I_2}$  and  $N_{22I_2}$  form a rotational field at this plane.

Figure 2.11 to Figure 2.13 show the electric field structures for the eigenfunction  $L_{22I_x}$  where  $L_{22I_x}$  and  $L_{22I_y}$  in the x-y plane with z=c/4,  $L_{22I_x}$  and  $L_{22I_z}$  in the x-z plane with y=b/4, and  $L_{22I_y}$  and  $L_{22I_z}$  in the y-z plane with x=a/4 are plotted orderly in Figure 2.11 to Figure 2.13. For the eigenfunction  $L_{22I_x}$ ,  $L_{22I_x}=0$  at x=a/4 and  $L_{22I_y}=0$  at y=b/4. However, in Figure 2.12 and Figure 2.13,  $L_{22I_x}$  and  $L_{22I_z}$  in the x-z plane with y=b/4, and  $L_{22I_y}$  and  $L_{22I_z}$  in the y-z plane with x=a/4 do not form a rotational field. It looks like there are some sink points and source points in Figure 2.12 and Figure 2.13.

# 2.1.3 Vector Wave Functions $\vec{L}_{nml}$ , $\vec{M}_{nml}$ and $\vec{N}_{nml}$ Satisfy Vector Helmholtz Equation

Since the electric fields satisfy the vector Helmholtz equation, the basis functions which are used to expand the electric fields should also meet the same requirement. The vector Helmholtz equation is expressed as

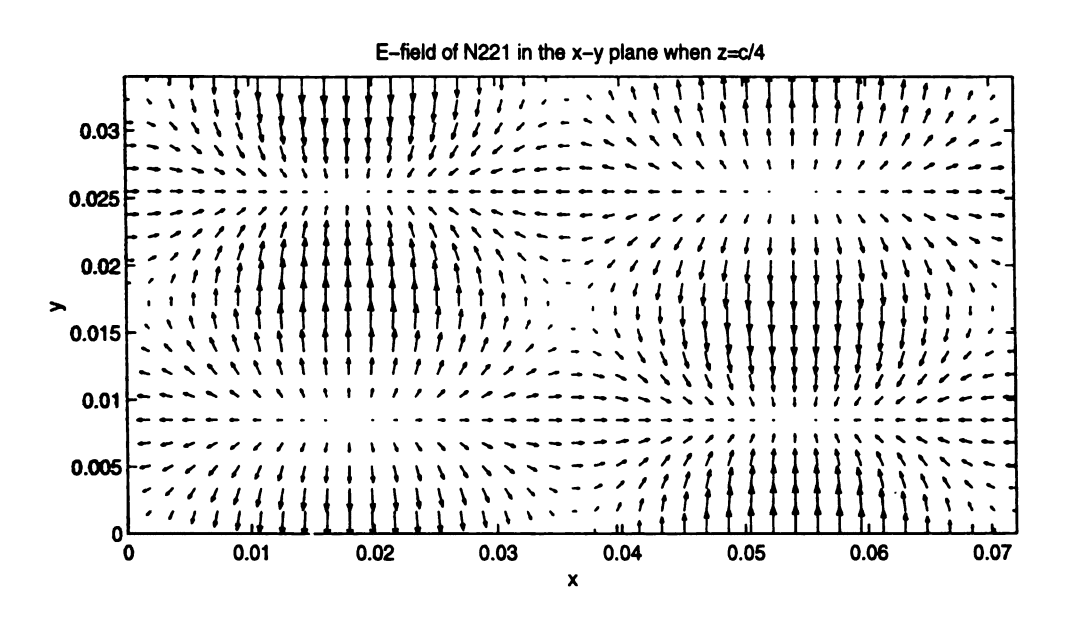


Figure 2.8 E-field structure of  $N_{221}$  in the x-y plane with z=c/4. The dimensions of the rectangular cavity are: a=0.072m, b=0.034m, and c=0.1163m.

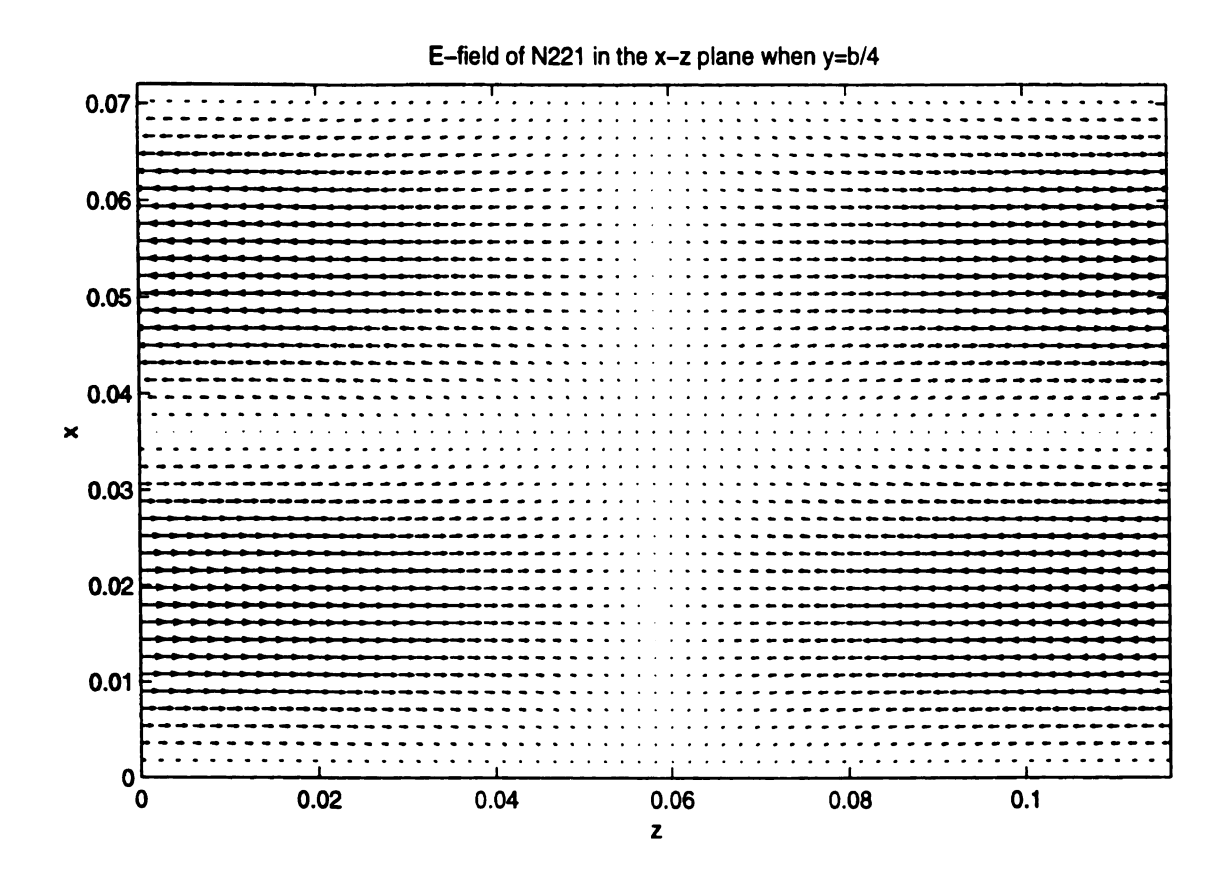


Figure 2.9 E-field structure of  $N_{221}$  in the x-z plane with y=b/4. The dimensions of the rectangular cavity are: a=0.072m, b=0.034m, and c=0.1163m.

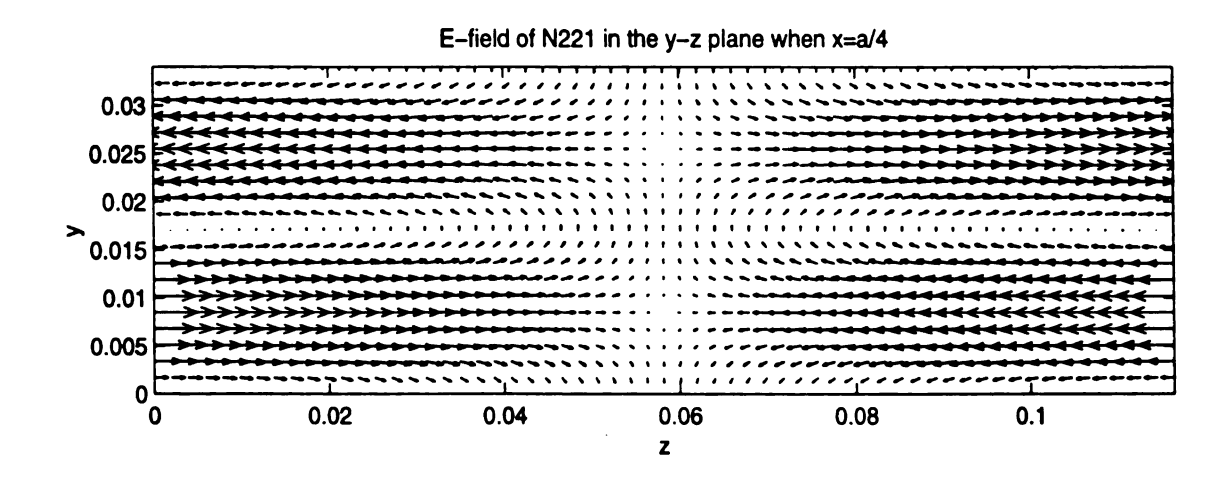


Figure 2.10 E-field structure of  $N_{221}$  in the y-z plane with x=a/4. The dimensions of the rectangular cavity are: a=0.072m, b=0.034m, and c=0.1163m.

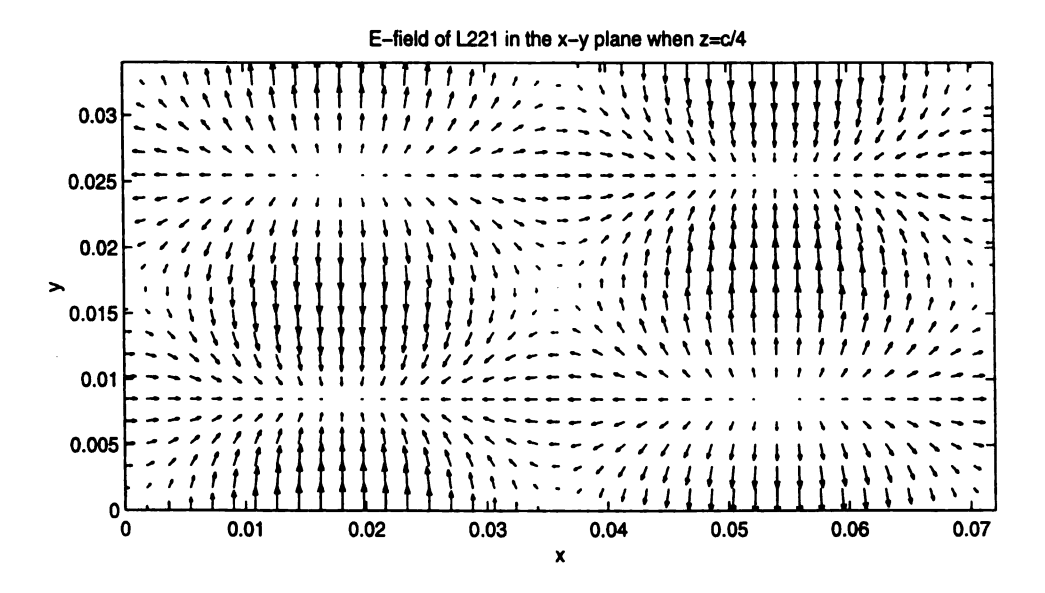


Figure 2.11 E-field structure of  $L_{221}$  in the x-y plane with z=c/4. The dimensions of the rectangular cavity are: a=0.072m, b=0.034m, and c=0.1163m.

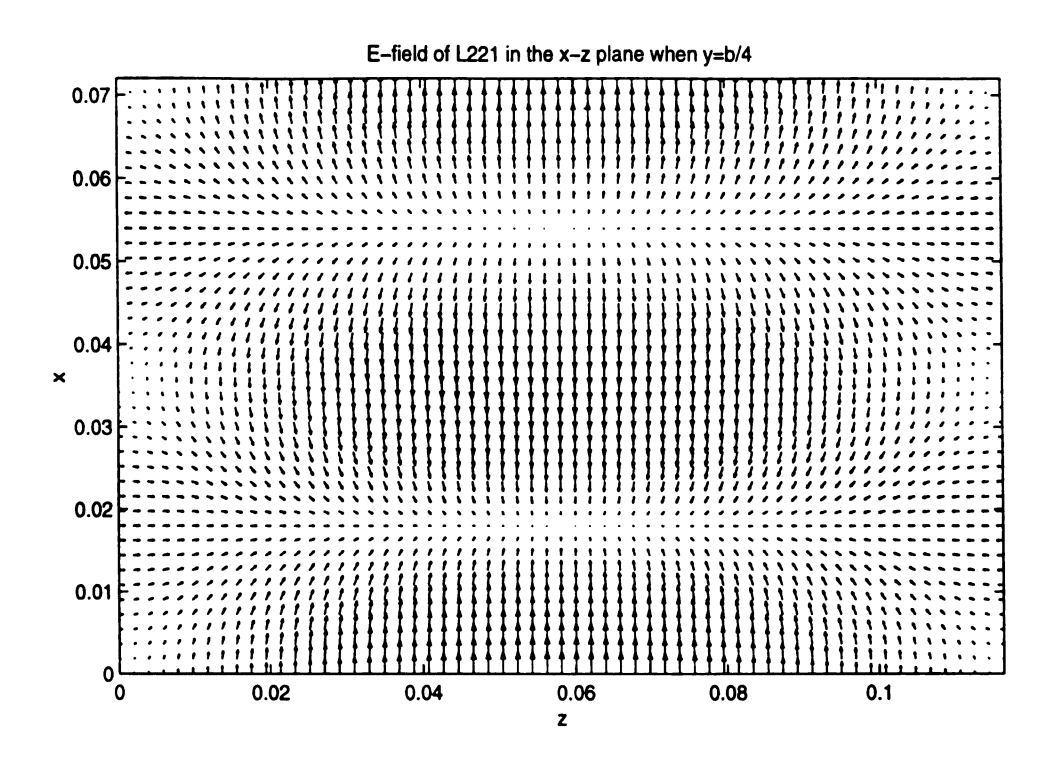


Figure 2.12 E-field structure of  $L_{221}$  in the x-z plane with y=b/4. The dimensions of the rectangular cavity are: a=0.072m, b=0.034m, and c=0.1163m.

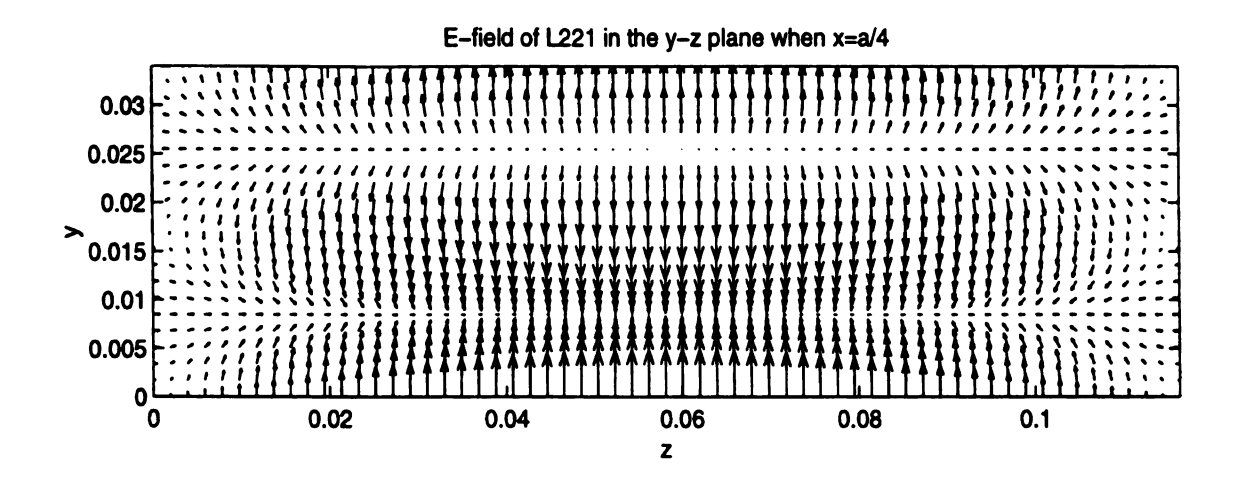


Figure 2.13 E-field structure of  $L_{221}$  in the y-z plane with x=a/4. The dimensions of the rectangular cavity are: a=0.072m, b=0.034m, and c=0.1163m.

$$\nabla^2 \vec{A} + k^2 \vec{A} = 0 \tag{2.34}$$

or

$$\nabla(\nabla \cdot \vec{A}) - \nabla \times \nabla \times \vec{A} + k^2 \vec{A} = 0$$
 (2.35)

### 1. Vector wave function $\hat{L}_{nml}$ satisfies the vector Helmholtz equation

Based on the property of the vector wave function  $\vec{L}_{nml}$  (2.9) and using eqs. (2.11) and (2.12), we have

$$\nabla \left(\nabla \cdot \vec{L}_{nml}\right) = \nabla \left(\nabla \cdot \frac{1}{k_{nml}} \nabla \phi_{nml}\right) = -k_{nml}^2 \vec{L}_{nml}$$
(2.36)

Therefore,

$$\nabla^2 \vec{L}_{nml} + k^2 \vec{L}_{nml} = \nabla \left( \nabla \cdot \vec{L}_{nml} \right) - \nabla \times \nabla \times \vec{L}_{nml} + k_{nml}^2 \vec{L}_{nml} = 0$$
 (2.37)

Namely, the vector wave function  $\hat{L}_{nml}$  satisfies the vector Helmholtz eq. (2.35).

### 2. Vector wave function $\overrightarrow{M}_{nml}$ satisfies the vector Helmholtz equation

Based on the property of the vector wave function  $\vec{M}_{nml}$  (2.7) and using eqs. (2.19) and (2.20), we have

$$\nabla \times \nabla \times \overrightarrow{M}_{nml} = -\nabla^2 \overrightarrow{M}_{nml} = -\hat{x} \nabla^2 M_{nmlx} - \hat{y} \nabla^2 M_{nmly}$$
 (2.38)

$$\nabla^2 M_{nmlx} = \nabla^2 \frac{\partial}{\partial y} \phi^M_{nml} = \frac{\partial}{\partial y} \nabla^2 \phi^M_{nml} = -k_{nml}^2 M_{nmlx}$$
 (2.39)

$$\nabla^2 M_{nmly} = -\nabla^2 \frac{\partial}{\partial x} \phi^M_{nml} = \frac{\partial}{\partial x} (\nabla^2 \phi^M_{nml}) = -k_{nml}^2 M_{nmly}$$
 (2.40)

Therefore,

$$\nabla \times \nabla \times \overrightarrow{M}_{nml} = -\nabla^2 \overrightarrow{M}_{nml} = k_{nml}^2 \overrightarrow{M}_{nml}$$
 (2.41)

or

$$\nabla^2 \overrightarrow{M}_{nml} + k_{nml}^2 \overrightarrow{M}_{nml} = 0 ag{2.42}$$

Thus, the vector wave function  $\overrightarrow{M}_{nml}$  satisfies the vector Helmholtz eq. (2.34).

## 3. Vector wave function $\vec{N}_{nml}$ satisfies the vector Helmholtz equation

Since the vector wave function  $\overrightarrow{N}_{nml}$  has the same property (2.8) as the vector wave function  $\overrightarrow{M}_{nml}$  has, using eqs. (2.26) and (2.27) and employing the same procedure as that used for the vector wave function  $\overrightarrow{M}_{nml}$ , we can obtain

$$\nabla \times \nabla \times \overrightarrow{N}_{nml} = -\nabla^2 \overrightarrow{N}_{nml} = k_{nml}^2 \overrightarrow{N}_{nml}$$
 (2.43)

i.e.

$$\nabla^2 \vec{N}_{nml} + k_{nml}^2 \vec{N}_{nml} = 0 \tag{2.44}$$

Therefore, the vector wave function  $\vec{N}_{nml}$  satisfies the vector Helmholtz eq. (2.34).

# **2.1.4** Orthogonality of the Vector Wave Functions $\vec{L}_{nml}$ , $\vec{M}_{nml}$ and $\vec{N}_{nml}$

That the vector wave functions  $\vec{L}_{nml}$ ,  $\vec{M}_{nml}$  and  $\vec{N}_{nml}$  are orthogonal mutually is necessary for them to form a set of basis functions in order to represent the unknown

electric field. We will prove that the vector wave functions are orthogonal for different indices by themselves and also orthogonal mutually.

#### 1. Vector wave functions $\overrightarrow{M}_{nml}$ are orthogonal for different indices.

We know the vector identity of

$$\nabla \cdot (\overrightarrow{M}_m \times \nabla \times \overrightarrow{M}_n - \overrightarrow{M}_n \times \nabla \times \overrightarrow{M}_m) = \overrightarrow{M}_n \cdot \nabla \times \nabla \times \overrightarrow{M}_m - \overrightarrow{M}_m \cdot \nabla \times \nabla \times \overrightarrow{M}_n \quad (2.45)$$

So

$$\int_{V} (\vec{M}_{n} \cdot \nabla \times \nabla \times \vec{M}_{m} - \vec{M}_{m} \cdot \nabla \times \nabla \times \vec{M}_{n}) dv$$

$$= \int_{V} \nabla \cdot (\vec{M}_{m} \times \nabla \times \vec{M}_{n} - \vec{M}_{n} \times \nabla \times \vec{M}_{m}) dv$$

$$= \oint_{V} \hat{n} \cdot (\vec{M}_{m} \times \nabla \times \vec{M}_{n} - \vec{M}_{n} \times \nabla \times \vec{M}_{m}) ds$$

$$= \oint_{S} \{ [(\hat{n} \times \vec{M}_{n}) \cdot (\nabla \times \vec{M}_{m})] - [(\hat{n} \times \vec{M}_{m}) \cdot (\nabla \times \vec{M}_{n})] \} ds$$
(2.46)

where the integration region is over the cavity volume V or the surface S of the cavity wall.

Because  $\hat{n} \times \overrightarrow{M}_n = 0$  on the perfectly conducting walls of the cavity, it can be concluded as

$$\int_{V} (\overrightarrow{M}_{n} \cdot \nabla \times \nabla \times \overrightarrow{M}_{m} - \overrightarrow{M}_{m} \cdot \nabla \times \nabla \times \overrightarrow{M}_{n}) dv = 0$$
 (2.47)

On the other hand,  $\overrightarrow{M}_{nml}$  satisfies the vector Helmholtz equation, then

$$\int_{V} (\overrightarrow{M}_{n} \cdot \nabla \times \nabla \times \overrightarrow{M}_{m} - \overrightarrow{M}_{m} \cdot \nabla \times \nabla \times \overrightarrow{M}_{n}) dv$$

$$= \int_{V} (\overrightarrow{M}_{n} \cdot k_{m}^{2} \overrightarrow{M}_{m} - \overrightarrow{M}_{m} \cdot k_{n}^{2} \overrightarrow{M}_{n}) dv = (k_{m}^{2} - k_{n}^{2}) \int_{V} (\overrightarrow{M}_{n} \cdot \overrightarrow{M}_{m}) dv$$
(2.48)

Based on eqs. (2.47) and (2.48), we conclude that

$$\int_{V} (\overrightarrow{M}_{n} \cdot \overrightarrow{M}_{m}) dv = 0 \qquad if \quad m \neq n$$
 (2.49)

That is, the vector wave functions  $\overrightarrow{M}_{nml}$  are orthogonal for different indices.

#### 2. Vector wave functions $\vec{N}_{nml}$ are orthogonal for different indices.

The same procedure used for the case of  $\vec{M}_{nml}$  can be applied to prove the same property for  $\vec{N}_{nml}$ .

### 3. Vector wave functions $\hat{L}_{nml}$ are orthogonal for different indices.

Using the identity of

$$\nabla \cdot (\phi_n^L \nabla \phi_m^L) = \nabla \phi_n^L \cdot \nabla \phi_m^L + \phi_n^L \nabla^2 \phi_m^L \tag{2.50}$$

and the properties of the vector wave functions  $\hat{L}_{nml}$ , we can prove the orthogonality of the vector wave functions  $\hat{L}_{nml}$  for different indices as follows:

$$\int_{V} (\overrightarrow{L}_{n} \cdot \overrightarrow{L}_{m}) dv = \frac{1}{k_{n} k_{m}} \int_{V} [\nabla \phi_{n}^{L} \cdot \nabla \phi_{m}^{L}] dv$$

$$= \frac{1}{k_{n} k_{m}} \int_{V} [\nabla \cdot (\phi_{n}^{L} \nabla \phi_{m}^{L}) - \phi_{n}^{L} \nabla^{2} \phi_{m}^{L}] dv$$

$$= \frac{1}{k_{n} k_{m}} \oint_{S} \phi_{n}^{L} \nabla \phi_{m}^{L} \cdot \overrightarrow{ds} - \frac{1}{k_{n} k_{m}} \int_{V} \phi_{n}^{L} \nabla^{2} \phi_{m}^{L} dv$$

$$= \frac{k_{m}}{k_{n}} \int_{V} \phi_{n}^{L} \phi_{m}^{L} dv$$
(2.51)

where the integration region is over the cavity volume V or the surface S of the cavity wall

and the integration over the surface S is zero due to the property of the scalar function  $\phi_n^L$ . Since the scalar function  $\phi_n^L$  has been given in eq. (2.18), it is obvious that they are orthogonal for different indices. If we assume that the scalar functions  $\phi_n$  have been normalized, that is

$$\int_{V} \phi_{m}^{L} \phi_{m}^{L} dv = \delta_{mn}$$
 (2.52)

then

$$\int_{V} (\vec{L}_n \cdot \vec{L}_m) dv = \frac{k_m}{k_n} \int_{V} \phi_n^L \phi_m^L dv = \delta_{mn}$$
 (2.53)

Therefore, the vector wave functions  $\hat{L}_{nml}$  are orthogonal for different indices and normalized as well.

# 4. Vector wave functions $\vec{L}_{nml}$ and $\vec{M}_{nml}$ are orthogonal.

Using the vector identity of

$$\nabla \cdot (\overrightarrow{A} \times \nabla \times \overrightarrow{B}) = \nabla \times \overrightarrow{A} \cdot \nabla \times \overrightarrow{B} - \overrightarrow{A} \cdot \nabla \times \nabla \times \overrightarrow{B}$$
 (2.54)

we have

$$\nabla \cdot (\vec{L}_n \times \nabla \times \vec{M}_m) = \nabla \times \vec{L}_n \cdot \nabla \times \vec{M}_m - \vec{L}_n \cdot \nabla \times \nabla \times \vec{M}_m$$

$$= -\vec{L}_n \cdot \nabla \times \nabla \times \vec{M}_m = -\vec{L}_n \cdot k_m^2 \vec{M}_m$$
(2.55)

Based on the properties of the vector wave functions  $\vec{L}_{nml}$  and  $\vec{M}_{nml}$ , we have

$$k_{m}^{2}\int_{V}(\vec{L}_{n}\cdot\vec{M}_{m})dv = -\int_{V}\nabla\cdot(\vec{L}_{n}\times\nabla\times\vec{M}_{m})dv$$

$$= -\oint_{V}\hat{n}\cdot\vec{L}_{n}\times\nabla\times\vec{M}_{m}ds = -\oint_{S}(\hat{n}\times\vec{L}_{n}\cdot\nabla\times\vec{M}_{m})ds = 0$$
(2.56)

using the boundary conditions. That is, the vector wave functions  $\vec{L}_{nml}$  and  $\vec{M}_{nml}$  are orthogonal.

## 5. Vector wave functions $\vec{L}_{nml}$ and $\vec{N}_{nml}$ are orthogonal

This can be proved if the same preceding procedure is employed.

# 6. Vector wave functions $\overrightarrow{M}_{nml}$ and $\overrightarrow{N}_{nml}$ are orthogonal.

Based on eqs. (2.41) and (2.43), we know that

$$\int_{V} (\overrightarrow{M}_{n} \cdot \nabla \times \nabla \times \overrightarrow{N}_{m} - \overrightarrow{N}_{m} \cdot \nabla \times \nabla \times \overrightarrow{M}_{n}) dv = (k_{m}^{2} - k_{n}^{2}) \int_{V} (\overrightarrow{M}_{n} \cdot \overrightarrow{N}_{m}) dv$$
 (2.57)

Using the vector identity of eq. (2.54), we have

$$\int_{V} (\overrightarrow{M}_{n} \cdot \nabla \times \nabla \times \overrightarrow{N}_{m} - \overrightarrow{N}_{m} \cdot \nabla \times \nabla \times \overrightarrow{M}_{n}) dv$$

$$= \int_{V} \nabla \cdot (\overrightarrow{N}_{m} \times \nabla \times \overrightarrow{M}_{n} - \overrightarrow{M}_{n} \times \nabla \times \overrightarrow{N}_{m}) dv$$

$$= \oint_{V} (\overrightarrow{N}_{m} \times \nabla \times \overrightarrow{M}_{n} - \overrightarrow{M}_{n} \times \nabla \times \overrightarrow{N}_{m}) \cdot \overrightarrow{n} ds$$

$$= \oint_{S} [(\overrightarrow{n} \times \overrightarrow{N}_{m}) \cdot (\nabla \times \overrightarrow{M}_{n}) - (\overrightarrow{n} \times \overrightarrow{M}_{n}) \cdot (\nabla \times \overrightarrow{N}_{m})] ds = 0$$
(2.58)

where the boundary conditions eqs. (2.5) and (2.6) have been employed in the last step. Therefore,

$$(k_m^2 - k_n^2) \int_{v} (\overrightarrow{M}_n \cdot \overrightarrow{N}_m) dv = 0$$

When  $k_m^2 \neq k_n^2$  the vector wave functions  $\overrightarrow{M}_{nml}$  and  $\overrightarrow{N}_{nml}$  are orthogonal. For degenerate modes, we can use the Gram-Schmidt orthogonalization procedure to construct a new subset of orthogonal modes[2].

So far, we have proved that the vector wave functions  $\vec{L}_{nml}$ ,  $\vec{M}_{nml}$  and  $\vec{N}_{nml}$  are orthogonal mutually.

# 2.1.5 Normalization of the Vector Wave Functions $\vec{L}_{nml}$ , $\vec{M}_{nml}$ and $\vec{N}_{nml}$

Up to now there are still three unknown coefficients  $A_{nml}$ ,  $B_{nml}$  and  $C_{nml}$  in the expressions for the vector wave functions  $\vec{L}_{nml}$ ,  $\vec{M}_{nml}$  and  $\vec{N}_{nml}$  which need to be determined by the normalizations of these vector wave functions.

#### 1. Normalization of $\vec{L}_{nml}$

The normalization of the vector wave function  $\hat{L}_{nml}$  is given by [10]

$$\int_{0}^{a} \int_{0}^{b} \int_{0}^{c} \vec{L}_{nml} \cdot \vec{L}_{nml} dv = 1$$
 (2.59)

that is,

$$\int_{0}^{a} \int_{0}^{b} \int_{0}^{c} \left(\frac{A_{nml}}{k_{nml}}\right)^{2} \left[\left(\frac{n\pi}{a}\right)^{2} \cos^{2}\left(\frac{n\pi}{a}x\right) \sin^{2}\left(\frac{m\pi}{b}y\right) \sin^{2}\left(\frac{l\pi}{c}z\right) + \left(\frac{m\pi}{b}\right)^{2} \sin^{2}\left(\frac{n\pi}{a}x\right) \cos^{2}\left(\frac{m\pi}{b}y\right) \sin^{2}\left(\frac{l\pi}{c}z\right) + \left(\frac{l\pi}{c}\right)^{2} \sin^{2}\left(\frac{n\pi}{a}x\right) \sin^{2}\left(\frac{m\pi}{b}y\right) \cos^{2}\left(\frac{l\pi}{c}z\right) \right] dv = 1$$

Considering the expression for  $L_{nml}$  given in eq. (2.17), we can observe that

 $\vec{L}_{nml}$  will be zero if any one of the three indices is zero. Hence,

$$A_{nml}^2 \frac{abc}{8} = 1$$
 without  $n = 0, or m = 0, or l = 0$  modes

or the normalization coefficient for the vector wave function  $\vec{L}_{nml}$  is given by

$$A_{nml} = \sqrt{\frac{8}{abc}} \tag{2.60}$$

# 2. Normalization of $\overrightarrow{M}_{nml}$

The normalization of the vector wave function  $\overrightarrow{M}_{nml}$  is given by [10]

$$\int_0^a \int_0^b \int_0^c \overrightarrow{M}_{nml} \cdot \overrightarrow{M}_{nml} dv = 1$$
 (2.61)

i.e.

$$\int_{0}^{a} \int_{0}^{b} \int_{0}^{c} B_{nml}^{2} \left[ \left( \frac{m\pi}{b} \right)^{2} \cos^{2} \left( \frac{n\pi}{a} x \right) \sin^{2} \left( \frac{m\pi}{b} y \right) \sin^{2} \left( \frac{l\pi}{c} z \right) + \left( \frac{n\pi}{a} \right)^{2} \right]$$

$$\sin^{2} \left( \frac{n\pi}{a} x \right) \cos^{2} \left( \frac{m\pi}{b} y \right) \sin^{2} \left( \frac{l\pi}{c} z \right) dv = 1$$

Thus, the normalization coefficient for the vector wave function  $\overrightarrow{M}_{nml}$  is derived as

$$B_{nml} = \sqrt{\frac{\varepsilon_{0n}\varepsilon_{0m}\varepsilon_{0l}}{abc}} \sqrt{\frac{1}{\left(\frac{n\pi}{a}\right)^2 + \left(\frac{m\pi}{b}\right)^2}}$$
(2.62)

where

$$\varepsilon_{0n} = \begin{cases} 1 & \text{if } n = 0 \\ 2 & \text{if } n \neq 0 \end{cases}$$
 (2.63)

#### 3. Normalization of $\vec{N}_{nml}$

The normalization of the vector wave function  $\vec{N}_{nml}$  is given by [10]

$$\int_{0}^{a} \int_{0}^{b} \int_{0}^{c} \vec{N}_{nml} \cdot \vec{N}_{nml} dv = 1$$
 (2.64)

i.e.

$$\left(\frac{C_{nml}}{k_{nml}}\right)^{2} \int_{0}^{a} \int_{0}^{b} \int_{0}^{c} \left\{ \left(\frac{n\pi l\pi}{a} \frac{l\pi}{c}\right)^{2} \cos^{2}\left(\frac{n\pi}{a}x\right) \sin^{2}\left(\frac{m\pi}{b}y\right) \sin^{2}\left(\frac{l\pi}{c}z\right) + \left(\frac{m\pi l\pi}{b} \frac{l\pi}{c}\right)^{2} \sin^{2}\left(\frac{n\pi}{a}x\right) \cos^{2}\left(\frac{m\pi}{b}y\right) \sin^{2}\left(\frac{l\pi}{c}z\right) + \left(\left(\frac{n\pi}{a}\right)^{2} + \left(\frac{m\pi}{b}\right)^{2}\right)^{2} \sin^{2}\left(\frac{n\pi}{a}x\right) \sin^{2}\left(\frac{m\pi}{b}y\right) \cos^{2}\left(\frac{l\pi}{c}z\right) dv = 1$$

So the normalization coefficient for the vector wave function  $\overrightarrow{N}_{nml}$  is given by

$$C_{nml} = \sqrt{\frac{\varepsilon_{0n}\varepsilon_{0m}\varepsilon_{0l}}{abc}} \sqrt{\frac{1}{\left(\frac{n\pi}{a}\right)^2 + \left(\frac{m\pi}{b}\right)^2}}$$
 (2.65)

# 2.1.6 Completeness of the Vector Wave Functions $\vec{L}_{nml}$ , $\vec{M}_{nml}$ and $\vec{N}_{nml}$

As well known, a vector function is uniquely defined only when both the solenoidal and lamellar or irrotational parts are given. Let the subscript l denote the lamellar part and the subscript r denote the rotational or solenoidal part. For any arbitrary vector field  $\overrightarrow{C}$  we have

$$\vec{C} = \vec{C}_l + \vec{C}_r \tag{2.66}$$

So in order to represent an unknown electric field which is both solenoidal and lamellar, we need a set of the basis functions which have both solenoidal and lamellar components. In the previous sections, we show that the vector wave functions  $\vec{M}_{nml}$  and  $\vec{N}_{nml}$  are solenoidal and  $\vec{L}_{nml}$  is lamellar or irrotational.

Conventional proof of the completeness of a set of orthonormal functions can be found in [2], [42] and [43]. It states: The notion of the completeness for the space of functions  $\psi_n(x)$  defined on the interval  $0 \le x \le a$  involves the following: Let f(x) be a piecewise continuous function on  $0 \le x \le a$ , that is, quadratically integrable with  $\sigma(x)$  as a weighting function, i.e.

$$\int_{0}^{a} |f(x)|^{2} \sigma(x) dx < \infty \tag{2.67}$$

We assume that  $\sigma(x)$  is always positive. Consider now the approximation

$$\sum_{n=1}^{N} c_n \psi_n(x) = f(x), \qquad c_n = \int_{0}^{a} \sigma(x) f(x) \psi_n(x) dx$$
 (2.68)

If the limit as  $N \to \infty$  of the integrated square of the error tends to zero, then the functions  $\psi_n(x)$  form a complete set. Completeness thus implies that

$$\lim_{N \to \infty} \int_{0}^{a} \left| f(x) - \sum_{n=1}^{N} c_n \psi_n(x) \right|^2 \sigma(x) dx = 0$$
 (2.69)

In our case,  $\vec{E}(\vec{r})$  is a three dimensional vector function which is piecewise continuous function in the cavity volume V, i.e.,  $0 \le x \le a$ ,  $0 \le y \le b$  and  $0 \le z \le c$  in the

rectangular cavity. The vector wave functions  $\vec{L}_{nml}$ ,  $\vec{M}_{nml}$  and  $\vec{N}_{nml}$  have been defined in the cavity volume V before. We then consider the approximation

$$\vec{E}(\hat{r}) = \sum_{n=1}^{N} \left[ a_n \vec{L}_n(\hat{r}) + b_n \vec{M}_n(\hat{r}) + c_n \vec{N}_n(\hat{r}) \right]$$
 (2.70)

where we assume that the vector wave function are normalized and

$$a_n = \int_{V_{cavin}} \vec{E}(\vec{r}_0) \cdot \vec{L}_n(\vec{r}_0) dv_0$$
 (2.71)

$$b_n = \int_{V_{cavity}} \vec{E}(\vec{r}_0) \cdot \vec{M}_n(\vec{r}_0) dv_0$$
 (2.72)

$$c_n = \int_{V_{cavity}} \vec{E}(\vec{r}_0) \cdot \vec{N}_n(\vec{r}_0) dv_0$$
 (2.73)

Let

$$\vec{F}(\vec{r}) = \vec{E}(\vec{r}) - \sum_{n=1}^{N} \left[ a_n \vec{L}_n(\vec{r}) + b_n \vec{M}_n(\vec{r}) + c_n \vec{N}_n(\vec{r}) \right]$$
 (2.74)

Substituting eqs. (2.71), (2.72) and (2.73) into eq. (2.74), we have

$$\vec{F}(\vec{r}) = \vec{E}(\vec{r}) - \sum_{n=1}^{N} \int_{V_{cavity}} \vec{E}(\vec{r}_0) \cdot [\vec{L}_n(\vec{r}_0)\vec{L}_n(\vec{r}) + \vec{M}_n(\vec{r}_0)\vec{M}_n(\vec{r}) + \vec{N}_n(\vec{r}_0)\vec{N}_n(\vec{r})] dv_0$$

$$= \vec{E}(\vec{r}) - \int_{V_{cavity}} \vec{E}(\vec{r}_0) \cdot \sum_{n=1}^{N} [\vec{L}_n(\vec{r}_0)\vec{L}_n(\vec{r}) + \vec{M}_n(\vec{r}_0)\vec{M}_n(\vec{r}) + \vec{N}_n(\vec{r}_0)\vec{N}_n(\vec{r})] dv_0$$

Then

$$\lim_{N\to\infty} \vec{F}(\vec{r}) = \vec{E}(\vec{r}) - \sum_{n=1}^{\infty} \int_{V_{cavin}} \vec{E}(\vec{r}_0) \cdot [\vec{L}_n(\vec{r}_0)\vec{L}_n(\vec{r}) + \vec{M}_n(\vec{r}_0)\vec{M}_n(\vec{r}) + \vec{N}_n(\vec{r}_0)\vec{N}_n(\vec{r})] d\nu_0$$

In Appendix B we have proved the following identity

$$\sum_{n=1}^{\infty} \left[ \vec{L}_n(\vec{r}_0) \vec{L}_n(\vec{r}) + \vec{M}_n(\vec{r}_0) \vec{M}_n(\vec{r}) + \vec{N}_n(\vec{r}_0) \vec{N}_n(\vec{r}) \right] = \bar{I} \delta(\vec{r} - \vec{r}_0)$$
 (2.75)

Thus, for sufficiently smooth electric field we have

$$\lim_{N\to\infty} \vec{F}(r) = 0$$

This implies

$$\lim_{N \to \infty} \int_{V_{cont}} \left| \vec{E}(\vec{r}) - \sum_{n=1}^{N} \left[ a_n \vec{L}_n(\vec{r}) + b_n \vec{M}_n(\vec{r}) + c_n \vec{N}_n(\vec{r}) \right] \right|^2 dv = 0$$
 (2.76)

Therefore, the vector wave functions  $\vec{L}_{nml}$ ,  $\vec{M}_{nml}$  and  $\vec{N}_{nml}$  form a set of complete orthonormal basis functions which can be used to expand the unknown electric field.

In case we know that the electric field is solenoidal, we can only use the vector wave functions  $\vec{M}_{nml}$  and  $\vec{N}_{nml}$  to represent the unknown electric field. That is, the vector wave functions  $\vec{M}_{nml}$  and  $\vec{N}_{nml}$  become complete within the space of solenoidal vector fields but not within the space of all vector fields [28]. The proof is as follows.

In this special case, we have

$$\nabla \cdot \vec{E}(\vec{r}) = 0 \tag{2.77}$$

Using the complete set of basis functions to expand the unknown electric field, we have

$$\vec{E}(\vec{r}) = \sum_{n=1}^{\infty} \left[ a_n \vec{L}_n(\vec{r}) + b_n \vec{M}_n(\vec{r}) + c_n \vec{N}_n(\vec{r}) \right]$$
 (2.78)

The expansion coefficient  $a_n$  will be equal to zero in this special case, because

$$a_n = \int_{V_{cavity}} \vec{E}(\vec{r}) \cdot \vec{L}_n(\vec{r}) dv = \int_{V_{cavity}} \vec{E}(\vec{r}) \cdot \frac{1}{k_n} (\nabla \phi_n^L) dv$$
 (2.79)

Using the identity of

$$\nabla \cdot \left[ \phi_n^L \vec{E}(\vec{r}) \right] = \nabla \phi_n^L \cdot \vec{E}(\vec{r}) + \phi_n^L \nabla \cdot \vec{E}(\vec{r})$$
 (2.80)

The expansion coefficient  $a_n$  is given by

$$a_n = \frac{1}{k_n} \left[ \int_{V_{cavity}} \nabla \cdot \left[ \phi_n^L \overrightarrow{E}(\overrightarrow{r}) \right] dv - \int_{V_{cavity}} \phi_n^L \nabla \cdot \overrightarrow{E}(\overrightarrow{r}) dv \right] = \frac{1}{k_n} \oint_{S_{cavity}} \widehat{n} \cdot \phi_n^L \overrightarrow{E}(\overrightarrow{r}) ds = 0 \quad (2.81)$$

based on the boundary condition for  $\vec{L}_{nml}$ . That is, the expansion of the solenoidal electric field can be based only on the solenoidal vector wave functions. In other words, we can conclude that the vector wave functions  $\vec{M}_{nml}$  and  $\vec{N}_{nml}$  are complete within the space of solenoidal vector fields.

# 2.2 Derivation of Dyadic Green's Function and Electric Field Integral Equation (*EFIE*) in Rectangular Cavities

In this section, based on Maxwell's equations we will investigate the electromagnetic fields behavior in a rectangular cavity with a non-ionic material sample placed inside the cavity. The dielectric parameters of the material sample under consideration are permittivity  $\varepsilon = \varepsilon' + j\varepsilon''$ , permeability  $\mu_0$  and conductivity  $\sigma$ . We also suppose that an initial cavity field has been set up before the material sample is placed inside the cavity.

#### 2.2.1 Maxwell's Equations in the Material Sample

The curl equations of the Maxwell's equations in the material sample can be written as

$$\begin{cases} \nabla \times \vec{E}(\vec{r}) = -j\omega\mu_0 \vec{H}(\vec{r}) \\ \nabla \times \vec{H}(\vec{r}) = \sigma \vec{E}(\vec{r}) + j\omega\varepsilon \vec{E}(\vec{r}) \end{cases}$$
(2.82)

where  $\vec{E}(\vec{r})$  and  $\vec{H}(\vec{r})$  are the unknown electric and magnetic fields in the material sample we aim to determine.

In the empty cavity, the Maxwell's equation is given by

$$\begin{cases} \nabla \times \vec{E}^{i}(\vec{r}) = -j\omega\mu_{0}\vec{H}^{i}(\vec{r}) \\ \nabla \times \vec{H}^{i}(\vec{r}) = j\omega\epsilon_{0}\vec{E}^{i}(\vec{r}) \end{cases}$$
(2.83)

where  $\vec{E}^i(\vec{r})$  and  $\vec{H}^i(\vec{r})$  are the initial electric and magnetic fields we assumed.

The initial cavity fields will induce electric currents and charges inside the material sample. These induced electric currents and charges, in turn, will produce the scattered fields or the secondary fields  $\vec{E}^s(\vec{r})$  and  $\vec{H}^s(\vec{r})$ . In case the material sample is of finite size or heterogeneous, there will be induced charges on the sample surface or at the heterogeneity boundaries. Thus,  $\nabla \cdot \vec{E}^s$  will not be zero at the locations of the induced charges. Or  $\vec{E}^s(\vec{r})$  has an irrotational component.

The total electromagnetic fields  $\vec{E}(\vec{r})$  and  $\vec{H}(\vec{r})$  can be expressed as

$$\vec{E}(\vec{r}) = \vec{E}^s(\vec{r}) + \vec{E}^i(\vec{r}) \tag{2.84}$$

$$\vec{H}(\vec{r}) = \vec{H}^{s}(\vec{r}) + \vec{H}^{i}(\vec{r}) \tag{2.85}$$

Substituting eqs. (2.84) and (2.85) into eqs. (2.82) and (2.83) leads to the equations for the scattered fields as

$$\nabla \times \dot{E}^{s}(\dot{r}) = -j\omega\mu_{0}\dot{H}^{s}(\dot{r}) \tag{2.86}$$

$$\nabla \times \overrightarrow{H}^{s}(\overrightarrow{r}) = \sigma \overrightarrow{E}(\overrightarrow{r}) + j\omega\varepsilon \overrightarrow{E}(\overrightarrow{r}) - j\omega\varepsilon_{0} \overrightarrow{E}^{i}(\overrightarrow{r}) = \overrightarrow{J}_{eq}(\overrightarrow{r}) + j\omega\varepsilon_{0} \overrightarrow{E}^{s}(\overrightarrow{r})$$
(2.87)

where

$$\hat{J}_{eq}(\hat{r}) = [\sigma + j\omega(\varepsilon - \varepsilon_0)]\hat{E}(\hat{r}) = \tau_e(\hat{r})\hat{E}(\hat{r})$$
(2.88)

is the equivalent current and  $\tau_e(r) = \sigma + j\omega(\varepsilon - \varepsilon_0)$  is the equivalent complex conductivity. Taking curl of eq. (2.86) and using eq. (2.87), we have

$$\nabla \times \nabla \times \overrightarrow{E}^{s}(\overrightarrow{r}) = -j\omega \mu_{0} \overrightarrow{J}_{eq}(\overrightarrow{r}) + k_{0}^{2} \overrightarrow{E}^{s}(\overrightarrow{r})$$
 (2.89)

where  $k_0^2 = \omega^2 \mu_0 \epsilon_0$ . Thus, we have the wave equation for the scattered electric field as

$$\nabla \times \nabla \times \vec{E}^{s}(\vec{r}) - k_0^2 \vec{E}^{s}(\vec{r}) = -j\omega \mu_0 \vec{J}_{eq}(\vec{r})$$
 (2.90)

# 2.2.2 Expansion of $\vec{E}^s(\vec{r})$ and Derivation of the Electric Dyadic Green's Function

The vector wave functions  $\vec{L}_{nml}$ ,  $\vec{M}_{nml}$  and  $\vec{N}_{nml}$  form a complete set of orthonormal basis functions, satisfy the same boundary conditions as the scattered electric field does and are the solutions of the homogeneous vector Helmholtz equation with

particular eigenvalues  $k_{nml}^2$ . This  $k_{nml}^2$  is not equal to  $k_0^2$  appearing in the inhomogeneous wave equation of (2.90). However, we can solve eq. (2.90) by expanding  $\vec{E}^s(\vec{r})$  in terms of the vector wave functions  $\vec{L}_{nml}$ ,  $\vec{M}_{nml}$  and  $\vec{N}_{nml}$ . That is,

$$\vec{E}^{s}(\dot{r}) = \sum_{n} \left[ a_{n} \vec{L}_{n}(\dot{r}) + b_{n} \vec{M}_{n}(\dot{r}) + c_{n} \vec{N}_{n}(\dot{r}) \right]$$
 (2.91)

where  $a_n$ ,  $b_n$  and  $c_n$  are unknown expansion coefficients. For simplicity, we use one index n instead of three indices n, m, and l in the summation of eq. (2.91). Substituting eq. (2.91) into eq. (2.90) gives

$$\nabla \times \nabla \times \sum_{n} [a_{n} \vec{L}_{n}(\vec{r}) + b_{n} \vec{M}_{n}(\vec{r}) + c_{n} \vec{N}_{n}(\vec{r})] - k_{0}^{2} \sum_{n} [a_{n} \vec{L}_{n}(\vec{r}) + b_{n} \vec{M}_{n}(\vec{r}) + c_{n} \vec{N}_{n}(\vec{r})]$$

$$= -j\omega \mu_{0} \vec{J}_{eq}(\vec{r})$$

Using the properties of the vector wave functions  $\vec{L}_{nml}$ ,  $\vec{M}_{nml}$  and  $\vec{N}_{nml}$  which we have derived in Section 2.1, the above equation can be rewritten as

$$\sum_{n} \left[ -k_0^2 a_n \vec{L}_n(\vec{r}) + b_n (k_n^2 - k_0^2) \vec{M}_n(\vec{r}) + c_n (k_n^2 - k_0^2) \vec{N}_n(\vec{r}) \right] = -j \omega \mu_0 \vec{J}_{eq}(\vec{r})$$
 (2.92)

Taking the scalar product of eq. (2.92) with  $\vec{L}_{nml}$ ,  $\vec{M}_{nml}$  and  $\vec{N}_{nml}$ , respectively and integrating over the volume V, then applying the orthonormal property of the vector wave functions  $\vec{L}_{nml}$ ,  $\vec{M}_{nml}$  and  $\vec{N}_{nml}$ , we obtain the expressions for the unknown expansion coefficients as

$$a_{n} = \frac{j\omega\mu_{0}}{k_{0}^{2}} \int_{V_{sample}} [\vec{J}_{eq}(\vec{r}_{0}) \cdot \vec{L}_{n}(\vec{r}_{0})] dv_{0}$$
 (2.93)

$$b_{n} = -\frac{j\omega\mu_{0}}{k_{n}^{2} - k_{0}^{2}} \int_{V_{sample}} [\vec{J}_{eq}(\vec{r}_{0}) \cdot \vec{M}_{n}(\vec{r}_{0})] dv_{0}$$
 (2.94)

$$c_n = -\frac{j\omega\mu_0}{k_n^2 - k_0^2} \int_{V_{sample}} [\vec{J}_{eq}(\vec{r}_0) \cdot \vec{N}_n(\vec{r}_0)] dv_0$$
 (2.95)

Therefore, the expression for the scattered electric field  $\vec{E}^s(r)$  becomes

$$\vec{E}^{s}(\hat{r}) = -j\omega\mu_{0} \int_{V_{sample}} \vec{J}_{eq}(\hat{r}_{0}) \cdot \sum_{n} \left[ \frac{-\vec{L}_{n}(\hat{r}_{0})\vec{L}_{n}(\hat{r})}{k_{0}^{2}} + \frac{\vec{M}_{n}(\hat{r}_{0})\vec{M}_{n}(\hat{r}) + \vec{N}_{n}(\hat{r}_{0})\vec{N}_{n}(\hat{r})}{k_{n}^{2} - k_{0}^{2}} \right]_{(2.96)}^{dv_{0}}$$

$$= -j\omega\mu_{0} \int_{V_{sample}} \vec{J}_{eq}(\hat{r}_{0}) \cdot \vec{G}_{e}(\hat{r}_{0}, \hat{r}) dv_{0}$$

where the integration region is over the material sample volume. The electric dyadic Green's function is identified as

$$\overline{G}_{e}(\mathring{r}_{0},\mathring{r}) = \sum_{n} \left[ \frac{-\vec{L}_{n}(\mathring{r}_{0})\vec{L}_{n}(\mathring{r})}{k_{0}^{2}} + \frac{\vec{M}_{n}(\mathring{r}_{0})\vec{M}_{n}(\mathring{r}) + \vec{N}_{n}(\mathring{r}_{0})\vec{N}_{n}(\mathring{r})}{k_{n}^{2} - k_{0}^{2}} \right]$$
(2.97)

### 2.2.3 Derivation of the Integral Equation in the Material Sample

Based on eq. (2.96) and the definition of the equivalent current  $\hat{J}_{eq}(\hat{r})$  given in eq. (2.88), the expression for the scattered field can be expressed as

$$\vec{E}^{s}(\dot{r}) = -j\omega\mu_{0} \int_{V_{sample}} \tau_{e}(\dot{r}_{0}) \vec{E}(\dot{r}_{0}) \cdot \vec{G}_{e}(\dot{r}_{0}, \dot{r}) dv_{0}$$
(2.98)

Substituting eq. (2.98) into eq. (2.84) gives the electric field integral equation (*EFIE*) for the unknown electric field  $\vec{E}(\hat{r})$  inside the material sample as

$$\vec{E}(\vec{r}) + j\omega\mu_0 \int_{v} \tau_e(\vec{r}_0) \vec{E}(\vec{r}_0) \cdot \vec{G}_e(\vec{r}_0, \vec{r}) dv_0 = \vec{E}^i(\vec{r})$$
(2.99)

where  $\overline{G}_e(r_0, r)$  is given by eq. (2.97).

#### 2.2.4 Expression of the Dyadic Green's Function

The identity (2.75) can be applied to the electric dyadic Green's function of eq. (2.97) to lead it to an almost identical expression for the electric dyadic Green's function derived by Rahmat-Samii [11]. Using identity (2.75), eq. (2.97) can be rewritten as

$$\overline{G}_{e}(\mathring{r}_{0},\mathring{r}) = \sum_{n} \left[ k_{n}^{2} \frac{\overrightarrow{M}_{n}(\mathring{r}_{0}) \overrightarrow{M}_{n}(\mathring{r}) + \overrightarrow{N}_{n}(\mathring{r}_{0}) \overrightarrow{N}_{n}(\mathring{r})}{k_{0}^{2} (k_{n}^{2} - k_{0}^{2})} \right] - \frac{\overline{I}\delta(\mathring{r} - \mathring{r}_{0})}{k_{0}^{2}}$$

$$= \overline{G}_{eo}(\mathring{r}_{0},\mathring{r}) - \frac{\overline{I}\delta(\mathring{r} - \mathring{r}_{0})}{k_{0}^{2}}$$
(2.100)

where

$$\overline{G}_{eo}(\mathring{r}_0,\mathring{r}) = \sum_{n} \left[ k_n^2 \frac{\overrightarrow{M}_n(\mathring{r}_0) \overrightarrow{M}_n(\mathring{r}) + \overrightarrow{N}_n(\mathring{r}_0) \overrightarrow{N}_n(\mathring{r})}{k_0^2 (k_n^2 - k_0^2)} \right]$$
(2.101)

Therefore, the EFIE of eq. (2.99) can be rewritten as

$$\vec{E}(\vec{r})\left(1 - \frac{j\omega\mu_0\tau_e}{k_0^2}\right) + j\omega\mu_0\int_{\nu}^{\nu}\tau_e(\vec{r}_0)\vec{E}(\vec{r}_0) \cdot \vec{G}_{eo}(\vec{r}_0, \vec{r})d\nu_0 = \vec{E}^i(\vec{r})$$
(2.102)

# 2.2.5 Detailed Expression of $\overline{G}_{eo}(\mathring{r}_0,\mathring{r})$ and Comparison with the Results of Y. Rahmat-Samii [11]

For simplicity, we derive only the coefficients for the different components of the dyadic Green's function  $\overline{G}_{eo}(\mathring{r}_0, \mathring{r})$  when we give the expressions of  $\overline{G}_{eo}(\mathring{r}_0, \mathring{r})$ , then we

compare the results with those derived by Y. Rahmat-Samii [11].

Substituting the expressions of  $\overrightarrow{M}_{nml}$  given in eq. (2.24) and  $\overrightarrow{N}_{nml}$  given in eq. (2.32) into eq. (2.101) and using the normalization constants of  $\overrightarrow{M}_{nml}$  and  $\overrightarrow{N}_{nml}$  given in eqs. (2.62) and (2.65), we obtain the expressions for the coefficients of the nine components of the dyadic Green's function  $\overline{G}_{eo}(\overset{\triangleright}{r}_0, \overset{\triangleright}{r})$  as follows:

(1) Coefficient for  $\hat{x}\hat{x}$  component of  $\overline{G}_{eo}(\hat{r}_0, \hat{r})$ 

$$g_{eoxx} = k_n^2 \frac{B_n^2 \left(\frac{m\pi}{b}\right)^2 + \frac{C_n^2}{k_n^2} \left(\frac{n\pi}{a}\right)^2 \left(\frac{l\pi}{c}\right)^2}{k_0^2 (k_n^2 - k_0^2)} = \frac{\varepsilon_{0n} \varepsilon_{0m} \varepsilon_{0l}}{abc} \frac{\left(\frac{m\pi}{b}\right)^2 + \left(\frac{l\pi}{c}\right)^2}{k_0^2 (k_n^2 - k_0^2)}$$
(2.103)

where  $B_n^2 = C_n^2$  based on eqs. (2.62) and (2.65).

(2) Coefficient for  $\hat{y}\hat{y}$  component of  $\overline{G}_{eo}(\hat{r}_0, \hat{r})$ 

$$g_{eoyy} = k_n^2 \frac{B_n^2 \left(\frac{n\pi}{a}\right)^2 + \frac{C_n^2}{k_n^2} \left(\frac{m\pi}{b}\right)^2 \left(\frac{l\pi}{c}\right)^2}{k_0^2 (k_n^2 - k_0^2)} = \frac{\varepsilon_{0n} \varepsilon_{0m} \varepsilon_{0l}}{abc} \frac{\left(\frac{n\pi}{a}\right)^2 + \left(\frac{l\pi}{c}\right)^2}{k_0^2 (k_n^2 - k_0^2)}$$
(2.104)

(3) Coefficient for  $\hat{z}\hat{z}$  component of  $\overline{G}_{eo}(\hat{r}_0, \hat{r})$ 

$$g_{eozz} = C_n^2 \frac{\left( \left( \frac{n\pi}{a} \right)^2 + \left( \frac{m\pi}{b} \right)^2 \right)^2}{k_0^2 (k_n^2 - k_0^2)} = \frac{\varepsilon_{0n} \varepsilon_{0m} \varepsilon_{0l}}{abc} \frac{\left( \frac{n\pi}{a} \right)^2 + \left( \frac{m\pi}{b} \right)^2}{k_0^2 (k_n^2 - k_0^2)}$$
(2.105)

(4) Coefficient for  $\hat{x}\hat{y}$  and  $\hat{y}\hat{x}$  component of  $\overline{G}_{eo}(\hat{r}_0, \hat{r})$ 

$$g_{eoxy} = k_n^2 \frac{-B_n^2 \left(\frac{n\pi}{a}\right) \left(\frac{m\pi}{b}\right) + \frac{C_n^2}{k_n^2} \left(\frac{n\pi}{a}\right) \left(\frac{m\pi}{b}\right) \left(\frac{l\pi}{c}\right)^2}{k_0^2 (k_n^2 - k_0^2)} = -\frac{\varepsilon_{0n} \varepsilon_{0m} \varepsilon_{0l}}{abc} \frac{\left(\frac{n\pi}{a}\right) \left(\frac{m\pi}{b}\right)}{k_0^2 (k_n^2 - k_0^2)}$$
(2.106)

(5) Coefficient for  $\hat{y}\hat{z}$  and  $\hat{z}\hat{y}$  component of  $\overline{G}_{eo}(\mathring{r}_0,\mathring{r})$ 

$$g_{eoyz} = -C_n^2 \frac{\left(\frac{n\pi}{a}\right)^2 + \left(\frac{m\pi}{b}\right)^2}{k_0^2 (k_n^2 - k_0^2)} \left(\frac{m\pi}{b}\right) \left(\frac{l\pi}{c}\right) = -\frac{\varepsilon_{0n} \varepsilon_{0m} \varepsilon_{0l}}{abc} \frac{\left(\frac{m\pi}{b}\right) \left(\frac{l\pi}{c}\right)}{k_0^2 (k_n^2 - k_0^2)}$$
(2.107)

(6) Coefficient for  $\hat{x}\hat{z}$  and  $\hat{z}\hat{x}$  component of  $\overline{G}_{eo}(\hat{r}_0,\hat{r})$ 

$$g_{eoxz} = -C_n^2 \frac{\left(\frac{n\pi}{a}\right)^2 + \left(\frac{m\pi}{b}\right)^2}{k_0^2 (k_n^2 - k_0^2)} \left(\frac{n\pi}{a}\right) \left(\frac{l\pi}{c}\right) = -\frac{\varepsilon_{0n} \varepsilon_{0m} \varepsilon_{0l}}{abc} \frac{\left(\frac{n\pi}{a}\right) \left(\frac{l\pi}{c}\right)}{k_0^2 (k_n^2 - k_0^2)}$$
(2.108)

Comparing all these coefficients with the expression (28) of Y. Rahmat-Samii [11], we find that they are almost the same except there is a minus sign difference. Checking carefully the results of (28) of Y. Rahmat-Samii [11], we found an error occurred in his expression (28). See Appendix A.

#### 2.2.6 Derivation of the Electrical Field Outside the Material Sample

Outside the material sample, the total electric field can also be expressed as

$$\vec{E}(\vec{r}) = \vec{E}^s(\vec{r}) + \vec{E}^i(\vec{r}) \tag{2.109}$$

where based on eq. (2.96) the scattered field maintained by the induced currents and charges in the material sample can be expressed as

$$\vec{E}^{s}(\vec{r}) = -j\omega\mu_{0} \int_{V_{sample}} \vec{J}_{eq}(\vec{r}_{0}) \cdot \vec{G}_{e}(\vec{r}_{0}, \vec{r}) dv_{0}$$
(2.110)

Because the field point  $\hat{r}$  is outside the material sample and the source point  $\hat{r}_0$  is inside the material sample, then in the expression of the electric dyadic Green's function  $\overline{G}_e(\hat{r}_0, \hat{r})$  given in eq. (2.100) the second term including the unit dyadic is always zero. That is,  $\overline{G}_e(\hat{r}_0, \hat{r})$  can be expressed as

$$\overline{G}_{e}(\stackrel{>}{r}_{0}, \stackrel{>}{r}) = \overline{G}_{eo}(\stackrel{>}{r}_{0}, \stackrel{>}{r}) \tag{2.111}$$

where  $\overline{G}_{eo}(\hat{r}_0, \hat{r})$  is given in eq. (2.101). Therefore the electric field outside the material sample is given by

$$\vec{E}(\vec{r}) = -j\omega\mu_0 \int_{V_{sample}} \tau_e(\vec{r}_0) \vec{E}(\vec{r}_0) \cdot \vec{G}_{eo}(\vec{r}_0, \vec{r}) dv_0 + \vec{E}^i(\vec{r})$$
(2.112)

where we assume that the electric field inside the material sample  $\vec{E}(\hat{r}_0)$  has been solved from the *EFIE* in the material sample given in eq. (2.102).  $\vec{E}^i(\hat{r})$  is the initial electric field we assumed before we place the material sample in the cavity. Therefore, after we obtain the solution of the electric field inside the material sample, the electromagnetic fields outside the material sample can be easily calculated based on eq. (2.112). For this reason, we will only show the electric field inside the material sample in the numerical examples in Chapter 3.

# 2.3 Derivation of the Magnetic Dyadic Green's Function and Magnetic Field Integral Equation (MFIE)

As in Section 2.2, the behaviors of the scattered fields  $(\vec{E}^s, \vec{H}^s)$  are described by eqs. (2.86) and (2.87). Taking curl of eq. (2.87) and using eq. (2.86), we have

$$\nabla \times \nabla \times \overrightarrow{H}^{s}(\mathring{r}) = \nabla \times \overrightarrow{J}_{eq}(\mathring{r}) + j\omega \varepsilon_0 \nabla \times \overrightarrow{E}^{s}(\mathring{r}) = \nabla \times \overrightarrow{J}_{eq}(\mathring{r}) + k_0^2 \overrightarrow{H}^{s}(\mathring{r})$$

Or the wave equation for the scattered magnetic field  $\vec{H}^s(r)$  can be expressed as

$$\nabla \times \nabla \times \overrightarrow{H}^{s}(\overrightarrow{r}) - k_0^2 \overrightarrow{H}^{s}(\overrightarrow{r}) = \nabla \times \overrightarrow{J}_{eq}(\overrightarrow{r})$$
 (2.113)

Based on Maxwell's equations, the magnetic field (total field or scattered field) is solenoidal inside the material sample or in the cavity. That is,

$$\nabla \cdot \overrightarrow{H}^{s}(\dot{r}) = 0 \tag{2.114}$$

So the wave eq. (2.113) can be rewritten as

$$\nabla^2 \vec{H}^s(\vec{r}) + k_0^2 \vec{H}^s(\vec{r}) = -\nabla \times \hat{J}_{eq}(\vec{r})$$
 (2.115)

Also the solenoidal vector wave functions are complete within the space of the solenoidal vector fields as discussed in Section 2.1.6. The orthogonality of the cavity magnetic eigenfunctions is well known [2], [10]. Thus, the cavity magnetic eigenfunctions which are solenoidal should be sufficient to be employed to expand the magnetic field for solving eq. (2.115).

The expansion of the scattered magnetic field  $\vec{H}^s(\vec{r})$  using the cavity magnetic eigenfunctions as the basis functions leads to

$$\vec{H}^{s}(\vec{r}) = \sum_{n} a_{n} \vec{H}_{n}(\vec{r}) \tag{2.116}$$

where  $\overrightarrow{H}_n(\overrightarrow{r})$  is the cavity resonant mode, and it satisfies the homogeneous vector Helmholtz equation as

$$\nabla^2 \vec{H}_n(\vec{r}) + k_n^2 \vec{H}_n(\vec{r}) = 0 \tag{2.117}$$

where  $k_n^2$  is the eigenvalue of the *nth* cavity mode [10].

Substituting eq. (2.116) into eq. (2.115) and using eq. (2.117), we have

$$\sum_{n} a_n (k_0^2 - k_n^2) \vec{H}_n(\vec{r}) = -\nabla \times \vec{J}_{eq}(\vec{r})$$
 (2.118)

Since

$$\int_{V_{caviny}} \overrightarrow{H}_n(\overrightarrow{r}) \cdot \overrightarrow{H}_m(\overrightarrow{r}) dv = \begin{cases} 0 & \text{if } n \neq m \\ N_n & \text{if } n = m \end{cases}$$
 (2.119)

where  $N_n$  can be found through the normalization of  $\vec{E}_n(\vec{r})$ , the *nth* cavity modes of electric field. That is, we suppose

$$\int_{v_{cavid}} \vec{E}_n(\vec{r}) \cdot \vec{E}_m(\vec{r}) dv = \begin{cases} 0 & \text{if } n \neq m \\ 1 & \text{if } n = m \end{cases}$$
 (2.120)

Based on Maxwell's equations for the electromagnetic eigenmodes, we have

$$N_{n} = \int_{\nu_{cavity}} \vec{H}_{n}(\hat{r}) \cdot \vec{H}_{n}(\hat{r}) dv = -\frac{1}{\omega_{n}^{2} \mu_{0}^{2} \nu_{cavity}} \nabla \times \vec{E}_{n}(\hat{r}) \cdot \nabla \times \vec{E}_{n}(\hat{r}) dv$$

$$= -\frac{1}{\omega_{n}^{2} \mu_{0}^{2} \nu_{cavity}} [\nabla \cdot (\vec{E}_{n}(\hat{r}) \times \nabla \times \vec{E}_{n}(\hat{r})) + \vec{E}_{n}(\hat{r}) \cdot \nabla \times \nabla \times \vec{E}_{n}(\hat{r})] dv$$

$$(2.121)$$

Therefore, based on boundary conditions and the property of the eigenmodes we have

$$N_n = \int_{\nu_{caviry}} \vec{H}_n(\vec{r}) \cdot \vec{H}_n(\vec{r}) d\nu = -\frac{\varepsilon_0}{\mu_0} \int_{\nu_{caviry}} \vec{E}_n(\vec{r}) \cdot \vec{E}_n(\vec{r}) d\nu = -\frac{\varepsilon_0}{\mu_0}$$
 (2.122)

Let's go back to eq. (2.118). Taking a scalar product of  $\vec{H}_l(\hat{r})$  with eq. (2.118), integrating over the cavity volume, and using the orthogonality of the cavity magnetic eigenfunctions, we derive the expansion coefficients as

$$a_n = \frac{-1}{N_n(k_0^2 - k_n^2)} \int_{V_{caviry}} \vec{H}_n(\vec{r}) \cdot \nabla \times \vec{J}_{eq}(\vec{r}) dv$$
 (2.123)

Substituting eq. (2.123) into eq. (2.116) leads to the expression for the scattered magnetic field  $\vec{H}^s(\vec{r})$  as

$$\vec{H}^{s}(\mathring{r}) = \sum_{n} \frac{\vec{H}_{n}(\mathring{r}_{0}) \cdot \nabla \times \vec{J}_{eq}(\mathring{r}_{0}) d\nu_{0}}{N_{n}(k_{n}^{2} - k_{0}^{2})} \vec{H}_{n}(\mathring{r}) \qquad (2.124)$$

Using the vector identity as

$$\nabla \cdot [\vec{H}_n(\vec{r}) \times \vec{J}_{eq}(\vec{r})] = [\nabla \times \vec{H}_n(\vec{r})] \cdot \vec{J}_{eq}(\vec{r}) - [\nabla \times \vec{J}_{eq}(\vec{r})] \cdot \vec{H}_n(\vec{r})$$
(2.125)

we have

$$\int_{v_{cavity}} \vec{H}_{n}(\mathring{r}_{0}) \cdot \nabla \times \mathring{J}_{eq}(\mathring{r}_{0}) dv_{0}$$

$$= \int_{v_{cavity}} \nabla_{0} \times \vec{H}_{n}(\mathring{r}_{0}) \cdot \mathring{J}_{eq}(\mathring{r}_{0}) dv' - \int_{v_{cavity}} \nabla_{0} \cdot [\vec{H}_{n}(\mathring{r}_{0}) \times \mathring{J}_{eq}(\mathring{r}_{0})] dv_{0}$$

$$= \int_{v_{sample}} \nabla_{0} \times \vec{H}_{n}(\mathring{r}_{0}) \cdot \mathring{J}_{eq}(\mathring{r}_{0}) dv_{0}$$
(2.126)

because  $\vec{J}_{eq}(\vec{r}_0)$  exists only inside the material sample, then  $\vec{J}_{eq}(\vec{r}_0) = 0$  on the walls of the cavity. Therefore,

$$\overrightarrow{H}^{s}(\mathring{r}) = \sum_{n} \frac{\sum_{sample} V_{sample}}{N_{n}(k_{n}^{2} - k_{0}^{2})} \overrightarrow{H}_{n}(\mathring{r})$$

$$= \sum_{n} \int_{v_{sample}} \frac{\overrightarrow{J}_{eq}(\mathring{r}_{0}) \cdot \nabla_{0} \times \overrightarrow{H}_{n}(\mathring{r}_{0})}{N_{n}(k_{n}^{2} - k_{0}^{2})} dv_{0} \overrightarrow{H}_{n}(\mathring{r})$$

$$= \int_{v_{sample}} \overrightarrow{J}_{eq}(\mathring{r}_{0}) \cdot \overrightarrow{G}_{m}(\mathring{r}_{0}, \mathring{r}) dv_{0}$$
(2.127)

where the magnetic Dyadic Green's function is identified as

$$\overline{G}_{m}(\mathring{r}_{0},\mathring{r}) = \sum_{n} \frac{\nabla_{0} \times \overrightarrow{H}_{n}(\mathring{r}_{0}) \overrightarrow{H}_{n}(\mathring{r})}{N_{n}(k_{n}^{2} - k_{0}^{2})}$$
(2.128)

The equivalent current  $\vec{J}_{eq}(\vec{r}) = \tau_e(\vec{r})\vec{E}(\vec{r})$  and based on a Maxwell's equation,

$$\vec{E}(\vec{r}) = \frac{\nabla \times \vec{H}(\vec{r})}{\sigma + i\omega \varepsilon} \tag{2.129}$$

the equivalent current can be expressed in terms of the magnetic field as

$$\vec{J}_{eq}(\vec{r}) = \tau_e(\vec{r}) \frac{\nabla \times \vec{H}(\vec{r})}{\sigma + i\omega \varepsilon}$$
 (2.130)

Substituting eq. (2.130) into eq. (2.127) and using eq. (2.85) leads to the magnetic field integral equation (MFIE) as

$$\vec{H}(\vec{r}) - \int_{v_{sumple}} \tau_e(\vec{r}_0) \frac{\nabla_0 \times \vec{H}(\vec{r}_0)}{\sigma + j\omega \varepsilon} \cdot \vec{G}_m(\vec{r}_0, \vec{r}) dv_0 = \vec{H}^i(\vec{r})$$
 (2.131)

#### 2.4 Comparison of EFIE with MFIE and Explanation of the Result

In MFIE (2.131), the unknown magnetic field appears in the form of the curl under the integral sign. If we use the pulse functions as the basis and testing functions in the moment method, there will be singularities occurred when taking curl of the unknown magnetic field at the boundaries of volume cells. On the other hand, we can solve EFIE (2.102) using the pulse functions as both the basis and the testing function without any difficulty because there is no differentiation for the unknown electric field involved. Actually, we can show that EFIE (2.102) and MFIE (2.131) are exactly the same. If the pulse functions are to be used as both the basis and testing functions, it is easier to find the unknown electric fields from the EFIE and then determine the unknown magnetic fields directly from a Maxwell's equation. Of course for higher numerical accuracy, we can try to use the continuous functions as the basis and the testing functions in the moment method. Then either EFIE or MFIE can be solved directly, and they should give the same results. We will show that EFIE and MFIE are identical.

Taking curl of both sides of MFIE (2.131) and using eq. (2.130), we have

$$\nabla \times \overrightarrow{H}(\overrightarrow{r}) - \nabla \times \int_{v_{sample}} \overrightarrow{J}_{eq}(\overrightarrow{r}_0) \cdot \overline{G}_m(\overrightarrow{r}_0, \overrightarrow{r}) dv_0 = \nabla \times \overrightarrow{H}^i(\overrightarrow{r})$$
 (2.132)

Based on eqs. (2.82) and (2.83), eq. (2.132) can be rewritten as

$$(\sigma + j\omega\varepsilon)\vec{E}(\vec{r}) - \int_{v_{sumple}} \tau_e(\vec{r}_0)\vec{E}(\vec{r}_0) \cdot \nabla \times \vec{G}_m(\vec{r}_0, \vec{r}) dv_0 = j\omega\varepsilon_0\vec{E}^i(\vec{r})$$
 (2.133)

Because

$$\nabla \times \overline{G}_{m}(\mathring{r}_{0}, \mathring{r}) = \nabla \times \sum_{n} \frac{\nabla_{0} \times \overrightarrow{H}_{n}(\mathring{r}_{0}) \overrightarrow{H}_{n}(\mathring{r})}{N_{n}(k_{n}^{2} - k_{0}^{2})}$$

$$= \sum_{n} \frac{\nabla_{0} \times \overrightarrow{H}_{n}(\mathring{r}_{0}) \nabla \times \overrightarrow{H}_{n}(\mathring{r})}{N_{n}(k_{n}^{2} - k_{0}^{2})} = -\sum_{n} \frac{\omega_{n}^{2} \varepsilon_{0}^{2} \overrightarrow{E}_{n}(\mathring{r}) \overrightarrow{E}_{n}(\mathring{r}_{0})}{N_{n}(k_{n}^{2} - k_{0}^{2})}$$

$$(2.134)$$

Substituting eq. (2.134) into eq. (2.133), we have

$$\frac{(\sigma + j\omega\varepsilon)}{j\omega\varepsilon_0}\vec{E}(\vec{r}) + \frac{1}{j\omega\varepsilon_0} \int_{\nu_{sample}} \tau_e(\vec{r}_0)\vec{E}(\vec{r}_0) \cdot \sum_n \frac{\omega_n^2 \varepsilon_0^2 \vec{E}_n(\vec{r})\vec{E}_n(\vec{r}_0)}{N_n(k_n^2 - k_0^2)} d\nu_0 = \vec{E}^i(\vec{r}) \quad (2.135)$$

Based on eq. (2.122) and  $\tau_e = \sigma + j\omega(\varepsilon - \varepsilon_0)$ , eq. (2.135) can be rewritten as

$$\left(1 - \frac{j\omega\mu_0}{k_0^2}\tau_e(\hat{r})\right)\vec{E}(\hat{r}) + \frac{j\omega\mu_0}{k_0^2}\int_{v_{sample}} \tau_e(\hat{r}_0)\vec{E}(\hat{r}_0) \cdot \sum_{n} \frac{k_n^2\vec{E}_n(\hat{r})\vec{E}_n(\hat{r}_0)}{k_n^2 - k_0^2} dv_0 = \vec{E}^i(\hat{r}) (2.136)$$

which is exactly the same integral equation as eq. (2.102). That is, even using different dyadic Green's functions, we still obtain the consistent results.

At this point, there will be a question raised: When we expand the magnetic field, we only use the solenoidal eigenfunctions as basis functions. However, we use both the solenoidal and the irrotational eigenfunctions as basis functions to expand the electric field. Where do the irrotational eigenfunctions come from if we derive the *EFIE* from the magnetic dyadic Green's function? How can these two different approaches reach the same result?

As stated before, because of the existence of the material sample of finite size in the cavity, the divergence of the electric field doesn't vanish at all points in the cavity, but the divergence of the magnetic field vanishes at any point inside the cavity. So when we expand the electric field, both the solenoidal and the irrotational eigenfunctions are

necessary. However, the solenoidal eigenfunctions are sufficient for expanding the magnetic field.

When we transform MFIE to EFIE, we take the curl of MFIE. Based on the definitions of the electric and magnetic dyadic Green's functions, the electric and magnetic fields can be expressed in terms of the corresponding dyadic Green's function as [20]

$$\vec{E}(\mathbf{r}) = -j\omega\mu_0 \iiint \vec{G}_e(\mathbf{r}_0, \mathbf{r}) \cdot \vec{J}(\mathbf{r}_0) dv_0$$
 (2.137)

$$\vec{H}(\vec{r}) = \iiint \vec{G}_m(\vec{r}_0, \vec{r}) \cdot \vec{J}(\vec{r}_0) dv_0$$
 (2.138)

The Maxwell's equations inside the material sample are given as

$$\nabla \times \vec{E}(\vec{r}) = -j\omega \mu_0 \vec{H}(\vec{r}) \tag{2.139}$$

$$\nabla \times \vec{H}(\vec{r}) = \vec{J}(\vec{r}) + j\omega \varepsilon \vec{E}(\vec{r})$$
 (2.140)

Combining eqs. (2.137) to (2.140) we can obtain the relationship between the electric and magnetic dyadic Green's functions as

$$\nabla \times \overline{G}_e = \overline{G}_m \tag{2.141}$$

$$\nabla \times \overline{G}_m = \overline{I}\delta(\mathring{r} - \mathring{r}_0) + k^2 \overline{G}_e$$
 (2.142)

That is, taking the curl of the magnetic dyadic Green's function, we introduce a singularity at the source point based on eq. (2.142). From eqs. (2.141) and (2.142), we observe that

$$\nabla \cdot \overline{G}_m = \vec{0} \tag{2.143}$$

and

$$\nabla \cdot \overline{G}_e \neq 0 \tag{2.144}$$

That is, the electric dyadic Green's function can have an irrotational component even though we derive it from the magnetic dyadic Green's function.

In the previous sections, we have obtained the electric and magnetic dyadic Green's functions as

$$\overline{G}_{e}(\hat{r}_{0},\hat{r}) = \sum_{n} \left[ \frac{-\dot{L}_{n}(\hat{r}_{0})\dot{L}_{n}(\hat{r})}{k_{0}^{2}} + \frac{\overrightarrow{M}_{n}(\hat{r}_{0})\overrightarrow{M}_{n}(\hat{r}) + \overrightarrow{N}_{n}(\hat{r}_{0})\overrightarrow{N}_{n}(\hat{r})}{k_{n}^{2} - k_{0}^{2}} \right]$$
(2.145)

and

$$\overline{G}_{m}(\hat{r}_{0}, \hat{r}) = \sum_{n} \frac{\nabla_{0} \times \overrightarrow{H}_{n}(\hat{r}_{0}) \overrightarrow{H}_{n}(\hat{r})}{N_{n}(k_{n}^{2} - k_{0}^{2})}$$
(2.146)

It can be verified that the electric and magnetic dyadic Green's functions (2.145) and (2.146) satisfy the relationship of eqs. (2.141) and (2.142).

After we obtain the appropriate expression for the electric dyadic Green's function and *EFIE*, we will numerically solve this *EFIE* (2.102) and present some numerical techniques and results in Chapter 3.

## CHAPTER 3

# NUMERICAL TECHNIQUES AND RESULTS ON THE INDUCED ELECTRIC FIELD IN A MATERIAL SAMPLE PLACED WITHIN A RECTANGULAR CAVITY

In Chapter 2, we have derived the *EFIE* for a material sample placed inside a rectangular cavity based on either the electric dyadic Green's function (2.101) or the magnetic dyadic Green's function (2.128). After the appropriate integral eq. (2.102) is acquired, it will be numerically solved by discretizing the material sample into a large number of volume cells using Galerkin's method.

In fact, in the expression of the electric dyadic Green's function (2.101) there are nine triple infinite summations which have very poor convergence properties [2]. To overcome this difficulty, a triple summation over cavity eigenfunctions is reduced to a double summation using two relations in [2]. For the reduced double summations, several methods are employed to obtain a faster computation.

The outline of this chapter is as follows: In Section 3.1, Galerkin's method is applied to the integral eq. (2.102). In Section 3.2, the convergence property of the dyadic Green's function (2.101) is studied and the results of the double summation and the triple summation are compared. Some numerical results are presented in Section 3.3. Several

methods are investigated to increase the convergence rate of the infinite double summations in Section 3.4.

### 3.1 Applying Galerkin's Method to EFIE

In order to increase the convergence rate of the dyadic Green's function, Galerkin's method is applied to the EFIE (2.102) with the pulse functions as both basis and testing functions. The material sample is divided into M volume cells where M is assumed to be large enough in order to generate satisfactory results.

The integral equation we are to solve is eq. (2.102) as

$$\vec{E}(\vec{r}) \left( 1 - \frac{j\omega\mu_0\tau_e(\vec{r})}{k_0^2} \right) + j\omega\mu_0 \int_{\nu} \tau_e(\vec{r}_0) \vec{E}(\vec{r}_0) \cdot \vec{G}_{eo}(\vec{r}_0, \vec{r}) d\nu_0 = \vec{E}^i(\vec{r})$$
(3.1)

and the pulse function is given by

$$p_n(\mathring{r}) = \begin{cases} 1 & \text{if } \mathring{r} \in v_n \\ 0 & \text{otherwise} \end{cases}$$
 (3.2)

where  $v_n$  is the *nth* cell volume. The unknown electric field  $\vec{E}(r)$  can then be expanded as

$$\vec{E}(\vec{r}) = \sum_{m=1}^{M} \vec{E}_m p_m(\vec{r}) \tag{3.3}$$

where the electric field in each volume cell is considered as a constant. Substituting eq. (3.3) into eq. (3.1) leads to

$$\sum_{m=1}^{M} \vec{E}_{m} p_{m}(\vec{r}) \left( 1 - \frac{j\omega\mu_{0}\tau_{e}(\vec{r})}{k_{0}^{2}} \right) + j\omega\mu_{0} \int_{v_{sample}} \tau_{e}(\vec{r}_{0}) \sum_{m=1}^{M} \vec{E}_{m} p_{m}(\vec{r}_{0}) \cdot \overline{G}_{eo}(\vec{r}_{0}, \vec{r}) dv_{0}$$

$$= \vec{E}^{i}(\vec{r})$$
(3.4)

Next, applying the testing function (3.2) to the integral eq. (3.4), we have

$$\int_{v_n} p_n(\mathring{r}) \sum_{m=1}^{M} \vec{E}_m p_m(\mathring{r}) \left( 1 - \frac{j\omega\mu_0 \tau_e(\mathring{r})}{k_0^2} \right) dv + \int_{v_n} p_n(\mathring{r}) j\omega\mu_0$$

$$\int_{v_{sample}} \tau_e(\mathring{r}_0) \sum_{m=1}^{M} \vec{E}_m p_m(\mathring{r}_0) \cdot \overline{G}_{eo}(\mathring{r}_0, \mathring{r}) dv_0 dv = \int_{v_n} \vec{E}_i(\mathring{r}) p_n(\mathring{r}) dv$$

$$(3.5)$$

where the initial electric field can be assumed to be a constant within each volume cell and the integration region is over the *nth* cell volume  $v_n$ . Equation (3.5) is integrated with respect to the variable  $\tilde{r}$  as

$$\vec{E}_{n}\left(1 - \frac{j\omega\mu_{0}}{k_{0}^{2}}\int_{v_{n}}\tau_{e}(\vec{r})dv\right) + j\omega\mu_{0}\int_{v_{sample}}\left(\tau_{e}(\vec{r}_{0})\sum_{m=1}^{M}\vec{E}_{m}p_{m}(\vec{r}_{0})\right)$$

$$\int_{v_{n}}p_{n}(\vec{r})\overline{G}_{eo}(\vec{r}_{0},\vec{r})dvdv_{0} = \vec{E}^{i}(\vec{r}_{n})\Delta V_{n}$$
(3.6)

Let's denote

$$\overline{G}_{ien}(\overset{\triangleright}{r}_0,\overset{\triangleright}{r}_n) = \int_{v_n} \overline{G}_{eo}(\overset{\triangleright}{r}_0,\overset{\triangleright}{r}) dv$$
 (3.7)

where  $\overline{G}_{ien}(\overset{*}{r}_0,\overset{*}{r}_n)$  specifies the integration of  $\overline{G}_{eo}(\overset{*}{r}_0,\overset{*}{r})$  with respect to  $\overset{*}{r}$  over the *nth* cell volume  $v_n$ . Equation (3.6) can then be rewritten as

$$\vec{E}_{n} \left( 1 - \frac{j\omega\mu_{0}}{k_{0}^{2}} \int_{v_{n}} \tau_{e}(\vec{r}) dv \right) + j\omega\mu_{0} \int_{v_{sample}m} \sum_{m=1}^{M} \vec{E}_{m} p_{m}(\vec{r}_{0}) \cdot \tau_{e}(\vec{r}_{0}) \vec{G}_{ien}(\vec{r}_{0}, \vec{r}_{n}) dv_{0}$$

$$= \vec{E}^{i}(\vec{r}_{n}) \Delta V_{n} \tag{3.8}$$

Because the number of volume cells is assumed to be large enough, in eq. (3.8) the integration which is over the total material sample volume can be estimated by the summation of the integrations over each cell volume as:

$$\vec{E}_{n} \left( 1 - \frac{j\omega\mu_{0}}{k_{0}^{2}} \int_{v_{n}} \tau_{e}(\vec{r}) dv \right) + j\omega\mu_{0} \sum_{l=1}^{M} \int_{v_{l}} \left( \sum_{m=1}^{M} \vec{E}_{m} p_{m}(\vec{r}_{0}) \cdot \tau_{e}(\vec{r}_{0}) \vec{G}_{ien}(\vec{r}_{0}, \vec{r}_{n}) \right) dv_{0}$$

$$= \vec{E}^{i}(\vec{r}_{n}) \Delta V_{n} \tag{3.9}$$

Let's denote

$$\overline{G}_{ienl}(\mathring{r}_l, \mathring{r}_n) = \int_{v_l} \tau_e(\mathring{r}_0) \overline{G}_{ien}(\mathring{r}_0, \mathring{r}_n) dv_0$$
(3.10)

where  $\overline{G}_{ienl}(\mathring{r}_l,\mathring{r}_n)$  specifies the integration of  $\tau_e(\mathring{r}_0)\overline{G}_{ien}(\mathring{r}_0,\mathring{r}_n)$  with respect to  $\mathring{r}_0$  over the volume  $v_l$  and  $\overline{E}_m p_m(\mathring{r}_0)$  is not equal to zero in the volume  $v_l$  only when m=l based on the definition of the pulse function  $p_m(\mathring{r})$  defined in eq. (3.2). Thus, eq. (3.9) can be rewritten as

$$\stackrel{\rightharpoonup}{E}_{n}\left(1 - \frac{j\omega\mu_{0}}{k_{0}^{2}} \int_{v_{n}} \tau_{e}(\mathring{r}) dv\right) + j\omega\mu_{0} \sum_{l=1}^{M} \stackrel{\rightharpoonup}{E}_{l} \cdot \overline{G}_{ienl}(\mathring{r}_{l}, \mathring{r}_{n}) = \stackrel{\rightharpoonup}{E}^{i}(\mathring{r}_{n}) \Delta V_{n} \tag{3.11}$$

Also we can express  $E_n \int_{v_n} \tau_e(\hat{r}) dv$  as

$$\vec{E}_n \int_{\nu_n} \tau_e(\vec{r}) d\nu = \sum_{l=1}^M \vec{E}_l \int_{\nu_l} \tau_e(\vec{r}) d\nu \cdot \bar{I} \delta_{nl}$$
 (3.12)

where  $\bar{I}$  is the unit dyadic and  $\delta_{nl} = \begin{cases} 1 & \text{if } n = l \\ 0 & \text{if } n \neq l \end{cases}$ . Therefore, based on eq. (3.12),

eq. (3.11) can be rewritten as

$$\sum_{l=1}^{M} \left[ \left( 1 - \frac{j\omega\mu_0}{k_0^2} \int_{v_n} \tau_e(\mathring{r}) dv \right) \bar{I} \delta_{nl} + j\omega\mu_0 \bar{G}_{ienl}(\mathring{r}_l, \mathring{r}_n) \right] \cdot \vec{E}_l = \vec{E}^i(\mathring{r}_n) \Delta V_n$$
 (3.13)

where n=1,2,...,M. Equation (3.13) can be expressed in a matrix format as

$$[\overline{A}_{nl}]_{M \times M} \cdot [\overrightarrow{E}_{l}]_{M \times 1} = [\overrightarrow{B}_{n}]_{M \times 1} \tag{3.14}$$

where n, l = 1, 2, ..., M and

$$\overline{A}_{nl} = \left(1 - \frac{j\omega\mu_0}{k_0^2} \int_{\nu_n} \tau_e(\mathring{r}) d\nu\right) \overline{I} \delta_{nl} + j\omega\mu_0 \tau_e \overline{G}_{ienl}(\mathring{r}_l, \mathring{r}_n)$$
(3.15)

$$\vec{B}_n = \vec{E}^i(\vec{r}_n) \Delta V_n \tag{3.16}$$

If we use the scalar components format instead of the vector format, the matrix eq. (3.14) can be expressed as

$$[A_{nl}]_{3M\times 3M} \cdot [E_l]_{3M\times 1} = [B_l]_{3M\times 1} \tag{3.17}$$

where

$$[E_l]_{3M\times 1} = [E_{1x}...E_{Mx}E_{1y}...E_{My}E_{1z}...E_{Mz}]^T$$
(3.18)

$$[B_{l}]_{3M\times 1} = [E_{x}^{i}(\hat{r}_{1})\Delta V_{1}...E_{x}^{i}(\hat{r}_{M})\Delta V_{M} E_{y}^{i}(\hat{r}_{1})\Delta V_{1}...E_{y}^{i}(\hat{r}_{M})\Delta V_{M}$$

$$E_{z}^{i}(\hat{r}_{1})\Delta V_{1}...E_{z}^{i}(\hat{r}_{M})\Delta V_{M}]^{T}$$
(3.19)

$$[A_{nl}]_{3M\times 3M} = \begin{bmatrix} [\bar{A}_{nl}]_{xx} \ [\bar{A}_{nl}]_{xy} \ [\bar{A}_{nl}]_{xz} \\ [\bar{A}_{nl}]_{yx} \ [\bar{A}_{nl}]_{yy} \ [\bar{A}_{nl}]_{yz} \\ [\bar{A}_{nl}]_{zx} \ [\bar{A}_{nl}]_{zy} \ [\bar{A}_{nl}]_{zz} \end{bmatrix}$$
(3.20)

and the dimensions of each submatrix in (3.20) are  $M \times M$ .

# 3.2 Convergence Property of Dyadic Green's Function in EFIE

In the numerical computation, the most difficult step in solving *EFIE* is to fill out the matrix  $[A_{nl}]_{3M\times3M}$  in eqs. (3.17) to (3.20). The integrations of the dyadic Green's function  $\overline{G}_{eo}(\overset{\star}{r}_0,\overset{\star}{r})$  at different points in the material sample with respect to both variables  $\overset{\star}{r}$  and  $\overset{\star}{r}_0$  as specified in eqs. (3.7) and (3.10) need to be carried out in the matrix composition. However, the convergence property of the integration of the dyadic Green's function  $\overline{G}_{eo}(\overset{\star}{r}_0,\overset{\star}{r})$  is still very poor even though the Galerkin's method is used.

The dyadic Green's function  $\overline{G}_{eo}(\mathring{r}_0,\mathring{r})$  in a triple summation format is given by eq. (2.101) in Chapter 2 as

$$\overline{G}_{eo}(\hat{r}_0, \hat{r}) = \sum_{n=0}^{\infty} \sum_{m=0}^{\infty} \sum_{l=0}^{\infty} \left[ k_{nml}^2 \frac{\overrightarrow{M}_{nml}(\hat{r}_0) \overrightarrow{M}_{nml}(\hat{r}) + \overrightarrow{N}_{nml}(\hat{r}_0) \overrightarrow{N}_{nml}(\hat{r})}{k_0^2 (k_{nml}^2 - k_0^2)} \right]$$
(3.21)

Since eq. (3.21) has a very poor convergence property [2], the integration of it has a poor convergence property as well. Several numerical results are shown here to illustrate the slow convergence of the integration of the dyadic Green's function  $\overline{G}_{eo}(\hat{r}_0, \hat{r})$ .

In these numerical results, we only show the convergence property of the integration of  $G_{eoxx}(\overset{*}{r}_0,\overset{*}{r})$  component at the different points and avoid the repetition of the computation for the other components of the dyadic Green's function  $\overline{G}_{eo}(\overset{*}{r}_0,\overset{*}{r})$  since they all have the similar convergence properties. The coefficient of  $G_{eoxx}(\overset{*}{r}_0,\overset{*}{r})$  was given in eq. (2.95) in Chapter 2, and the expression of  $G_{eoxx}(\overset{*}{r}_0,\overset{*}{r})$  is then given by

$$G_{eoxx}(\mathring{r}_0,\mathring{r}) = \sum_{n=0}^{\infty} \sum_{m=1}^{\infty} \sum_{l=1}^{\infty} \frac{4\varepsilon_{0n}}{abc} \frac{\left(\frac{m\pi}{b}\right)^2 + \left(\frac{l\pi}{c}\right)^2}{k_0^2 (k_n^2 - k_0^2)} \cos\left(\frac{n\pi}{a}x\right) \cos\left(\frac{n\pi}{a}x_0\right)$$

$$\sin\left(\frac{m\pi}{b}y\right) \sin\left(\frac{m\pi}{b}y_0\right) \sin\left(\frac{l\pi}{c}z\right) \sin\left(\frac{l\pi}{c}z_0\right)$$
(3.22)

where  $\varepsilon_{0n}$  is defined in eq. (2.63).

In the following computations, we assume that the initial cavity mode is  $TE_{101}$ , then the eigenvalue (wavenumber) of this initial mode is given by

$$k_0^2 = \left(\frac{\pi}{a}\right)^2 + \left(\frac{\pi}{c}\right)^2 \tag{3.23}$$

and in eq. (3.22) we will change the summation upper limit from  $\infty$  to N. We aim to choose some value of N which makes the integration of the triple summation series (3.22) converge. The dimensions of the rectangular cavity are a = 0.072m, b = 0.034m and c = 0.1163m. The initial resonant frequency is then  $f_0 = 2.45GHz$  based on eq. (3.23).

The integration of  $G_{eoxx}(\hat{r}_0, \hat{r})$  with respect to  $\hat{r}$  and  $\hat{r}_0$  in regions  $v_n$  and  $v_{n0}$  is expressed as

$$\int_{x}^{x+\Delta xy+\Delta yz+\Delta z} \int_{y_0}^{x} \int_{z_0}^{z} \int_{y_0}^{z} \int_{z_0}^{z} G_{eoxx}(\mathring{r}_0,\mathring{r}) du dv dw du_0 dv_0 dw_0$$

$$= \sum_{n=1}^{N} \sum_{m=1}^{N} \sum_{l=1}^{N} \sum_{abc}^{x} \frac{8}{abc} \frac{\left(\frac{m\pi}{b}\right)^2 + \left(\frac{l\pi}{c}\right)^2}{k_0^2 (k_n^2 - k_0^2)} \frac{1}{\left(\frac{n\pi}{a}\right)^2 \left(\frac{m\pi}{b}\right)^2 \left(\frac{l\pi}{c}\right)^2} \left[\sin\frac{n\pi}{a}(x + \Delta x) - \sin\frac{n\pi}{a}x\right]$$

$$\left[\sin\frac{n\pi}{a}(x_0 + \Delta x) - \sin\frac{n\pi}{a}x_0\right] \left[\cos\frac{m\pi}{b}(y + \Delta y) - \cos\frac{m\pi}{b}y\right] \left[\cos\frac{m\pi}{b}(y_0 + \Delta y) - \cos\frac{m\pi}{b}y\right]$$

$$-\cos\frac{m\pi}{b}y_0 \left[\cos\frac{l\pi}{c}(z + \Delta z) - \cos\frac{l\pi}{c}z\right] \left[\cos\frac{l\pi}{c}(z_0 + \Delta z) - \cos\frac{l\pi}{c}z_0\right]$$

for  $n \neq 0$  and

$$\int_{x}^{x+\Delta x} \int_{y}^{x+\Delta y} \int_{z}^{x} \int_{x_{0}}^{x} \int_{y_{0}}^{x} \int_{z_{0}}^{z} G_{eoxx}(\mathring{r}_{0},\mathring{r}) du dv dw du_{0} dv_{0} dw_{0}$$

$$= \sum_{m=1}^{N} \sum_{l=1}^{N} \frac{4}{abc} \frac{\left(\frac{m\pi}{b}\right)^{2} + \left(\frac{l\pi}{c}\right)^{2}}{k_{0}^{2}(k_{n}^{2} - k_{0}^{2})} \frac{\Delta x^{2}}{\left(\frac{m\pi}{b}\right)^{2} \left(\frac{l\pi}{c}\right)^{2}} \left[\cos\frac{m\pi}{b}(y + \Delta y) - \cos\frac{m\pi}{b}y\right]$$

$$\left[\cos\frac{m\pi}{b}(y_{0} + \Delta y) - \cos\frac{m\pi}{b}y_{0}\right] \left[\cos\frac{l\pi}{c}(z + \Delta z) - \cos\frac{l\pi}{c}z\right] \left[\cos\frac{l\pi}{c}(z_{0} + \Delta z) - \cos\frac{l\pi}{c}z_{0}\right]$$

for n = 0. We choose  $\Delta x = \Delta y = \Delta z = 0.002m$  in the following computations.

One thing which needs a special attention in the computation is when  $k_n^2 = k_0^2$ , the summation term will have a singularity. This occurs because one of the summation modes is exactly equal to the initial mode, that is,  $n = n_0$ ,  $m = m_0$  and  $l = l_0$ , where  $n_0$ ,  $m_0$  and  $l_0$  specify the indices of the initial mode. From the experiments we observed that when a material sample is placed into the cavity, the resonant frequency of the initial mode will

shift down about 1% to 10% depending on the geometry of the material sample (this resonant frequency shift is also shown in [68]). Based on this experimental observation, when  $k_n^2 = k_0^2$  we will make the approximation of

$$k_n^2 - k_0^2 \cong -sk_0^2 \tag{3.26}$$

where s is the shift rate of the resonant eigenvalue. The followings are the integrations of  $G_{eox}(r_0, r)$  at different points with the assumed resonant frequency shift rate to be 5%.

- 1. When  $\dot{r} = \dot{r}_0$ , the integration of  $\overline{G}_{eoxx}(\dot{r}_0, \dot{r})$  is shown in Figure 3.1. The source and observation points are  $\dot{r} = \dot{r}_0 = [0.033m, 0.014m, 0.0551m]$ .
- 2. when  $\dot{r} \neq \dot{r}_0$ ,
- (a) The source and observation points are  $\mathring{r}=[0.035m, 0.014m, 0.0551m]$ ,  $\mathring{r}_0=[0.033m, 0.014m, 0.0551m]$ , the integration of  $G_{eox}(\mathring{r}_0, \mathring{r})$  is shown in Figure 3.2.
- (b) The source and observation points are  $\hat{r} = [0.035m, 0.016m, 0.0553m]$ ,  $\hat{r}_0 = [0.033m, 0.014m, 0.0551m]$ , the integration of  $G_{eoxx}(\hat{r}_0, \hat{r})$  is shown in Figure 3.3. In Figure 3.1 to Figure 3.3, the horizontal axes are the value of N and the vertical axes are the integration of  $G_{eoxx}(\hat{r}_0, \hat{r})$ .

In all of these computations, we varied N from 1 to 400. These figures show that when  $\dot{r} = \dot{r}_0$ , the convergence rate is slower than those of  $\dot{r} \neq \dot{r}_0$ . Also when  $x \neq x_0$ ,  $y \neq y_0$  and  $z \neq z_0$ , the integration converges fastest. Thus, we can conclude that the farther the distance between the observation point and the source point is, the faster this

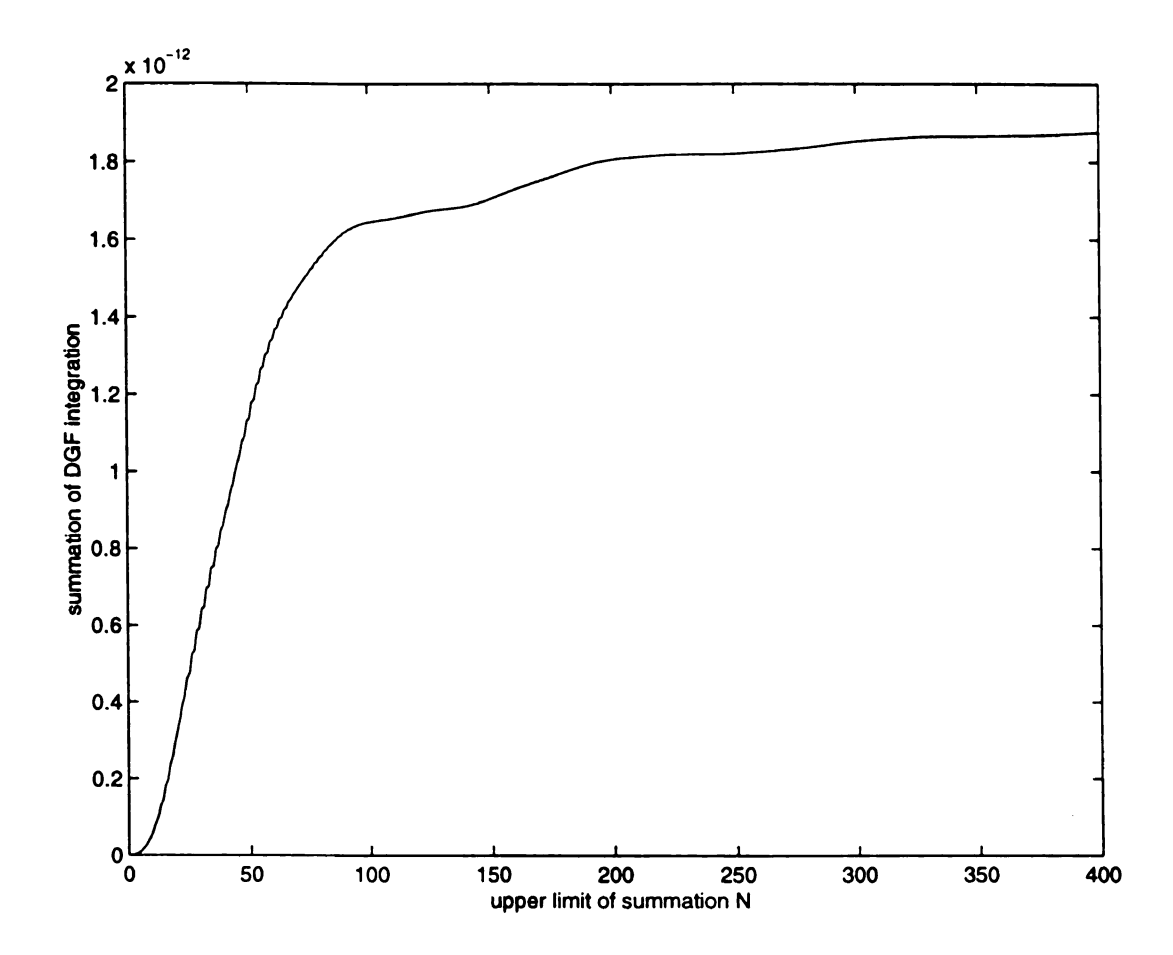


Figure 3.1 Integration of the triple summation format  $G_{eoxx}(\mathring{r}_0,\mathring{r})$  vs. the number of summation modes when  $\mathring{r}=\mathring{r}_0$ ,  $\mathring{r}=[0.033m,0.014m,0.0551m]$  and  $\Delta x=\Delta y=\Delta z=0.002m$ . The dimensions of the rectangular cavity are: a=0.072m, b=0.034m and c=0.1163m.

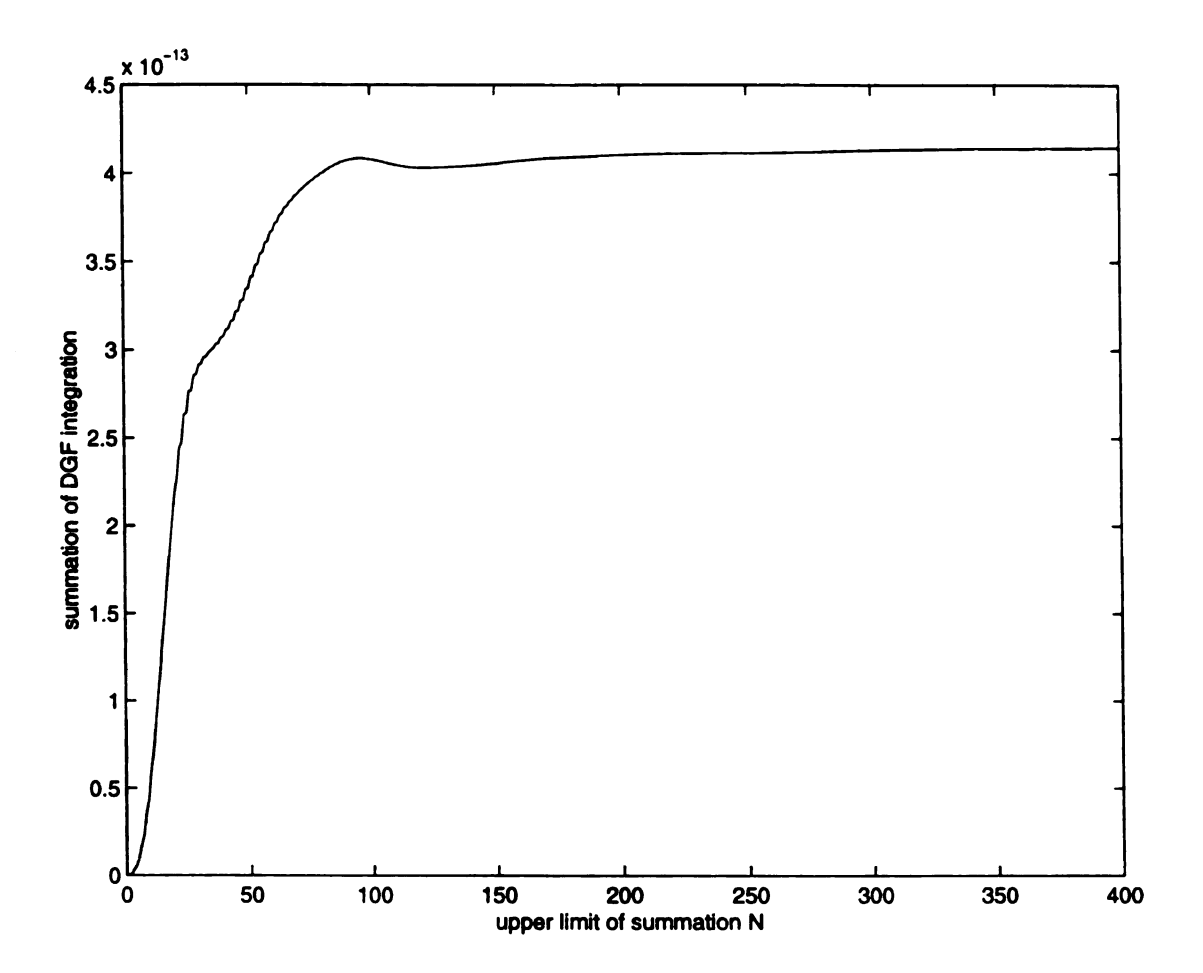


Figure 3.2 Integration of the triple summation format  $G_{eoxx}(\hat{r}_0, \hat{r})$  vs. the number of summation modes when  $\hat{r} = [0.035m, 0.014m, 0.0551m]$ ,

 $r_0$ = [0.033m, 0.014m, 0.0551m] and  $\Delta x = \Delta y = \Delta z = 0.002m$ . The dimensions of the rectangular cavity are: a = 0.072m, b = 0.034m and c = 0.1163m.

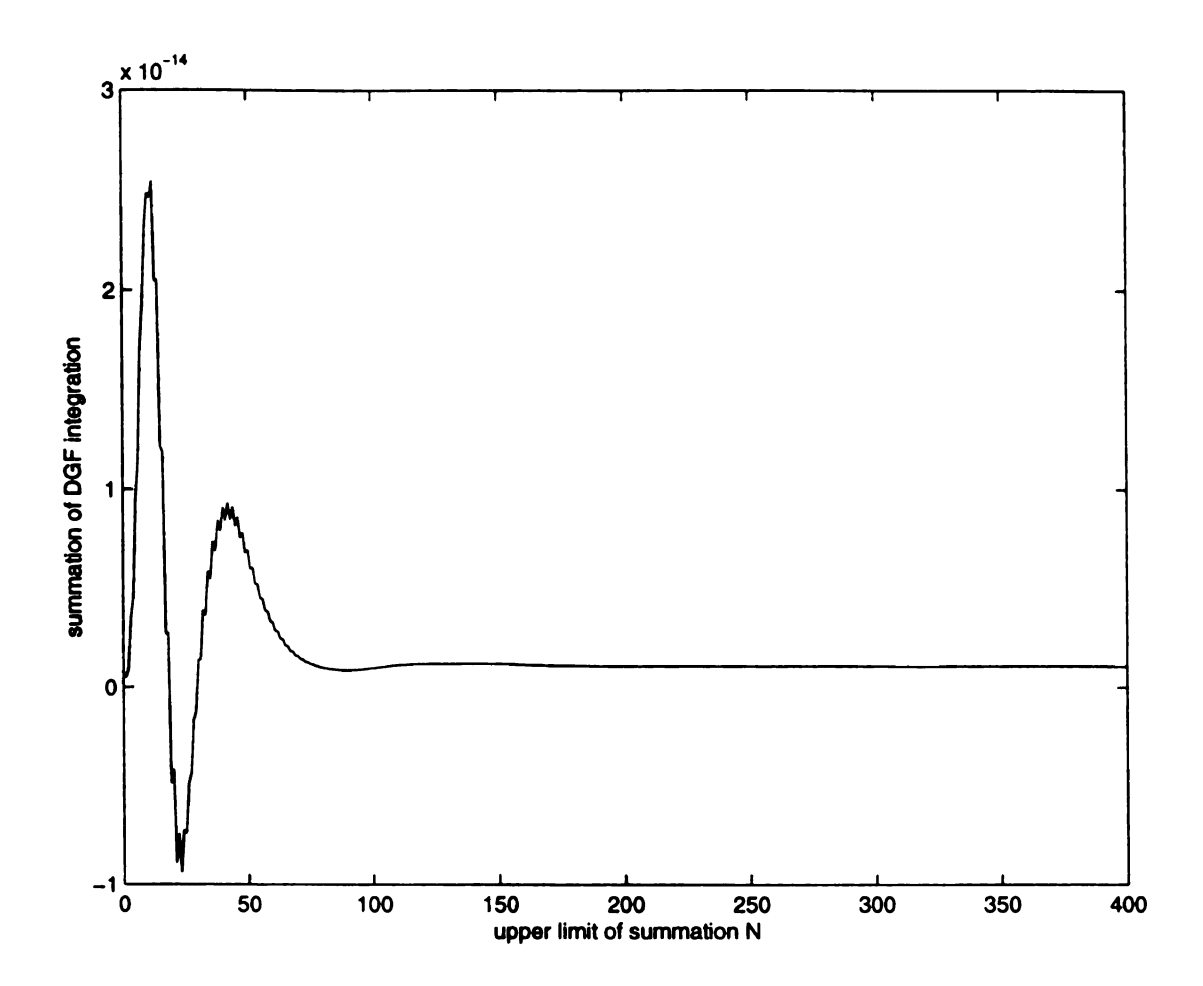


Figure 3.3 Integration of the triple summation format  $G_{eox}(\grave{r}_0, \grave{r})$  vs. the number of summation modes when  $\grave{r}=[0.035m, 0.016m, 0.0553m]$ ,  $\grave{r}_0=[0.033m, 0.014m, 0.0551m]$  and  $\Delta x=\Delta y=\Delta z=0.002m$ . The dimensions of the rectangular cavity are: a=0.072m, b=0.034m and c=0.1163m.

integration converges. However, when  $\dot{r} = \dot{r}_0$  with the parameters chosen in case 1, the convergence value in Figure 3.1 is about  $1.88 \times 10^{-12}$  and those in Figure 3.2 and Figure 3.3 are about  $4.15 \times 10^{-13}$  and  $1.05 \times 10^{-15}$  with the parameters chosen in case 2(a) and case 2(b). The  $\dot{r} = \dot{r}_0$  terms are on the diagonal lines of each submatrix in (3.20) and they are dominant in this matrix in terms of the numerical results.

Observing these three figures and considering the trade-off between the numerical accuracy and the computation time, we conclude that when N=200 we can obtain the satisfactory convergence results for these three cases. However, this is over 8 million terms summation! This indicates that the convergence rate of the integration of the dyadic Green's function  $\overline{G}_{eo}(\stackrel{*}{r}_0, \stackrel{*}{r})$  is extremely slow.

To save computation time we can reduce the triple summation in the dyadic Green's function to a double summation based on the following two relations:

$$\sum_{n=1}^{\infty} \frac{\sin(\frac{n\pi}{a}x)\sin(\frac{n\pi}{a}x_0)}{k_n^2 - k_0^2} = \frac{a}{2k_{gml}\sin(k_{gml}a)}\sin(k_{gml}(a - x_b))\sin(k_{gml}x_s)$$
 (3.27)

$$\sum_{n=0}^{\infty} \frac{\varepsilon_{0n} \cos\left(\frac{n\pi}{a}x\right) \cos\left(\frac{n\pi}{a}x_{0}\right)}{2(k_{n}^{2} - k_{0}^{2})} = \frac{-a}{2k_{gml} \sin(k_{gml}a)} \cos(k_{gml}(a - x_{b})) \cos(k_{gml}x_{s}) \quad (3.28)$$

where  $\varepsilon_{0n}$  is defined in eq. (2.63) and

$$k_n^2 = \left(\frac{n\pi}{a}\right)^2 + \left(\frac{m\pi}{b}\right)^2 + \left(\frac{l\pi}{c}\right)^2 \tag{3.29}$$

$$k_{gml} = \sqrt{k_0^2 - \left(\frac{m\pi}{b}\right)^2 - \left(\frac{l\pi}{c}\right)^2}$$
 (3.30)

It will be convenient to define the following

$$x_b \equiv the \ greater \ of \ x \ or \ x_0$$
 (3.31)

$$x_s \equiv the \ lesser \ of \ x \ or \ x_0$$
 (3.32)

 $x_b$  and  $x_s$  will be referred later for the same definitions. Detailed derivation of the last two relations (3.27) and (3.28) and the representation of  $\overline{G}_{eo}$  in the double summation format can be found in Appendix C. For simplicity, we will only perform the integration of  $G_{eox}(\overset{\bullet}{r}_0,\overset{\bullet}{r})$  represented in the double summation format.

In order to obtain the expression for  $G_{eoxx}(\grave{r}_0, \grave{r})$  in the double summation format, we can sum over any one of the indices n, m, l in eq. (3.22) using the relations given by eqs. (3.27) and (3.28). However, since there is a factor of  $\left(\frac{m\pi}{b}\right)^2 + \left(\frac{l\pi}{c}\right)^2$  in the numerator of the eq. (3.22), we can obtain the simplest expression for  $G_{eoxx}(\grave{r}_0, \grave{r})$  in the double summation format if we sum over the index n by eq. (3.28) in the triple summation (3.22). Using eq. (C.19), the expression for  $G_{eoxx}(\grave{r}_0, \grave{r})$  in the double summation format can be expressed as

$$\overline{G}_{eoxx}(\dot{r}_{0}, \dot{r}) = -\frac{1}{k_{0m}^{2}} \sum_{l=1}^{\infty} \sum_{l=1}^{\infty} \frac{4}{bc} \frac{\left(\frac{m\pi}{b}\right)^{2} + \left(\frac{l\pi}{c}\right)^{2}}{k_{gml} \sin(ak_{gml})} g_{ml}(x, x_{0}) \sin\frac{m\pi}{b} y$$

$$\sin\frac{m\pi}{b} y_{0} \sin\frac{l\pi}{c} z \sin\frac{l\pi}{c} z_{0}$$
(3.33)

where  $k_{gml}$  has been defined in eq. (3.30) and

$$g_{ml}(x, x_0) = \cos(k_{gml}(a - x_b))\cos(k_{gml}x_s)$$
 (3.34)

It is noted that there is a factor of  $k_{gml}\sin(ak_{gml})$  in the denominator in eq. (3.33). When  $k_{gml}=0$ , there exists singularity. For this case, we can not use the double summation format expression of  $G_{eoxx}(\overset{\circ}{r}_0,\overset{\circ}{r})$  (3.33). We should sum over the index n directly for this special case taking into account of a slight shift in the resonant frequency. These summations can be found in Appendix C. From eq. (C.38), for  $n_0=0$ , where  $n_0$  is one of the indices of the initial cavity mode, the summation over index n becomes

$$-\frac{1}{a}\frac{1}{sk_0^2} + \sum_{n=1}^{\infty} \frac{2}{a} \frac{\cos\frac{n\pi}{a}x\cos\frac{n\pi}{a}x_0}{\left(\frac{n\pi}{a}\right)^2} \cong -\frac{1}{a}\frac{1}{sk_0^2} + \frac{1}{2a}(x^2 + x_0^2) + \frac{a}{3} - x_b$$
 (3.35)

and for  $n_0 \neq 0$ , eq. (C.39) gives the summation over index n as:

$$\sum_{n=0}^{\infty} \frac{\varepsilon_{0n}}{a} \frac{1}{\left(\frac{n\pi}{a}\right)^2 - \left(\frac{n_0\pi}{a}\right)^2} \cos\frac{n\pi}{a}x \cos\frac{n\pi}{a}x_0$$

$$\approx \sum_{n=1}^{4n_0} \frac{2}{a} \frac{\left(\frac{n_0\pi}{a}\right)^2}{\left(\frac{n\pi}{a}\right)^2 \left(\left(\frac{n\pi}{a}\right)^2 - \left(\frac{n_0\pi}{a}\right)^2\right)} \cos\frac{n\pi}{a}x \cos\frac{n\pi}{a}x_0 - \frac{1}{a}\left(\frac{a}{n_0\pi}\right)^2 + \frac{1}{2a}(x^2 + x_0^2)$$

$$+ \frac{a}{3} - x_b - \frac{2}{a} \left(\frac{1}{\left(\frac{n_0\pi}{a}\right)^2 + \frac{1}{sk_0^2}\right)} \cos\frac{n_0\pi}{a}x \cos\frac{n_0\pi}{a}x_0$$
(3.36)

where s has been defined in eq. (3.26).

Substituting eqs. (3.35) and (3.36) into eq. (3.22), we can obtain another alternative representation of  $G_{eoxx}(\mathring{r}_0,\mathring{r})$ . Fortunately, the variables x, y, z are separable in the summation, thus, we can integrate  $G_{eoxx}(\mathring{r}_0,\mathring{r})$  with respect to them independently.

In the double summation format representation of  $G_{eoxx}(\mathring{r}_0,\mathring{r})$  given by eq. (3.33), the factor  $k_{gml}$  may be a real number, eq. (3.30) or an imaginary number for most cases because we usually assume the initial mode to be a lower order mode. When  $k_{gml}$  is an imaginary number,

$$k_{gml} = i \sqrt{\left(\frac{m\pi}{b}\right)^2 + \left(\frac{l\pi}{c}\right)^2 - k_0^2} = i k_{gmli}$$
 (3.37)

where  $k_{gmli}$  is a real number, eq. (3.34) can be rewritten as

$$g_{mli}(x, x_0) = \cosh(k_{gmli}(a - x_b))\cosh(k_{gmli}x_s)$$
 (3.38)

and the double summation format representation of  $G_{eoxx}(\mathring{r}_0,\mathring{r})$  can be rewritten as

$$\overline{G}_{eoxx}(\hat{r}_0, \hat{r}) = \frac{1}{k_{0m=1}^2} \sum_{l=1}^{\infty} \sum_{l=1}^{\infty} \frac{4}{bc} \frac{\left(\frac{m\pi}{b}\right)^2 + \left(\frac{l\pi}{c}\right)^2}{k_{gmli} \sinh(ak_{gmli})} g_{mli}(x, x_0) \sin\frac{m\pi}{b} y \\
\sin\frac{m\pi}{b} y_0 \sin\frac{l\pi}{c} z \sin\frac{l\pi}{c} z_0$$
(3.39)

In the actual computation, we find that  $\sinh(ak_{gmli})$  grows exponentially due to  $ak_{gmli} \gg 1$ . Based on this condition,  $\sinh(ak_{gmli})$  can be estimated by

$$\sinh(ak_{gmli}) \cong \frac{e^{ak_{gmli}}}{2} \tag{3.40}$$

and eq. (3.38) can then be rewritten as

$$g_{mli}(x, x_0) = \frac{1}{4} \left( e^{k_{gmli}(a - x_b)} + e^{-k_{gmli}(a - x_b)} \right) \left( e^{k_{gmli}x_s} + e^{-k_{gmli}x_s} \right)$$

$$= \frac{1}{4} e^{ak_{gmli}} \left( e^{-k_{gmli}x_b} + e^{-k_{gmli}(2a - x_b)} \right) e^{k_{gmli}x_s}$$
(3.41)

In eq. (3.41), because  $ak_{gmli} \gg 1$ , x < a and  $x_0 < a$ , it can be estimated as

$$g_{mli}(x, x_0) = \frac{1}{4} e^{ak_{gmli}} e^{-k_{gmli}|x-x_0|}$$
(3.42)

Substituting eqs. (3.40) and (3.42) into eq. (3.39) leads to

$$G_{eoxx}(\dot{r}_{0}, \dot{r}) = \frac{1}{k_{0m}^{2}} \sum_{l=1}^{\infty} \sum_{l=1}^{\infty} \frac{4}{bc} \frac{\left(\frac{m\pi}{b}\right)^{2} + \left(\frac{l\pi}{c}\right)^{2}}{2k_{gmli}} e^{-k_{gmli}|x-x_{0}|} \sin\frac{m\pi}{b} y$$

$$\sin\frac{m\pi}{b} y_{0} \sin\frac{l\pi}{c} z \sin\frac{l\pi}{c} z_{0}$$
(3.43)

Based on these alternative representations of  $G_{eoxx}(\hat{r}_0, \hat{r})$  for different cases, i.e., if  $k_{gml}$  is real or imaginary or if there is any singularity, the integration of eq. (3.33) is given by

$$-\frac{1}{k_{0m}^{2}}\sum_{l=1}^{\infty}\sum_{l=1}^{\infty}\frac{4}{bc}\frac{\left(\frac{m\pi}{b}\right)^{2}+\left(\frac{l\pi}{c}\right)^{2}x+\Delta x x_{0}+\Delta x}{\left(\frac{m\pi}{b}\right)^{2}\left(\frac{l\pi}{c}\right)^{2}}\int_{x}^{x+\Delta x}\int_{x_{0}}^{x}\frac{1}{k_{gml}\sin\left(ak_{gml}\right)}g_{ml}(u,u_{0})dudu_{0}$$

$$\left[\cos\frac{m\pi}{b}(y+\Delta y)-\cos\frac{m\pi}{b}y\right]\left[\cos\frac{m\pi}{b}(y_{0}+\Delta y)-\cos\frac{m\pi}{b}y_{0}\right]$$

$$\left[\cos\frac{l\pi}{c}(z+\Delta z)-\cos\frac{l\pi}{c}z\right]\left[\cos\frac{l\pi}{c}(z_{0}+\Delta z)-\cos\frac{l\pi}{c}z_{0}\right]$$
(3.44)

Although in the expression of  $g_{ml}(x, x_0)$  there are different equations for  $x > x_0$  and

 $x < x_0$ , also for the different  $k_{gml}$ , the expressions of the  $g_{ml}(x, x_0)$  involves only sine or cosine and exponential functions of x and  $x_0$  as given in eqs. (3.34) and (3.42), the integrations of  $g_{ml}(x, x_0)$  with respect to x and  $x_0$  become easier for  $x > x_0$  or  $x < x_0$ . However, when  $x = x_0$ , we need to pay a special attention to the integration.

1. When  $x \neq x_0$  and  $k_{gml}$  is real, the integration of  $g_{ml}(x, x_0)$  with respect to x and  $x_0$  is given by

$$\int_{x}^{x+\Delta x x_{0}+\Delta x} \int_{x_{0}}^{x} \frac{1}{k_{gml} \sin(ak_{gml})} g_{ml}(u, u_{0}) du du_{0}$$

$$= \frac{-1}{k_{gml}^{3} \sin(ak_{gml})} \left[ \sin(k_{gml}(a-x_{b}-\Delta x)) - \sin(k_{gml}(a-x_{b})) \right]$$

$$[\sin(k_{gml}(x_{s}+\Delta x)) - \sin(k_{gml}x_{s})]$$
(3.45)

2. When  $x \neq x_0$  and  $k_{gml}$  is imaginary, the integration of  $g_{ml}(x, x_0)$  with respect to x and  $x_0$  is given by

$$\int_{x}^{x + \Delta x} \int_{x_{0}}^{x_{0} + \Delta x} \frac{1}{2k_{gmli}} e^{-k_{gmli}|u - u_{0}|} du du_{0} = -\frac{1}{k_{gmli}^{3}} e^{-k_{gmli}|x - x_{0}|} (1 - \cosh(k_{gmli}\Delta x))$$
(3.46)

- 3. When  $k_{gml}$  is chosen in such a way that there is a singularity occurring, the integrations of  $g_{ml}(x, x_0)$  with respect to x and  $x_0$  are those of eqs. (3.35) and (3.36) with respect to x and  $x_0$ .
- (1) When  $n_0 = 0$  and  $x \neq x_0$ , the integration is given by

$$\int_{x}^{x+\Delta x x_{0}+\Delta x} \int_{x_{0}}^{x} \left( -\frac{1}{a} \frac{1}{s k_{0}^{2}} + \frac{1}{2a} (u^{2} + u_{0}^{2}) + \frac{a}{3} - x_{b} \right) du du_{0}$$

$$= -\frac{1}{a} \frac{\Delta x^{2}}{s k_{0}^{2}} + \frac{\Delta x}{6a} [(x + \Delta x)^{3} - x^{3} + (x_{0} + \Delta x)^{3} - x_{0}^{3}]$$

$$+ \frac{a \Delta x^{2}}{3} - \frac{1}{2} ((x_{b} + \Delta x)^{2} - x_{b}^{2}) \Delta x$$
(3.47)

(2) When  $n_0 \neq 0$  and  $x \neq x_0$ , the integration is given by

$$\int_{x}^{x+\Delta x x_{0}+\Delta x} \int_{x_{0}}^{4n_{0}} \int_{n=1}^{2} \frac{2}{a} \frac{\left(\frac{n_{0}\pi}{a}\right)^{2}}{\left(\frac{n\pi}{a}\right)^{2} \left(\left(\frac{n\pi}{a}\right)^{2} - \left(\frac{n_{0}\pi}{a}\right)^{2}\right)} \cos \frac{n\pi}{a} u \cos \frac{n\pi}{a} u_{0} - \frac{1}{a} \left(\frac{a}{n_{0}\pi}\right)^{2} + \frac{$$

4. When  $x = x_0$  and  $k_{gml}$  is real, the integration of  $g_{ml}(x, x_0)$  with respect to x and  $x_0$  is given by

$$\int_{x}^{x+\Delta x} \int_{x}^{\Delta x} \frac{1}{k_{gml} \sin(ak_{gml})} g_{ml}(t, t_0) dt dt_0$$

$$= \int_{x}^{x+\Delta x} \frac{1}{k_{gml} \sin(ak_{gml})} \left[ \int_{x}^{t} g_{ml}(t, t_0) dt_0 + \int_{t}^{x+\Delta x} g_{ml}(t, t_0) dt_0 \right] dt$$

$$= \frac{1}{k_{gml}} \sin(k_{gml}a) \Delta x + \frac{2 \sin\left(k_{gml}\frac{\Delta x}{2}\right)}{k_{gml}^2} \bullet$$

$$\left[ \sin\left(k_{gml}\frac{\Delta x}{2}\right) \cos(k_{gml}(a-2x-\Delta x)) - \sin\left(k_{gml}\left(a-\frac{\Delta x}{2}\right)\right) \right]$$
(3.49)

5. When  $x = x_0$  and  $k_{gml}$  is imaginary, the integration of  $g_{ml}(x, x_0)$  with respect to x and  $x_0$  is given by

$$\int_{x}^{x+\Delta xx+\Delta x} \int_{x}^{1} \frac{1}{2k_{gmli}} e^{-k_{gmli}|t-t_0|} dt dt_0 = \frac{\Delta x}{k_{gmli}^2} + \frac{1}{k_{gmli}^3} [e^{-k_{gmli}\Delta x} - 1]$$
 (3.50)

- 6. When there is a singularity occurring and  $x = x_0$ , the integration of  $g_{ml}(x, x_0)$  with respect to x and  $x_0$  is given by
- (1) for  $n_0 = 0$ ,

$$\int_{x}^{x+\Delta x} \int_{x}^{\Delta x} \left( -\frac{1}{a} \frac{1}{sk_0^2} + \frac{1}{2a} (t^2 + t_0^2) + \frac{a}{3} - t_b \right) dt dt_0$$

$$= \frac{1}{6} [(x + \Delta x)^3 - x^3] \left[ \frac{2\Delta x}{a} - 1 \right] + \frac{(x + \Delta x)^2 (x - \Delta x)}{2} - \frac{x^3}{2} + \left( \frac{a}{3} - \frac{1}{a} \frac{1}{sk_0^2} \right) \Delta x^2$$
(3.51)

 $(2) \text{ for } n_0 \neq 0,$ 

$$\int_{x}^{x+\Delta xx+\Delta x} \int_{x}^{4n_0} \sum_{n=1}^{2} \frac{2}{a} \frac{\left(\frac{n_0\pi}{a}\right)^2}{\left(\frac{n\pi}{a}\right)^2 - \left(\frac{n_0\pi}{a}\right)^2} \cos \frac{n\pi}{a} t \cos \frac{n\pi}{a} t_0 - \frac{1}{a} \left(\frac{a}{n_0\pi}\right)^2$$

$$+ \frac{1}{2a} (t^2 + t_0^2) + \frac{a}{3} - t_b - \frac{2}{a} \left(\frac{1}{\left(\frac{n_0\pi}{a}\right)^2} + \frac{1}{sk_0^2}\right) \cos \frac{n_0\pi}{a} t \cos \frac{n_0\pi}{a} t_0 dt dt_0$$

$$= \sum_{n=1}^{4n_0} \frac{2}{a} \frac{\left(\frac{n_0\pi}{a}\right)^2}{\left(\frac{n\pi}{a}\right)^4 \left(\left(\frac{n\pi}{a}\right)^2 - \left(\frac{n_0\pi}{a}\right)^2\right)} \left[\sin \frac{n\pi}{a} (x + \Delta x) - \sin \frac{n\pi}{a} x\right]^2 - \left(\frac{a}{(n_0\pi)^2} - \frac{a}{3}\right) \Delta x^2$$

$$+ \frac{\Delta x}{3a} [(x + \Delta x)^3 - x^3] + \frac{(x + \Delta x)^3 + 2x^3}{6} - \frac{(x + \Delta x)^2 (x - \Delta x)}{2}$$

$$- \frac{2}{a \left(\frac{n_0\pi}{a}\right)^2} \left(\frac{1}{\left(\frac{n_0\pi}{a}\right)^2} + \frac{1}{sk_0^2}\right) \left[\sin \frac{n_0\pi}{a} (x + \Delta x) - \sin \frac{n_0\pi}{a} x\right]^2$$

In the following computations, we will use eqs. (3.44) to (3.52) to perform the integration of  $G_{eoxx}(\mathring{r}_0, \mathring{r})$ . In eq. (3.44), we will use a finite number of N instead of  $\infty$  as the summation upper limit and find some value of N which can lead to the converged results which is consistent with the results of the triple summation. The dimensions of the cavity, the initial mode, the resonant frequency shift,  $\Delta x$ ,  $\Delta y$ ,  $\Delta z$  and the choices of the source and observation points  $\mathring{r}$  and  $\mathring{r}_0$  remain the same as those for the triple summation in order to compare the convergence property of the triple and double summations.

Figure 3.4 is the integration of  $G_{eoxx}(\mathring{r}_0,\mathring{r})$  when  $\mathring{r}=\mathring{r}_0$ . Figure 3.5 and Figure 3.6 are the integrations of  $G_{eoxx}(\mathring{r}_0,\mathring{r})$  when  $\mathring{r}\neq\mathring{r}_0$ . In Figure 3.4 to Figure 3.6, the

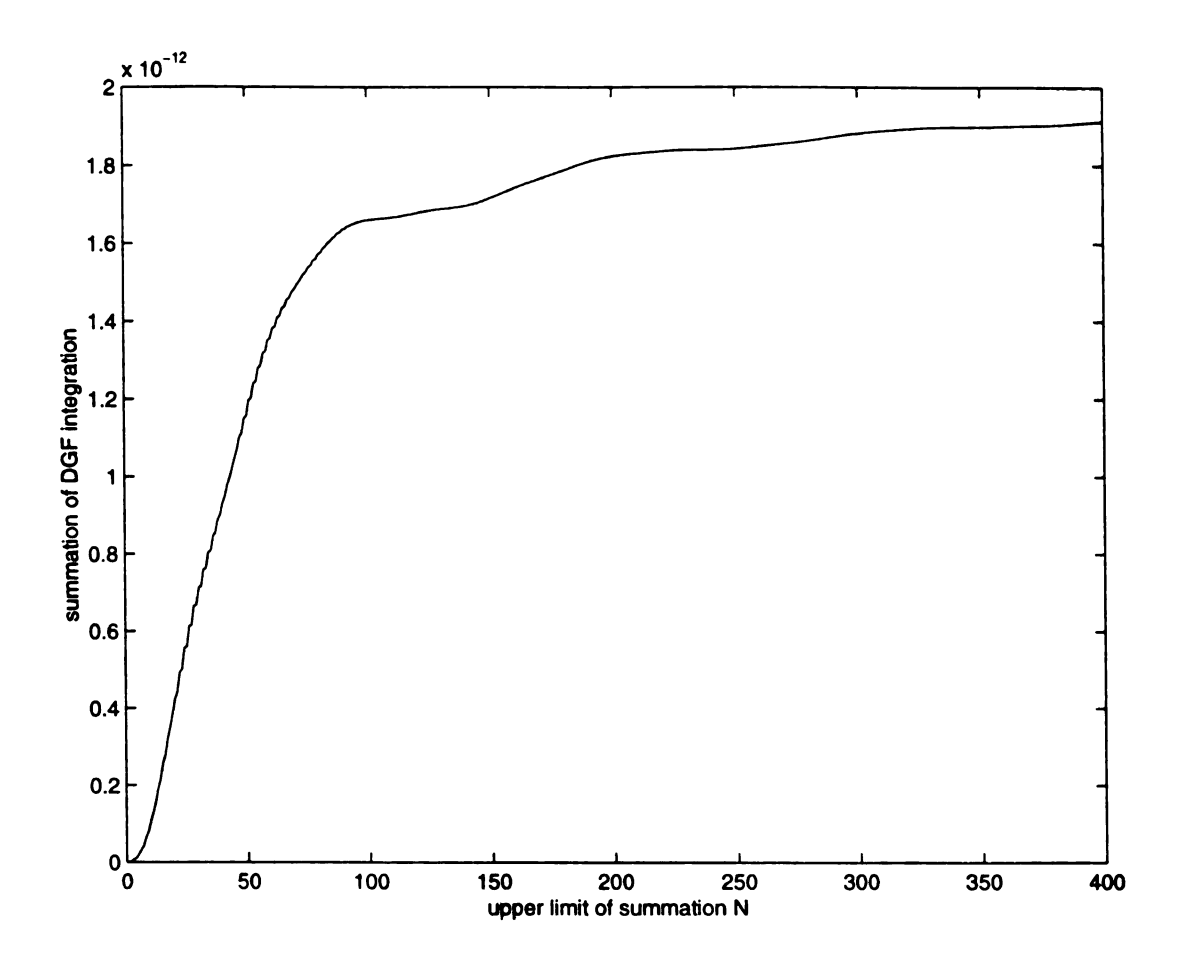


Figure 3.4 Integration of the double summation format  $G_{eoxx}(\overset{\bullet}{r}_0,\overset{\bullet}{r})$  vs. the number of summation modes when  $\overset{\bullet}{r}=\overset{\bullet}{r}_0$ ,  $\overset{\bullet}{r}=[0.033m,0.014m,0.0551m]$  and  $\Delta x=\Delta y=\Delta z=0.002m$ . The dimensions of the rectangular cavity are: a=0.072m, b=0.034m and c=0.1163m.

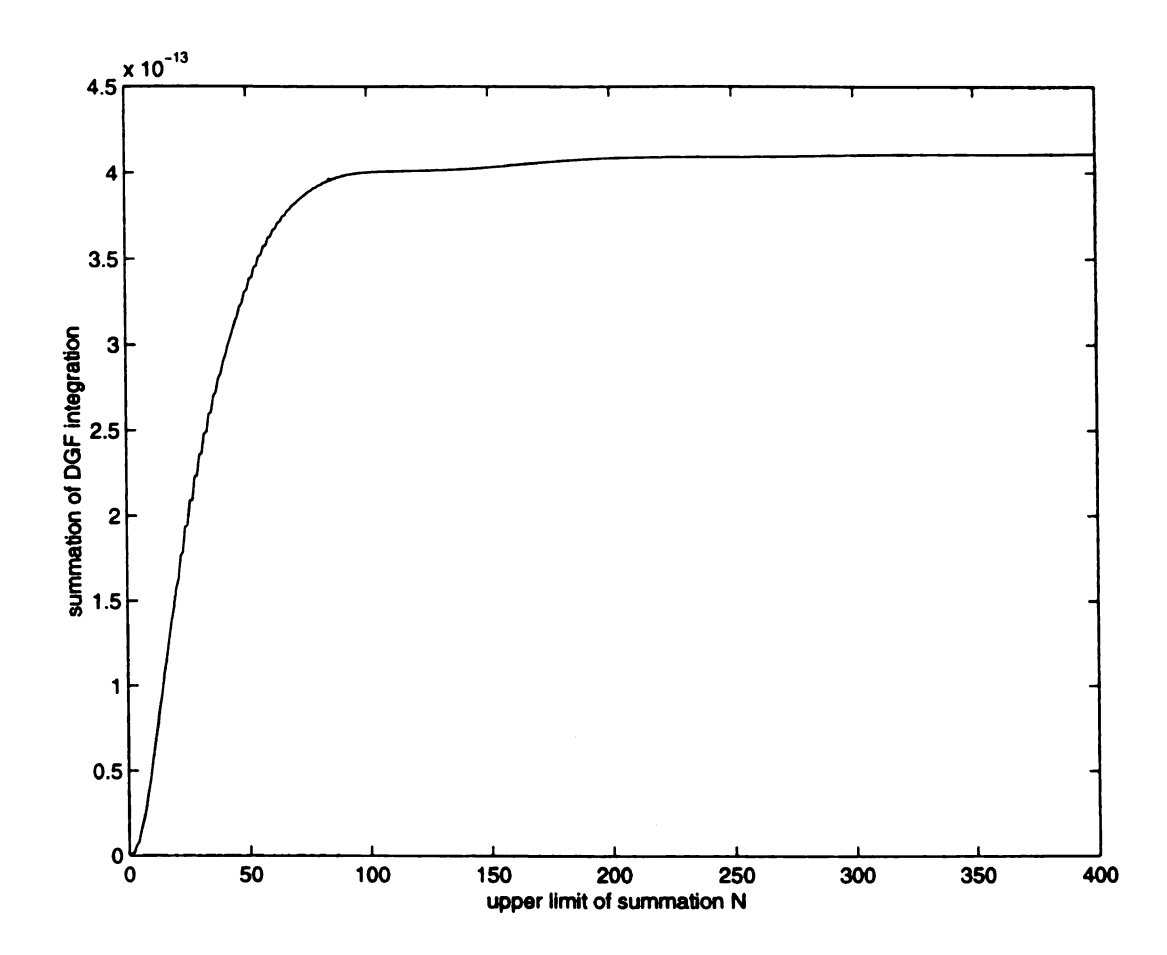


Figure 3.5 Integration of the double summation format  $G_{eoxx}(\mathring{r}_0, \mathring{r})$  vs. the number of summation modes when  $\mathring{r}=[0.035m, 0.014m, 0.0551m]$ ,  $\mathring{r}_0=[0.033m, 0.014m, 0.0551m]$  and  $\Delta x=\Delta y=\Delta z=0.002m$ . The dimensions of the rectangular cavity are: a=0.072m, b=0.034m and c=0.1163m.

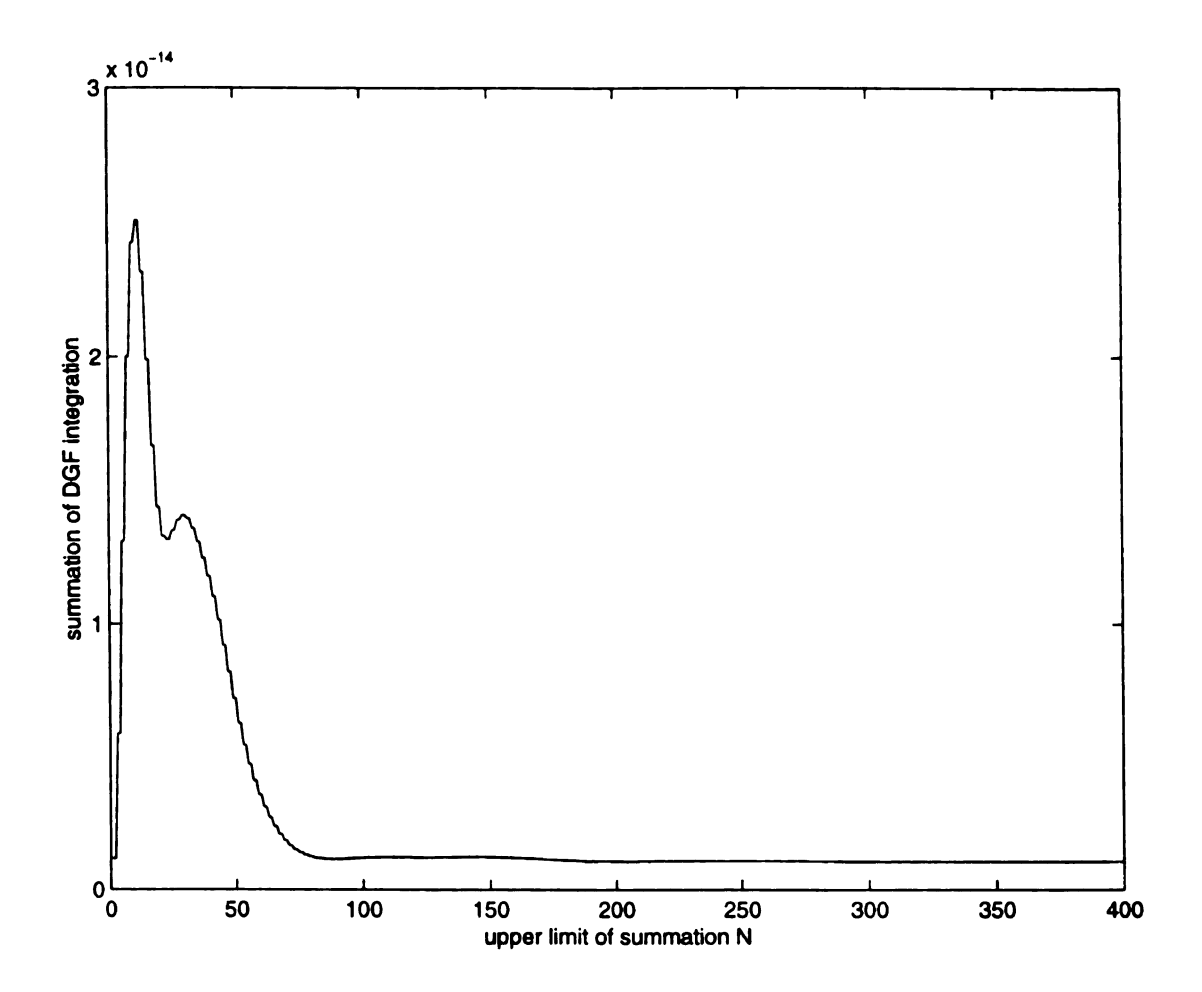


Figure 3.6 Integration of the double summation format  $G_{eoxx}(\mathring{r}_0, \mathring{r})$  vs. the number of summation modes when  $\mathring{r}=[0.035m, 0.016m, 0.0553m]$ ,  $\mathring{r}_0=[0.033m, 0.014m, 0.0551m]$  and  $\Delta x=\Delta y=\Delta z=0.002m$ . The dimensions of the rectangular cavity are: a=0.072m, b=0.034m and c=0.1163m.

horizontal axes are the value of N and the vertical axes are the integration of  $G_{eax}(r_0, r)$ .

Comparing Figure 3.1 with Figure 3.4, Figure 3.2 with Figure 3.5 and Figure 3.3 with Figure 3.6, which have the same selected parameters values, we observe that the convergence rate is the same for the cases of the double and triple summations. Also both cases converge to almost the same value at N = 200. Therefore, in the double summation, we can set the same upper limit as that in the triple summation. However, the double summation includes only 40,000 terms instead of 8 millions terms if the triple summation is used. This drastic simplification is achieved because we used a closed form evaluation to sum over one of the three indices.

# 3.3 Numerical Examples

In the following numerical computations, we suppose that a rectangular material sample is placed in the center of the rectangular cavity and the dimensions of the rectangular cavity are shown in Figure 3.7. The initial field is assumed to be  $TE_{101}$  mode and the resonant frequency of the empty cavity operating at this initial mode is 2.45 GHz with the wavelength  $\lambda$  equal to 0.12245m.

In order to quantify the induced electric field inside the material sample, we uniformly divide the material sample into  $M = n_d \times m_d \times l_d$  volume cells, where  $n_d$ ,  $m_d$  and  $l_d$  are the number of volume cells in the x, y and z directions, respectively. Several special cases with the selected shape and dimensions of the material sample, which can be compared with some theoretical approximations, have been studied.

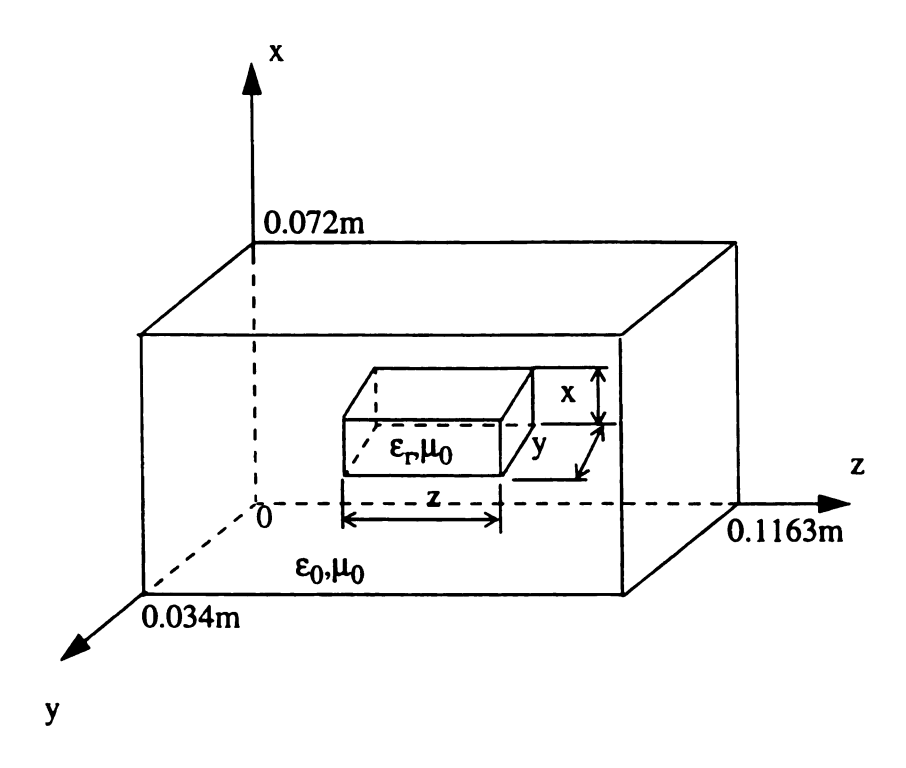


Figure 3.7 Dimensions of the rectangular cavity and the material sample. The center of the material sample is consistent with the center of the cavity.

#### 1. Cubic case

A cubic material sample, having equal three sides, is placed in the center of the rectangular cavity. The dimensions of the material sample are set to be x=0.004m, y=0.004m, z=0.004m and with the relative permittivity of  $\varepsilon_r=2.5$  and lossless. In the computation, we chose  $n_d=2$ ,  $m_d=2$  and  $l_d=2$ . The dimensions of each volume cell are:  $\Delta x=\frac{x}{n_d}$ ,  $\Delta y=\frac{y}{m_d}$  and  $\Delta z=\frac{z}{l_d}$ .  $(x_i,y_j,z_k)$ ,  $i=1,n_d$ ,  $j=1,m_d$  and  $k=1,l_d$ , will be used to denote the center of the volume cells in the material sample. Based on the convergence property discussed in Section 3.2 we chose the upper limit in the double summation of N=200.

Since  $x/\lambda=0.0327$ , which is electrically very small, we may use the static electric field induced inside of a dielectric sphere  $E=\frac{3}{2+\epsilon_r}E^i$  [14], [38] to estimate the induced electric field in this cubic material sample. We also assume the resonant frequency shift to be 5% after placing the material sample in the rectangular cavity. The numerical results are shown in Figure 3.8 in which the ratios of  $E_y/E_y^i$  at the different volume cells in the material sample are given.

The numerical results are  $E_y^i = 321.5729$  based on eq. (2.24), or the normalization of the cavity field as discussed in Chapter 2, and  $E_y = 203.9074$  obtained from the moment method.  $E_y$  and  $E_y^i$  are shown to be almost constant in each volume cell in the material sample. This is expected because the dimensions of the material

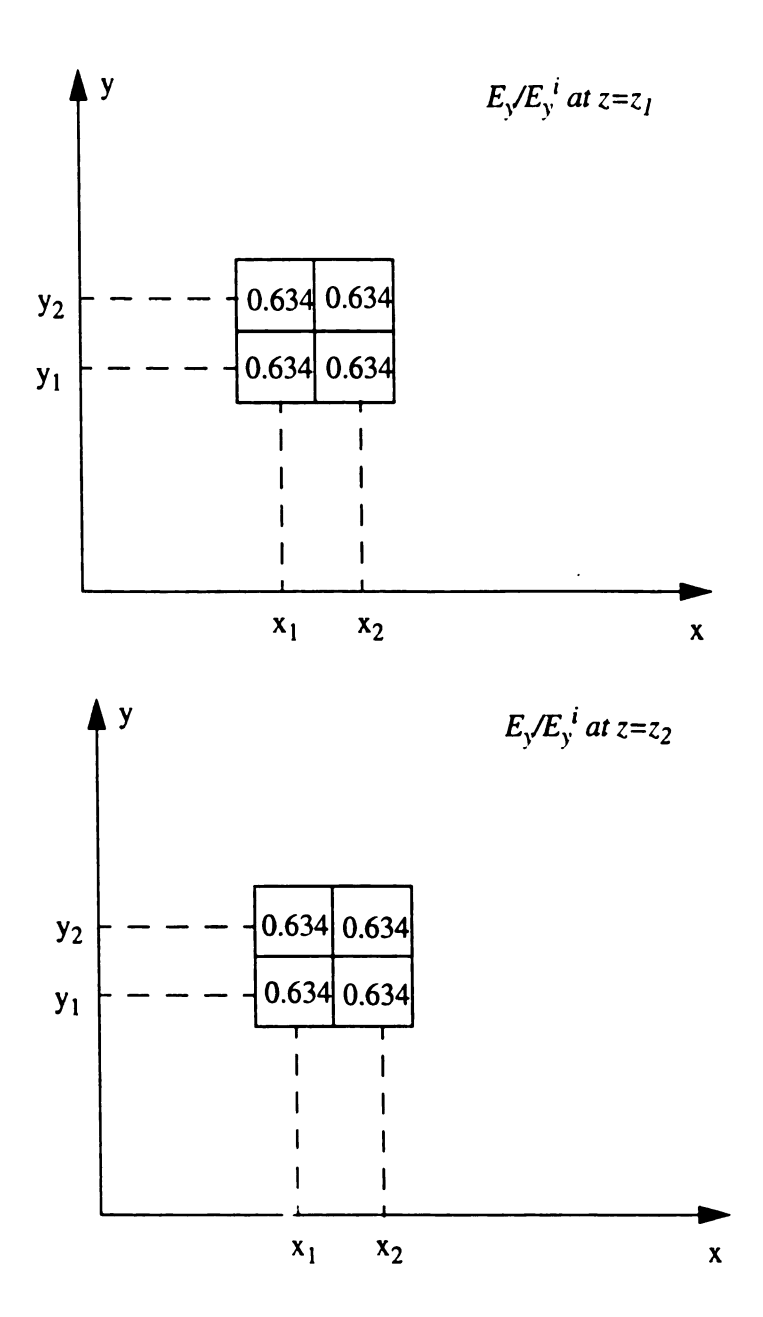


Figure 3.8 Ratios of  $E_y/E_y^i$  at different volume cells in the 4-mm cubic material sample, where the relative permittivity of the material sample is assumed to be  $\varepsilon_r = 2.5$ . The geometry of the rectangular cavity is shown in Figure 3.7. The resonant frequency shift is assumed to be 5%.

sample are very small compared with the dimensions of the rectangular cavity. The ratio of  $E_y/E_y^i$  is 0.634 in Figure 3.8. The electrostatic estimation of  $E_y/E_y^i = \frac{3}{2+\epsilon_r}$  gives the approximation of 0.667. The closeness of the numerical result and the electrostatic estimation gives confidence to the numerical accuracy.

Because the induced charge on the material sample surface and the induced current in the material sample can maintain a scattered field, the other components of the electric field are induced to satisfy the boundary conditions. The induced electric field inside the material sample has  $E_x$  and  $E_z$  components with the amplitudes of 5.494 and 5.552 in each volume cell, which are very small compared with the y component of the induced electric field. This shows that the initial mode still dominates inside the material sample although the other modes are also induced.

In order to assure that the upper limit is chosen properly, we change N, the upper limit in the double summation, from 160 to 1000 with the same resonant frequency shift of 5%. The results are shown in Table 3.1. As stated before, the induced electric field inside the 4-mm cubic material sample is almost constant. Since the y component of the induced electric field dominates, we only compare the results of the y component of the induced electric field for the different values of N at one volume cell, say  $(x_1, y_1, z_1)$ . From this table we observe that as we increase N, the ratio of  $E_y/E_y^i$  gets closer to 0.667. Considering the accuracy of the numerical results and the computation time, we choose N=200 as a compromise and this upper limit will be used in the following computations.

For different relative permittivities, the results of the 4-mm cubic material sample are shown in Table 3.2. We chose the resonant frequency shift to be 5% in the

89

Table 3.1 Induced electric field inside the 4-mm cubic material sample and its ratio to the initial electric field for different values of N, where the relative permittivity of the sample is assumed to be  $\varepsilon_r=2.5$ , the resonant frequency shift is 5% and the initial electric field is  $E_y^i=321.5729$ . The geometry of the rectangular cavity is shown in Figure 3.7.

N	$E_{y}$	$E_y / E_y^{\ i}$	Electrostatic approximation
160	202.0437	0.628	0.667
200	203.9074	0.634	0.667
300	206.9128	0.643	0.667
400	208.6385	0.649	0.667
500	209.6048	0.652	0.667
600	210.2009	0.654	0.667
700	210.6752	0.655	0.667
800	211.0442	0.656	0.667
1000	211.5217	0.658	0.667

Table 3.2 Induced electric field inside the 4-mm cubic material sample and its ratio to the initial electric field for different relative permittivities of the material sample, where the resonant frequency shift is 5% and the initial electric field is

 $E_y^i = 321.5729$ . The geometry of the rectangular cavity is shown in Figure 3.7.

ε,	$E_y$	$E_y/E_y^i = R_c$	Electrostatic approximation R <sub>a</sub>	Relative Difference (R <sub>a</sub> -R <sub>c</sub> )/R <sub>a</sub>
2.5	203.9074	0.634	0.667	4.95%
4.0	149.4301	0.4647	0.5	7.06%
7.0	97.4436	0.303	0.333	9.01%
10.0	72.3061	0.225	0.25	10.04%

computations. Also in Table 3.2, the induced electric field is shown only in one volume cell. We define the relative difference as  $\frac{R_a - R_c}{R_a}$ , where  $R_a$  is the ratio of the induced electric field to the initial electric field based on the electrostatic approximation of  $\frac{3}{2 + \epsilon_r}$  as shown in the fourth column of Table 3.2,  $R_c$  is the ratio of the calculated induced electric field to the initial electric field as shown in the third column of Table 3.2. From this table we observe that the computational difference tends to increase as the relative permittivity  $\epsilon_r$  is increased. This is expected because as the relative permittivity  $\epsilon_r$  is increased, the wavelength in the material sample decreases accordingly and the volume cell becomes electrically larger if the physical dimensions of the volume cell are kept constant.

The results shown in Table 3.3 are the calculated induced electric field inside the material sample with the change of the resonant frequency shift. From experiments the resonant frequency will shift down about 1% to 10% after a material sample is placed inside the rectangular cavity. The resonant frequency shift depends on the geometry and the dielectric parameters of the material sample. In the previous computations, we assumed the resonant frequency shift to be 5%. In this table we change the frequency shift from 1% to 10%. The relative permittivity of the 4-mm cubic material sample is  $\varepsilon_r = 2.5$  and lossless. In this table we only show the y component of the induced electric field in one volume cell. From this table we observe that the induced electric field inside the material sample does not change significantly when the resonant frequency shift is changed from 1% to 10%. Therefore, it is reasonable to assume the resonant frequency

Table 3.3 Induced electric field and the ratio vs. the resonant frequency shift. The relative permittivity of the 4-mm cubic material sample is assumed to be  $\varepsilon_r=2.5$  and the initial electric field is  $E_y^i=321.5729$ . The geometry of the rectangular cavity is shown in Figure 3.7.

Frequency Shift	E <sub>y</sub>	E <sub>y</sub> /E <sub>y</sub> <sup>i</sup>
1%	197.1854	0.613
2%	201.3336	0.626
3%	202.8700	0.631
4%	203.0814	0.632
5%	203.9074	0.634
6%	204.0814	0.635
7%	204.3603	0.636
8%	204.5175	0.636
9%	204.6399	0.636
10%	204.7275	0.637

shift to be 5% in the numerical calculation.

In order to check the stability of the numerical results, we change the dimensions of the material sample and compute the induced electric field in the material samples. First, we consider a 5-mm cubic material sample with the dimensions of x=0.005m, y=0.005m, z=0.005m and  $n_d=2$ ,  $m_d=2$  and  $l_d=2$ . The relative permittivity of the material sample is assumed to be  $\varepsilon_r=2.5$ , and the resonant frequency shift to be 5%. The computed results are  $E_y^i=321.3347$  and  $E_y=204.1318$ . They are almost constant in each volume cell. The ratio of  $E_y/E_y^i$  is 0.635 which is nearly identical to the case of 4-mm cubic material sample. The x and z components  $E_x$  and  $E_z$  are 5.557 and 5.573 which are very small compared with  $E_y$ . If we consider a 6-mm cubic material sample with the dimensions of x=0.006m, y=0.006m, z=0.006m and  $n_d=3$ ,  $m_d=3$  and  $l_d=3$ , the numerical results are shown in Figures 3.9.

Since the material sample is placed in the center of the rectangular cavity and the initial  $TE_{101}$  mode is symmetrical with respect to the center of the rectangular cavity, we expect that the induced electric field will also be symmetric with respect to the center of the rectangular cavity. Therefore, we only show the electric fields at  $z=z_1$  and  $z=z_2$  in Figures 3.9. The values of the initial electric field at each volume cell are 320.3034 at  $(x_1, y_1, z_1)$ , 321.5269 at  $(x_2, y_1, z_1)$ , 320.7714 at  $(x_1, y_1, z_2)$ , and 321.9967 at  $(x_2, y_1, z_2)$ .

Figure 3.9a shows the ratios of the y component of the induced electric field to that of the initial electric field at different volume cells inside the material sample. Although the initial electric field is not a function of y, the induced electric field inside the material

sample changes as y is varied. Also the induced electric field becomes less uniform compared with the case of the 4-mm cubic sample because of the increase in the sample dimensions. Figure 3.9b and Figure 3.9c show the x and z components of the induced electric field inside the material sample and they are very small compared with the y component of the induced electric field and can be ignored.

For a 2-cm cubic material sample with the dimensions of material sample as x=0.02m, y=0.02m, z=0.02m, if we set  $n_d = 10$ ,  $m_d = 10$  and  $l_d = 10$ , that is, the volume cell dimensions remain 0.002m at each side, then there will be 1,000 volume cells for such a material sample and the dimensions of the matrix (3.20) will be 3,000. Due to the limitation of our present computer resources, we were not able to solve this problem over half a month of computing time. We were then forced to divide the material sample with  $n_d = 6$ ,  $m_d = 6$  and  $l_d = 6$ . The relative permittivity of the material sample is chosen as  $\varepsilon_r = 2.5$  and it is lossless. Observing the numerical results, we find that the y component still dominates the x and z components of the induced electric field in the material sample. Due to the symmetry only a half of the ratios of the y component of the induced electric field to that of the initial electric field as a function of x for different locations of y and z are plotted in Figure 3.10. Observing Figure 3.10, the computed y component of the induced electric field does not change significantly with respect to x and z but changes somewhat more with respect to y. The ratios have been reduced from 0.634 for the 4-mm cubic sample to around 0.32-0.36 for the 2-cm cubic sample due to a larger dimensions of the material sample. There is a possibility that these reduced ratios may be due to the numerical errors since larger volume cells were used in the calculation.

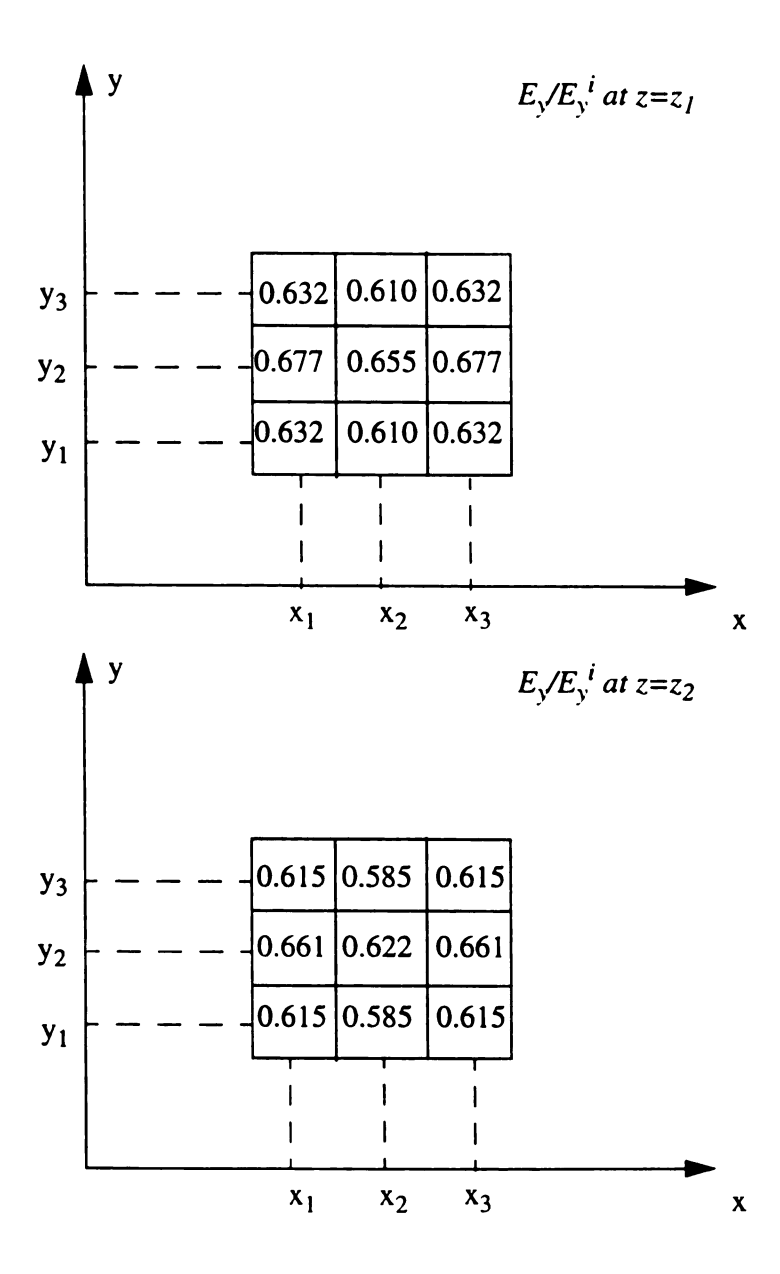


Figure 3.9a The ratios of  $E_y/E_y^i$  at different volume cells in the 6-mm cubic material sample, where the relative permittivity of the material sample is assumed to be  $\varepsilon_r = 2.5$ . The geometry of the rectangular cavity is shown in Figure 3.7. The resonant frequency shift is assumed to be 5%.

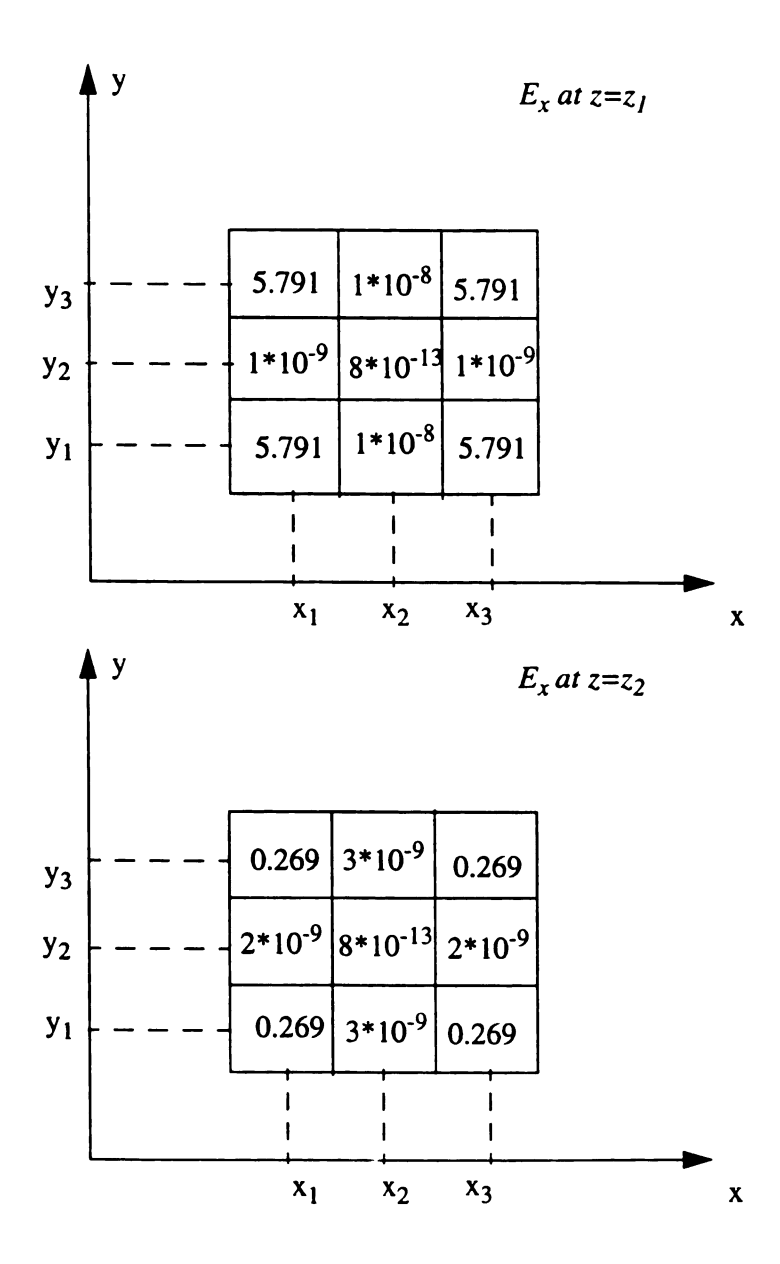


Figure 3.9b The x component of the induced electric field at different volume cells of the 6-mm cubic material sample, where the relative permittivity of the material sample is assumed to be  $\varepsilon_r=2.5$ . The geometry of the rectangular cavity is shown in Figure 3.7. The resonant frequency shift is assumed to be 5%.

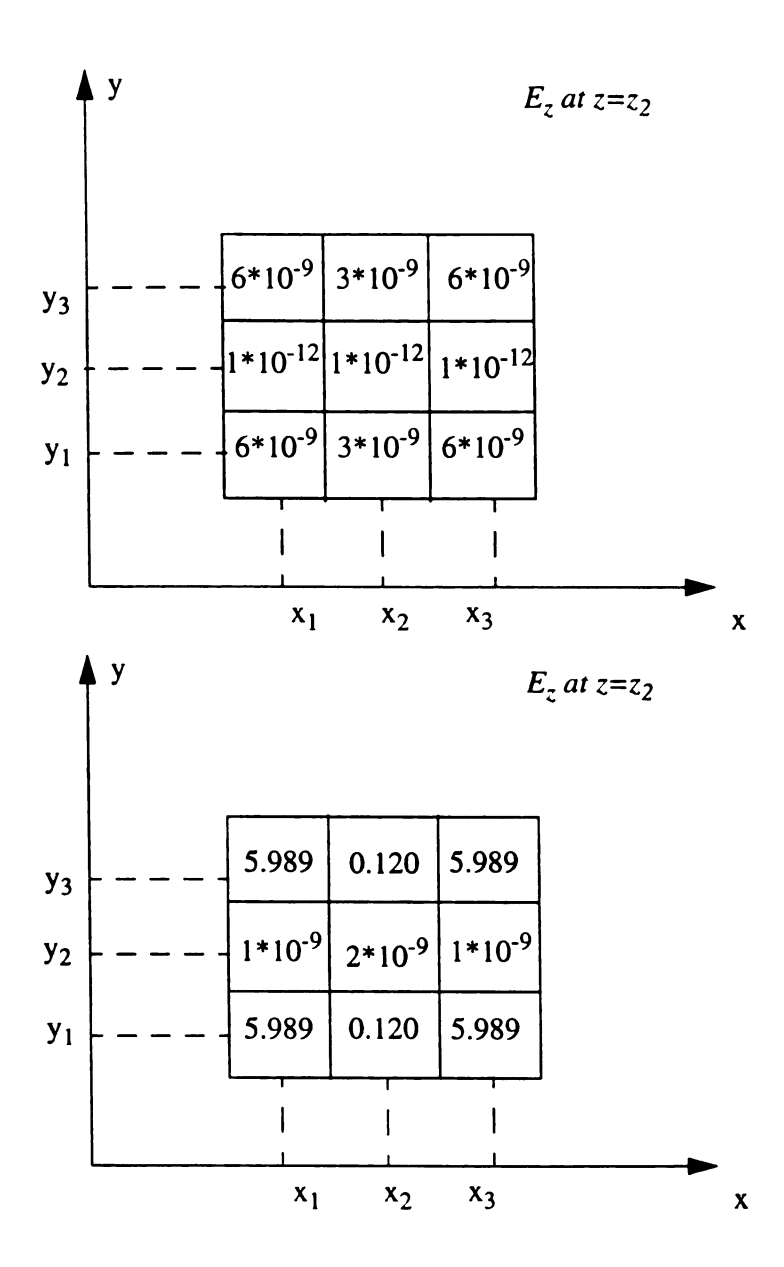


Figure 3.9c The z component of the induced electric field at different volume cells of the 6-mm cubic material sample, where the relative permittivity of the material sample is assumed to be  $\varepsilon_r=2.5$ . The geometry of the rectangular cavity is shown in Figure 3.7. The resonant frequency shift is assumed to be 5%.

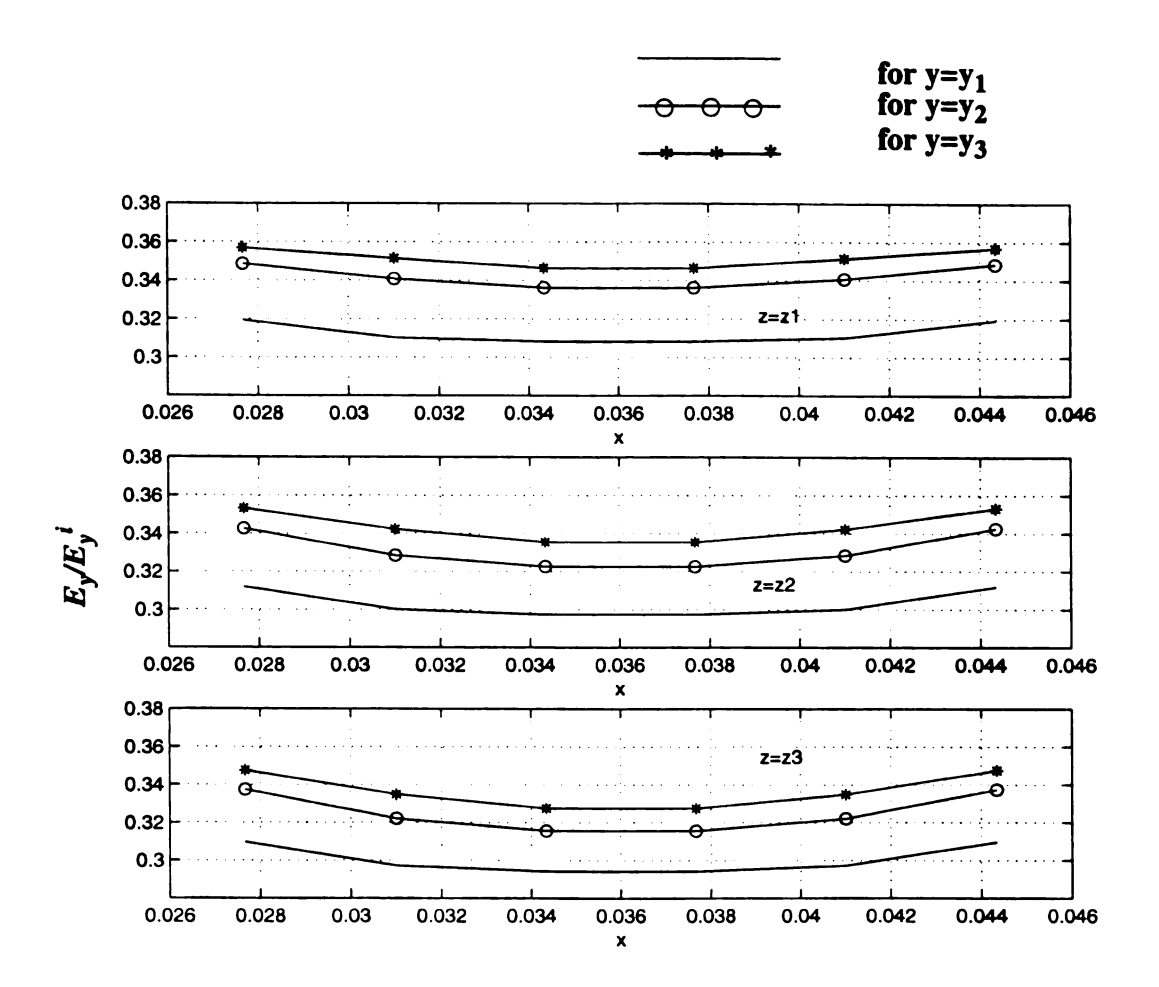


Figure 3.10 Ratios of  $E_y/E_y^i$  varies in the x-direction. Each curve represents this ratio as a function of x for different locations of y and z. The relative permittivity of the 2-cm cubic material sample is  $\varepsilon_r = 2.5$ . The geometry of the rectangular cavity is shown in Figure 3.7. The resonant frequency shift is assumed to be 8%.

#### 2. Thin square plate case

The material sample with a shape of a thin square plate, having its height much smaller than its width, is placed in the center of the cavity. The dimensions of the rectangular cavity are shown in Figure 3.7 and the dimensions of the material sample are: x=0.02m, y=0.002m, z=0.02m with  $n_d=10$ ,  $m_d=1$  and  $l_d=10$ . The relative permittivity of the material sample is assumed to be  $\varepsilon_r=2.5$ . Since the initial mode  $TE_{101}$  contains only the y component of the electric field and the material sample has a thin flat geometry, the induced electric field inside the material sample can be estimated by the boundary condition of  $E=(1/\varepsilon_r)E^i$ .

The numerical results are shown in Figure 3.11, where only the induced electric fields in a half of the plate,  $z=z_1$  to  $z=z_5$  are shown due to the symmetry. In Figure 3.11, ratios of the y component of the induced electric field in the material sample to that of the initial electric field are plotted as a function of x. Each curve in Figure 3.11 represents this ratio as a function of x for different locations of z. The highest one is for  $z=z_1$  and the lowest one for  $z=z_5$ . We observe that the electric field is higher at the edges of plate, an expected edge effect. The induced electric field inside the material sample is almost constant. Theoretical estimation of this ratio based on the boundary condition of  $1/\varepsilon_r$  gives  $\frac{1}{2.5} = 0.4$ . Our numerical results varies between 0.315 to 0.39 which are in agreement with this theoretical estimation.

The x and z components of the induced electric field in the material sample are extremely small  $(1.0*10^{-8})$  in all volume cells. This is expected because the sample is very

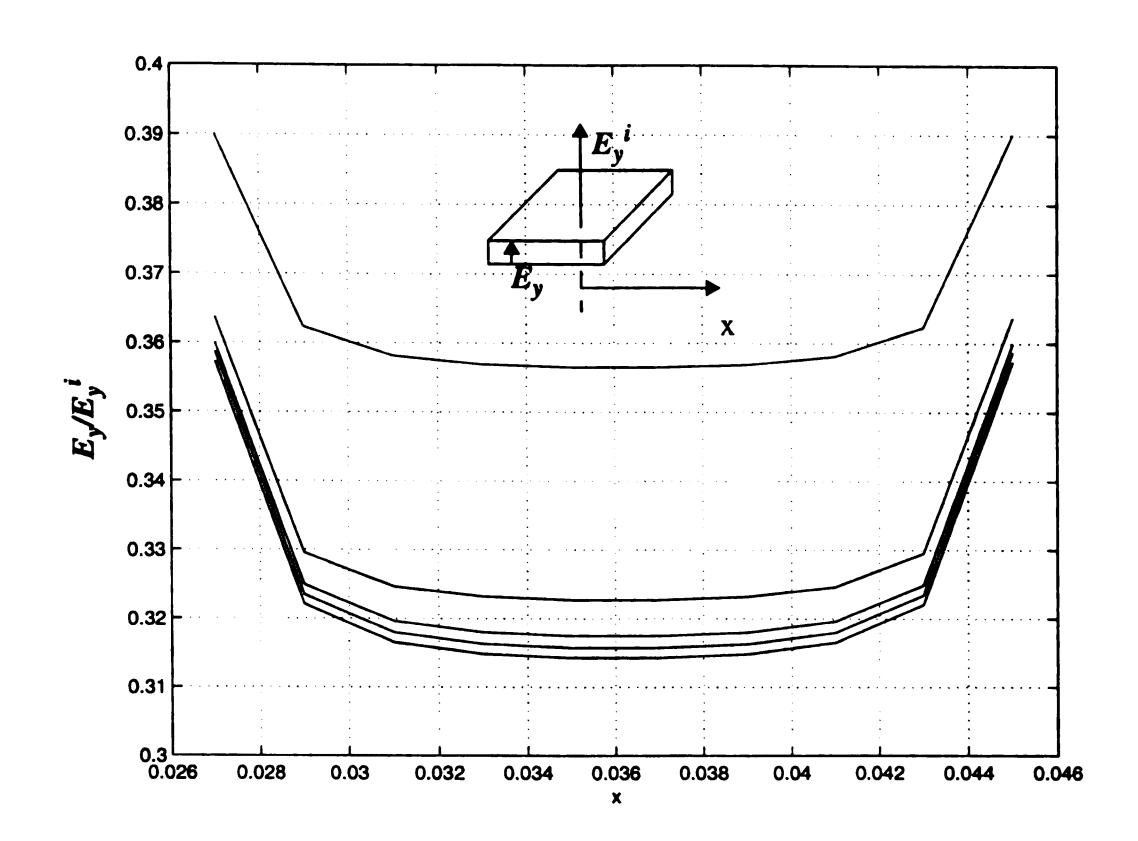


Figure 3.11 Ratios of  $E_y/E_y^i$  varies in the x-direction. Each curve represents this ratio as a function of x for different locations of z. The highest one is for  $z=z_1$  and the lowest one for  $z=z_5$ . The relative permittivity of the thin square plate material sample is  $\varepsilon_r=2.5$  and the geometry of the cavity is shown in Figure 3.7. The resonant frequency shift is assumed to be 1%.

thin in the y direction that no significant x and z components of the electric field can be induced. Therefore, the y component of the induced electric field in the material sample dominates.

#### 3. Narrow strip case.

We consider next a material sample with a geometry of a narrow strip case. The dimensions of the material sample are: x=0.002m, y=0.02m, z=0.002m with  $n_d=1$ ,  $m_d=10$  and  $l_d=1$ . The relative permittivity of the material sample is assumed to be  $\varepsilon_r=2.5$ . Theoretical estimation of the induced electric field in the material sample may be close to the initial electric field because the initial electric field is tangential to the major part of the material sample surface, and the continuity of the tangential component of the electric field at the material sample surface requires this estimation. Based on this estimation, we expect that more terms will be needed in the computation of the induced electric field because we have evaluated a delta function out the integration sign when we derived EFIE (2.102). If we need the induced electric field to be equal to the initial electric field, then there needs to be another delta function coming out of the integration sign to cancel the previous delta function. Thus, the convergence rate may be slower in this case.

In this computation we assume the resonant frequency shift to be 1%. The numerical results are shown in Figure 3.12. In this figure, the maximum value of the ratio of the induced electric field to the initial electric field is 0.82. If we change the upper limit in the double summation, the numerical results are shown in Figure 3.13. In Figure 3.13 we observe that the ratio becomes closer to I as we increase the upper limit of the double summation; when N=1000, the maximum ratio becomes 0.896; and when N=1500, the maximum ratio becomes 0.903. Increasing N leads to an increase in the computing time.

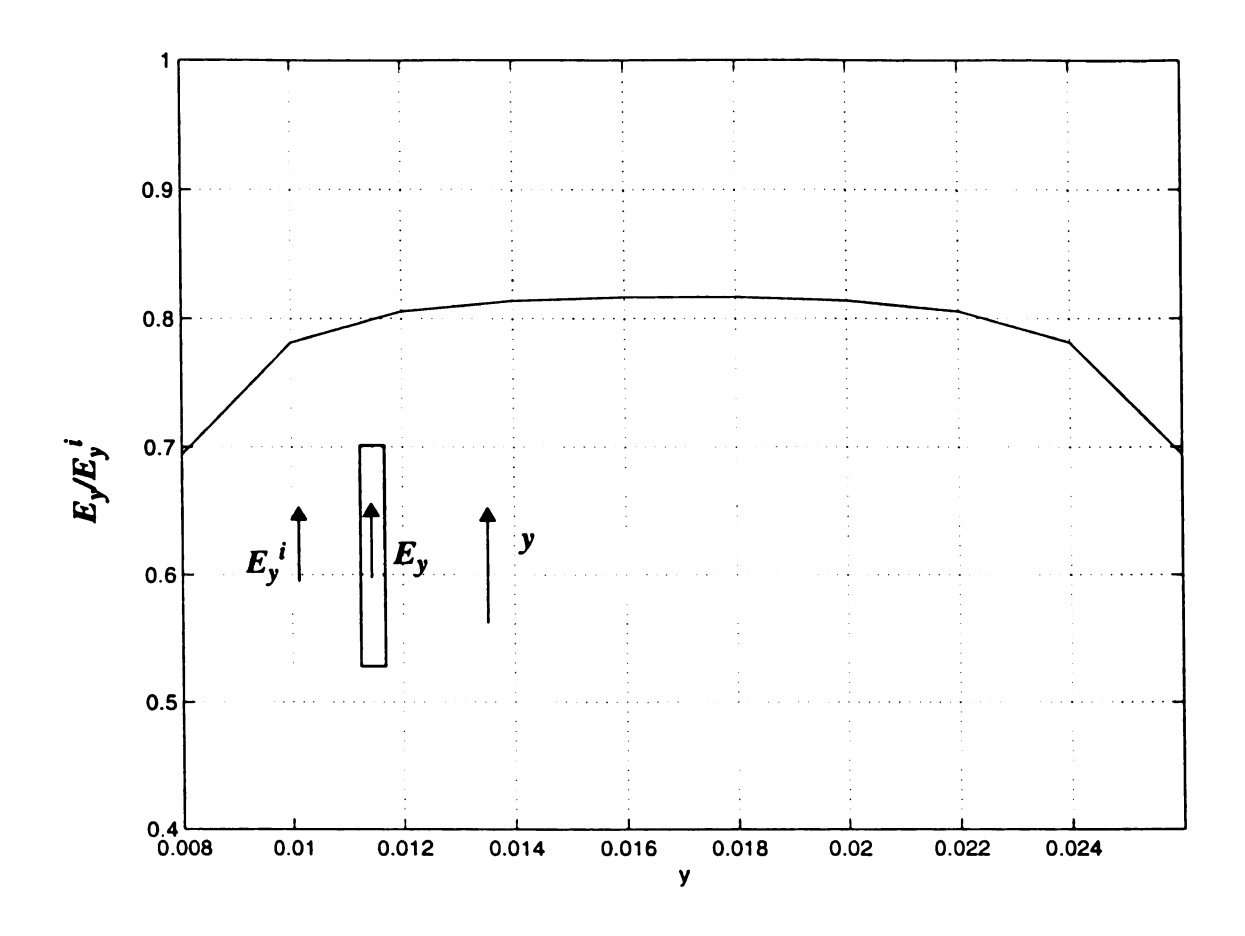


Figure 3.12 Ratios of  $E_y/E_y^i$  varies as a function of y. The dimensions of the material sample are: x=0.002m, y=0.02m, z=0.002m and the geometry of the cavity is shown in Figure 3.7. The resonant frequency shift is assumed to be 1%. The upper limit in the double summation is chosen to be N=200.

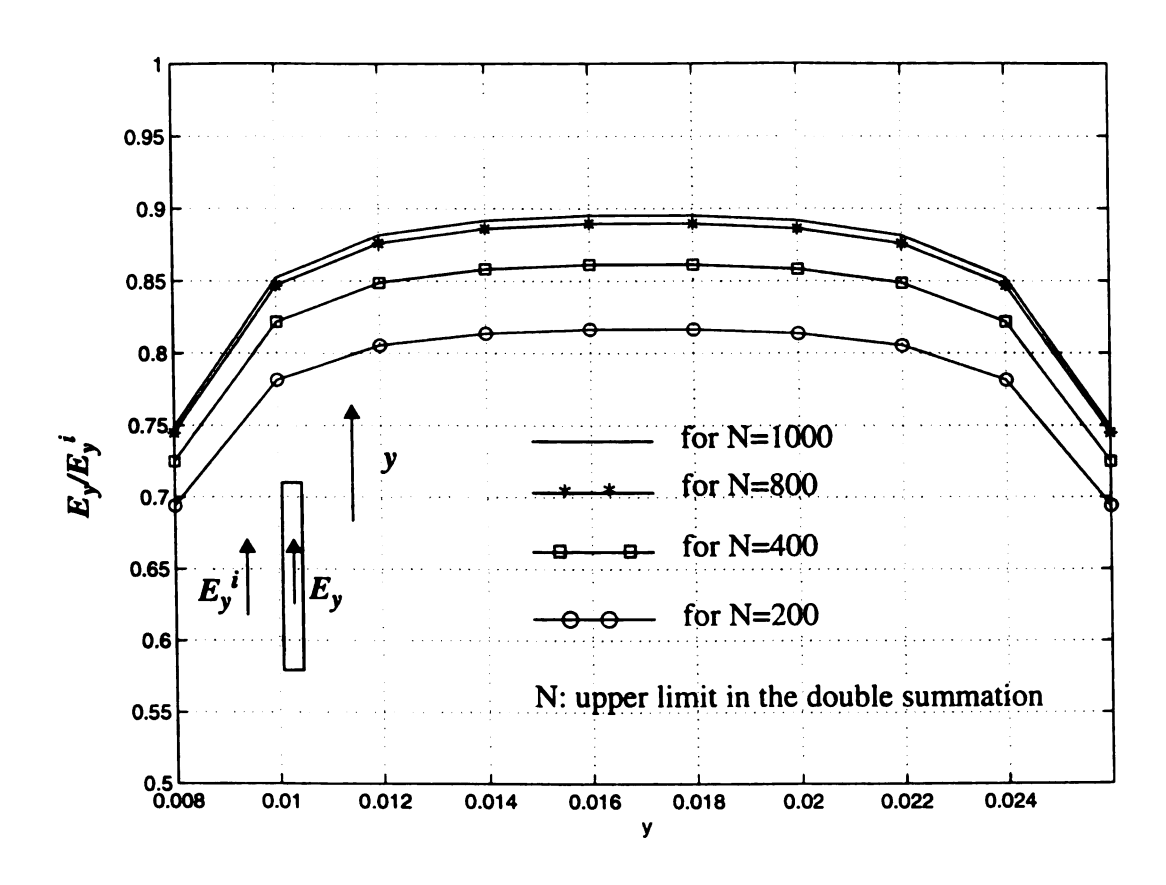


Figure 3.13 Ratios of  $E_y/E_y^i$  varies as a function of y for different N. The dimensions of the material sample are: x=0.002m, y=0.02m, z=0.002m and the geometry of the cavity is shown in Figure 3.7. The resonant frequency shift is assumed to be 1%.

For such cases, we suggest the scheme of separating the material sample into interior volume and boundary layer cells as will be discussed later.

### 3.4 Some Methods to Increase the Convergence Rate

#### 1. Separation of the material sample into the boundary layer and interior regions

In Section 2.1.6 we showed that the vector wave functions  $\vec{M}_{nml}$  and  $\vec{N}_{nml}$  are complete within the space of the solenoidal vector fields. We also explained that the divergence of the electric field doesn't vanish at all points in the cavity after placing a material sample inside. In fact, the divergence of the electric field doesn't vanish only at the boundary of a homogeneous material sample of finite size where the induced electric charges reside. The divergence of the electric field still vanishes in the interior of a homogeneous material sample.

Based on this observation, in the determination of the induced electric field in the material sample, we may divide the material sample into two groups of volume cells: boundary layer and interior volume cells. For the boundary layer volume cells we use the vector wave functions  $\vec{L}_{nml}$ ,  $\vec{M}_{nml}$  and  $\vec{N}_{nml}$  as the complete set of basis functions to expand the unknown induced electric field. For the interior volume cells only the vector wave functions  $\vec{M}_{nml}$  and  $\vec{N}_{nml}$  are used to expand the solenoidal electric field. Thus, the Electric Field Integral Equation (*EFIE*) will be quite different for these two groups of volume cells. The *EFIE* at the boundary layer is the same as that used before, eq. (2.102). The *EFIE* for the interior volume cells is obtained as follows.

In Chapter 2, the scattered electric field is shown to satisfy the Helmholtz eq.

(2.90). As we use only the vector wave functions  $\vec{M}_{nml}$  and  $\vec{N}_{nml}$  to expand this scattered electric field in the interior region of the material sample, the scattered field can be expressed as

$$\vec{E}^{s}(\vec{r}) = \sum_{n=1}^{\infty} \left[ a_n \vec{M}_n(\vec{r}) + b_n \vec{N}_n(\vec{r}) \right]$$
 (3.53)

Substituting eq. (3.53) into eq. (2.90) we have

$$\nabla \times \nabla \times \sum_{n} \left[ a_{n} \overrightarrow{M}_{n}(\overrightarrow{r}) + b_{n} \overrightarrow{N}_{n}(\overrightarrow{r}) \right] - k_{0}^{2} \sum_{n} \left[ a_{n} \overrightarrow{M}_{n}(\overrightarrow{r}) + b_{n} \overrightarrow{N}_{n}(\overrightarrow{r}) \right] = -j \omega \mu_{0} \overrightarrow{J}_{eq}(\overrightarrow{r}) \quad (3.54)$$

Based on the properties of the vector wave functions  $\overrightarrow{M}_{nml}$  and  $\overrightarrow{N}_{nml}$ , eq. (3.54) can be written as

$$\sum_{n} \left[ a_{n} (k_{n}^{2} - k_{0}^{2}) \overrightarrow{M}_{n}(\mathring{r}) + b_{n} (k_{n}^{2} - k_{0}^{2}) \overrightarrow{N}_{n}(\mathring{r}) \right] = -j \omega \mu_{0} \overrightarrow{J}_{eq}(\mathring{r})$$
 (3.55)

Taking the scalar product of eq. (3.55) with  $\vec{M}_{nml}$  and  $\vec{N}_{nml}$ , respectively and integrating over the cavity volume V, then applying the orthonormal property of the vector wave functions  $\vec{M}_{nml}$  and  $\vec{N}_{nml}$ , we obtain the expressions for the expansion coefficients as

$$a_{n} = -\frac{j\omega\mu_{0}}{k_{n}^{2} - k_{0}^{2}V_{sample}} \int_{eq}^{2} \vec{J}_{eq}(\vec{r}_{0}) \cdot \vec{M}_{n}(\vec{r}_{0}) dv_{0}$$
 (3.56)

$$b_{n} = -\frac{j\omega\mu_{0}}{k_{n}^{2} - k_{0}^{2}V_{\text{torrole}}} \int_{eq} \dot{\vec{r}}_{0} \cdot \vec{N}_{n}(\dot{\vec{r}}_{0}) dv_{0}$$
(3.57)

where the integration region is over the sample volume. Therefore, the expression for the scattered field  $\vec{E}^s(\vec{r})$  becomes

$$\vec{E}^{s}(\hat{r}) = -j\omega\mu_{0} \int_{V_{sample}} \vec{J}_{eq}(\hat{r}_{0}) \cdot \sum_{n} \left[ \frac{\vec{M}_{n}(\hat{r}_{0})\vec{M}_{n}(\hat{r}) + \vec{N}_{n}(\hat{r}_{0})\vec{N}_{n}(\hat{r})}{k_{n}^{2} - k_{0}^{2}} \right] dv_{0}$$

$$= -j\omega\mu_{0} \int_{V_{sample}} \vec{J}_{eq}(\hat{r}_{0}) \cdot \vec{G}_{es}(\hat{r}_{0}, \hat{r}) dv_{0}$$
(3.58)

where the dyadic Green's function in the interior region is identified as

$$\overline{G}_{es}(\mathring{r}_0, \mathring{r}) = \sum_{n} \left[ \frac{\overrightarrow{M}_n(\mathring{r}_0) \overrightarrow{M}_n(\mathring{r}) + \overrightarrow{N}_n(\mathring{r}_0) \overrightarrow{N}_n(\mathring{r})}{k_n^2 - k_0^2} \right]$$
(3.59)

Finally, the Electric Field Integral Equation (*EFIE*) for the induced electric field in the interior region can be derived as

$$\vec{E}(\vec{r}) + j\omega\mu_0 \int_{v} \tau_e(\vec{r}_0) \vec{E}(\vec{r}_0) \cdot \vec{G}_{es}(\vec{r}_0, \vec{r}) dv_0 = \vec{E}^i(\vec{r})$$
(3.60)

Comparing with  $\overline{G}_{eo}(\hat{r}_0, \hat{r})$  in the *EFIE* (2.102) for the boundary layer region,  $\overline{G}_{es}(\hat{r}_0, \hat{r})$  can converge faster. Some numerical results are given to show this point.

In the following computations, we only show the convergence property of the integration of  $G_{esxx}(\mathring{r}_0,\mathring{r})$  component with respect to  $\mathring{r}$  and  $\mathring{r}_0$  in regions  $V_n$  and  $V_{n0}$ .

In Chapter 2, eqs. (2.24) and (2.32) give the expressions of the vector wave functions  $\vec{M}_{nml}$  and  $\vec{N}_{nml}$ , from which the coefficient of  $G_{esxx}(\hat{r}_0, \hat{r})$  can be obtained as

$$\frac{\varepsilon_{0n}\varepsilon_{0m}\varepsilon_{0l}}{abc} \frac{\left(\frac{m\pi}{b}\right)^2 + \left(\frac{l\pi}{c}\right)^2}{k_n^2(k_n^2 - k_0^2)}$$
(3.61)

Thus,  $G_{esxx}(\mathring{r}_0,\mathring{r})$  can be expressed in a double summation format as

$$G_{esxx}(\hat{r}_{0}, \hat{r}) = -\sum_{m=1}^{\infty} \sum_{l=1}^{\infty} \frac{4}{bc} \frac{\left(\frac{m\pi}{b}\right)^{2} + \left(\frac{l\pi}{c}\right)^{2}}{k_{0}^{2}} \left[ \frac{g_{ml1}(x, x_{0})}{k_{gml1} \sin(k_{gml1}a)} - \frac{g_{ml2}(x, x_{0})}{k_{gml2} \sin(k_{gml2}a)} \right]_{(3.62)}$$

$$\sin\left(\frac{m\pi}{b}y\right) \sin\left(\frac{m\pi}{b}y_{0}\right) \sin\left(\frac{l\pi}{c}z\right) \sin\left(\frac{l\pi}{c}z_{0}\right)$$

where  $k_{gml1}$  is given by eq. (3.30) and

$$k_{gml2} = \sqrt{-\left(\left(\frac{m\pi}{b}\right)^2 + \left(\frac{l\pi}{c}\right)^2\right)}$$
 (3.63)

$$g_{mlp}(x, x_0) = \cos(k_{gmlp}(a - x_b))\cos(k_{gmlp}x_s)$$
 (3.64)

p=1,2 in eq. (3.64). From eqs. (3.63) and (3.30), we find that  $k_{gml2}$  is always imaginary and  $k_{gml1}$  will be approximately close to  $k_{gml2}$  as m and l increase and this is the reason why  $G_{esxx}(\mathring{r}_0,\mathring{r})$  has a better convergence property.

The integration of  $G_{esxx}(r_0, r)$  with respect to r and  $r_0$  in regions  $V_n$  and  $V_{n0}$  is

$$\int_{x}^{x+\Delta xy + \Delta yz + \Delta z} \int_{y_{0}}^{x+\Delta y} \int_{z_{0}}^{x+\Delta y} \int_{y_{0}}^{x+\Delta y} \int_{z_{0}}^{x+\Delta y} \int_{y_{0}}^{x+\Delta y} \int_{z_{0}}^{x+\Delta y} \int_{y_{0}}^{x+\Delta y} \int_{z_{0}}^{x+\Delta y} \int_{z_{0}}^{x+\Delta y} \int_{z_{0}}^{x+\Delta y} \int_{z_{0}}^{x+\Delta y} \left[ \int_{z_{0}}^{x+\Delta y} \int_{z_{0}}^{x+\Delta y} \left[ \int_{z_{0}^{x+\Delta y} \left[ \int_{z_{0}}^{x+\Delta y} \left[ \int_{z_{0}}^{x$$

The details of the integration of

$$\int_{x}^{x+\Delta x} \int_{x_0}^{x_0+\Delta x} \left[ \frac{g_{ml1}(u, u_0)}{k_{gml1} \sin(k_{gml1}a)} - \frac{g_{ml2}(u, u_0)}{k_{gml2} \sin(k_{gml2}a)} \right] du du_0$$
 (3.66)

for different cases can be carried out in a similar way as that in Section 3.2.

In the following computations, the dimensions of the rectangular cavity are assumed to be the same as that shown in Figure 3.7. We also assume the initial mode to be  $TE_{101}$ . We choose  $\Delta x = \Delta y = \Delta z = 0.002m$  in the following computations. The integrations of  $G_{esxx}(\mathring{r}_0, \mathring{r})$  are calculated at different positions of  $\mathring{r}$  and  $\mathring{r}_0$  (we will use the same source and observation points as those in Section 3.2 in order to compare the results of both integrations) with the assumption of the resonant frequency shift to be 5%.

Figure 3.14 is for  $r = r_0$  while Figure 3.15 and Figure 3.16 for  $r \neq r_0$ , where the horizontal axes are the value of N and the vertical axes are the integration of  $G_{esxx}(r_0, r)$  in these three figures. In Figure 3.14 to Figure 3.16, we find that the integrations converge much faster than those in Figure 3.4 to Figure 3.6 or Figure 3.1 to Figure 3.3. These integrations converge when  $N \geq 80$  for the different positions. This is because as m and l increase,  $k_{gmll}$  becomes approximately equal to  $k_{gml2}$ . Then the difference in the eq. (3.65) becomes nearly equal to zero. Thus, the summation terms are greatly reduced leading to the reduced computation time.

The scheme of the separation of the material sample into boundary layer and interior region has been successfully applied to the narrow strip case in Section 3.3. In this case we choose the dimensions of the sample as x=0.003m, y=0.021m, z=0.003m with  $n_d=1$ ,  $m_d=10$  and  $l_d=1$  as the division for the interior region. The dimensions of

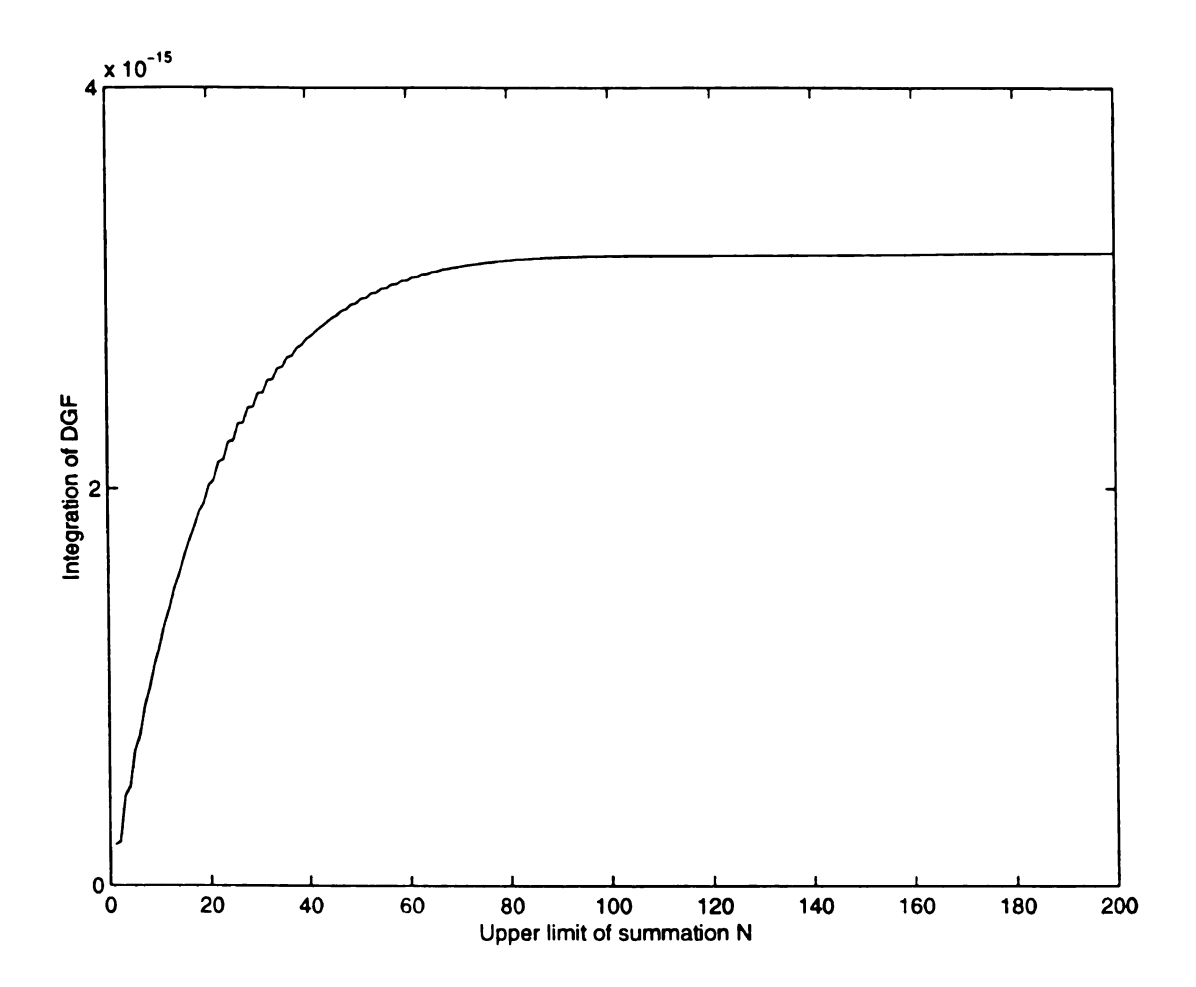


Figure 3.14 Integration of  $G_{esxx}(\mathring{r}_0,\mathring{r})$  vs. number of summation modes when  $\mathring{r} = \mathring{r}_0$ ,  $\mathring{r} = [0.033m, 0.014m, 0.0551m]$  and  $\Delta x = \Delta y = \Delta z = 0.002m$ .

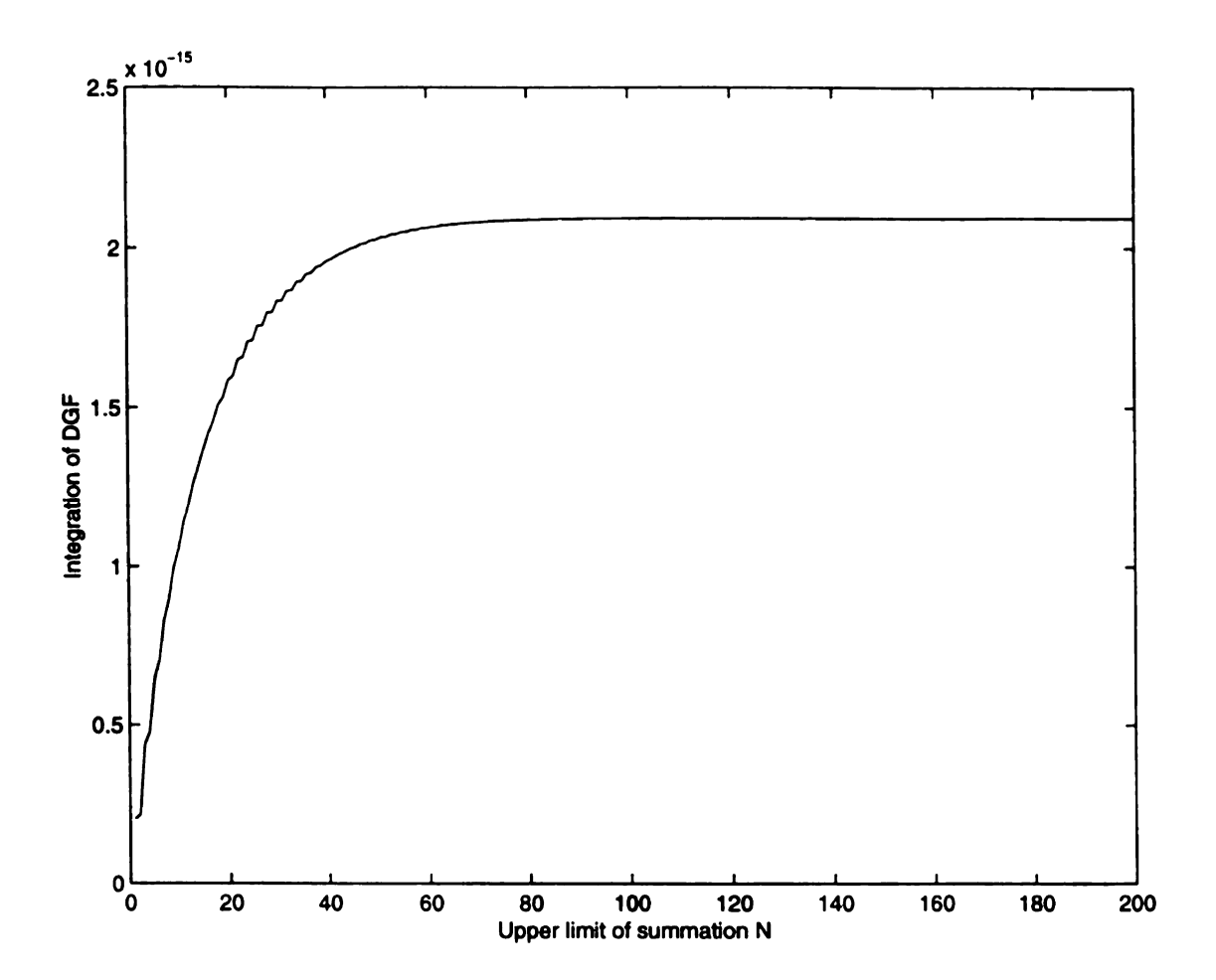


Figure 3.15 Integration of  $G_{esxx}(\overset{\bullet}{r}_0,\overset{\bullet}{r})$  vs. number of summation modes when  $\overset{\bullet}{r}=[0.035m,0.014m,0.0551m], \overset{\bullet}{r}_0=[0.033m,0.014m,0.0551m]$  and  $\Delta x=\Delta y=\Delta z=0.002m$ .

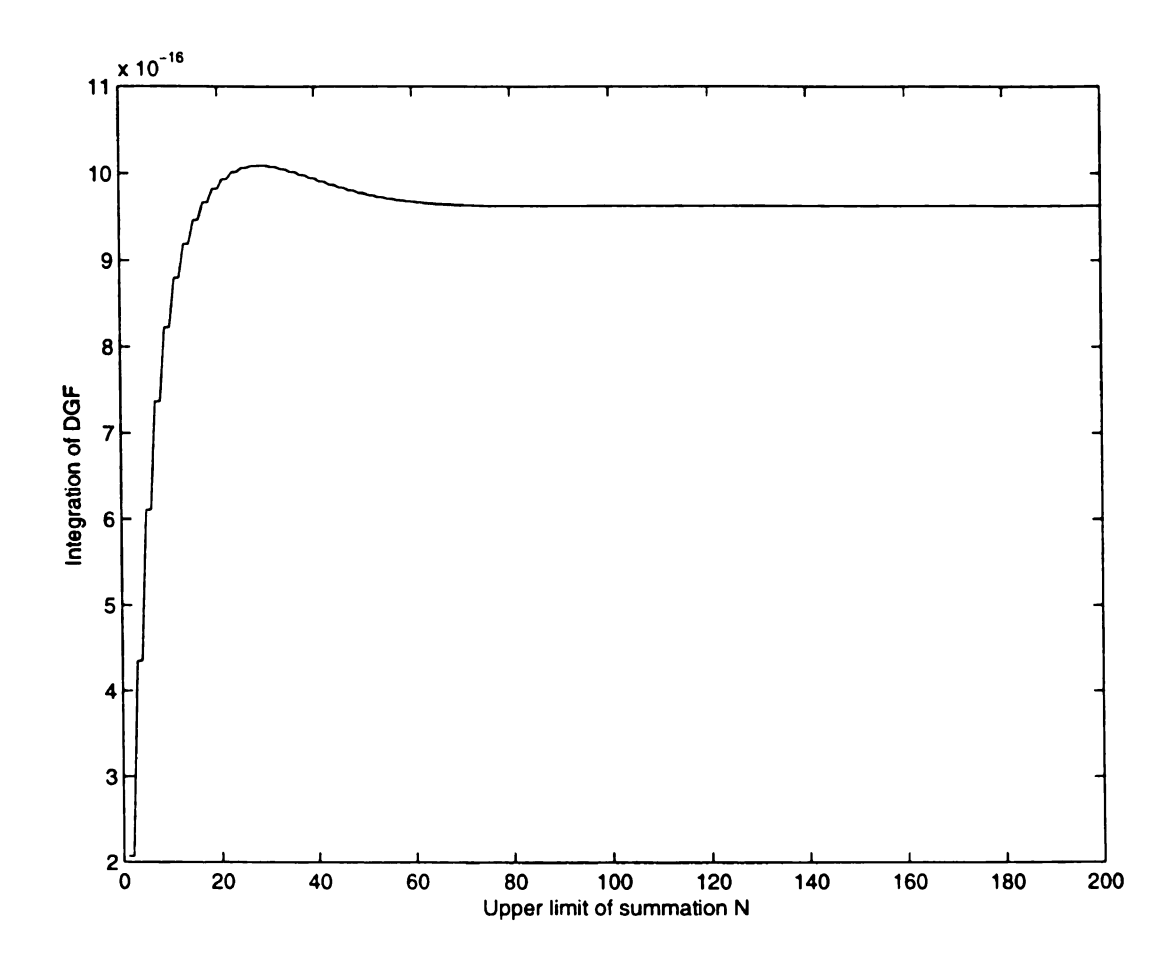


Figure 3.16 Integration of  $G_{esxx}(\hat{r}_0, \hat{r})$  vs. number of summation modes when  $\hat{r} = [0.035m, 0.016m, 0.0553m], \hat{r}_0 = [0.033m, 0.014m, 0.0551m]$  and  $\Delta x = \Delta y = \Delta z = 0.002m$ .

the volume cells in the boundary layer region are chosen as bx=0.0008m, by=0.0008m, bz=0.0008m. The dimensions of the interior region are  $x_i=0.0014m$ ,  $y_i=0.0194m$ ,  $z_i=0.0014m$  and the dimensions of each volume cell in the interior region are ix=0.0014m, iy=0.00194m, iz=0.0014m. The number of total volume cells in the boundary layer region and interior region is  $(n_d+2)\times(m_d+2)\times(l_d+2)=108$ . In the computation, we suppose the resonant frequency shift to be 1% and choose the upper limits of the double summation to be  $N_i=150$  for the interior region and  $N_b=400$  for the boundary layer region. The numerical results are shown in Figure 3.17.

Since we are only interested in the induced electric field inside the material sample, only the solutions for the volume cells in the interior region are presented in Figure 3.17 while those for the boundary layer region are omitted. It is noted that the solutions for the volume cells in the boundary layer region are usually not reasonable and should be discarded. This is justified because the boundary layer region is artificially created to contain the induced surface charge for a mathematical reason. In Figure 3.17 we only show the ratio of the y component of the induce electric field in the interior region to that of the initial mode varies in the y direction. We see that the ratio is 1.04 which is very close to 1 that is required by the continuity of the tangential electric field at the same surface. The x and z components are around  $1.0 \times 10^{-10}$  which can be neglected. In this computation we can also show that it reduces the computation time.

In Section 3.3 the numerical result is 0.903 when N = 1500 for the narrow strip case. We mentioned that the construction of the matrix (3.20) in the moment method cost root of the computation time. From the definition of this matrix, it consists of the series

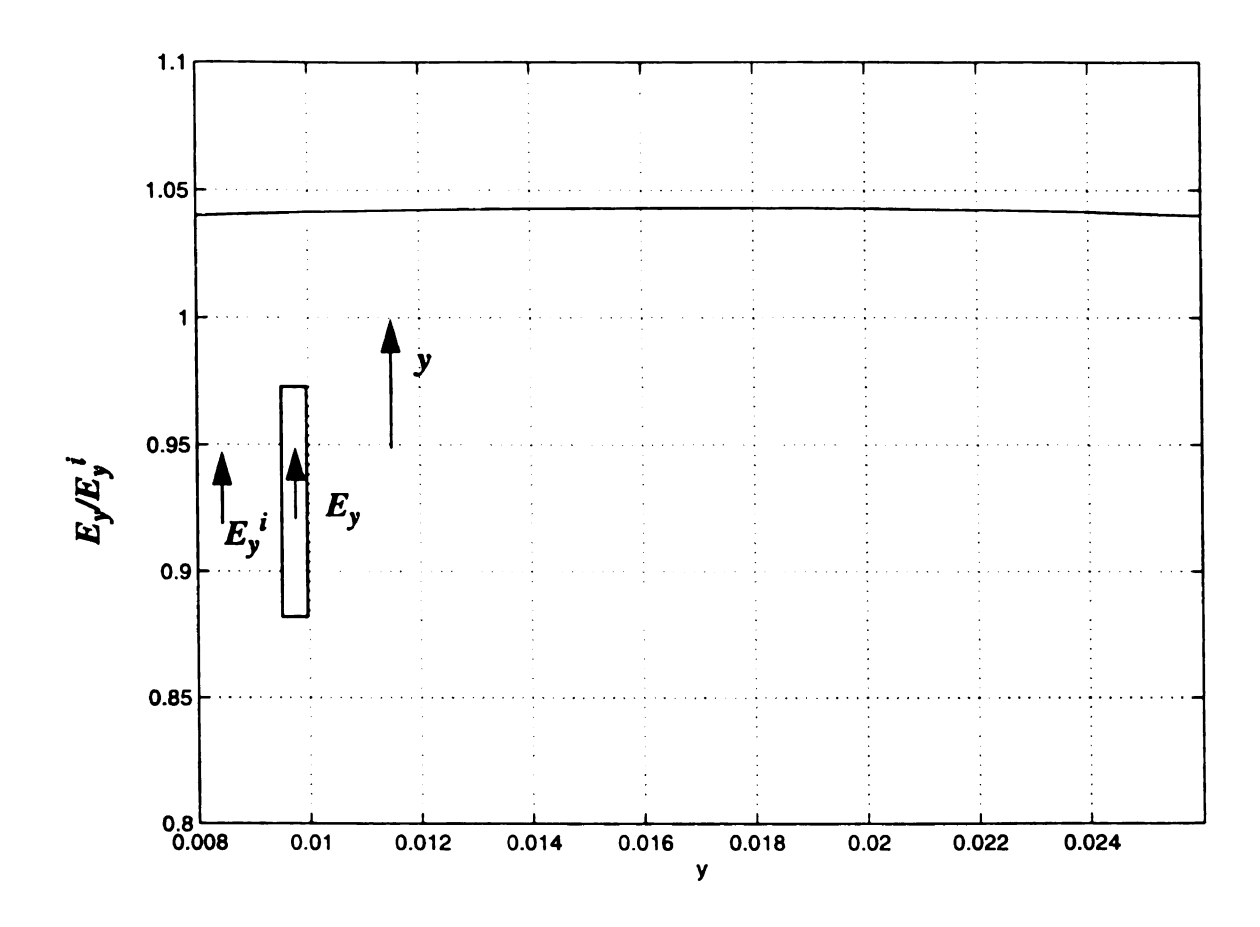


Figure 3.17 Numerical results obtained with the scheme of separating the material sample into boundary layer region and interior region. The ratio of  $E_y/E_y^i$  varies as a function of y coordinate. The sample dimensions are: x=0.003m, y=0.021m, z=0.003m and the geometry of the cavity is shown in Figure 3.7. The resonant frequency shift is assumed to be 1%.

summation, and this summation will be dominant in the computation time. In this case the number of summations is  $10 \times 1500 \times 1500 = 22,500,000$ . If we use the scheme of separating the material sample into boundary layer and interior region, the number of the summations becomes  $98 \times N_b^2 + 10 \times N_i^2 = 15,905,000$ . Therefore, the computation time is about 71% of that in Section 3.2 and furthermore we obtain a better result.

Also we observe that in the scheme of separating the material sample into the boundary layer and interior region for the narrow strip case, the major portion of the computation time is consumed in the boundary layer region due to the small dimensions of the material sample. Thus, this scheme will be effective if the number of volume cells in the interior region is greater than that in the boundary layer region, or for the cases such as a narrow strip, where a very large number of eigenfunctions are required to produce accurate results if the sample is not separated into the interior and boundary layer regions and eq. (2.102) is directly solved.

#### 2. Poisson summation

As stated before, we found that the most difficult step is to fill out the matrix  $[A_{nl}]_{3M\times3M}$  in eqs. (3.17) to (3.20) in the numerical computation due to the slow convergence property of the dyadic Green's function. Now we will apply the Possion summation method [2],[32],[42] to accelerate the convergence property of the double summation in the construction of the matrix (3.20). As before we will consider only the integration of  $G_{eax}(\mathring{r}_0,\mathring{r})$  component for brevity.

The double summation evaluation of  $G_{eoxx}(\mathring{r}_0,\mathring{r})$  can be found in eqs. (3.33) to (3.34) as

$$G_{eoxx}(\hat{r}_0, \hat{r}) = -\frac{1}{k_{0m}^2} \sum_{l=1}^{\infty} \sum_{l=1}^{\infty} \frac{4}{bc} \frac{\left(\frac{m\pi}{b}\right)^2 + \left(\frac{l\pi}{c}\right)^2}{k_{gml} \sin(ak_{gml})} g_{ml}(x, x_0) \sin\frac{m\pi}{b} y$$

$$\sin\frac{m\pi}{b} y_0 \sin\frac{l\pi}{c} z \sin\frac{l\pi}{c} z_0$$
(3.67)

where

$$k_{gml} = \sqrt{k_0^2 - \left(\left(\frac{m\pi}{b}\right)^2 + \left(\frac{l\pi}{c}\right)^2\right)}$$
 (3.68)

$$g_{ml}(x, x_0) = \cos(k_{gml}(a - x_b))\cos(k_{gml}x_s)$$
 (3.69)

Usually we suppose the initial mode to be a lower order mode. Thus,  $k_{gml}$  will be an imaginary number as the indices m and l increase in the double summation (3.67) and it can be approximated by

$$k_{gml} = i \sqrt{\left(\frac{m\pi}{b}\right)^2 + \left(\frac{l\pi}{c}\right)^2} = i k_{gmli}$$
 (3.70)

when m and l become larger. Equation (3.69) can then be expressed by eq. (3.42). Thus, the double summation (3.67) is rewritten as

$$G_{eoxx}(\hat{r}_{0}, \hat{r}) = \frac{2}{k_{0m}^{2}} \sum_{m=m_{i}l=l_{i}}^{\infty} \sum_{bck_{gmli}}^{\infty} \frac{\left(\frac{m\pi}{b}\right)^{2} + \left(\frac{l\pi}{c}\right)^{2}}{bck_{gmli}} e^{-k_{gmli}|x-x_{0}|} \sin\frac{m\pi}{b} y \sin\frac{m\pi}{b} y_{0} \sin\frac{l\pi}{c} z$$

$$\sin\frac{l\pi}{c} z_{0} - \frac{1}{k_{0m}^{2}} \sum_{l=1}^{m_{i}} \sum_{l=1}^{l_{i}} \frac{4}{bck_{gml}} \frac{\left(\frac{m\pi}{b}\right)^{2} + \left(\frac{l\pi}{c}\right)^{2}}{bck_{gml}} g_{ml}(x, x_{0}) \sin\frac{m\pi}{b} y \sin\frac{m\pi}{b} y_{0} \sin\frac{l\pi}{c} z \sin\frac{l\pi}{c} z_{0}$$
(3.71)

where  $m_i$  and  $l_i$  are chosen in such a way that  $k_{gml}$  is an imaginary number and can be approximated by eq. (3.70). In the summation (3.71), the first term is what we need to

consider and the second term is a finite summation which doesn't affect the convergence property. The first summation is denoted as

$$G_{eoxx1}(\hat{r}_0, \hat{r}) = \frac{2}{bck_{0m}^2} \sum_{m=m_i l=l_i}^{\infty} \sum_{bck_{gmli}}^{\infty} \frac{\left(\frac{m\pi}{b}\right)^2 + \left(\frac{l\pi}{c}\right)^2}{bck_{gmli}} e^{-k_{gmli}|x-x_0|} \sin\frac{m\pi}{b} y \sin\frac{m\pi}{b} y_0$$

$$\sin\frac{l\pi}{c} z \sin\frac{l\pi}{c} z_0$$
(3.72)

Since  $k_{gmli}$  can be approximated by (3.70), eq. (3.72) can then be expressed as

$$G_{eoxx1}(\hat{r}_0, \hat{r}) = \frac{2}{bck_{0m}^2} \sum_{m=m_i l=l_i}^{\infty} \sqrt{\left(\frac{m\pi}{b}\right)^2 + \left(\frac{l\pi}{c}\right)^2} e^{-\sqrt{\left(\frac{m\pi}{b}\right)^2 + \left(\frac{l\pi}{c}\right)^2} |x - x_0|} \\ \sin\frac{m\pi}{b} y \sin\frac{m\pi}{b} y_0 \sin\frac{l\pi}{c} z \sin\frac{l\pi}{c} z_0$$
(3.73)

The expression (3.73) can converge faster if  $x \neq x_0$ , i.e. off-plane case. However, it will converge very slow when  $x = x_0$ , i.e. on plane case.

The Poisson summation formula [2],[32],[42] can sometimes be used to convert a slowly converging series into a rapidly converging one by allowing the series to be summed over in the Fourier transform domain, that is, if a series spreads out, then its Fourier transform must be concentrated around the origin.

The Poisson summation formula is given by [2],[32],[42] as

$$\sum_{n=-\infty}^{\infty} f(n\alpha) = \frac{1}{\alpha} \sum_{m=-\infty}^{\infty} F\left(\frac{2m\pi}{\alpha}\right)$$
 (3.74)

where F is the Fourier transform of f. In [32] the Fourier transform of

$$f_1(x) = \frac{e^{-L\sqrt{x^2 + k_m^2}}}{\sqrt{x^2 + k_m^2}} \cos(xA_0)$$
 (3.75)

is given as

$$K_0 \left\{ k_m \sqrt{L^2 + (\omega - A_0)^2} \right\} + K_0 \left\{ k_m \sqrt{L^2 + (\omega + A_0)^2} \right\}$$
 (3.76)

where  $K_0$  is the modified Bessel function of the second kind and it decays rapidly  $(K_0(0) = \infty, K_0(0.5) = 0.9244, K_0(1) = 0.4210$  and  $K_0(1) = 0.1139$ ). Then using the Poisson summation formula, we have

$$\sum_{n=-\infty}^{\infty} f\left(n\frac{\pi}{b}\right) = \frac{b}{\pi} \sum_{m=-\infty}^{\infty} F(2mb)$$
(3.77)

Therefore, we obtain the following summation by the Poisson summation:

$$\sum_{n=-\infty}^{\infty} \frac{e^{-L\sqrt{\left(\frac{n\pi}{b}\right)^{2} + k_{m}^{2}}}}{\sqrt{\left(\frac{n\pi}{b}\right)^{2} + k_{m}^{2}}} \cos\left(\frac{n\pi}{b}A_{0}\right)$$

$$= \frac{b}{\pi} \sum_{m=-\infty}^{\infty} \left[ K_{0} \left\{ k_{m} \sqrt{L^{2} + (2mb - A_{0})^{2}} \right\} + K_{0} \left\{ k_{m} \sqrt{L^{2} + (2mb + A_{0})^{2}} \right\} \right]$$
(3.78)

After some algebraic manipulation we have [32]

$$\sum_{m=1}^{\infty} \frac{e^{-|x-x_0|} \sqrt{\left(\frac{m\pi}{b}\right)^2 + \left(\frac{l\pi}{c}\right)^2}}{\sqrt{\left(\frac{m\pi}{b}\right)^2 + \left(\frac{l\pi}{c}\right)^2}} \sin\frac{m\pi}{b} y \sin\frac{m\pi}{b} y_0$$

$$= \frac{b}{2\pi} \sum_{m=-\infty}^{\infty} \left[ K_0 \left\{ \frac{l\pi}{c} \sqrt{(x-x_0)^2 + (2mb-y+y_0)^2} \right\} + K_0 \left\{ \frac{l\pi}{c} \sqrt{(x-x_0)^2 + (2mb-y-y_0)^2} \right\}$$

$$-K_0 \left\{ \frac{l\pi}{c} \sqrt{(x-x_0)^2 + (2mb-y-y_0)^2} \right\}$$

$$-K_0 \left\{ \frac{l\pi}{c} \sqrt{(x-x_0)^2 + (2mb+y+y_0)^2} \right\}$$

$$-K_0 \left\{ \frac{l\pi}{c} \sqrt{(x-x_0)^2 + (2mb+y+y_0)^2} \right\}$$

Due to the rapid decay of the modified Bessel function of the second kind, the only significant term in eq. (3.79) is that for m=0. Hence eq. (3.79) can be approximated as

$$\sum_{m=1}^{\infty} \frac{e^{-|x-x_0|} \sqrt{\left(\frac{m\pi}{b}\right)^2 + \left(\frac{l\pi}{c}\right)^2}}{\sqrt{\left(\frac{m\pi}{b}\right)^2 + \left(\frac{l\pi}{c}\right)^2}} \sin\frac{m\pi}{b} y \sin\frac{m\pi}{b} y_0$$

$$= \frac{b}{\pi} \left[ K_0 \left\{ \frac{l\pi}{c} \sqrt{(x-x_0)^2 + (y-y_0)^2} \right\} - K_0 \left\{ \frac{l\pi}{c} \sqrt{(x-x_0)^2 + (y+y_0)^2} \right\} \right]$$
(3.80)

In order to employ eq. (3.80) to accelerate the series convergence rate of the dyadic Green's function, we rewrite the eq. (3.71) as

$$G_{eoxx}(\hat{r}_{0}, \hat{r}) = \frac{2}{k_{0m}^{2}} \sum_{l=1}^{\infty} \sum_{l=1}^{\infty} \frac{\sqrt{\left(\frac{m\pi}{b}\right)^{2} + \left(\frac{l\pi}{c}\right)^{2}}}{bc} e^{-k_{gmli}|x - x_{0}|} \sin\frac{m\pi}{b} y \sin\frac{m\pi}{b} y_{0}$$

$$\sin\frac{l\pi}{c} z \sin\frac{l\pi}{c} z_{0} - \frac{1}{k_{0m}^{2}} \sum_{l=1}^{m_{i}} \sum_{l=1}^{l_{i}} \frac{4}{bc} \left[ \frac{\sqrt{\left(\frac{m\pi}{b}\right)^{2} + \left(\frac{l\pi}{c}\right)^{2}}}{2} e^{-k_{gmli}|x - x_{0}|} + \frac{\left(\frac{m\pi}{b}\right)^{2} + \left(\frac{l\pi}{c}\right)^{2}}{k_{gml} \sin(ak_{gml})} g_{ml}(x, x_{0}) \right] \sin\frac{m\pi}{b} y \sin\frac{m\pi}{b} y_{0} \sin\frac{l\pi}{c} z \sin\frac{l\pi}{c} z_{0}$$

$$(3.81)$$

where the first summation can be accelerated by eq. (3.80) and the second term is a finite summation.

The first summation is denoted as

$$G_{eoxx2}(\hat{r}_0, \hat{r}) = \frac{2}{k_{0m}^2} \sum_{n=1}^{\infty} \sum_{l=1}^{\infty} \frac{\sqrt{\left(\frac{m\pi}{b}\right)^2 + \left(\frac{l\pi}{c}\right)^2}}{bc} e^{-k_{smli}|x - x_0|}$$

$$\sin \frac{m\pi}{b} y \sin \frac{m\pi}{b} y_0 \sin \frac{l\pi}{c} z \sin \frac{l\pi}{c} z_0$$
(3.82)

In the Galerkin's method we need to integrate the dyadic Green's function with respect to variables  $\hat{r}$  and  $\hat{r}_0$ . For the  $G_{eoxx2}(\hat{r}_0,\hat{r})$ , whether  $x=x_0$  or  $x\neq x_0$  will determine the convergence rate. Let's consider the integration of  $G_{eoxx2}(\hat{r}_0,\hat{r})$  with respect to x and  $x_0$  for brevity. The integration of  $G_{eoxx2}(\hat{r}_0,\hat{r})$  when  $x=x_0$  is given by

$$\int_{x}^{x+\Delta x} \int_{x_0}^{x_0+\Delta x} G_{eoxx2}(\mathring{r}_0,\mathring{r}) du_0 du$$

$$= \frac{4}{bck_{0m}^{2}} \sum_{m=1}^{\infty} \sum_{l=1}^{\infty} \left[ \left( \frac{m\pi}{b} \right)^{2} + \left( \frac{l\pi}{c} \right)^{2} \right] \left[ \frac{\Delta x}{\left( \frac{m\pi}{b} \right)^{2} + \left( \frac{l\pi}{c} \right)^{2}} + \frac{e^{-\sqrt{\left( \frac{m\pi}{b} \right)^{2} + \left( \frac{l\pi}{c} \right)^{2}} \Delta x}}{\left( \left( \frac{m\pi}{b} \right)^{2} + \left( \frac{l\pi}{c} \right)^{2} + \left( \frac{l\pi}{c} \right)^{2}} \right]$$
(3.83)

 $\sin\frac{m\pi}{b}y\sin\frac{m\pi}{b}y_0\sin\frac{l\pi}{c}z\sin\frac{l\pi}{c}z_0$ 

$$= \frac{4}{bck_{0m}^2} \sum_{m=1}^{\infty} \sum_{l=1}^{\infty} \left[ \Delta x + \frac{e^{-\sqrt{\left(\frac{m\pi}{b}\right)^2 + \left(\frac{l\pi}{c}\right)^2} \Delta x}}{\sqrt{\left(\frac{m\pi}{b}\right)^2 + \left(\frac{l\pi}{c}\right)^2}} \right] \sin \frac{m\pi}{b} y \sin \frac{m\pi}{b} y_0 \sin \frac{l\pi}{c} z \sin \frac{l\pi}{c} z_0$$

and when  $x \neq x_0$  is given by

$$\int_{x}^{x+\Delta x} \int_{x_0}^{x_0} G_{eoxx2}(\mathring{r}_0,\mathring{r}) du_0 du$$

$$= -\frac{4}{bck_0^2} \sum_{m=1}^{\infty} \sum_{l=1}^{\infty} \frac{e^{-\sqrt{\left(\frac{m\pi}{b}\right)^2 + \left(\frac{l\pi}{c}\right)^2}|x-x_0|}}{\sqrt{\left(\frac{m\pi}{b}\right)^2 + \left(\frac{l\pi}{c}\right)^2}} \left[1 - \cosh\left(\Delta x \sqrt{\left(\frac{m\pi}{b}\right)^2 + \left(\frac{l\pi}{c}\right)^2}\right)\right]$$

$$\sin \frac{m\pi}{b} y \sin \frac{m\pi}{b} y_0 \sin \frac{l\pi}{c} z \sin \frac{l\pi}{c} z_0$$
(3.84)

The first summation in eq. (3.83) is just a delta function  $\delta(\hat{r} - \hat{r}_0)$  divided by  $k_0^2$ . The second term in eq. (3.83) and eq. (3.84) can be summed by eq. (3.80). Therefore, the approximation of eqs. (3.83) and (3.84) by eq. (3.80) can be expressed as

$$\int_{x}^{x+\Delta x} \int_{x_{0}}^{x+\Delta x} G_{eoxx2}(\mathring{r}_{0},\mathring{r}) du_{0} du$$

$$= \frac{\Delta x}{k_{0}^{2}} \delta(\mathring{r} - \mathring{r}_{0}) + \frac{4}{\pi c k_{0}^{2}} \sum_{l=1}^{\infty} \left[ K_{0} \left\{ \frac{l\pi}{c} \sqrt{\Delta x^{2} + (y - y_{0})^{2}} \right\} - K_{0} \left\{ \frac{l\pi}{c} \sqrt{\Delta x^{2} + (y + y_{0})^{2}} \right\} \right] + K_{0} \left\{ \frac{l\pi}{c} |y - y_{0}| \right\} - K_{0} \left\{ \frac{l\pi}{c} (y + y_{0}) \right\} \right] \sin \frac{l\pi}{c} z \sin \frac{l\pi}{c} z_{0}$$
(3.85)

for  $x = x_0$  and

$$\int_{x}^{x+\Delta x} \int_{x_{0}}^{x} G_{eoxx2}(\mathring{r}_{0},\mathring{r}) du_{0} du$$

$$= \frac{4}{\pi c k_{0}^{2}} \sum_{l=1}^{\infty} \left[ K_{0} \left\{ \frac{l\pi}{c} \sqrt{(x-x_{0})^{2} + (y-y_{0})^{2}} \right\} - K_{0} \left\{ \frac{l\pi}{c} \sqrt{(x-x_{0})^{2} + (y+y_{0})^{2}} \right\} - K_{0} \left\{ \frac{l\pi}{c} \sqrt{(|x-x_{0}| - \Delta x)^{2} + (y-y_{0})^{2}} \right\} / 2$$

$$+ K_{0} \left\{ \frac{l\pi}{c} \sqrt{(|x-x_{0}| - \Delta x)^{2} + (y+y_{0})^{2}} \right\} / 2 \right] \sin \frac{l\pi}{c} z \sin \frac{l\pi}{c} z_{0}$$
(3.86)

for  $x \neq x_0$ . Comparing eqs. (3.85) and (3.86) with eqs. (3.83) and (3.84), we find that the double summations in eqs. (3.83) and (3.84) are approximated by the single summations in eqs. (3.85) and (3.86) when Poisson summation formula (3.77) is used.

In the numerical computation, we set  $m_i$  and  $l_i$  to be 5 in eq. (3.81) and the summation index l to be from l to 25 in eqs. (3.85) and (3.86). Then we apply eqs. (3.85) and (3.86) to our numerical examples as discussed in Section 3.3.

The material sample of a 4-mm cubic shape is placed in the center of the rectangular cavity. The relative permittivity of the material sample is assumed to be

 $\varepsilon_r=2.5$ . The material sample is divided as  $n_d=2$ ,  $m_d=2$  and  $l_d=2$ . The numerical results using Poisson summation formula are: 5.09 (5.4949) for the x component, 193.65 (203.9074) for the y component and 4.91 (5.552) for the z component of the induced electric field in each volume cell of the material sample, where the values in the parentheses indicate the numerical results of the double summation for the 4-mm cubic shape material sample which we obtained before. The ratio of the y component of the induced electric field to that of the initial electric field is 0.60 while it is 0.634 if the double summation is applied. Thus, we can conclude that these approximation results are satisfactory.

If we increase the dimensions of the cubic material sample to have 0.006m in each side and divide the material sample as  $n_d = 3$ ,  $m_d = 3$  and  $l_d = 3$  while keeping the other parameters the same as previous cases, we found that the computed electric field is still dominated by the y component and all the components of the induced electric field are symmetric with respect to the center of the rectangular cavity. The y component of the induced electric field does not change significantly with respect to the variables x and z but change somewhat more with respect to the variable y. The values of the y component of the electric field are 194.88 for  $y=y_1$ , 220.73 for  $y=y_2$  and 194.88 for  $y=y_3$ . The ratios of the y component of the electric field to that of the initial electric field are 0.61 for  $y=y_1$  and 0.69 for  $y=y_2$  while the ratios are 0.632 for  $y=y_1$  and 0.677 for  $y=y_2$  if the double summation is applied to this 6-mm cubic material sample. Comparing these numerical results we observe that the numerical results with the Poisson summation are very close to the theoretical approximation and the previous numerical results using double summation.

In the Poisson summation scheme, for each component of the dyadic Green's

function, the summation in each volume cell is only  $2 \times 5 \times 5 + 25 = 75$  based on eqs. (3.81), (3.85) and (3.86) while in the double summation there are over 40,000 summation terms. It is noted that even though we need a numerical integration of the modified Bessel function with respect to the variables y and  $y_0$  in this scheme, the overall computation time is still saved about 60% due to the decrease in the summation terms.

## **CHAPTER 4**

# QUANTIFICATION OF THE INDUCED ELEC-TRIC FIELD IN A MATERIAL SAMPLE PLACED WITHIN A CYLINDRICAL CAVITY

In the microwave heating of material samples, a cylindrical microwave cavity is more commonly used than a rectangular microwave cavity. Theoretical analysis of the induced electric field inside a material sample placed within an energized cylindrical cavity is more involved than that of a rectangular cavity case as studied in Chapter 2 and Chapter 3.

In this chapter, we will quantify the induced electric fields inside material samples of various geometries and dielectric parameters which are placed within an energized cylindrical cavity. The theoretical method used in Chapter 2 can be employed to obtain the induced electric field inside the material sample placed within a cylindrical cavity. That is,

we will use the vector wave functions  $\vec{L}_{nml}$ ,  $\vec{M}_{nml}$  and  $\vec{N}_{nml}$  which will be defined in the Cylindrical cavity as a complete set of basis functions to determine the induced electric field inside the material sample.

In the cylindrical cavity, the definitions for the vector wave functions  $\vec{L}_{nml}$ ,  $\vec{M}_{nml}$ 

and  $\vec{N}_{nml}$  are the same as that in the rectangular cavity as given in eqs. (2.1), (2.2) and (2.3). These vector wave functions also satisfy the same boundary conditions (2.4), (2.5) and (2.6) at the perfectly conducting walls of the cavity. We will show that the vector wave functions  $\vec{L}_{nml}$ ,  $\vec{M}_{nml}$  and  $\vec{N}_{nml}$  in a cylindrical cavity are orthogonal and form a complete set of basis functions and satisfy the vector Helmholtz equations based on the proofs given in Section 2.1.3, Section 2.1.4 and Section 2.1.6 in Chapter 2. However, they have completely different expressions in a cylindrical cavity.

The outline of this chapter is as follows: In Section 4.1 we will derive the expressions for the vector wave functions  $\vec{L}_{nml}$ ,  $\vec{M}_{nml}$  and  $\vec{N}_{nml}$  in the cylindrical cavity. In Section 4.2 the normalization of these three vector wave functions will be carried out and some field structures of the vector wave functions  $\vec{L}_{nml}$ ,  $\vec{M}_{nml}$  and  $\vec{N}_{nml}$  will be plotted. In Section 4.3 the expression for the dyadic Green's function in the cylindrical cavity will be obtained. Some numerical examples will be presented in Section 4.4.

# 4.1 Expressions for Vector Wave Functions $\vec{L}_{nml}$ , $\vec{M}_{nml}$ and $\vec{N}_{nml}$ in Cylindrical Cavities

The cylindrical cavity under consideration has the geometry shown in Figure 4.1.

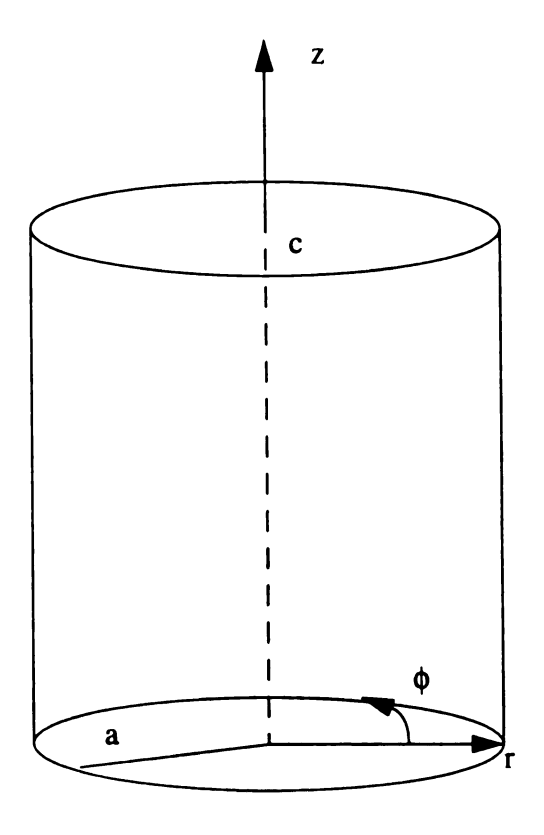


Figure 4.1 A cylindrical cavity and the designation of the coordinate system

#### 4.1.1 Expression for Vector Wave Function $\hat{L}_{nml}$

Based on the definition and the boundary conditions of the vector wave function

 $L_{nml}$  given in eqs. (2.1) and (2.4), we have

$$\hat{L}_{nml} = \frac{1}{k_{nml}} (\nabla \phi_{nml}^L) \tag{4.1}$$

$$\hat{n} \times \hat{L}_{nml} = 0 \tag{4.2}$$

where the scalar eigenfunction  $\phi_{nml}^L$  satisfies the scalar Helmholtz equation of

$$(\nabla^2 + k_{nml}^2)\phi_{nml}^L = 0 (4.3)$$

and  $\nabla^2 = \frac{1}{r} \frac{\partial}{\partial r} \left( r \frac{\partial}{\partial r} \right) + \frac{1}{r^2} \frac{\partial^2}{\partial \varphi^2} + \frac{\partial^2}{\partial z^2}$  in the cylindrical coordinate system. Applying the

variables separation method to eq. (4.3), we obtain the solution of the scalar eigenfunction  $\phi_{nml}^{L}$  as

$$\phi_{nml}^{L} = A_{nml}J_{n}(k_{r}r) \begin{cases} \cos(n\varphi) \\ \sin(n\varphi) \end{cases} \begin{cases} \cos(k_{z}z) \\ \sin(k_{z}z) \end{cases}$$
(4.4)

where  $J_n(k_r r)$  denotes the first kind of the *nth* order Bessel function, n is an integer and  $A_{nml}$  is an unknown constant which will be determined by the normalization of the vector

wave function  $\hat{L}_{nml}$ . The eigenvalue  $k_{nml}$  is then expressed as

$$k_{nml}^2 = k_r^2 + k_z^2 (4.5)$$

If n=0, the solution of the scalar eigenfunction  $\phi_{0ml}^{L}$  is given by

$$\phi_{0ml}^{L} = A_{0ml} J_0(k_r r) \begin{cases} \cos(k_z z) \\ \sin(k_z z) \end{cases}$$
 (4.6)

Using the definition (4.1), applying the boundary conditions (4.2) and after some manipulations, we obtain the expressions for the three components of the vector wave

function  $\hat{L}_{nml}$  as

$$L_{nmlr} = \frac{A_{nml}p_{nm}}{k_{nml}} J_{n} \left(\frac{p_{nm}}{a}r\right) \left\{\frac{\cos(n\varphi)}{\sin(n\varphi)}\right\} \sin\left(\frac{l\pi}{c}z\right)$$
(4.7)

$$L_{nml\phi} = \frac{A_{nml}n}{k_{nml}r} J_n \left(\frac{p_{nm}}{a}r\right) \left\{ \frac{-\sin(n\phi)}{\cos(n\phi)} \right\} \sin\left(\frac{l\pi}{c}z\right)$$
(4.8)

$$L_{nmlz} = \frac{A_{nml} l\pi}{k_{nml}} \int_{c}^{l} \int_{c}^{l} \left( \frac{p_{nm}}{a} r \right) \left\{ \frac{\cos(n\varphi)}{\sin(n\varphi)} \right\} \cos\left( \frac{l\pi}{c} z \right)$$
(4.9)

while the eigenvalue is determined by

$$k_{nml}^2 = \left(\frac{p_{nm}}{a}\right)^2 + \left(\frac{l\pi}{c}\right)^2 \tag{4.10}$$

In eq. (4.7),  $J_n'(k_r r)$  denotes the derivative of the bessel function  $J_n(k_r r)$  with respect to  $k_r r$  and  $p_{nm}$  denotes the *mth* root of the first kind of the *nth* order Bessel function, that is,  $J_n(p_{nm}) = 0$ . The expression for the scalar eigenfunction  $\phi_{nml}^L$  is then given by

$$\phi_{nml}^{L} = A_{nml} J_n \left( \frac{p_{nm}}{a} r \right) \left\{ \frac{\cos(n\varphi)}{\sin(n\varphi)} \right\} \sin\left( \frac{l\pi}{c} z \right)$$
 (4.11)

When n=0, the expression of the vector wave function  $\vec{L}_{0ml}$  is given by

$$L_{0mlr} = \frac{A_{0ml}}{k_{0ml}} \frac{p_{0m}}{a} J_0 \left( \frac{p_{0m}}{a} r \right) \sin \left( \frac{l\pi}{c} z \right)$$
 (4.12)

$$L_{0mlz} = \frac{A_{0ml}l\pi}{k_{0ml}} \frac{l\pi}{c} J_0 \left(\frac{p_{0m}}{a}r\right) \cos\left(\frac{l\pi}{c}z\right)$$
(4.13)

and  $L_{0ml\phi} = 0$ .

#### **4.1.2** Expression for Vector Wave Function $\overrightarrow{M}_{nml}$

Based on the definition and the boundary conditions of the vector wave function  $\vec{M}_{nml}$  given in eqs.(2.2) and (2.5), we have

$$\overrightarrow{M}_{nml} = \nabla \times (\hat{z} \phi_{nml}^{M}) \tag{4.14}$$

$$\hat{n} \times \overrightarrow{M}_{nml} = 0 \tag{4.15}$$

where the scalar eigenfunction  $\phi_{nml}^{M}$  satisfies the scalar Helmholtz equation of

$$(\nabla^2 + q_{nml}^2)\phi_{nml}^M = 0 (4.16)$$

Applying the variables separation method to eq. (4.16), we obtain the solution of the scalar eigenfunction  $\phi_{nml}^{M}$  as

$$\phi_{nml}^{M} = B_{nml}J_{n}(k_{r}r) \begin{cases} \cos(n\varphi) \\ \sin(n\varphi) \end{cases} \begin{cases} \cos(k_{z}z) \\ \sin(k_{z}z) \end{cases}$$
(4.17)

and the eigenvalue  $q_{nml}$  is expressed as

$$q_{nml}^2 = k_r^2 + k_z^2 (4.18)$$

where  $\boldsymbol{B}_{nml}$  is an unknown constant which can be determined by the normalization of the

vector wave function  $\overrightarrow{M}_{nml}$ .

If n=0, the solution of the scalar function  $\phi_{0ml}^{M}$  is given by

$$\phi_{0ml}^{M} = B_{0ml} J_0(k_r r) \begin{cases} \cos(k_z z) \\ \sin(k_z z) \end{cases}$$
 (4.19)

Hence, using the definition (4.14), applying the boundary conditions (4.15) and after some manipulations, we obtain the expressions for the two components of the vector wave

function  $\vec{M}_{nml}$  as

$$M_{nmlr} = \frac{B_{nml}}{r} n J_n \left( \frac{p_{nm'}}{a} r \right) \begin{cases} -\sin(n\varphi) \\ \cos(n\varphi) \end{cases} \sin\left(\frac{l\pi}{c}z\right)$$
(4.20)

$$M_{nml\phi} = -B_{nml} \frac{p_{nm'}}{a} J_{n'} \left( \frac{p_{nm'}}{a} r \right) \left\{ \frac{\cos(n\phi)}{\sin(n\phi)} \right\} \sin\left( \frac{l\pi}{c} z \right)$$
(4.21)

while the eigenvalue is determined by

$$q_{nml}^2 = \left(\frac{p_{nm}}{a}\right)^2 + \left(\frac{l\pi}{c}\right)^2 \tag{4.22}$$

where  $p_{nm}$  denotes the *mth* root of the derivative of the *nth* order Bessel function of the first kind, that is,  $J_n'(p_{nm}') = 0$ . The expression for the scalar eigenfunction  $\phi_{nml}^M$  is then given by

$$\phi_{nml}^{M} = B_{nml} J_{n} \left( \frac{p_{nm}}{a} r \right) \left\{ \frac{\cos(n\varphi)}{\sin(n\varphi)} \right\} \sin\left( \frac{l\pi}{c} z \right)$$
 (4.23)

When n=0, the expression for the vector wave function  $\overrightarrow{M}_{0ml}$  is given by

$$M_{0ml\varphi} = -B_{0ml} \frac{p_{0m}}{a} J_0 \left( \frac{p_{0m}}{a} r \right) \sin \left( \frac{l\pi}{c} z \right)$$
 (4.24)

and  $M_{0mlr} = 0$ .

## **4.1.3** Expression for Vector Wave Function $\vec{N}_{nml}$

Based on the definition and the boundary conditions of the vector wave function  $\vec{N}_{nml}$  given in eqs. (2.3) and (2.6), we have

$$\vec{N}_{nml} = \frac{1}{k_{nml}} \nabla \times \nabla \times (\hat{z} \phi_{nml}^{N})$$
 (4.25)

$$\hat{n} \times \vec{N}_{nml} = 0 \tag{4.26}$$

where the scalar eigenfunction  $\phi_{nml}^{N}$  satisfies the scalar Helmholtz equation of

$$(\nabla^2 + k_{nml}^2)\phi_{nml}^N = 0 (4.27)$$

Applying the variables separation method to eq. (4.27), we obtain the solution of

the scalar eigenfunction  $\phi_{nml}^{N}$  as

$$\phi_{nml}^{N} = C_{nml}J_{n}(k_{r}r) \begin{cases} \cos(n\varphi) \\ \sin(n\varphi) \end{cases} \begin{cases} \cos(k_{z}z) \\ \sin(k_{z}z) \end{cases}$$
(4.28)

and the eigenvalue is determined by

$$k_{nml}^2 = k_r^2 + k_z^2 (4.29)$$

where  $C_{nml}$  is an unknown constant which can be determined by the normalization of the vector wave function  $\overrightarrow{N}_{nml}$ .

If n=0, the solution of the scalar eigenfunction  $\phi_{0ml}^N$  is given by

$$\phi_{0ml}^{N} = C_{0ml} J_0(k_r r) \begin{cases} \cos(k_z z) \\ \sin(k_z z) \end{cases}$$
 (4.30)

Using eqs. (4.25) and (4.28) and applying the boundary conditions (4.26), we obtain the expressions for the three components of the vector wave function  $\vec{N}_{nml}$  as

$$N_{nmlr} = -\frac{C_{nml}p_{nm}l\pi}{k_{nml}}\frac{1}{a}\frac{l\pi}{c}J_{n}\left(\frac{p_{nm}}{a}r\right)\left\{\frac{\cos(n\varphi)}{\sin(n\varphi)}\right\}\sin\left(\frac{l\pi}{c}z\right)$$
(4.31)

$$N_{nml\phi} = -\frac{C_{nml}nl\pi}{k_{nml}r}\frac{l\pi}{r}J_n\left(\frac{p_{nm}}{a}r\right)\left\{\frac{-\sin(n\phi)}{\cos(n\phi)}\right\}\sin\left(\frac{l\pi}{c}z\right)$$
(4.32)

$$N_{nmlz} = -\frac{C_{nml}}{k_{nml}} \left(\frac{p_{nm}}{a}\right)^2 J_n \left(\frac{p_{nm}}{a}r\right) \left\{\frac{\cos(n\varphi)}{\sin(n\varphi)}\right\} \cos\left(\frac{l\pi}{c}z\right)$$
(4.33)

while the eigenvalue is determined by

$$k_{nml}^2 = \left(\frac{p_{nm}}{a}\right)^2 + \left(\frac{l\pi}{c}\right)^2 \tag{4.34}$$

The expression for the scalar eigenfunction  $\phi_{nml}^{N}$  is then given by

$$\phi_{nml}^{N} = C_{nml} J_n \left( \frac{p_{nm}}{a} r \right) \left\{ \frac{\cos(n\varphi)}{\sin(n\varphi)} \right\} \cos\left( \frac{l\pi}{c} z \right)$$
 (4.35)

When n=0, the expression of the vector wave function  $\overrightarrow{N}_{0ml}$  is given by

$$N_{0mlr} = -\frac{C_{0ml}}{k_{0ml}} \frac{p_{0m}}{a} \frac{l\pi}{c} J_0' \left( \frac{p_{0m}}{a} r \right) \sin \left( \frac{l\pi}{c} z \right)$$
 (4.36)

$$N_{0mlz} = -\frac{C_{0ml}}{k_{0ml}} \left(\frac{p_{0m}}{a}\right)^2 J_0 \left(\frac{p_{0m}}{a}r\right) \cos\left(\frac{l\pi}{c}z\right)$$
(4.37)

and  $N_{0ml\phi} = 0$ .

In the expressions of the vector wave functions  $\vec{L}_{nml}$ ,  $\vec{M}_{nml}$  and  $\vec{N}_{nml}$ , we did not specify their dependences on the variable  $\varphi$ . The variations of these functions with respect to the variable  $\varphi$  can be determined by the location of the excitation probe and the  $\varphi$  dependences of the r and z components of the electric field. All the vector wave functions should have the same dependence on the variable  $\varphi$  because they are excited by the same source.

If the excitation probe is located at  $\varphi = 0$  and the r and z components are even functions of the variable  $\varphi$ , then the expressions for the vector wave functions  $\vec{L}_{nml}$ ,  $\vec{M}_{nml}$  and  $\vec{N}_{nml}$  can be given by

$$\hat{L}_{nml} = \frac{A_{nml}}{k_{nml}} \left[ \hat{r} \frac{p_{nm}}{a} J_n' \left( \frac{p_{nm}}{a} r \right) \cos(n\varphi) \sin\left( \frac{l\pi}{c} z \right) \right. \\
\left. - \hat{\varphi} \frac{n}{r} J_n \left( \frac{p_{nm}}{a} r \right) \sin(n\varphi) \sin\left( \frac{l\pi}{c} z \right) + \hat{z} \frac{l\pi}{c} J_n \left( \frac{p_{nm}}{a} r \right) \cos(n\varphi) \cos\left( \frac{l\pi}{c} z \right) \right] \tag{4.38}$$

$$\overrightarrow{M}_{nml} = B_{nml} \left[ \hat{r} \frac{n}{r} J_n \left( \frac{p_{nm}}{a} r \right) \cos(n\varphi) \sin\left( \frac{l\pi}{c} z \right) \right]$$

$$-\hat{\varphi} \frac{p_{nm}}{a} J_n \left( \frac{p_{nm}}{a} r \right) \sin(n\varphi) \sin\left( \frac{l\pi}{c} z \right)$$
(4.39)

$$\vec{N}_{nml} = -\frac{C_{nml}}{k_{nml}} \left[ \hat{r} \frac{p_{nm} l\pi}{a} J_n' \left( \frac{p_{nm}}{a} r \right) \cos(n\varphi) \sin\left( \frac{l\pi}{c} z \right) - \hat{\varphi} \frac{n l\pi}{r} J_n \left( \frac{p_{nm}}{a} r \right) \right] 
\sin(n\varphi) \sin\left( \frac{l\pi}{c} z \right) + \hat{z} \left( \frac{p_{nm}}{a} \right)^2 J_n \left( \frac{p_{nm}}{a} r \right) \cos(n\varphi) \cos\left( \frac{l\pi}{c} z \right)$$
(4.40)

It is noted that these eqs. (4.38) to (4.40) are valid only for  $n \neq 0$  case. For n = 0 case, we have already derived the expressions in eqs. (4.12), (4.13), (4.24), (4.36) and (4.37).

# 4.2 Normalization of Vector Wave Functions $\vec{L}_{nml}$ , $\vec{M}_{nml}$ and $\vec{N}_{nml}$ in Cylindrical Cavities

### 4.2.1 Normalization of Vector Wave Function $\hat{L}_{nml}$

Based on eq. (2.59) the normalization of the vector wave function  $\vec{L}_{nml}$  is given by

$$\int_0^a \int_0^{2\pi} \int_0^c \left( \vec{L}_{nml} \cdot \vec{L}_{nml} \right) r dr d\varphi dz = 1$$
 (4.41)

That is,

$$\int_{0}^{a} \int_{0}^{2\pi} \int_{0}^{c} \left( \overrightarrow{L}_{nml} \cdot \overrightarrow{L}_{nml} \right) r dr d\phi dz = \int_{0}^{a} \int_{0}^{2\pi} \int_{0}^{c} \phi_{nml}^{L} \phi_{nml}^{L} r dr d\phi dz$$

$$= \int_{0}^{a} \int_{0}^{2\pi} \int_{0}^{c} A_{nml}^{2} \left( J_{n} \left( \frac{p_{nm}}{a} r \right) \cos(n\phi) \sin\left( \frac{l\pi}{c} z \right) \right)^{2} r dr d\phi dz = 1$$
(4.42)

where we have used the following relation

$$\hat{L}_{nml} \cdot \hat{L}_{nml} = \frac{1}{k_{nml}^2} \nabla \phi_{nml}^L \cdot \nabla \phi_{nml}^L$$

$$= \frac{1}{k_{nml}^2} \nabla \cdot (\phi_{nml}^L \nabla \phi_{nml}^L) - \frac{1}{k_{nml}^2} \phi_{nml}^L \nabla^2 \phi_{nml}^L$$

$$= \frac{1}{k_{nml}^2} \nabla \cdot (\phi_{nml}^L \nabla \phi_{nml}^L) + \phi_{nml}^L \phi_{nml}^L$$

$$(4.43)$$

and the integration of  $\frac{1}{k_{nml}^2} \nabla \cdot (\phi_{nml}^L \nabla \phi_{nml}^L)$  over the cavity volume is zero using the

boundary conditions. Equation (4.42) can then be simplified as

$$A_{nml}^2 \frac{2\pi c}{\varepsilon_{0n} \varepsilon_{0l}} \int_0^a J_n^2 \left(\frac{p_{nm}}{a}r\right) r dr = 1$$
 (4.44)

where  $\varepsilon_{0n}$  has been defined by eq. (2.63) in Chapter 2. The identity for the integration of the Bessel function is given in [64] and [65] as

$$\int x J_n^2(ax) dx = \frac{x^2}{2} \left[ J_n^2(ax) + \left( 1 - \frac{n^2}{a^2 x^2} \right) J_n^2(ax) \right]$$
 (4.45)

Hence, using eq. (4.45) and after some manipulations, we may obtain the integration in eq. (4.44) as

$$\int_{0}^{a} J_{n}^{2} \left(\frac{p_{nm}}{a}r\right) r dr = \frac{a^{2}}{2} J_{n}^{2}(p_{nm})$$
(4.46)

The normalization constant for the vector wave function  $\vec{L}_{nml}$  is then expressed as

$$A_{nml} = \sqrt{\frac{\varepsilon_{0n}\varepsilon_{0l}}{\pi c}} \frac{1}{aJ'_{n}(p_{nm})}$$
 (4.47)

When n = 0, the normalization of the vector wave function  $\hat{L}_{0ml}$  is given by

$$\int_{0}^{a} \int_{0}^{2\pi} \int_{0}^{c} \left( \vec{L}_{0ml} \cdot \vec{L}_{0ml} \right) r dr d\phi dz = 2\pi \int_{0}^{a} \int_{0}^{c} \phi_{0ml}^{L} \phi_{0ml}^{L} r dr dz$$

$$= 2\pi \int_{0}^{a} \int_{0}^{c} A_{0ml}^{2} \left( J_{0} \left( \frac{p_{0m}}{a} r \right) \sin \left( \frac{l\pi}{c} z \right) \right)^{2} r dr dz = 1$$
(4.48)

Based on eq. (4.46), the normalization constant for the vector wave function  $\vec{L}_{0ml}$  is then expressed as

$$A_{0ml} = \sqrt{\frac{\varepsilon_{0l}}{\pi c} \frac{1}{aJ_{0}(p_{0m})}} \tag{4.49}$$

### **4.2.2** Normalization of Vector Wave Function $\overrightarrow{M}_{nml}$

Based on eq. (2.61), the normalization of the vector wave function  $\overrightarrow{M}_{nml}$  is given by

$$\int_{0}^{a} \int_{0}^{2\pi} \int_{0}^{c} (\overrightarrow{M}_{nml} \cdot \overrightarrow{M}_{nml}) r dr d\varphi dz = 1$$
 (4.50)

Substituting eq. (4.39) into eq. (4.50), we have

$$B_{nml}^{2} \int_{0}^{a} \int_{0}^{2\pi c} \left[ \left( \frac{n}{r} J_{n} \left( \frac{p_{nm}}{a} r \right) \sin(n\varphi) \sin\left( \frac{l\pi}{c} z \right) \right)^{2} + \left( \frac{p_{nm}}{a} J_{n} \left( \frac{p_{nm}}{a} r \right) \cos(n\varphi) \sin\left( \frac{l\pi}{c} z \right) \right)^{2} \right] r dr d\varphi dz = 1$$

$$(4.51)$$

After integrating with respect to the variables z and  $\varphi$  in eq. (4.51), we obtain that

$$B_{nml}^2 \frac{2\pi c}{\varepsilon_{0n} \varepsilon_{0l}} \int_0^a \left[ \frac{n^2}{r} J_n^2 \left( \frac{p_{nm}}{a} r \right) + \left( \frac{p_{nm}}{a} \right)^2 J_n^2 \left( \frac{p_{nm}}{a} r \right) r \right] dr = 1$$
 (4.52)

Using the identities of the Bessel function of

$$J_{n+1}(x) = \frac{2n}{x} J_n(x) - J_{n-1}(x)$$
 (4.53)

$$xJ_{n}'(x) = xJ_{n-1}(x) - nJ_{n}(x)$$
(4.54)

$$J_{n}'(x) = \frac{1}{2} [J_{n-1}(x) - J_{n+1}(x)]$$
 (4.55)

we may obtain the following relations as

$$\frac{1}{x}J_n^2(x) = \frac{1}{2n}[J_n(x)J_{n+1}(x) + J_{n-1}(x)J_n(x)]$$
 (4.56)

$$xJ_n^{2}(x) = xJ_{n-1}^{2}(x) - \frac{3n}{2}J_{n-1}(x)J_n(x) + \frac{n}{2}J_n(x)J_{n+1}(x)$$
 (4.57)

After changing the integration variable, we can modify the integration in eq. (4.52) as

$$\int_{0}^{a} \left[ \frac{n^{2}}{r} J_{n}^{2} \left( \frac{p_{nm}}{a} r \right) + \left( \frac{p_{nm}}{a} \right)^{2} J_{n}^{2} \left( \frac{p_{nm}}{a} r \right) r \right] dr = \int_{0}^{p_{nm}} \left[ \frac{n^{2}}{r} J_{n}^{2}(r) + J_{n}^{2}(r) r \right] dr$$
(4.58)

Substituting eqs. (4.56) and (4.57) into eq. (4.58), we have

$$\int_{0}^{p_{nm}} \left[ \frac{n^{2}}{r} J_{n}^{2}(r) + J_{n}^{2}(r)r \right] dr = \int_{0}^{p_{nm}} [nJ_{n}(r)[J_{n+1}(r) - J_{n-1}(r)] + J_{n-1}^{2}(r)r] dr$$
 (4.59)

Based on eq. (4.55), eq. (4.59) can be expressed as

$$\int_{0}^{p_{nm'}} \left[ \frac{n^{2}}{r} J_{n}^{2}(r) + J_{n'}^{2}(r) r \right] dr = \int_{0}^{p_{nm'}} \left[ J_{n-1}^{2}(r) r - 2n J_{n}(r) J_{n'}(r) \right] dr$$

$$= \frac{p_{nm'}^{2}}{2} \left[ J_{n-1}^{2}(p_{nm'}) + \left( 1 - \left( \frac{n-1}{p_{nm'}} \right)^{2} \right) J_{n-1}^{2}(p_{nm'}) \right] - n J_{n}^{2}(p_{nm'})$$
(4.60)

where we have used the integration (4.45). Rearranging eq. (4.54) leads to

$$J_{n-1}(x) = J_n'(x) + \frac{n}{x}J_n(x)$$
 (4.61)

then we have

$$J_{n-1}(p_{nm'}) = J_{n'}(p_{nm'}) + \frac{n}{p_{nm}}J_{n}(p_{nm'}) = \frac{n}{p_{nm}}J_{n}(p_{nm'})$$
(4.62)

Using identities (4.53) and (4.54), we have

$$J_{n-1}'(x) = \frac{n-1}{x} J_{n-1}(x) - J_n(x)$$
 (4.63)

Hence,

$$J_{n-1}'(p_{nm}') = \frac{n-1}{p_{nm}} J_{n-1}(p_{nm}') - J_n(p_{nm}') = \frac{n(n-1) - p_{nm}'^2}{p_{nm}'^2} J_n(p_{nm}')$$
(4.64)

Substituting eqs. (4.62) and (4.64) into eq. (4.60) and after some manipulations we have

$$\int_{0}^{p_{nm}} \left[ \frac{n^{2}}{r} J_{n}^{2}(r) + J_{n}^{2}(r) r \right] dr = \frac{1}{2} (p_{nm}^{2} - n^{2}) J_{n}^{2}(p_{nm})$$
 (4.65)

Therefore, based on eqs. (4.52), (4.58) and (4.65), the normalization constant for the vector wave function  $\overrightarrow{M}_{nml}$  is given by

$$B_{nml} = \sqrt{\frac{\varepsilon_{0n}\varepsilon_{0l}}{\pi c}} \frac{1}{p_{nm}' \sqrt{1 - n^2/p_{nm}'^2} J_n(p_{nm}')}$$
(4.66)

When n = 0, the normalization of the vector wave function  $\overrightarrow{M}_{0ml}$  is given by

$$\int_{0}^{a} \int_{0}^{2\pi} \int_{0}^{c} M_{0ml\phi}^{2} r dr d\phi dz = 1$$
 (4.67)

because  $M_{0mlr} = 0$ . Equation (4.67) can then be expressed as

$$B_{0ml}^{2} \int_{0}^{a} \int_{0}^{2\pi} \int_{0}^{c} \left( \frac{p_{0m}}{a} J_{0} \left( \frac{p_{0m}}{a} r \right) \sin \left( \frac{l\pi}{c} z \right) \right)^{2} r dr d\phi dz = 1$$
 (4.68)

or

$$B_{0ml}^2 \frac{2\pi c}{\varepsilon_{0l}} \int_0^{p_{0m}} J_0^{'2}(r) r dr = 1$$
 (4.69)

It is noted that  $J_0'(r) = -J_1(r)$ , so based on the integration (4.45), the integration in eq. (4.69) is given by

$$\int_0^{p_{0m}} J_0^{2}(r) r dr = \int_0^{p_{0m}} J_1^2(r) r dr = \frac{p_{0m}^2}{2} J_1^2(p_{0m})$$
 (4.70)

Also using the identities (4.53) and (4.54), we have

$$J_{n+1}'(x) = J_n(x) - \frac{n}{x} J_{n+1}(x)$$
 (4.71)

that is,

$$J_1'(p_{0m}') = J_0(p_{0m}') (4.72)$$

and the normalization constant for the vector wave function  $\overrightarrow{M}_{0ml}$  is given by

$$B_{0ml} = \sqrt{\frac{\varepsilon_{0l}}{\pi c}} \frac{1}{p_{0m} J_0(p_{0m})}$$
 (4.73)

## 4.2.3 Normalization of Vector Wave Function $\vec{N}_{nml}$

Based on the definition of the vector wave function  $\vec{N}_{nml}$  eq. (2.64), the normalization of the vector wave function  $\vec{N}_{nml}$  is given by

$$\int_0^a \int_0^{2\pi} \int_0^c (\vec{N}_{nml} \cdot \vec{N}_{nml}) r dr d\phi dz = 1$$
 (4.74)

Substituting eq. (4.40) into eq. (4.74), we have

$$\frac{C_{nml}^2}{k_{nml}^2} \int_0^a \int_0^c \left[ \left( \frac{p_{nm}}{a} \frac{l\pi}{c} J_n \left( \frac{p_{nm}}{a} r \right) \cos(n\varphi) \sin\left( \frac{l\pi}{c} z \right) \right)^2 + \left( \frac{n l\pi}{r} J_n \left( \frac{p_{nm}}{a} r \right) \right)^2 + \left( \sin(n\varphi) \sin\left( \frac{l\pi}{c} z \right) \right)^2 + \left( \left( \frac{p_{nm}}{a} \right)^2 J_n \left( \frac{p_{nm}}{a} r \right) \cos(n\varphi) \cos\left( \frac{l\pi}{c} z \right) \right)^2 \right] r dr d\varphi dz = 1$$
(4.75)

After integrating with respect to the variables z and  $\varphi$ , changing the integration variables, we can modify eq. (4.75) as

$$\frac{C_{nml}^2}{k_{nml}^2} \frac{2\pi c}{\varepsilon_{0n} \varepsilon_{0l}} \int_0^{p_{nm}} \left[ \left( \frac{l\pi}{c} J_n'(r) \right)^2 r + \frac{n^2}{r} \left( \frac{l\pi}{c} J_n(r) \right)^2 + \left( \frac{p_{nm}}{a} J_n(r) \right)^2 r \right] dr = 1$$
 (4.76)

Using eq. (4.60), we can derive the integration of the first two terms in eq. (4.76) as

$$\int_{0}^{p_{nm}} \left[ \frac{n^{2}}{r} J_{n}^{2}(r) + J_{n}^{2}(r) r \right] dr$$

$$= \frac{p_{nm}^{2}}{2} \left[ J_{n-1}^{2}(p_{nm}) + \left( 1 - \left( \frac{n-1}{p_{nm}} \right)^{2} \right) J_{n-1}^{2}(p_{nm}) \right] - n J_{n}^{2}(p_{nm})$$
(4.77)

Using eqs. (4.54) and (4.63), we have the following relations as

$$J_{n-1}(p_{nm}) = J_n'(p_{nm}) + \frac{n}{x}J_n(p_{nm}) = J_n'(p_{nm})$$
 (4.78)

$$J_{n-1}'(p_{nm}) = \frac{n-1}{p_{nm}} J_{n-1}(p_{nm}) - J_n(p_{nm}) = \frac{n-1}{p_{nm}} J_n'(p_{nm})$$
(4.79)

Hence, based on eqs. (4.78) and (4.79), and after some manipulations, we may rewrite eq. (4.77) as

$$\int_{0}^{p_{nm}} \left[ \frac{n^{2}}{r} J_{n}^{2}(r) + J_{n}^{2}(r) r \right] dr = \frac{p_{nm}}{2} J_{n}^{2}(p_{nm})$$
 (4.80)

Based on eq. (4.45), the remaining part of the integration in eq. (4.76) can be derived as

$$\int_{0}^{p_{nm}} r J_{n}^{2}(r) dr = \frac{p_{nm}^{2}}{2} J_{n}^{2}(p_{nm})$$
 (4.81)

Substituting eqs. (4.80) and (4.81) into eq. (4.76), we have

$$C_{nml}^2 \frac{\pi c}{\varepsilon_{0n} \varepsilon_{0l}} p_{nm}^2 J_n^2(p_{nm}) = 1$$
 (4.82)

Therefore, the normalization constant for the vector wave function  $\overrightarrow{N}_{nml}$  is expressed as

$$C_{nml} = \sqrt{\frac{\varepsilon_{0n}\varepsilon_{0l}}{\pi c}} \frac{1}{p_{nm}J_n'(p_{nm})}$$
(4.83)

When n = 0, the normalization constant of the vector wave function  $\overrightarrow{N}_{0ml}$  is given by

$$\frac{C_{0ml}^2}{k_{0ml}^2} \int_0^a \int_0^{2\pi} \int_0^c \left[ \left( \frac{p_{0m}}{a} \frac{l\pi}{c} J_0 \left( \frac{p_{0m}}{a} r \right) \sin \left( \frac{l\pi}{c} z \right) \right)^2 + \left( \left( \frac{p_{0m}}{a} \right)^2 J_0 \left( \frac{p_{0m}}{a} r \right) \cos \left( \frac{l\pi}{c} z \right) \right)^2 \right] r dr d\phi dz = 1$$
(4.84)

After integrating with respect to the variables z and  $\varphi$ , changing the integration variable r, we have

$$\frac{C_{0ml}^2 2\pi c}{k_{0ml}^2} \int_0^{p_{0m}} \left[ \left( \frac{l\pi}{c} J_0'(r) \right)^2 r + \left( \frac{p_{0m}}{a} J_0(r) \right)^2 r \right] dr = 1$$
 (4.85)

Using eqs. (4.70) and (4.71), we have

$$\int_0^{p_{0m}} J_0^{2}(r) r dr = \int_0^{p_{0m}} J_1^2(r) r dr = \frac{p_{0m}^2}{2} J_1^2(p_{0m})$$
 (4.86)

Thus, based on eqs. (4.53) and (4.54) we obtain

$$J_{n+1}(x) = \frac{n}{r} J_n(x) - J_n'(x)$$
 (4.87)

Hence,

$$J_1(p_{0m}) = -J_0'(p_{0m}) (4.88)$$

and eq. (4.86) can be written as

$$\int_0^{p_{0m}} J_0^{2}(r) r dr = \frac{p_{0m}^2}{2} J_0^{2}(p_{0m})$$
 (4.89)

Using eq. (4.45) we have

$$\int_{0}^{p_{0m}} r J_0^2(r) dr = \frac{p_{0m}^2}{2} J_0^{2}(p_{0m})$$
 (4.90)

Substituting eqs. (4.89) and (4.90) into eq. (4.85), we obtain the normalization constant of the vector wave function  $\vec{N}_{0ml}$  as

$$C_{0ml} = \sqrt{\frac{\varepsilon_{0l}}{\pi c}} \frac{1}{p_{0m} J_0'(p_{0m})}$$
 (4.91)

## **4.2.4** Some Field Structures of Vector Wave Functions in Cylindrical Cavities

In this subsection, several electric field structures are plotted for the vector wave functions  $\vec{L}_{nml}$ ,  $\vec{M}_{nml}$  and  $\vec{N}_{nml}$ .

In the calculations, we assume the dimensions of the cylindrical cavity as: the radius a=0.0762m and the height c=0.15458m. In Figure 4.2 and Figure 4.3 we plot the electric field structures for the  $\vec{N}_{012}$  in the r-z plane with  $\phi=121^\circ$  and in the r- $\phi$  plane with z=0.0271m. We can identify that it is just the normal  $TM_{012}$  mode. In Figure 4.4 and Figure 4.5 the electric field structures for the  $\vec{M}_{111}$  are plotted in the r-z plane with  $\phi=121^\circ$  and in the r- $\phi$  plane with z=0.0271m. It is noted that this is the normal  $TE_{111}$  mode. The electric field structures for the  $\vec{L}_{112}$  are plotted in Figure 4.6 and Figure 4.7 in the r-z plane with  $\phi=121^\circ$  and in the r- $\phi$  plane with z=0.0271m.

So far we have obtained the normalized expressions for the vector wave functions

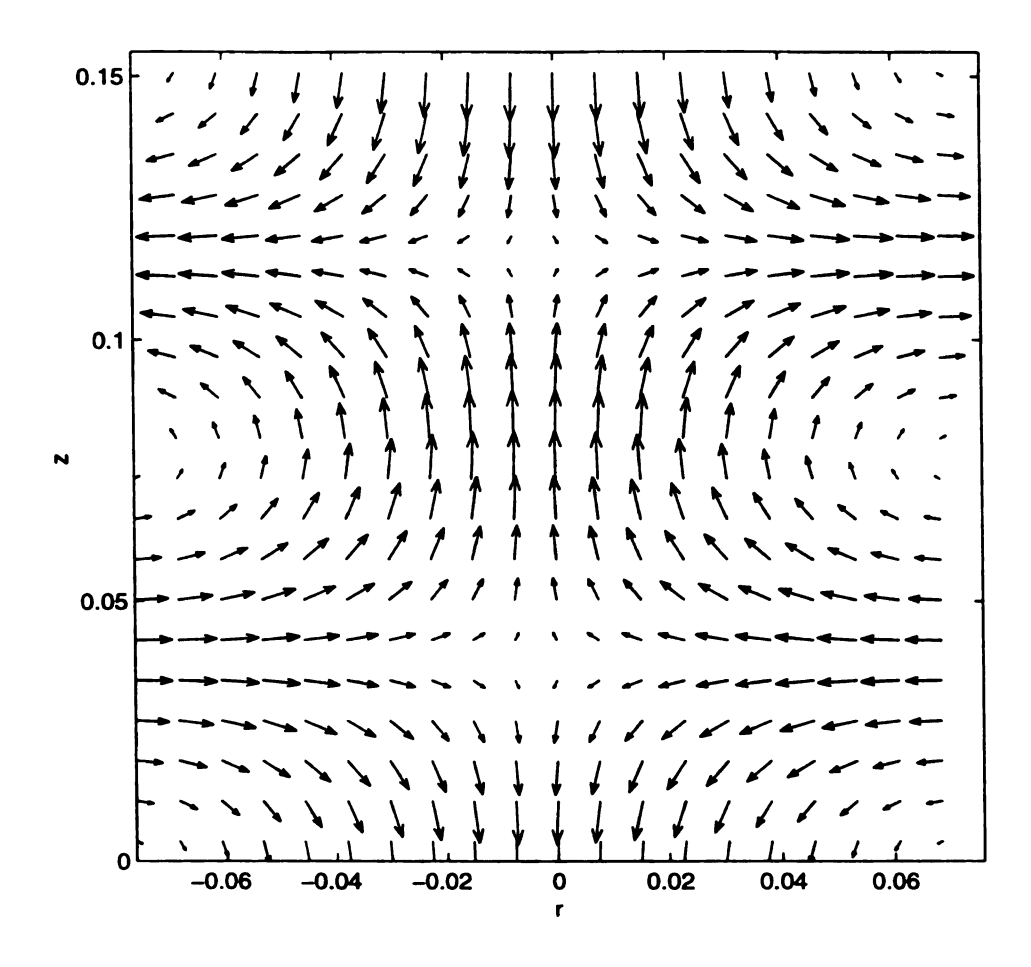


Figure 4.2 E-field structure of  $N_{012}$  in the r-z plane with  $\varphi = 121^{\circ}$ . The dimensions of the cylindrical cavity are a=0.0762m, c=0.15458m.

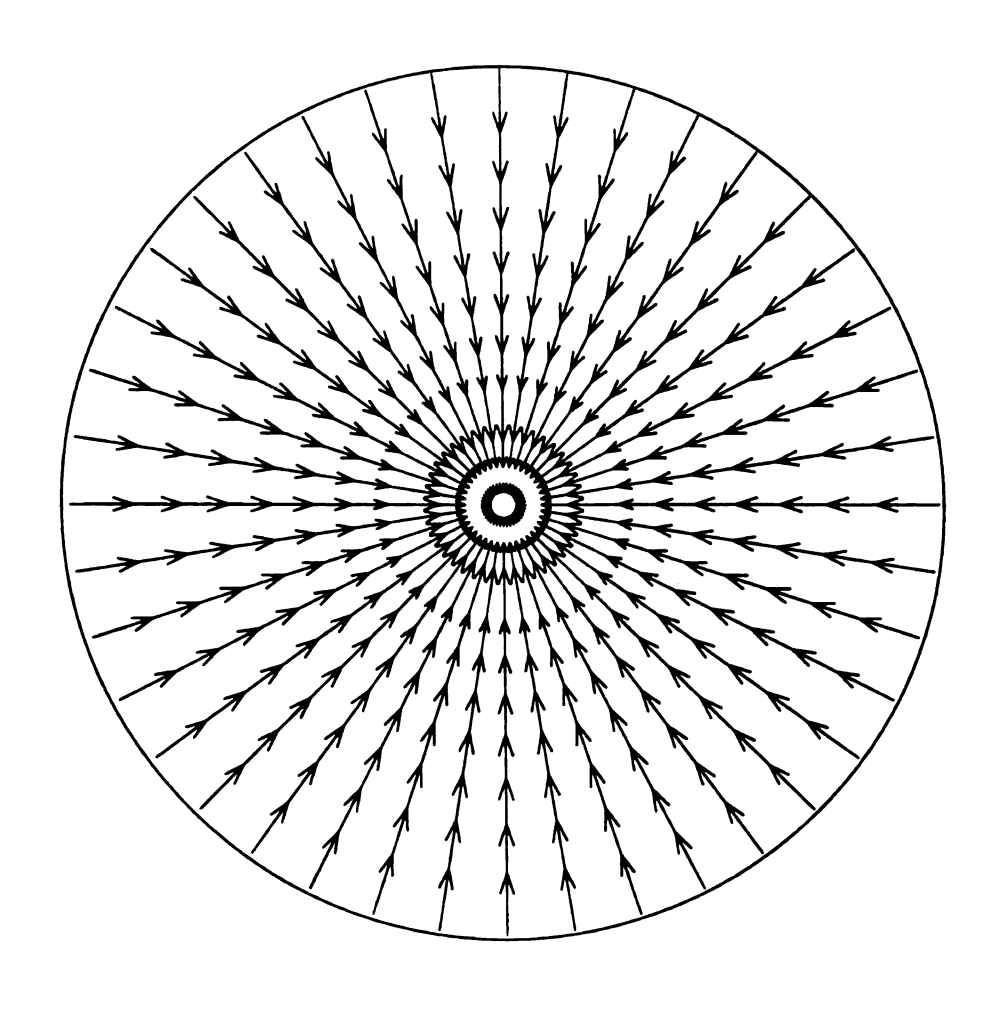


Figure 4.3 E-field structure of  $N_{012}$  in the r- $\phi$  plane with z=0.0271m. The dimensions of the cylindrical cavity are a=0.0762m, c=0.15458m.

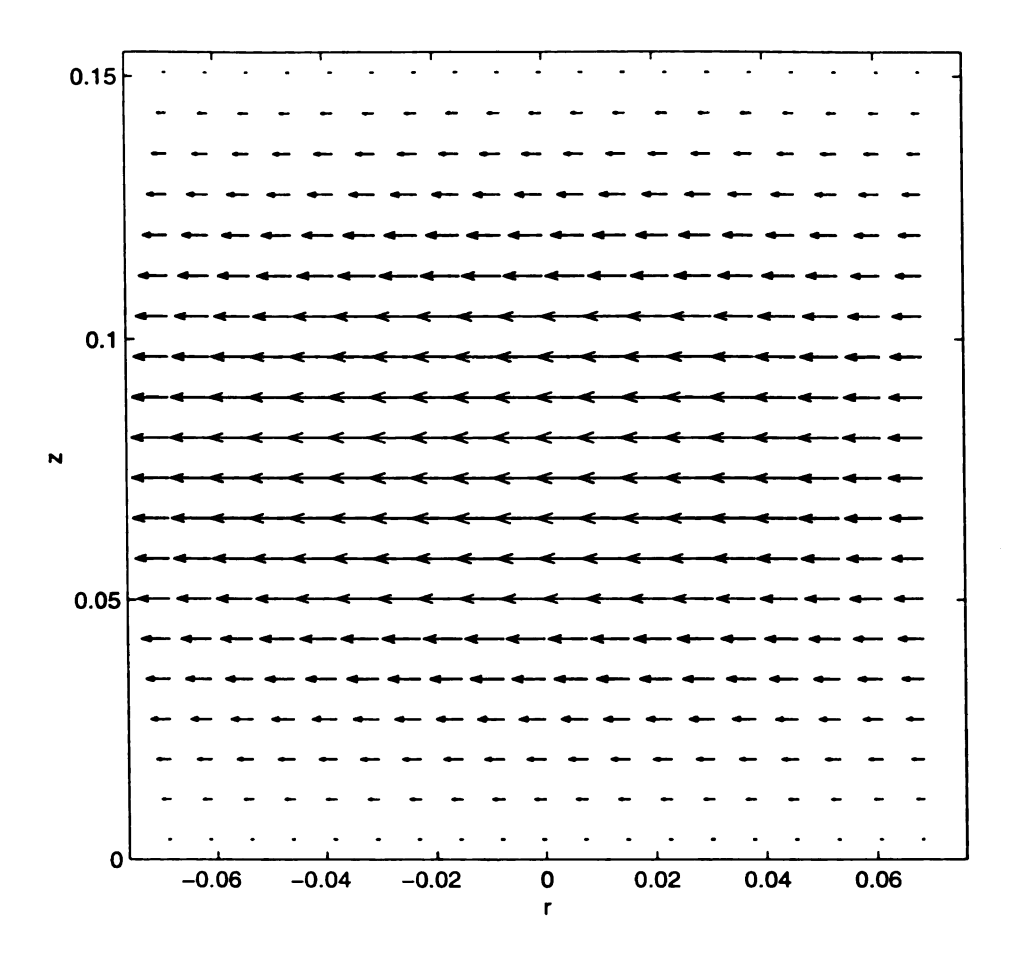


Figure 4.4 E-field structure of  $M_{111}$  in the r-z plane with  $\varphi = 121^{\circ}$  The dimensions of the cylindrical cavity are a=0.0762m, c=0.15458m.

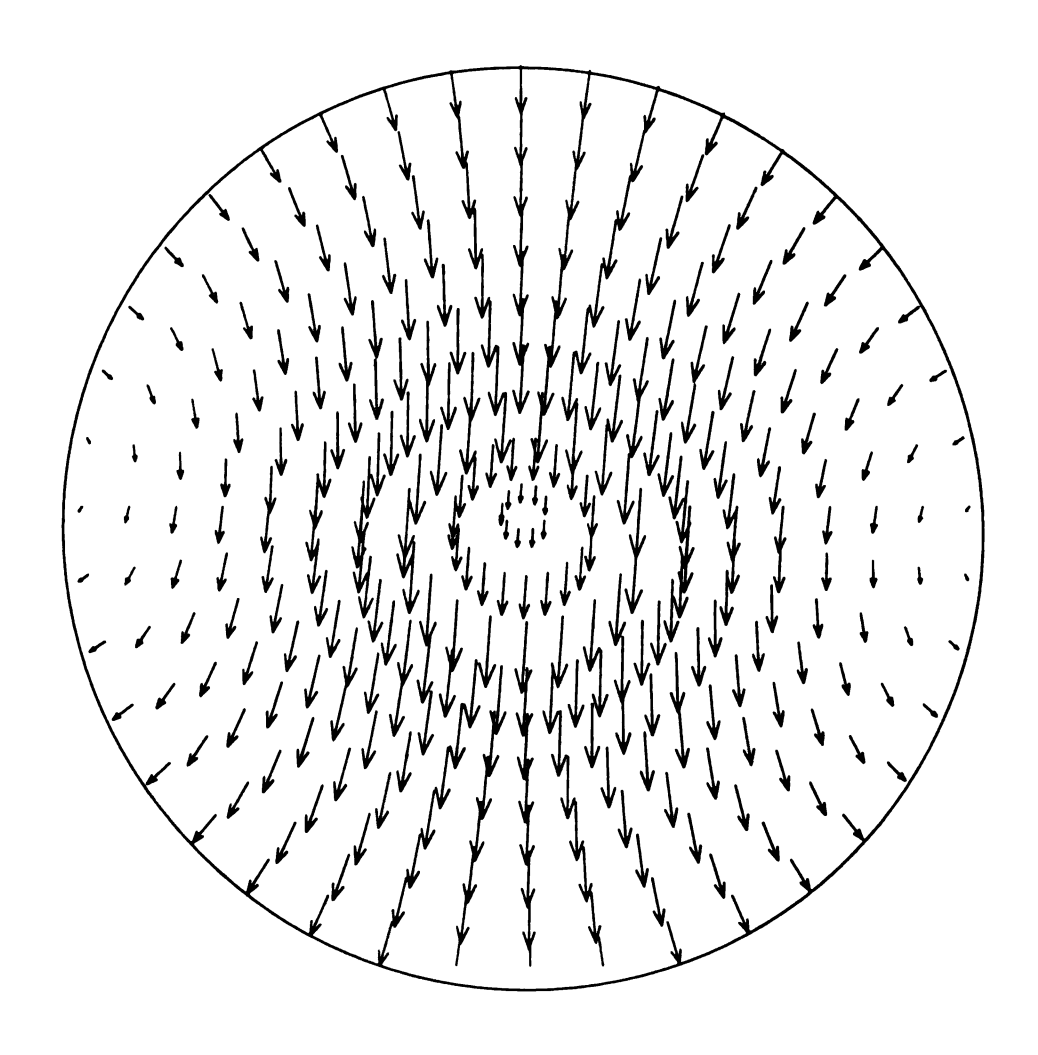


Figure 4.5 E-field structure of  $M_{111}$  in the r- $\phi$  plane with z=0.0271m. The dimensions of the cylindrical cavity are a=0.0762m, c=0.15458m.

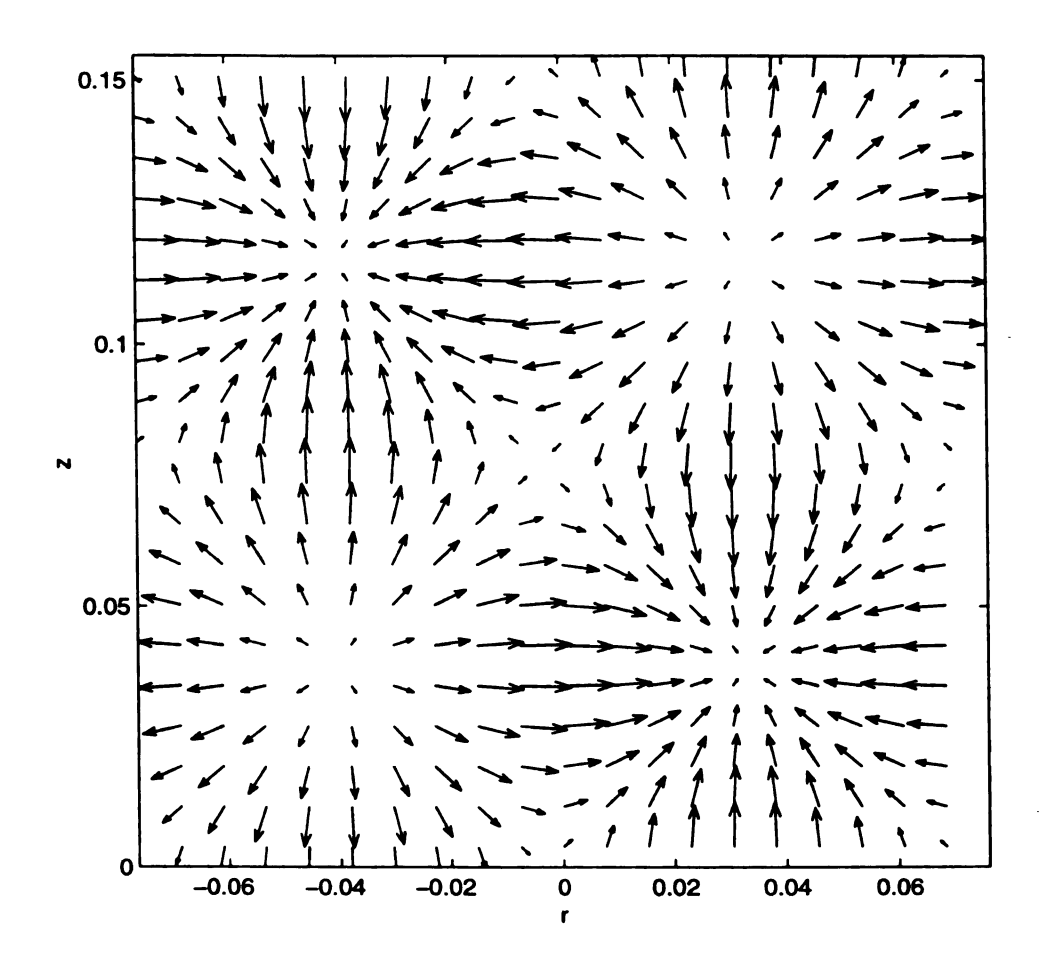


Figure 4.6 E-field structure of  $L_{112}$  in the r-z plane with  $\varphi = 121^{\circ}$  The dimensions of the cylindrical cavity are a=0.0762m, c=0.15458m.

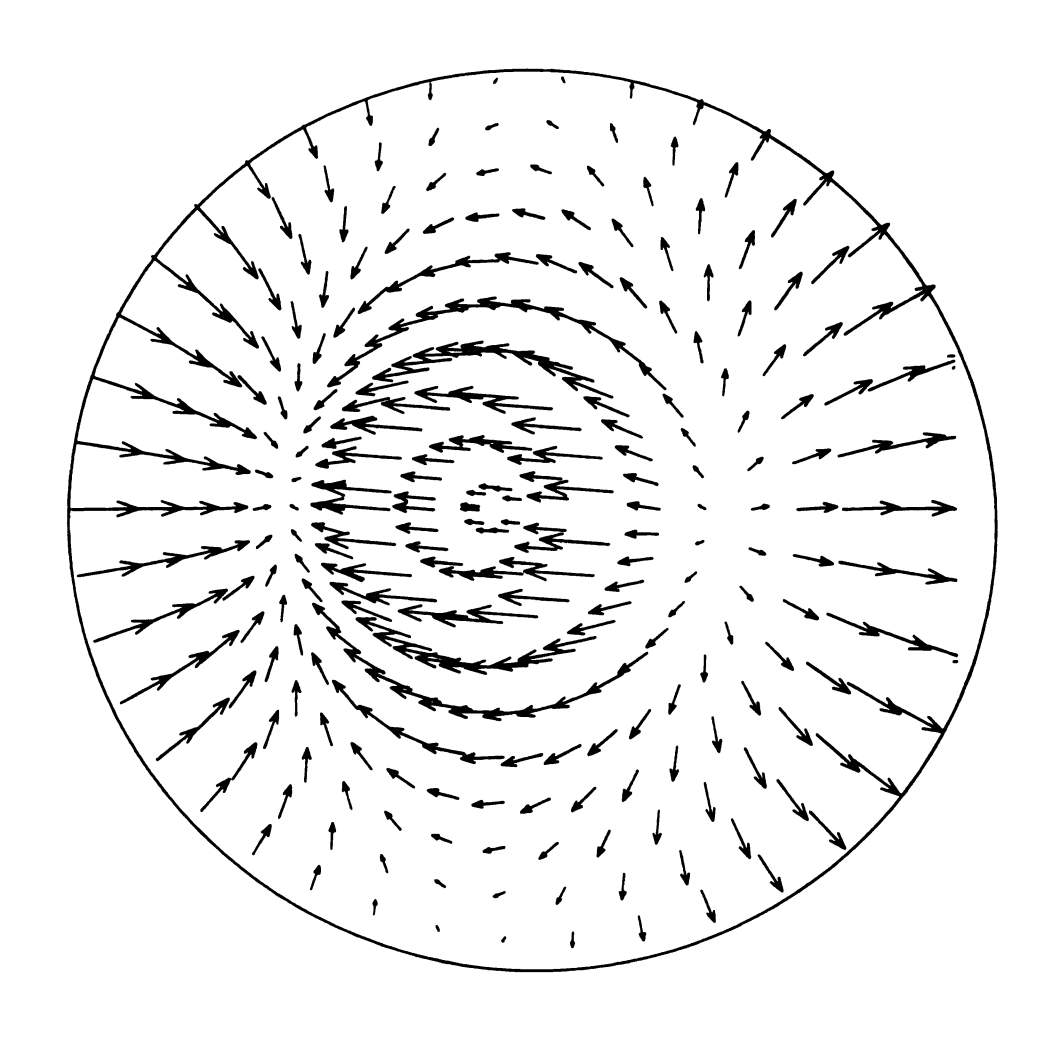


Figure 4.7 E-field structure of  $L_{112}$  in the r- $\phi$  plane with z=0.0271m. The dimensions of the cylindrical cavity are a=0.0762m, c=0.15458m.

 $\vec{L}_{nml}$ ,  $\vec{M}_{nml}$  and  $\vec{N}_{nml}$  in cylindrical cavities. They are orthogonal and form a complete set of basis functions based on the proofs given in Chapter 2. Therefore, they can be employed to express any unknown electric field inside the cylindrical cavity.

The Electric Field Integral Equation for a material sample which is placed in the cylindrical cavity can be obtained in the same way as that used in Chapter 2. We can also obtain the same *EFIE* as that expressed in the eq. (2.102) as

$$\vec{E}(\vec{r})\left(1 - \frac{j\omega\mu_0\tau_e}{k_0^2}\right) + j\omega\mu_0\int_{\nu}\tau_e(\vec{r}_0)\vec{E}(\vec{r}_0) \cdot \vec{G}_{eo}(\vec{r}_0, \vec{r})d\nu_0 = \vec{E}^i(\vec{r})$$
(4.92)

However, due to the different eigenvalues for the vector wave functions  $\overrightarrow{M}_{nml}$  and  $\overrightarrow{N}_{nml}$  in the cylindrical cavity as given in eqs. (4.22) and (4.34), the dyadic Green's function  $\overline{G}_{eo}(\overset{*}{r}_{0},\overset{*}{r})$  need to be modified from eq. (2.101) as

$$\overline{G}_{eo}(\mathring{r}_0, \mathring{r}) = \sum_{n} \left[ q_n^2 \frac{\overrightarrow{M}_n(\mathring{r}_0) \overrightarrow{M}_n(\mathring{r})}{k_0^2 (q_n^2 - k_0^2)} + k_n^2 \frac{\overrightarrow{N}_n(\mathring{r}_0) \overrightarrow{N}_n(\mathring{r})}{k_0^2 (k_n^2 - k_0^2)} \right]$$
(4.93)

for the cylindrical cavity and we need to give the detailed expression for the dyadic Green's function (4.93) in the cylindrical cavity in order to solve the *EFIE* (4.92) using the Galerkin's method.

#### 4.3 Dyadic Green's Function in the Cylindrical Cavity

In this section the detailed expression of the dyadic Green's function (4.93) in a cylindrical cavity will be derived. As in Chapter 3, the dyadic Green's function (4.93) is a triple summation over the cavity eigenfunctions and we can reduce it to a double

summation format based on the relations (3.27) and (3.28) in Chapter 3. Substituting the expressions for the vector wave functions  $\vec{M}_{nml}$  and  $\vec{N}_{nml}$  (4.39) and (4.40) and the normalization constants (4.66) and (4.83) into eq. (4.93), we can obtain the expressions for the different components of the dyadic Green's function  $\vec{G}_{eo}(\hat{r}_0, \hat{r})$  as follows:

1.  $\hat{r}\hat{r}$  component of the dyadic Green's function  $\overline{G}_{eo}(\hat{r}_0,\hat{r})$  in the triple summation format is given by:

$$G_{eorr}(\mathring{r}_{0},\mathring{r}) = \frac{1}{k_{0n}^{2}} \sum_{n=0}^{\infty} \sum_{m=1}^{\infty} \sum_{l=1}^{\infty} \frac{\varepsilon_{0n} \varepsilon_{0l}}{\pi c} \left[ \frac{q_{n}^{2}}{q_{n}^{2} - k_{0}^{2} (p_{nm})^{2} - n^{2}) J_{n}^{2} (p_{nm})} \frac{n^{2}}{r r'} J_{n} \left( \frac{p_{nm}}{a} r \right) \right]$$

$$J_{n} \left( \frac{p_{nm}}{a} r_{0} \right) + \frac{1}{k_{n}^{2} - k_{0}^{2}} \frac{1}{a^{2} J_{n}^{2} (p_{nm})} \left( \frac{l\pi}{c} \right)^{2} J_{n} \left( \frac{p_{nm}}{a} r \right) J_{n} \left( \frac{p_{nm}}{a} r_{0} \right) \right]$$

$$\cos(n\varphi) \cos(n\varphi_{0}) \sin\left( \frac{l\pi}{c} z \right) \sin\left( \frac{l\pi}{c} z_{0} \right)$$

$$(4.94)$$

Equation (4.22) gives the eigenvalue  $q_n^2$  of the vector wave function  $\overrightarrow{M}_{nml}$ , and the first summation term in eq. (4.94) is then split into two parts as:

$$\frac{1}{k_{0n}^{2}} \sum_{n=0}^{\infty} \sum_{m=1}^{\infty} \sum_{l=1}^{\infty} \frac{\varepsilon_{0n} \varepsilon_{0l}}{\pi c} \frac{q_{n}^{2}}{q_{n}^{2} - k_{0}^{2} (p_{nm'}^{2} - n^{2}) J_{n}^{2} (p_{nm'}^{2})} \frac{n^{2}}{r r'} J_{n} \left(\frac{p_{nm}}{a} r\right) 
J_{n} \left(\frac{p_{nm}}{a} r_{0}\right) \cos(n\phi) \cos(n\phi_{0}) \sin\left(\frac{l\pi}{c}z\right) \sin\left(\frac{l\pi}{c}z_{0}\right) 
= \frac{1}{k_{0n}^{2}} \sum_{n=0}^{\infty} \sum_{m=1}^{\infty} \sum_{l=1}^{\infty} \frac{\varepsilon_{0n} \varepsilon_{0l}}{\pi c} \left[\frac{\left(\frac{p_{nm}}{a}\right)^{2}}{q_{n}^{2} - k_{0}^{2}} + \frac{\left(\frac{l\pi}{c}\right)^{2}}{q_{n}^{2} - k_{0}^{2}}\right] \frac{1}{(p_{nm'}^{2} - n^{2}) J_{n}^{2} (p_{nm'}^{2})} \frac{n^{2}}{r r_{0}} 
J_{n} \left(\frac{p_{nm'}}{a} r\right) J_{n} \left(\frac{p_{nm'}}{a} r_{0}\right) \cos(n\phi) \cos(n\phi_{0}) \sin\left(\frac{l\pi}{c}z\right) \sin\left(\frac{l\pi}{c}z_{0}\right)$$
(4.95)

Using the relation (3.27) in Chapter 3, the first term in the summation (4.95) can be summed over the index l as

$$\sum_{l=1}^{\infty} \frac{\varepsilon_{0l} \left(\frac{p_{nm}}{a}\right)^2}{c q_n^2 - k_0^2} \sin\left(\frac{l\pi}{c}z\right) \sin\left(\frac{l\pi}{c}z_0\right) = \left(\frac{p_{nm}}{a}\right)^2 \frac{f_1(z, z_0)}{k_{g1} \sin(k_{g1}c)}$$
(4.96)

where

$$k_{g1} = \sqrt{k_0^2 - \left(\frac{p_{nm}'}{a}\right)^2} \tag{4.97}$$

$$f_1(z, z_0) = \sin(k_{g1}(c - z_b))\sin(k_{g1}z_s)$$
 (4.98)

and it is convenient to define the following (they will be used later for the same definition):

$$z_h \equiv the \ greater \ of \ z \ or \ z_0$$
 (4.99)

$$z_s \equiv the \ lesser \ of \ z \ or \ z_0$$
 (4.100)

Also in [21] it gives

$$\sum_{l=1}^{\infty} \frac{\varepsilon_{0l} \left(\frac{l\pi}{c}\right)^2}{c^2 q_n^2 - k_0^2} \sin\left(\frac{l\pi}{c}z\right) \sin\left(\frac{l\pi}{c}z_0\right)$$

$$= \frac{\partial^2}{\partial z^2} \sum_{l=1}^{\infty} \frac{\varepsilon_{0l}}{c} \frac{1}{q_n^2 - k_0^2} \sin\left(\frac{l\pi}{c}z\right) \sin\left(\frac{l\pi}{c}z_0\right) = \frac{k_{g1} f_1(z, z_0)}{\sin(k_{g1}c)} - \delta(z - z_0)$$
(4.101)

Thus, based on eq. (4.101), we can obtain the closed form evaluation of the summation over index l for the second term of the summation (4.95).

The other terms in the summation (4.94) can be summed over the index l in the same way. So after some algebraic manipulations, we obtain the double summation format

of the  $\hat{r}\hat{r}$  component of the dyadic Green's function  $\overline{G}_{eo}(\hat{r}',\hat{r})$  as

$$G_{eorr}(\dot{r}_{0}, \dot{r}) = \frac{1}{k_{0n}^{2}} \sum_{n=0}^{\infty} \sum_{m=1}^{\infty} \frac{\varepsilon_{0n}}{\pi} \left[ \frac{1}{(p_{nm}^{2} - n^{2})J_{n}^{2}(p_{nm}^{2})} \frac{n^{2}}{rr'} J_{n} \left( \frac{p_{nm}}{a} r \right) J_{n} \left( \frac{p_{nm}}{a} r_{0} \right) \right]$$

$$\frac{k_{0}^{2}}{k_{g1} \sin(k_{g1}c)} f_{1}(z, z_{0}) + \frac{1}{a^{2}J_{n}^{2}(p_{nm})} J_{n} \left( \frac{p_{nm}}{a} r \right) J_{n} \left( \frac{p_{nm}}{a} r_{0} \right) \frac{k_{g2}f_{2}(z, z_{0})}{\sin(k_{g2}c)}$$

$$\cos(n\varphi) \cos(n\varphi_{0}) - \frac{1}{k_{0n}^{2}} \sum_{n=0}^{\infty} \sum_{m=1}^{\infty} \frac{\varepsilon_{0n}}{\pi} \left[ \frac{1}{(p_{nm}^{2} - n^{2})J_{n}^{2}(p_{nm}^{2})} \frac{n^{2}}{rr'} J_{n} \left( \frac{p_{nm}}{a} r \right) \right]$$

$$J_{n} \left( \frac{p_{nm}}{a} r_{0} \right) + \frac{1}{a^{2}J_{n}^{2}(p_{nm})} J_{n} \left( \frac{p_{nm}}{a} r \right) J_{n} \left( \frac{p_{nm}}{a} r_{0} \right) \right] \cos(n\varphi) \cos(n\varphi_{0}) \delta(z - z_{0})$$

$$(4.102)$$

where

$$k_{g2} = \sqrt{k_0^2 - \left(\frac{p_{nm}}{a}\right)^2} \tag{4.103}$$

and

$$f_2(z, z_0) = \sin(k_{g2}(c - z_b))\sin(k_{g2}z_s)$$
 (4.104)

2.  $\hat{\varphi}\hat{\varphi}$  component of the dyadic Green's function  $\overline{G}_{eo}(\hat{r}_0, \hat{r})$  in the triple summation format is given by:

$$G_{eo\phi\phi}(\vec{r}_{0}, \vec{r}) = \frac{1}{k_{0n}^{2}} \sum_{n=0}^{\infty} \sum_{m=1}^{\infty} \sum_{l=1}^{\infty} \frac{\varepsilon_{0n} \varepsilon_{0l}}{\pi c} \left[ \frac{q_{n}^{2}}{q_{n}^{2} - k_{0}^{2} (p_{nm}'^{2} - n^{2}) J_{n}^{2} (p_{nm}')} J_{n}' \left( \frac{p_{nm}}{a} r \right) \right]$$

$$J_{n}' \left( \frac{p_{nm}}{a} r_{0} \right) + \frac{1}{k_{n}^{2} - k_{0}^{2} p_{nm}^{2} J_{n}'^{2} (p_{nm})} \frac{n^{2}}{r r'} J_{n} \left( \frac{p_{nm}}{a} r \right) J_{n} \left( \frac{p_{nm}}{a} r_{0} \right) \right] \sin(n\phi)$$

$$\sin(n\phi_{0}) \sin\left( \frac{l\pi}{c} z \right) \sin\left( \frac{l\pi}{c} z_{0} \right)$$

$$(4.105)$$

Applying the same procedure used for  $\hat{r}\hat{r}$  component to the summation (4.105), we obtain the double summation format for the  $\hat{\varphi}\hat{\varphi}$  component as

$$G_{eo\phi\phi}(\overset{>}{r}_{0},\overset{>}{r}) = \frac{1}{k_{0n}^{2}} \sum_{n=0}^{\infty} \sum_{m=1}^{\infty} \frac{\varepsilon_{0n}}{\pi} \left[ \frac{\left(\frac{p_{nm}}{a}\right)^{2}}{(p_{nm}^{2} - n^{2})J_{n}^{2}(p_{nm}^{2})} J_{n}^{2} \left(\frac{p_{nm}}{a}r\right) J_{n}^{2} \left(\frac{p_{nm}}{a}r\right) \right]$$

$$\frac{k_{0}^{2}f_{1}(z,z_{0})}{k_{g1}\sin(k_{g1}c)} + \frac{1}{p_{nm}^{2}J_{n}^{2}(p_{nm})} \frac{n^{2}}{r^{r}} J_{n}^{2} \left(\frac{p_{nm}}{a}r\right) J_{n}^{2} \left(\frac{p_{nm}}{a}r\right) J_{n}^{2} \left(\frac{p_{nm}}{a}r\right) \frac{k_{g2}f_{2}(z,z_{0})}{\sin(k_{g2}c)} \sin(n\phi)$$

$$\sin(n\phi_{0}) - \frac{1}{k_{0n}^{2}} \sum_{n=0}^{\infty} \sum_{m=1}^{\infty} \frac{\varepsilon_{0n}}{\pi} \left[ \frac{\left(\frac{p_{nm}}{a}\right)^{2}}{(p_{nm}^{2} - n^{2})J_{n}^{2}(p_{nm}^{2})} J_{n}^{2} \left(\frac{p_{nm}}{a}r\right) J_{n}^{2} \left(\frac{p_{nm}}{a}r\right) \right]$$

$$+ \frac{1}{p_{nm}^{2}J_{n}^{2}(p_{nm})} \frac{n^{2}}{r^{r}} J_{n}^{2} \left(\frac{p_{nm}}{a}r\right) J_{n}^{2} \left(\frac{p_{nm}}{a}r\right) \int_{n}^{\infty} \sin(n\phi) \sin(n\phi_{0}) \delta(z-z_{0})$$

3.  $\hat{r}\hat{\varphi}$  component of the dyadic Green's function  $\overline{G}_{eo}(\hat{r}_0,\hat{r})$  in the triple summation format is given by:

$$G_{eor\phi}(\dot{r}_{0}, \dot{r}) = -\frac{1}{k_{0n}^{2}} \sum_{n=0}^{\infty} \sum_{m=1}^{\infty} \sum_{l=1}^{\infty} \frac{\varepsilon_{0n} \varepsilon_{0l}}{\pi c} \left[ \frac{q_{n}^{2}}{q_{n}^{2} - k_{0}^{2} (p_{nm}^{2} - n^{2}) J_{n}^{2} (p_{nm}^{2})} J_{n} \left( \frac{p_{nm}}{a} r \right) + \frac{1}{k_{n}^{2} - k_{0}^{2} p_{nm}^{2} J_{n}^{2} (p_{nm}^{2})} \frac{\left( \frac{l\pi}{c} \right)^{2} P_{nm}}{a} \frac{n}{r} J_{n} \left( \frac{p_{nm}}{a} r \right) J_{n} \left( \frac{p_{nm}}{a} r_{0} \right) \right] \cos(n\phi) \sin(n\phi_{0})$$

$$\sin\left(\frac{l\pi}{c}z\right) \sin\left(\frac{l\pi}{c}z_{0}\right)$$

The double summation format of the  $\hat{r}\hat{\varphi}$  component is then expressed as

$$G_{eor\phi}(\overset{*}{r}_{0},\overset{*}{r}) = -\frac{1}{k_{0n}^{2}} \sum_{n=0}^{\infty} \sum_{m=1}^{\infty} \frac{\varepsilon_{0n}}{\pi} \left[ \frac{\frac{p_{nm}'n}{a'r}}{(p_{nm}'^{2} - n^{2})J_{n}^{2}(p_{nm}')} J_{n} \left( \frac{p_{nm}'}{a'r} \right) J_{n}' \left( \frac{p_{nm}'}{a} r_{0} \right) \right]$$

$$\frac{k_{0}^{2} f_{1}(z, z_{0})}{k_{g1} \sin(k_{g1}c)} + \frac{\frac{p_{nm}n}{a'r'}}{p_{nm}^{2} J_{n}'^{2}(p_{nm})} J_{n}' \left( \frac{p_{nm}}{a'r} \right) J_{n} \left( \frac{p_{nm}}{a'r} \right) J_{n} \left( \frac{p_{nm}}{a'r} r_{0} \right) \frac{k_{g2} f_{2}(z, z_{0})}{\sin(k_{g2}c)} \cos(n\phi)$$

$$\sin(n\phi_{0}) + \frac{1}{k_{0n}^{2}} \sum_{n=0}^{\infty} \sum_{m=1}^{\infty} \frac{\varepsilon_{0n}}{\pi} \left[ \frac{\frac{p_{nm}'n}}{(p_{nm}'^{2} - n^{2})J_{n}^{2}(p_{nm}')} J_{n} \left( \frac{p_{nm}'}{a'r} \right) J_{n}' \left( \frac{p_{nm}'r}{a} r_{0} \right) + \frac{\frac{p_{nm}n}n}{a'r'} J_{n}' \left( \frac{p_{nm}}{a'r} r_{0} \right) J_{n} \left( \frac{p_{nm}n}{a'r'} r_{0} \right) \right] \cos(n\phi) \sin(n\phi_{0}) \delta(z - z_{0})$$

4. Similarly, the  $\hat{\phi}\hat{r}$  component of the dyadic Green's function  $\overline{G}_{eo}(\hat{r}_0, \hat{r})$  in the double summation format is given by:

$$G_{eo\varphi r}(\overset{*}{r}_{0},\overset{*}{r}) = -\frac{1}{k_{0}^{2}} \sum_{n=0}^{\infty} \sum_{m=1}^{\infty} \frac{\varepsilon_{0n}}{\pi} \left[ \frac{\frac{p_{nm}'n}{a} r_{0}}{(p_{nm}'^{2} - n^{2}) J_{n}^{2}(p_{nm}')} J_{n}(\frac{p_{nm}'r}{a}) J_{n}(\frac{p_{nm}'r}{a}) J_{n}(\frac{p_{nm}'r}{a}) \right]$$

$$\frac{k_{0}^{2} f_{1}(z, z_{0})}{k_{g1} \sin(k_{g1}c)} + \frac{\frac{p_{nm}n}{a} r}{p_{nm}^{2} J_{n}^{2}(p_{nm})} J_{n}(\frac{p_{nm}}{a}r) J_{n}(\frac{p_{nm}}{a}r_{0}) \frac{k_{g2} f_{2}(z, z_{0})}{\sin(k_{g2}c)} \sin(n\varphi)$$

$$\cos(n\varphi_{0}) + \frac{1}{k_{0}^{2}} \sum_{n=0}^{\infty} \sum_{m=1}^{\infty} \frac{\varepsilon_{0n}}{\pi} \left[ \frac{\frac{p_{nm}'n}{a} r_{0}}{(p_{nm}'^{2} - n^{2}) J_{n}^{2}(p_{nm}')} J_{n}(\frac{p_{nm}'r}{a}r) J_{n}(\frac{p_{nm}'r}{a}r_{0}) + \frac{\frac{p_{nm}n}{a} r_{0}}{p_{nm}^{2} J_{n}^{2}(p_{nm})} J_{n}(\frac{p_{nm}}{a}r_{0}) \right]$$

$$+ \frac{\frac{p_{nm}n}{a} r}{p_{nm}^{2} J_{n}^{2}(p_{nm})} J_{n}(\frac{p_{nm}}{a}r) J_{n}(\frac{p_{nm}}{a}r_{0}) \sin(n\varphi) \cos(n\varphi_{0}) \delta(z - z_{0})$$

5.  $\hat{z}\hat{z}$  component of the dyadic Green's function  $\overline{G}_{eo}(r_0, r)$  in the triple summation format

is given by

$$G_{eozz}(\hat{r}_{0}, \hat{r}) = \frac{1}{k_{0n}^{2}} \sum_{n=0}^{\infty} \sum_{m=1}^{\infty} \sum_{l=0}^{\infty} \frac{\varepsilon_{0n} \varepsilon_{0l}}{\pi c} \frac{1}{k_{n}^{2} - k_{0}^{2}} \frac{\left(\frac{p_{nm}}{a}\right)^{2}}{a^{2} J_{n}^{2} (p_{nm})} J_{n}\left(\frac{p_{nm}}{a}r\right)$$

$$J_{n}\left(\frac{p_{nm}}{a}r_{0}\right) \cos(n\varphi) \cos(n\varphi_{0}) \cos\left(\frac{l\pi}{c}z\right) \cos\left(\frac{l\pi}{c}z_{0}\right)$$
(4.110)

Applying the relation (3.28) in Chapter 3 to the summation (4.110), we obtain the double summation format for the  $\hat{z}\hat{z}$  component as

$$G_{eozz}(\hat{r}_{0}, \hat{r}) = -\frac{1}{k_{0n}^{2}} \sum_{n=0}^{\infty} \sum_{m=1}^{\infty} \frac{\varepsilon_{0n}}{\pi} \frac{\left(\frac{p_{nm}}{a}\right)^{2}}{a^{2} J_{n}^{2}(p_{nm})} J_{n}\left(\frac{p_{nm}}{a}r\right) J_{n}\left(\frac{p_{nm}}{a}r_{0}\right)$$

$$\cos(n\varphi)\cos(n\varphi_{0}) \frac{g_{2}(z, z_{0})}{k_{g2}\sin(k_{g2}c)}$$
(4.111)

where

$$g_2(z, z_0) = \cos(k_{g2}(c - z_b))\cos(k_{g2}z_s)$$
 (4.112)

6.  $\hat{r}\hat{z}$  component of the dyadic Green's function  $\overline{G}_{eo}(\hat{r}_0,\hat{r})$  in the triple summation format is given by

$$G_{eorz}(\dot{r}_0, \dot{r}) = \frac{1}{k_{0n}^2} \sum_{n=0}^{\infty} \sum_{m=1}^{\infty} \sum_{l=1}^{\infty} \frac{\varepsilon_{0n} \varepsilon_{0l}}{\pi c} \frac{1}{k_n^2 - k_0^2} \frac{\frac{p_{nm} l\pi}{a} \frac{l\pi}{c}}{a^2 J_n^{2}(p_{nm})} J_n(\frac{p_{nm}}{a} r)$$

$$J_n(\frac{p_{nm}}{a} r_0) \cos(n\varphi) \cos(n\varphi_0) \sin(\frac{l\pi}{c} z) \cos(\frac{l\pi}{c} z_0)$$

$$(4.113)$$

In [21], it gives

$$\sum_{l=1}^{\infty} \frac{\varepsilon_{0l}}{c} \frac{1}{k_n^2 - k_0^2} \frac{l\pi}{c} \sin\left(\frac{l\pi}{c}z\right) \cos\left(\frac{l\pi}{c}z_0\right)$$

$$= \frac{\partial}{\partial z} \sum_{l=0}^{\infty} \frac{\varepsilon_{0l}}{c} \frac{1}{k_n^2 - k_0^2} \cos\left(\frac{l\pi}{c}z\right) \cos\left(\frac{l\pi}{c}z_0\right)$$

$$= \frac{1}{\sin(k_{g2}c)} f_{g2}(z, z_0)$$
(4.114)

where

$$f_{g2}(z, z_0) = \begin{cases} \sin(k_{g2}(c-z))\cos(k_{g2}z_0) & z > z_0 \\ -\sin(k_{g2}z)\cos(k_{g2}(c-z_0)) & z < z_0 \end{cases}$$
(4.115)

The double summation format for the  $\hat{r}\hat{z}$  component is then given by

$$G_{eorz}(\dot{r}_{0}, \dot{r}) = \frac{1}{k_{0n=0}^{2}} \sum_{m=1}^{\infty} \sum_{m=1}^{\infty} \frac{\varepsilon_{0n}}{\pi} \frac{\frac{p_{nm}}{a}}{a^{2} J_{n}^{2}(p_{nm})} J_{n}(\frac{p_{nm}}{a}r)$$

$$J_{n}(\frac{p_{nm}}{a}r_{0}) \cos(n\varphi) \cos(n\varphi_{0}) \frac{f_{g2}(z, z_{0})}{\sin(k_{g2}c)}$$
(4.116)

7. Similarly, the  $\hat{z}\hat{r}$  component of the dyadic Green's function  $\overline{G}_{eo}(\hat{r}',\hat{r})$  in the double summation format is given by

$$G_{eozr}(\mathring{r}_{0},\mathring{r}) = \frac{1}{k_{0n}^{2}} \sum_{n=0}^{\infty} \sum_{m=1}^{\infty} \frac{\varepsilon_{0n}}{\pi} \frac{\frac{p_{nm}}{a}}{a^{2} J_{n}^{2}(p_{nm})} J_{n}(\frac{p_{nm}}{a}r)$$

$$J_{n}(\frac{p_{nm}}{a}r_{0}) \cos(n\varphi) \cos(n\varphi_{0}) \frac{f_{g1}(z,z_{0})}{\sin(k_{g2}c)}$$
(4.117)

where

$$f_{g1}(z, z_0) = \begin{cases} -\cos(k_{g2}(c-z))\sin(k_{g2}z_0) & z > z_0\\ \cos(k_{g2}z)\sin(k_{g2}(c-z_0)) & z < z_0 \end{cases}$$
(4.118)

8.  $\hat{\varphi}\hat{z}$  component of the dyadic Green's function  $\overline{G}_{eo}(\mathring{r}_0,\mathring{r})$  in the triple summation format is given by

$$G_{eo\varphi z}(\hat{r}_{0}, \hat{r}) = -\frac{1}{k_{0n}^{2}} \sum_{n=0}^{\infty} \sum_{m=1}^{\infty} \sum_{l=1}^{\infty} \frac{\varepsilon_{0n} \varepsilon_{0l}}{\pi c} \frac{1}{k_{n}^{2} - k_{0}^{2}} \frac{\frac{n l \pi}{r c}}{a^{2} J_{n}^{2}(p_{nm})} J_{n}(\frac{p_{nm}}{a} r)$$

$$J_{n}(\frac{p_{nm}}{a} r_{0}) \sin(n\varphi) \cos(n\varphi_{0}) \sin(\frac{l \pi}{c} z) \cos(\frac{l \pi}{c} z_{0})$$

$$(4.119)$$

The double summation format is then expressed as

$$G_{eo\varphi_z}(\dot{r}_0, \dot{r}) = -\frac{1}{k_{0n}^2} \sum_{n=0}^{\infty} \sum_{m=1}^{\infty} \frac{\varepsilon_{0n}}{\pi} \frac{\frac{n}{r}}{a^2 J_n^{2}(p_{nm})} J_n(\frac{p_{nm}}{a}r)$$

$$J_n(\frac{p_{nm}}{a}r_0) \sin(n\varphi) \cos(n\varphi_0) \frac{f_{g2}(z, z_0)}{\sin(k_{g2}c)}$$
(4.120)

9. Similarly, the  $\hat{z}\hat{\varphi}$  component of the dyadic Green's function  $\overline{G}_{eo}(\hat{r}_0, \hat{r})$  in the double summation format is given by

$$G_{eoz\phi}(\vec{r}_{0}, \vec{r}) = -\frac{1}{k_{0n}^{2}} \sum_{n=0}^{\infty} \sum_{m=1}^{\infty} \frac{\varepsilon_{0n}}{\pi} \frac{\frac{n}{r_{0}}}{a^{2} J_{n}^{2}(p_{nm})} J_{n} \left(\frac{p_{nm}}{a}r\right)$$

$$J_{n} \left(\frac{p_{nm}}{a}r_{0}\right) \cos(n\varphi) \sin(n\varphi_{0}) \frac{f_{g1}(z, z_{0})}{\sin(k_{g2}c)}$$
(4.121)

After we derived the detailed expression for the dyadic Green's function, we can numerically solve the *EFIE* (4.92) in the material sample by the same Galerkin's method as that used in Chapter 3. That is, the material sample is divided into a large number of

volume cells and the pulse functions are employed as both the basis and testing functions. After some similar manipulations as those used in Chapter 3, we can transfer the *EFIE* (4.92) to the similar matrices eqs. (3.17) to (3.20) which can be solved to obtain the unknown electric field. Detailed discussions on the numerical techniques will be presented in Section 4.4.

#### **4.4** Numerical Examples

In Chapter 3, we have studied the convergence property of the dyadic Green's function in both the triple and double summation formats. Based on those results, in the following numerical examples we will adopt the same volume cell dimensions in the Galerkin's method and the same upper limit N=200 in the double summation format of the dyadic Green's function as those used in Chapter 3 to assure the convergence of the numerical results.

In the application of the Galerkin's method, there will be integrations with respect to both variables  $\dot{r}$  and  $\dot{r}$  as shown in eqs. (3.7) and (3.10). In the cylindrical cavity, we deal with the Bessel functions or their derivatives and their numerical integrations in the formation of the matrix (3.20). These numerical integrations consume much more computing time than the case of the rectangular cavity. Thus, in general it is very difficult to find the numerical solution of a *EFIE* even for a material sample with small dimensions with our present computer resources. However, for some special cases we can simplify the expression of the dyadic Green's function and numerically solve the *EFIE* in the cylindrical cavity.

We assume that the material sample, which is azimuthally symmetrical, is placed

in the center of a cylindrical cavity. If the initial cavity mode is not a function of variable  $\varphi$ , for example  $TM_{012}$ , then due to the symmetry property [2],[39] the scattered electric field induced by this material sample and the total electric field will not be functions of variable  $\varphi$ . Therefore, in the numerical computation for this special case, the eigenmodes with n=0 will be sufficient to represent the unknown electric field and the expression for the dyadic Green's function in the double summation format over indices n and m will be further reduced to one summation format over index m.

In the following numerical computations, we assume the dimensions of the cylindrical cavity to be: the radius a=0.0762m and the height c=0.15458m. The initial cavity mode is  $TM_{012}$  and the resonant frequency of this mode is f=2.45 GHz for these dimensions of the cavity. This resonant frequency of the cavity will shift slightly downward when a material sample is placed inside as discussed in Chapter 3. A material sample with the diameter  $d_0$  and the height  $h_0$  is placed in the center of the cylindrical cavity as shown in Figure 4.8. The relative permittivity of the material sample is assumed to be  $\varepsilon_r=2.5$  and it is lossless. Using the Galerkin's method, the material sample is uniformly divided into  $M=n_d\times l_d$  volume cells, where  $n_d$  and  $l_d$  are the numbers of the volume cells in the r and z directions, respectively. Several numerical calculations are carried out for the material sample with selected shapes and dimensions.

#### 1. Cubic material sample

A cubic material sample, having the diameter equal to the height, is placed in the center of the cylindrical cavity. The dimensions of the material sample are chosen as: diameter  $d_0=0.004m$  and height  $h_0=0.004m$  with  $n_d=1$  and  $l_d=2$ . The cavity

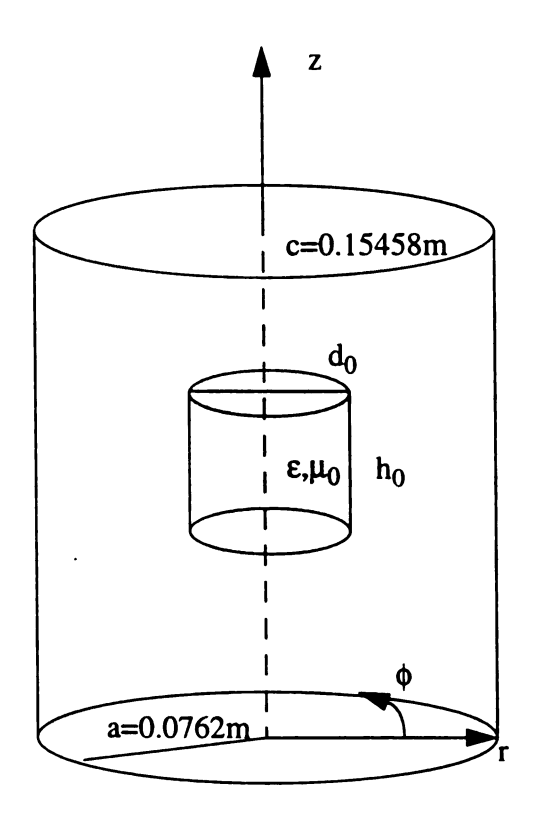


Figure 4.8 Dimensions of the cylindrical cavity and the material sample. The center of the material sample is consistent with the center of the cavity.

resonant frequency is assumed to shift down 5% after the material sample is placed inside the cavity. Since the wavelength  $\lambda$  of the initial mode is 0.12245m which is much larger than the dimensions of the sample  $(h_0/\lambda = 0.0327)$ , the induced electric field inside the material sample can be estimated by the electrostatic field induced inside of a dielectric sphere as  $E = \frac{3}{2 + \epsilon_r} E^i$ .

Observing the electric field structures for the initial mode  $TM_{0I2}$  in Figure 4.2 and Figure 4.3, we find that there is only  $E_z$  component of the electric field which is significant near the center of the cavity. Due to the small dimensions of the material sample, the numerical results are uniform in each volume cell and the  $E_z$  component of the induced electric field dominates the other two components. The ratio of the  $E_z$  component of the induced electric field to that of the initial electric field in the material sample is found to be 0.65 in each volume cell while the electrostatic estimation of  $E_y/E_y^i = \frac{3}{2+\varepsilon_r}$  gives the approximation of 0.667. Thus, numerical results and the theoretical estimation are in satisfactory agreement.

For the stability check of the numerical results, we increase the dimensions of the cubic material sample to:  $d_0=0.008m$  and  $h_0=0.008m$  with  $n_d=2$  and  $l_d=4$ . The cavity resonant frequency is assumed to shift down 5% after the placement of the material sample. The numerical results show that the  $E_z$  component of the induced electric field still dominates and the ratios of the  $E_z$  component of the induced electric field to that of the initial electric field becomes 0.61, 0.64, 0.64 and 0.70 at the different volume cells in the material sample. These values are still close to the electrostatic estimation of 0.667.

For a larger cubic material sample with the dimensions:  $d_0=0.02m$  and  $h_0=0.02m$  with  $n_d=5$  and  $l_d=10$ , the numerical results are shown in Figure 4.9, where the cavity resonant frequency shift is assumed to be 8% after the placement of the material sample. Since the z component of the induced electric field dominates only the ratios of the z components of the induced electric field to that of the initial electric field in the material sample are plotted, in Figure 4.9, as a function of r, for the lower half of the sample. (Numerical results are symmetrical with respect to the center of the sample.) We observe that due to the increase in the material sample dimensions, the ratios in Figure 4.9 are now reduced to about 0.51 to 0.62. This indicates that the induced electric field in a larger sample will be smaller than the value given by the electrostatic estimation.

### 2. Thin chip case

A material sample with the shape of a thin chip, having its height much smaller than its diameter, is placed in the center of the cylindrical cavity. The dimensions of the material sample are  $h_0=0.002m$  and  $d_0=0.04m$  with  $n_d=10$  and  $l_d=1$ . The cavity resonant frequency shift is assumed to be 1% after the material sample is placed inside. Because only the z component of the initial electric field is significant near the center of the cylindrical cavity and the material sample has a thin chip geometry, theoretically the induced electric field in the material sample can be estimated by the boundary condition of  $E=(1/\epsilon_r)E^i=0.4E^i$ . The numerical results are shown in Figure 4.10.

In Figure 4.10, the ratios of the z component of the induced electric field to that of the initial electric field are plotted as a function of the radial distance, r, of the material sample. We observe that the numerical results are consistent with the theoretic estimation

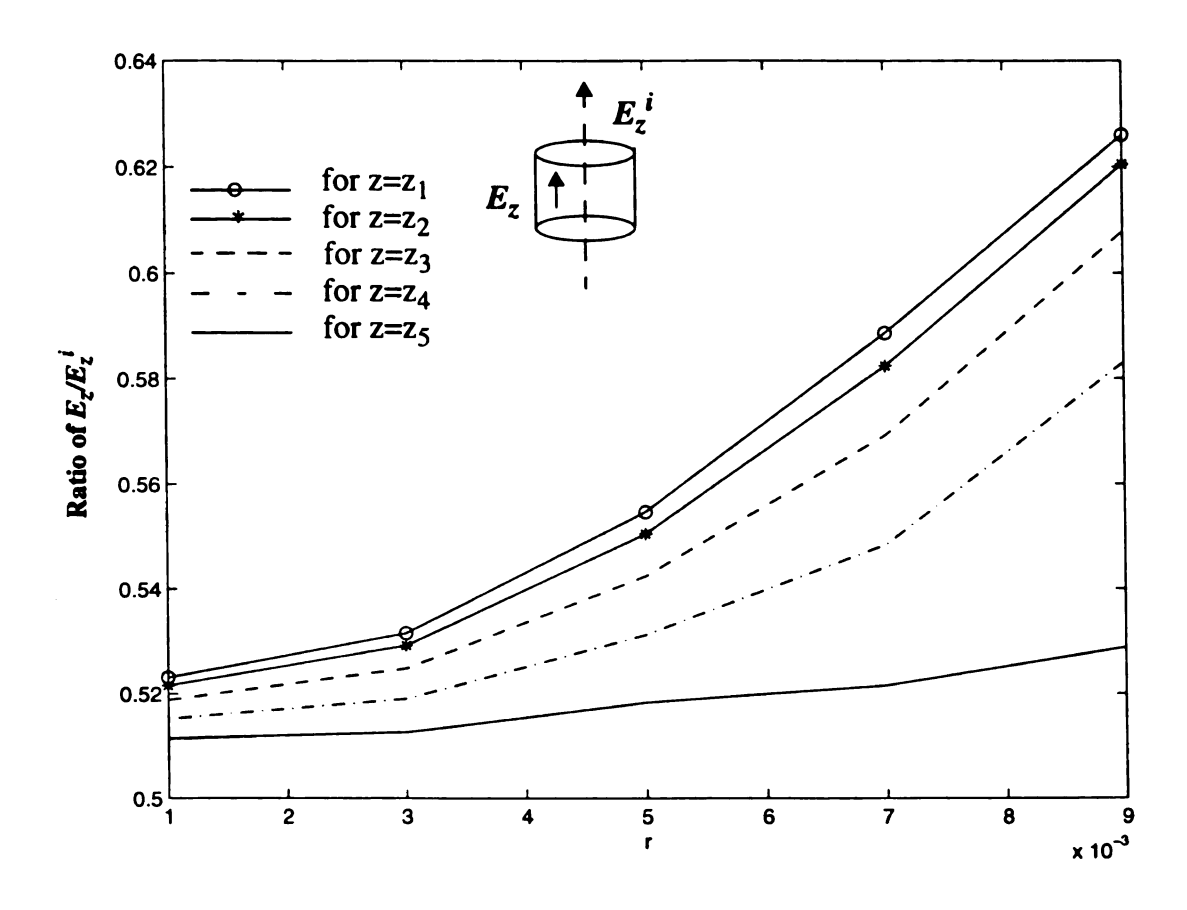


Figure 4.9 Ratio of  $E_z/E_z^i$  varies in the r direction at the different locations of z. The dimensions of the material sample are  $d_0=0.02$ m and  $h_0=0.02$ m with the relative permittivity of  $\varepsilon_r=2.5$ . The dimensions of the cylindrical cavity are shown in Figure 4.8.

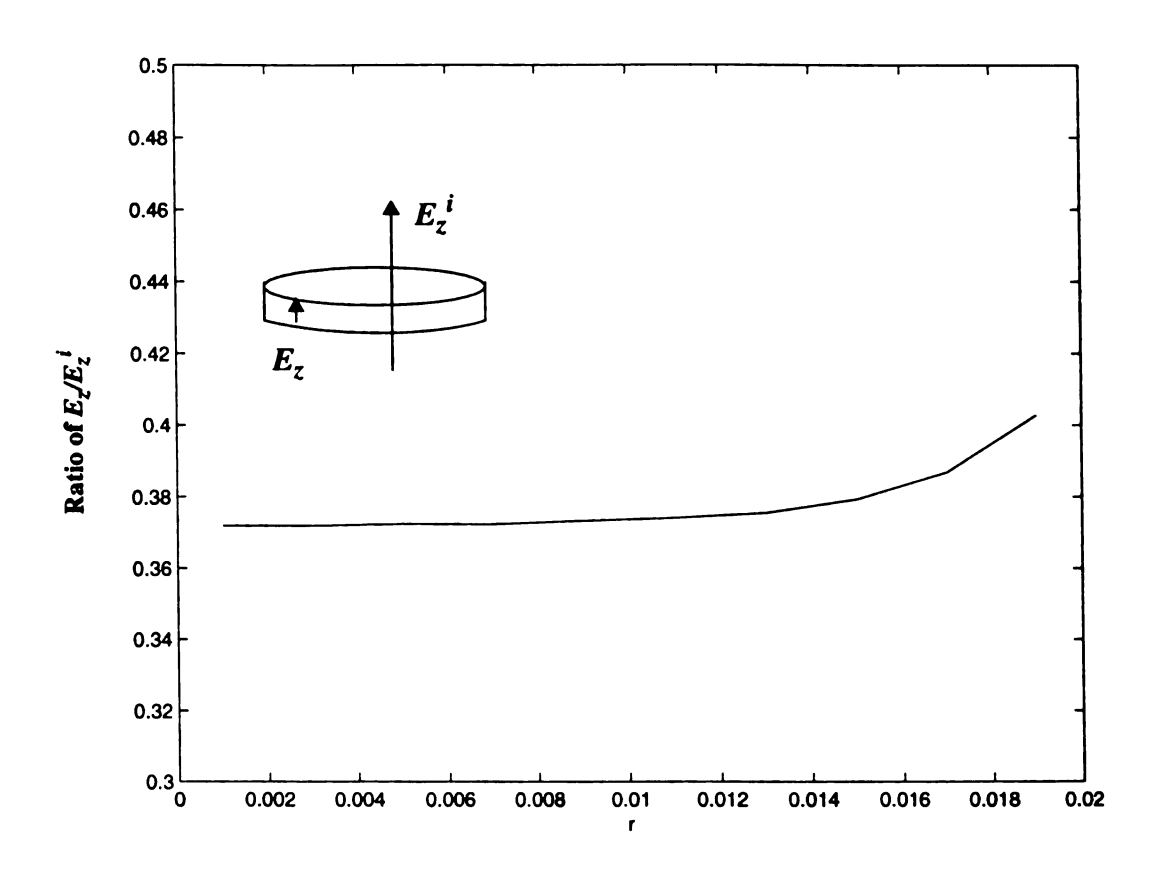


Figure 4.10 Ratio of  $E_z/E_z^i$  varies in the r direction. The dimensions of the material sample are  $d_0$ =0.04m and  $h_0$ =0.002m with the relative permittivity of  $\varepsilon_r = 2.5$ . The dimensions of the cylindrical cavity are shown in Figure 4.8.

as expected.

#### 3. Thin pipe case

A material sample with the dimensions:  $h_0=0.044m$  and the diameter  $d_0=0.008m$  is placed in the center of the cylindrical cavity. The material sample is divide with  $n_d=2$  and  $l_d=22$ , the number of the volume cells being 44, and the cavity resonant frequency shift is assumed to be 1% after the material sample is placed inside. For this case, the induced electric field inside the material sample should be approximately equal to the initial electric field because the initial electric field is tangential to the major part of the material sample surface, and the continuity of the tangential component of the electric field at the material sample surface requires this estimation. The numerical results are shown in Figure 4.11.

In Figure 4.11, we observe that the maximum ratio of the z-component of the induced electric field to that of the initial electric field is around 0.8 which is not very close to 1. This is because when we derived the EFIE (4.92), we have extracted a delta function out the integration sign and if we expect the induced electric field to be equal to the initial electric field, another delta function is needed to be generated under the integration sign in EFIE (4.92) to cancel the former delta function. Thus, we will need much more summation terms for this special case to meet this requirement just like the narrow strip case in Chapter 3. If we increase the upper limit in the double summation, the numerical results become closer to the theoretic estimation but at the expense of increasing the computation time.

For this thin pipe shaped material sample, if we employ the scheme of separating the material sample into boundary layer and interior cells as that used in Chapter 3,

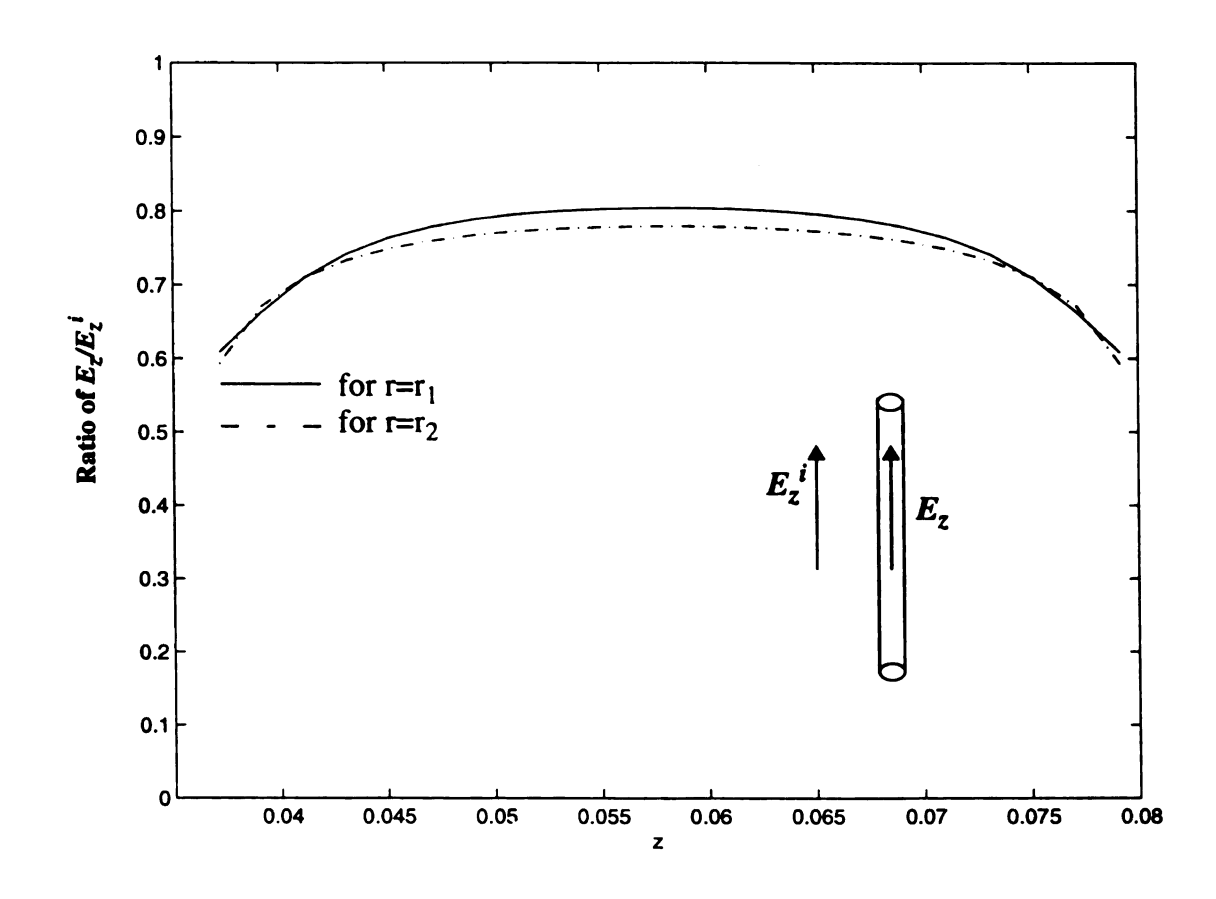


Figure 4.11 Ratio of  $E_z/E_z^i$  varies in the z direction at the different locations of r. The dimensions of the material sample are  $d_0$ =0.008m and  $h_0$ =0.044m with the relative permittivity of  $\epsilon_r=2.5$ . The dimensions of the cylindrical cavity are shown in Figure 4.8.

the results are improved and at the same time the computation time is reduced. In this computation, the dimensions of the material sample are:  $d_0$ =0.008m and  $h_0$ =0.044m with  $n_d = 1$  and  $l_d = 20$ . The dimensions of the volume cells in the boundary layer region are: br=0.002m and bz=0.002m in the r and z directions, respectively and the dimensions of each volume cell in the interior region are: ir=0.002m and iz=0.002m in the r and z directions, respectively. The number of the total volume cells in the boundary layer and interior regions is:  $2 \times 22 = 44$  which is the same as the previous computation. The cavity resonant frequency shift is assumed to be 1% after the material sample is placed inside. The upper limits in the mode summation are chosen as 200 for the boundary layer region and 150 for the interior region. The numerical results are shown in Figure 4.12.

Since we are only interested in the induced electric field inside the material sample, only the solutions for the volume cells in the interior region are plotted in Figure 4.12. Because the numerical results show that the z components of the induced electric field dominate in the material sample, only the ratios for the z components of the induced electric fields to that of the initial electric field in the interior region are plotted as a function of z in Figure 4.12. We observe that the ratios are now very close to I.

In the scheme of the separating the material sample into the boundary layer and interior regions for the thin pipe shaped material sample, we keep the number of the volume cells the same as the previous computation. However, the upper limit of the mode summation in the interior region is reduced to 150. Hence, the computation time is saved and at the same time better results are obtained.

## 4. Lossy material sample

In this numerical example, we will assume that the material sample has a complex

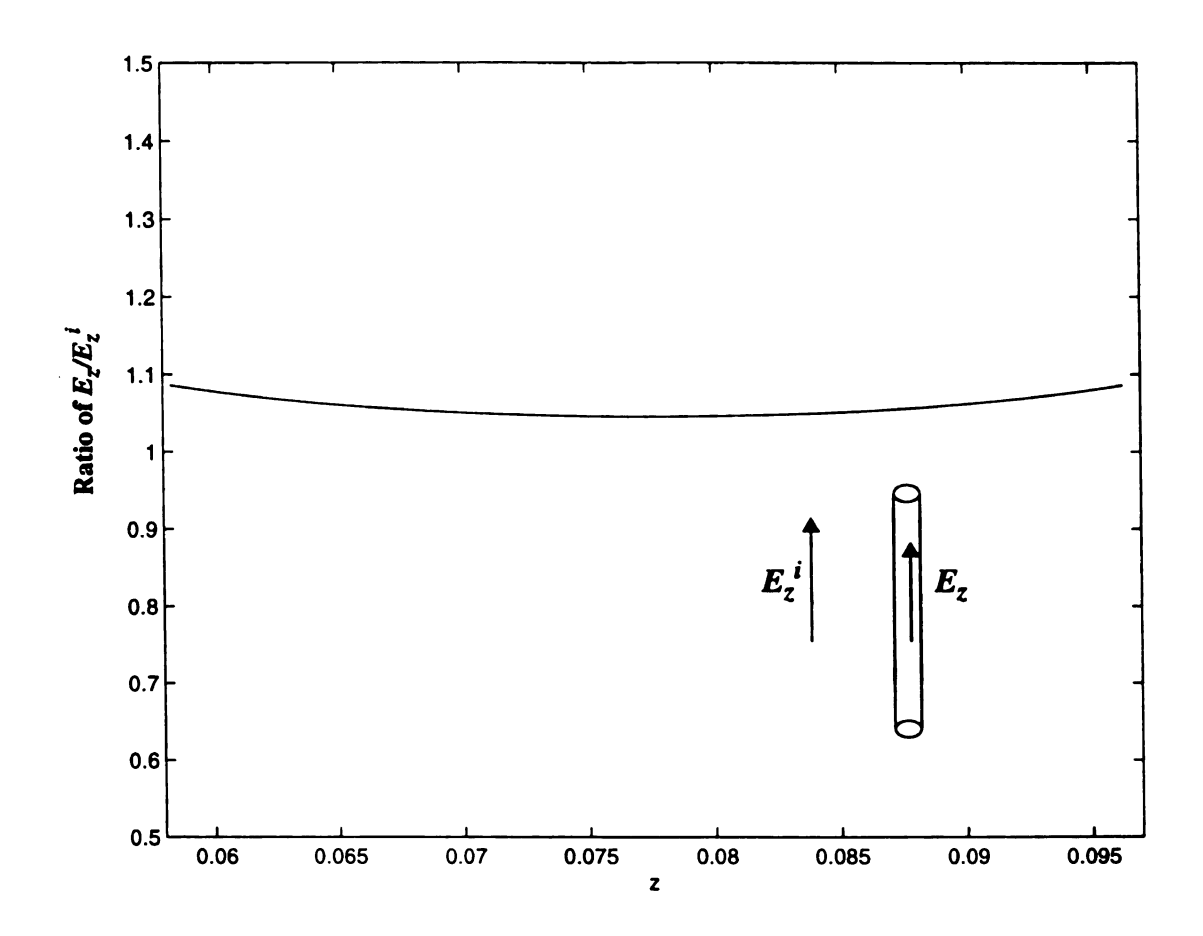


Figure 4.12 Ratio of  $E_z/E_z^i$  varies in the z direction with the scheme of separating the material sample into the boundary layer and interior regions. The dimensions of the material sample are  $d_0$ =0.008m and  $h_0$ =0.044m with the relative permittivity of  $\varepsilon_r=2.5$ . The dimensions of the cylindrical cavity are shown in Figure 4.8.

permittivity of  $\varepsilon_r = \varepsilon' - j\varepsilon''$ ; where  $\varepsilon'$  is the real permittivity (electrical polarizability) of the material sample, the magnitude of which reflects its ability to store electric energy;  $\varepsilon''$  represents the loss factor of the material sample, and its magnitude determines its ability to dissipate electric energy into thermal energy [63]. In the computation, we assume  $\varepsilon' = 2.5$  and  $\varepsilon'' = 0.5$  with the dimensions of the material sample as: diameter  $d_0 = 0.008m$  and height  $h_0 = 0.008m$ . The numerical results are shown in Figure 4.13.

In Figure 4.13, we plot the ratios of the z components of the induced electric field to that of the initial electric field inside the material sample. Due to the complex permittivity of the material sample, the induced electric field has both the real and imaginary parts. In Figure 4.13 the upper graphs are for the real parts and the lower ones are for the imaginary parts of the ratios. Comparing the real parts of the ratios in Figure 4.13 (about 0.62 to 0.68) with that for a lossless cubic material sample of the same dimensions (about 0.61 to 0.70), we find that the real parts of the ratios remain relatively unchanged if the material sample has a complex permittivity. Also the numerical results indicate that if the imaginary part of the relative permittivity is increased, the real parts of the ratios will decrease while the imaginary parts of the ratios will increase. The numerical results shown in Figure 4.14 can demonstrate this finding where we assume the complex relative permittivity of the material sample as  $\varepsilon' = 2.5$  and  $\varepsilon'' = 1.5$  with the same sample dimensions as that in Figure 4.13.

In Figure 4.13, where the relative permittivity is  $\varepsilon' = 2.5$  and  $\varepsilon'' = 0.5$ , the real parts of the ratios are about 0.62 to 0.68, while in Figure 4.14, where the relative permittivity is  $\varepsilon' = 2.5$  and  $\varepsilon'' = 1.5$ , the real parts of the ratios are about 0.54 to 0.63.

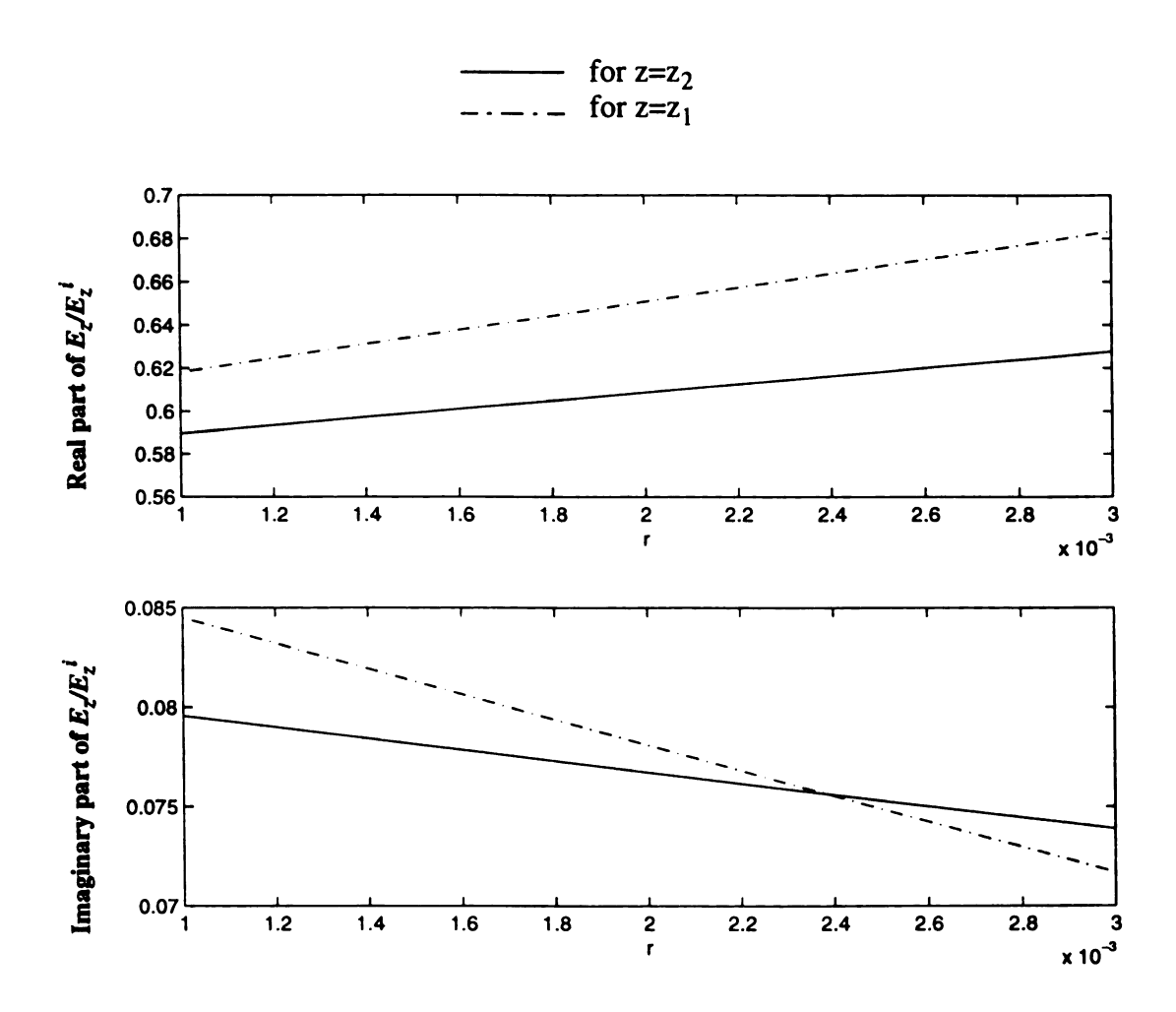


Figure 4.13 Ratios of  $E_z/E_z^i$  varies in the r direction. Each curve represents this ratio as a function of r for different locations of z in a material sample when the material sample has a complex permittivity of  $\varepsilon_r=2.5-j0.5$ . The dimensions of the material sample are: diameter  $d_0=0.008m$  and height  $h_0=0.008m$ . The upper graphs are for the real parts of the ratios and the lower ones are for the imaginary parts of the ratios.

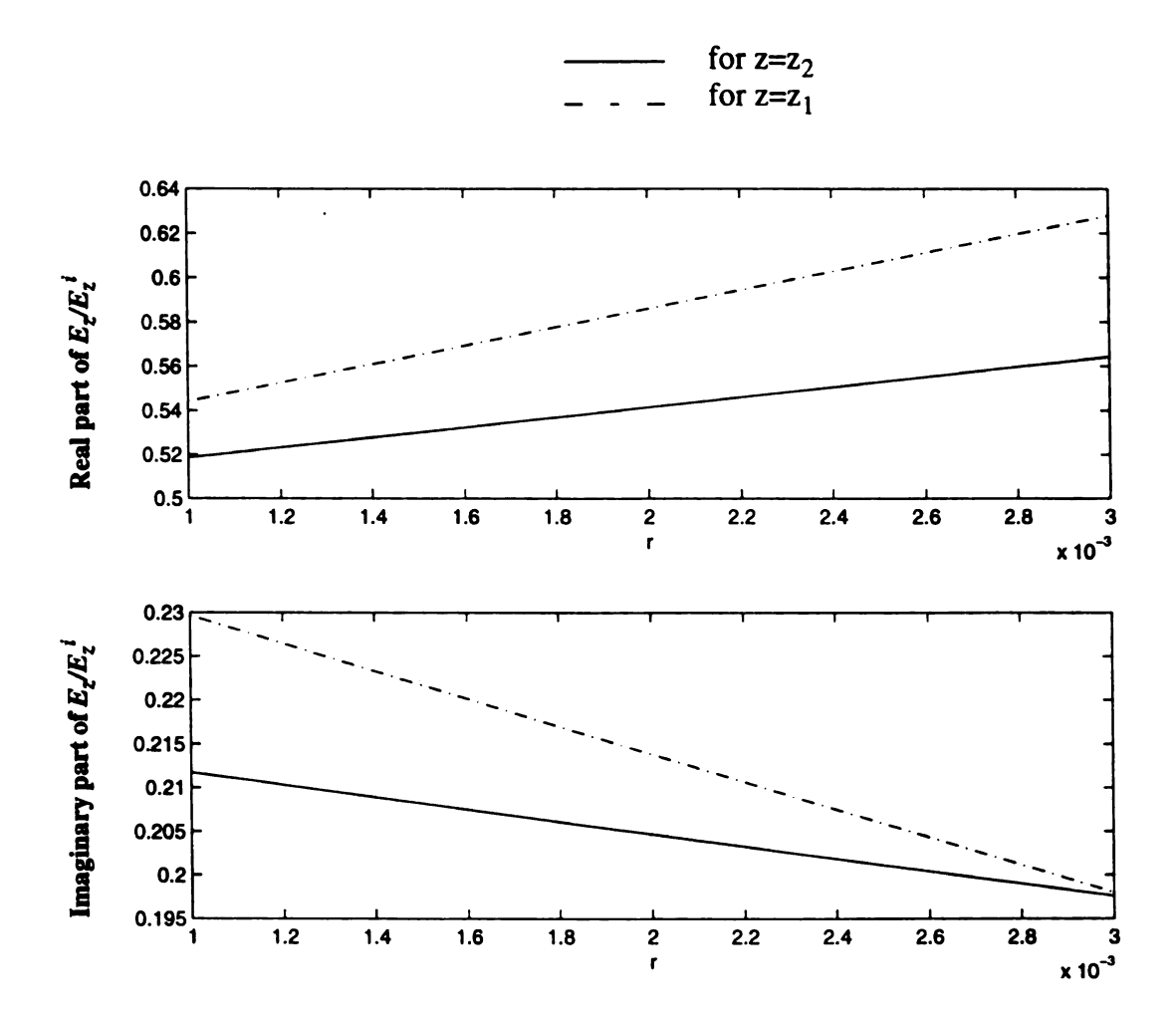


Figure 4.14 Ratios of  $E_z/E_z^i$  varies in the r direction. Each curve represents this ratio as a function of r for different locations of z in a material sample when the material sample has a complex permittivity of  $\varepsilon_r=2.5-j1.5$ . The dimensions of the material sample are: diameter  $d_0=0.008m$  and height  $h_0=0.008m$ . The upper graphs are for the real parts of the ratios and the lower ones are for the imaginary parts of the ratios.

However, the imaginary parts of the ratios in Figure 4.13 are about 0.072 to 0.085 while that in Figure 4.14 are about 0.2 to 0.23. Thus, a larger imaginary permittivity causes more power loss or more microwave power dissipated in the material sample.

### 5. Inhomogeneous material sample

In this numerical example, we assume that the material sample is composed of two kinds of dielectric materials as shown in Figure 4.15. The relative permittivities of the two regions of the material sample are denoted as  $\varepsilon_1$  and  $\varepsilon_2$  and their radii and heights denoted as  $r_1$ ,  $r_2$  and  $h_1$ ,  $h_2$ , respectively.

If the dimensions of the material sample are electrically small compared with the operating wavelength, we can estimate the ratios of the z components of the induced electric fields inside the material sample to that of the initial electric field by the electrostatic approximations, which are given in Appendix D (D.45) and (D.47), as

$$\frac{E_1}{E_0} = \frac{-9\varepsilon_0 \varepsilon_2 r_1^{-3}}{(\varepsilon_1 + 2\varepsilon_2)(\varepsilon_2 + 2\varepsilon_0)r_1^{-3} + 2(\varepsilon_1 - \varepsilon_2)(\varepsilon_2 - \varepsilon_0)r_2^{-3}}$$
(4.122)

$$\frac{E_2}{E_0} = 3\varepsilon_0 \frac{(\varepsilon_1 - \varepsilon_2)r^{-3} - (\varepsilon_1 + 2\varepsilon_2)r_1^{-3}}{(\varepsilon_1 + 2\varepsilon_2)(\varepsilon_2 + 2\varepsilon_0)r_1^{-3} + 2(\varepsilon_1 - \varepsilon_2)(\varepsilon_2 - \varepsilon_0)r_2^{-3}}$$
(4.123)

In this numerical example, the dimensions of this inhomogeneous material sample are chosen as:  $r_1 = 0.004m$ ,  $h_1 = 0.008m$ ,  $r_2 = 0.008m$  and  $h_2 = 0.016m$ , and with the relative permittivities assumed to be  $\varepsilon_1 = 2.5$  and  $\varepsilon_2 = 4.0$ . The eqs. (4.122) and (4.123) give the ratios of the z components of the induced electric fields in the inhomogeneous material sample to that of the initial electric field as  $R_1 = 0.5818$  in

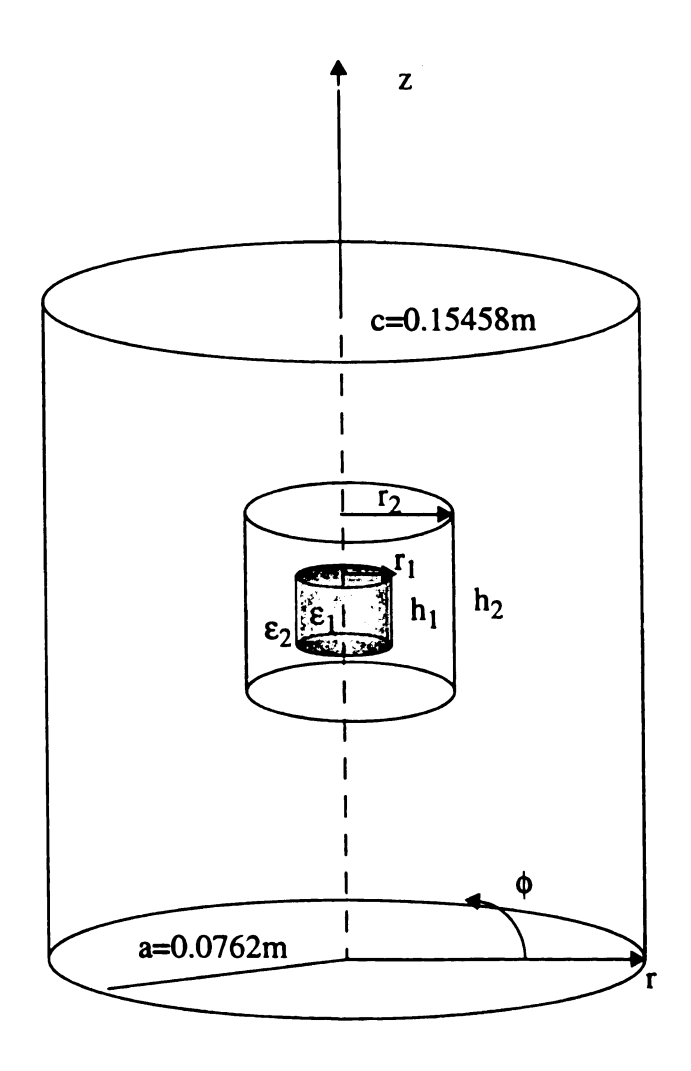


Figure 4.15 An inhomogeneous material sample is placed in the center of a cylindrical cavity.

region 1 and  $R_2 \approx 0.5091$  in region 2.

The numerical results are shown in Figure 4.16, where we observe that the numerical results are smaller than the electrostatic estimations. This is because the dimensions of the inhomogeneous material sample are not very small compared with the operating wavelength.

If we change the dimensions of the material sample to  $r_1 = 0.002m$ ,  $h_1 = 0.004m$ ,  $r_2 = 0.004m$  and  $h_2 = 0.008m$ , and remain the relative permittivities of the material sample unchanged, the numerical results are shown in Figure 4.17. In this figure, we observe that the numerical results become more consistent with the electrostatic estimations.

### 6. Irregularly shaped material sample

In this numerical example, we assume the material sample to have a irregular shape but keep the material sample azimuthally symmetrical in order to save the computation time. The shape of the material sample is shown in Figure 4.18. We assume the dimensions of the material sample as:  $h_1 = 0.004m$ ,  $h_2 = 0.008m$ ,  $d_1 = 0.016m$  and  $d_2 = 0.008m$ , and with the relative permittivity of  $\varepsilon_1 = 2.5$ . The numerical results are shown in Figure 4.19.

After we have quantified the induced electric field inside the material sample, the dissipated power is determined [66] as  $P = \omega \varepsilon_0 \varepsilon'' |\vec{E}|^2$ , where  $\varepsilon''$  is the imaginary part of the permittivity and  $\vec{E}$  is the induced electric field inside the material sample. This dissipated power becomes a volumetrically-distributed heat source. The temperature

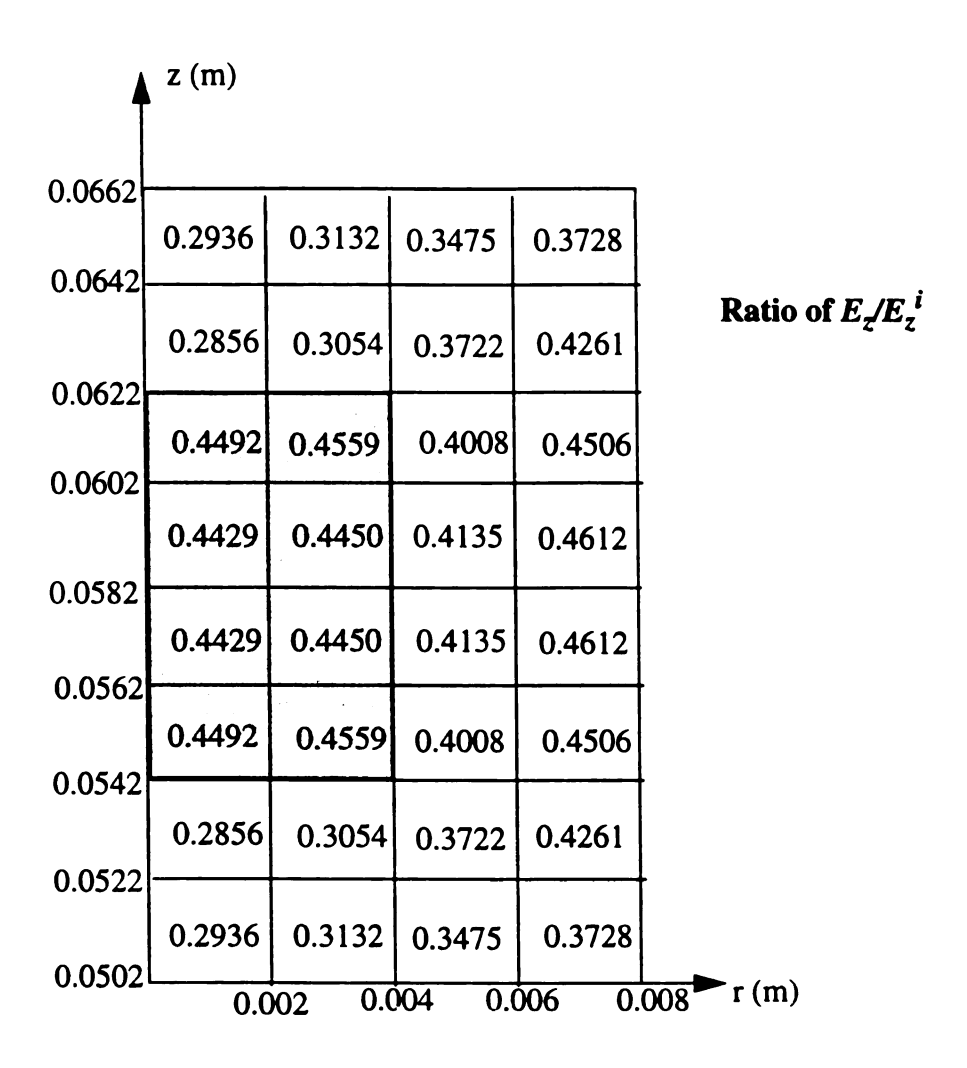


Figure 4.16 Ratios of  $E_z/E_z^i$  in an inhomogeneous material sample with the dimensions of  $r_1=0.004m$ ,  $h_1=0.008m$ ,  $r_2=0.008m$  and  $h_2=0.016m$ , where the relative permittivity in the shadowed region is  $\epsilon_1=2.5$  and that in the non-shadowed region is  $\epsilon_2=4.0$ . The electrostatic estimations of the ratios are  $R_1=0.5818$  and  $R_2=0.5091$ .

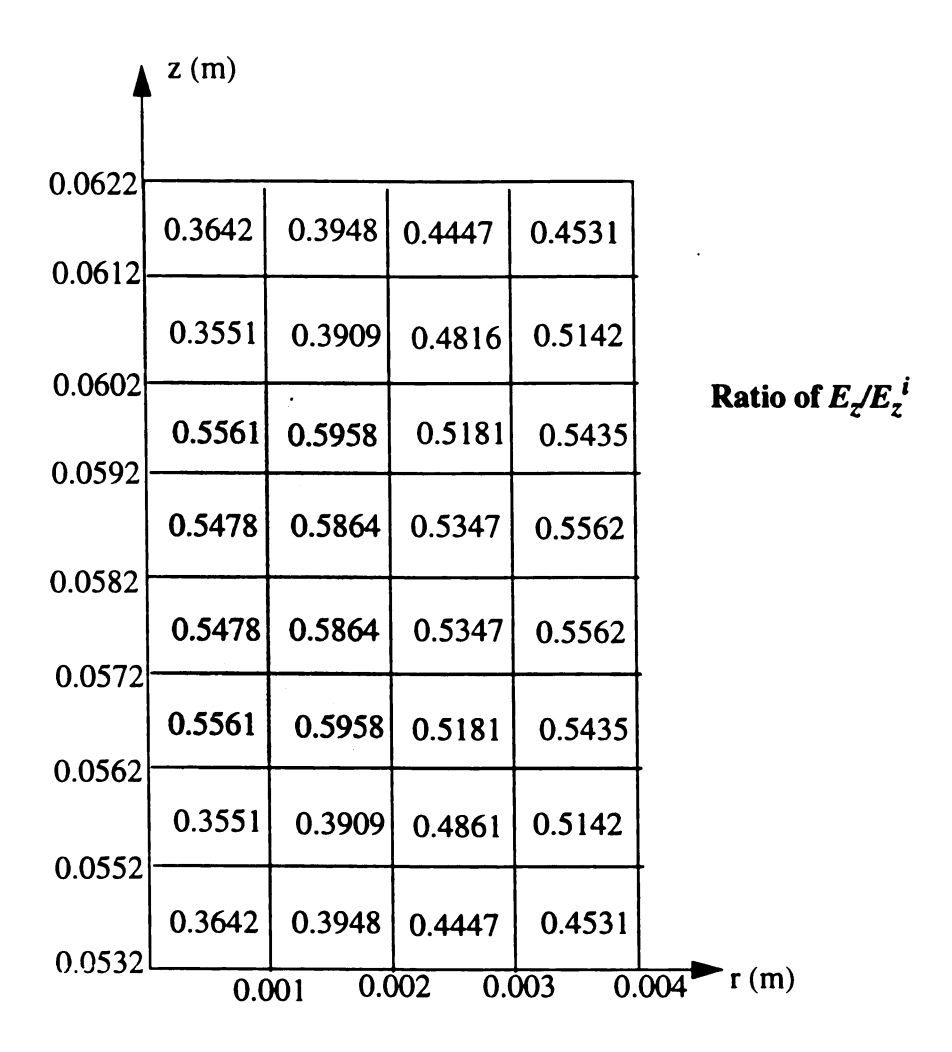


Figure 4.17 Ratios of  $E_z/E_z^i$  in the inhomogeneous material sample with the dimensions of  $r_1=0.002m$ ,  $h_1=0.004m$ ,  $r_2=0.004m$  and  $h_2=0.008m$ , where the relative permittivity in the shadowed region is  $\epsilon_1=2.5$  and that in the non-shadowed region is  $\epsilon_2=4.0$ . The electrostatic estimations of the ratios are  $R_1=0.5818$  and  $R_2=0.5091$ 

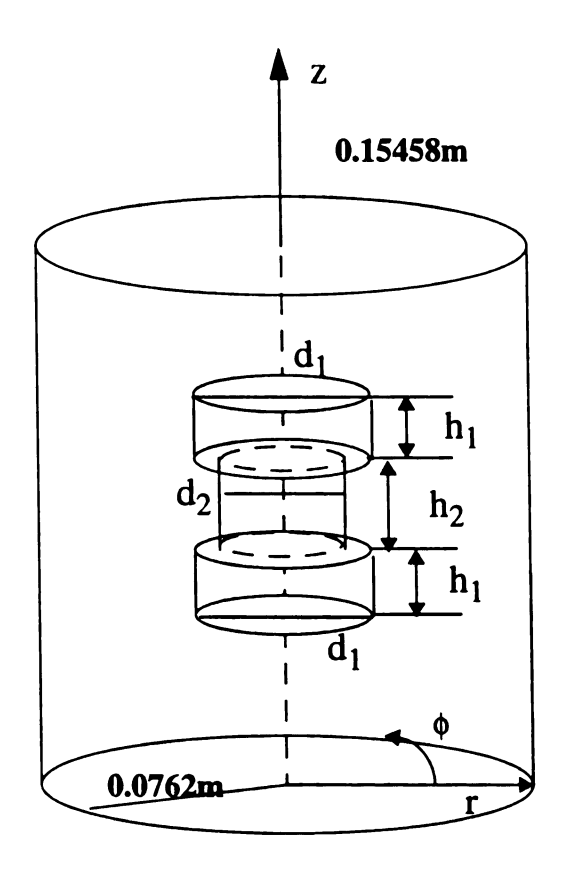


Figure 4.18 Geometry of an irregularly shaped material sample placed in the cylindrical cavity. The material sample is azimuthally symmetrical and the center of the material sample is consistent with the center of the cylindrical cavity.

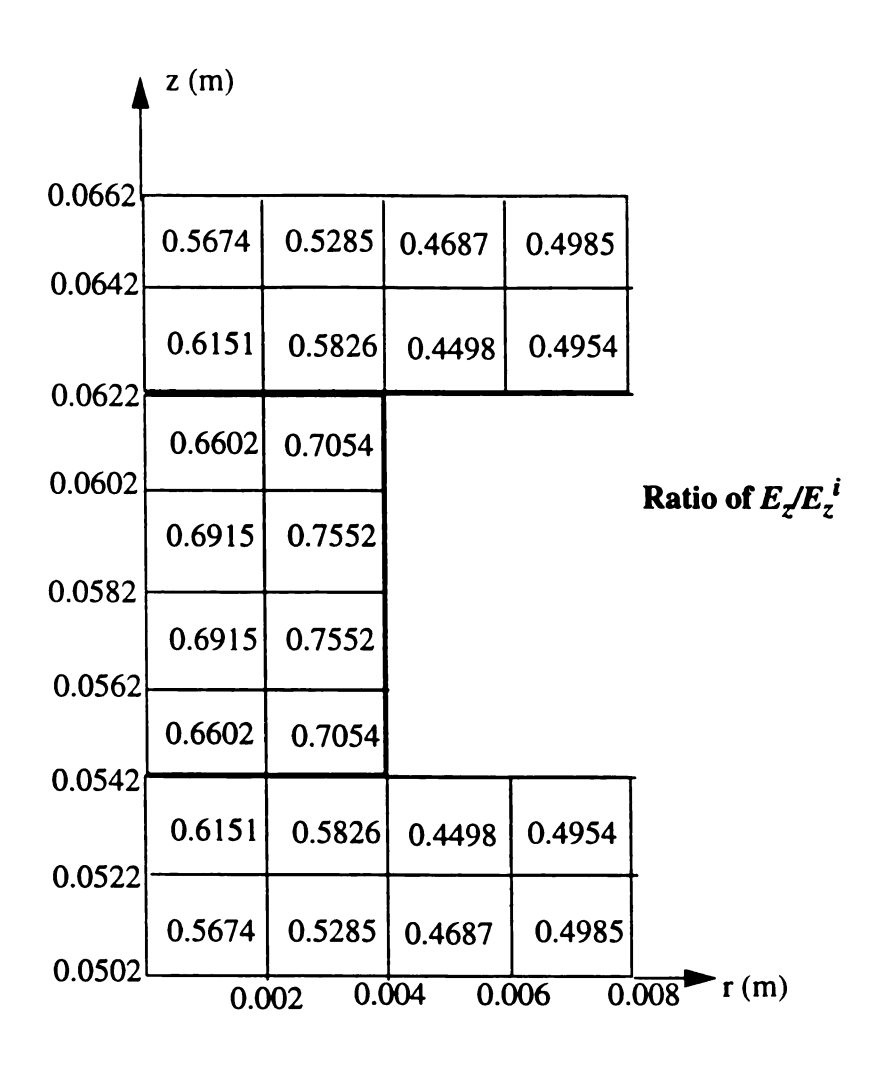


Figure 4.19 Ratios of  $E_z/E_z^i$  in an irregularly shaped material sample.

distribution in a material sample due to the microwave radiation is thus governed by the interaction and absorption of the radiation by the material and the accompanying transport processes due to the dissipation of electric energy into heat [3]. Detailed discussion about the heating processing of the material sample are available in [66] to [67].

## **CHAPTER 5**

# QUANTIFICATION OF THE INDUCED ELEC-TRIC FIELD IN A MATERIAL SAMPLE PLACED INSIDE AN EM CAVITY USING MODE MATCHING METHOD

In the previous chapters, the induced electric field inside a material sample placed in an energized cavity has been determined based on the numerical solution of an electric field integral equation (*EFIE*) or a magnetic field integral equation (*MFIE*). These integral equations were obtained after the dyadic Green's function in an *EM* cavity was derived. It has been demonstrated that the integral equation method is a very powerful technique because it can handle the material samples of arbitrary shapes and heterogeneities. The only disadvantage of this method is its slow numerical convergence and a large computation time. The reason is that we used the vector wave functions,  $\vec{L}_{nml}$ ,  $\vec{M}_{nml}$  and  $\vec{N}_{nml}$ , to represent the induced electric field inside the material sample and it requires the summation a very large number of these vector wave functions to reach a convergent numerical result.

When the material sample is of a simple cylindrical geometry and homogeneous, the mode-matching method can be employed to determine the induced electric field inside

the material sample placed within an energized cylindrical cavity. This method will be investigated in this chapter.

Applying the mode-matching method to a homogeneous material sample with a simple cylindrical geometry placed within a cylindrical cavity, we can divide the cavity into three waveguide regions as shown in Figure 5.1, where regions I and III are the normal waveguide regions filled with a homogeneous material or empty and region II is the inhomogeneously filled waveguide region containing the material sample. The waveguide eigenmodes in region II are derived first while those in regions I and III are well known. The *EM* fields in each region are expressed in terms of its eigenmodes, and the tangential component of the electric and magnetic fields are matched at the junctions of the three regions. The equations resulted from the matching of the boundary conditions are then numerically solved.

The outline of this chapter is as follows: In Section 5.1 the eigenmodes in the inhomogeneously filled waveguide containing the material sample are derived and those in the normal waveguide regions are introduced. The mode-matching method is applied to these three regions in Section 5.2. And the numerical examples are shown and the results are compared with that of Chapter 4 in Section 5.3.

## 5.1 Eigenmodes in Different Waveguide Regions

# 5.1.1 Eigenmodes in a Homogeneously Filled Waveguide

The eigenmodes in an empty or homogeneously filled waveguide have two categories [10]: *TM* and *TE* mode. They are complete and orthogonal. The expressions for *TM* eigenmodes are: (We only show the propagation mode in the plus z direction for

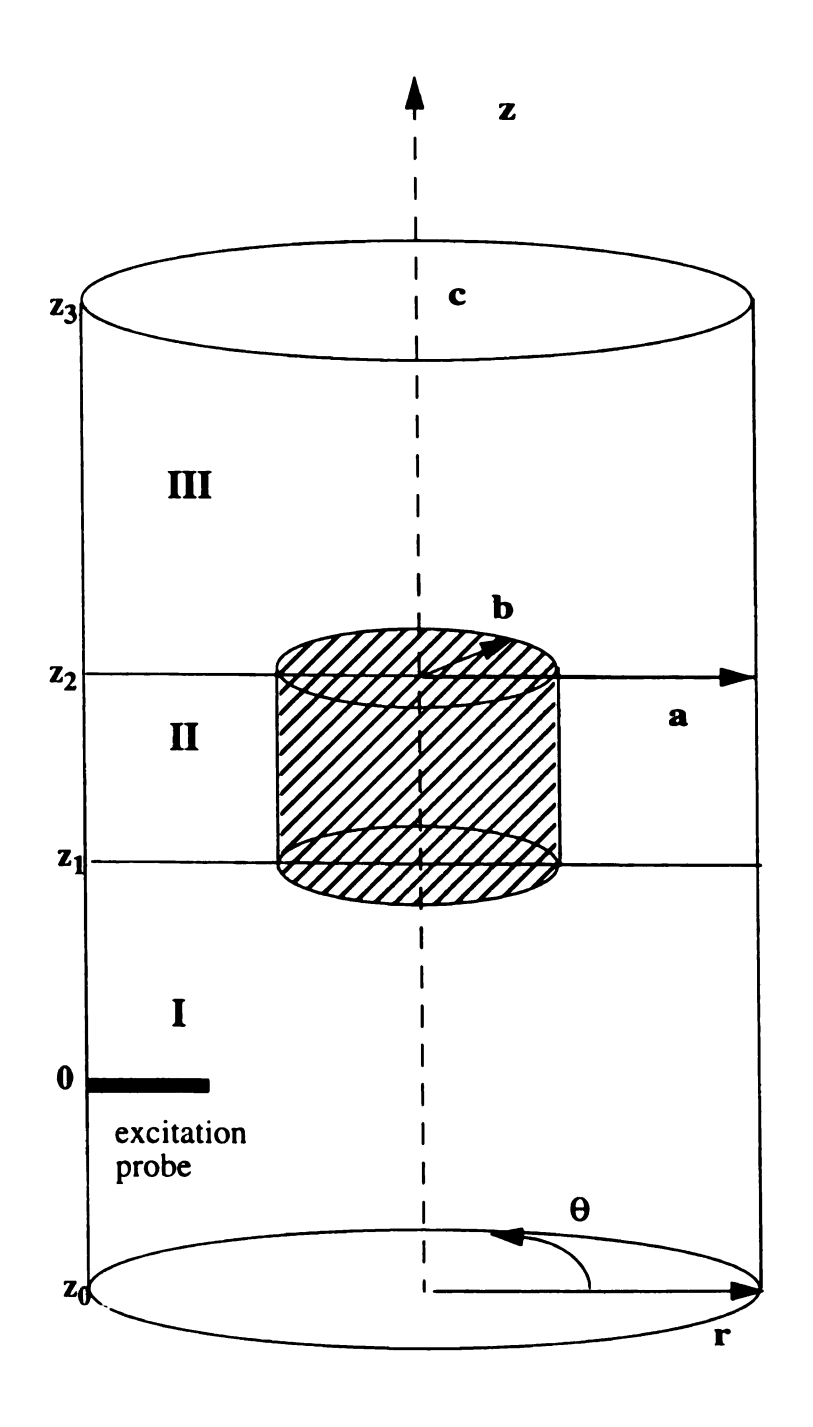


Figure 5.1 Geometry of the material sample placed in a cylindrical cavity driven by an excitation probe.

simplicity.)

$$E_z = A_{nm} \left(\frac{p_{nm}}{a}\right)^2 J_n \left(\frac{p_{nm}}{a}r\right) \cos n\theta e^{-\Gamma_{nm}z}$$
 (5.1)

$$E_r = -A_{nm} \Gamma_{nm} \frac{p_{nm}}{a} J_n \left( \frac{p_{nm}}{a} r \right) \cos n\theta e^{-\Gamma_{nm} z}$$
 (5.2)

$$E_{\theta} = A_{nm} \Gamma_{nm} \frac{n}{r} J_n \left( \frac{p_{nm}}{a} r \right) \sin n\theta e^{-\Gamma_{nm} z}$$
 (5.3)

$$H_r = -j\omega \varepsilon A_{nm} \frac{n}{r} J_n \left(\frac{p_{nm}}{a}r\right) \sin n\theta e^{-\Gamma_{nm}z}$$
(5.4)

$$H_{\theta} = -j\omega \varepsilon A_{nm} \frac{p_{nm}}{a} J_{n} \left( \frac{p_{nm}}{a} r \right) \cos n\theta e^{-\Gamma_{nm} z}$$
 (5.5)

where  $\left(\frac{p_{nm}}{a}\right)^2 = \omega^2 \mu \varepsilon + \Gamma_{nm}^2$ . For n=0, the expressions for *TM* eigenmodes are:

$$E_z = A_{0m} \left(\frac{p_{0m}}{a}\right)^2 J_0 \left(\frac{p_{0m}}{a}r\right) e^{-\Gamma_{0m}z}$$
 (5.6)

$$E_r = -A_{0m} \Gamma_{0m} \frac{p_{0m}}{a} J_0 \left( \frac{p_{0m}}{a} r \right) e^{-\Gamma_{0m} z}$$
 (5.7)

$$H_{\theta} = -j\omega \varepsilon A_{0m} \frac{p_{0m}}{a} J_n \left( \frac{p_{0m}}{a} r \right) e^{-\Gamma_{0m} z}$$
(5.8)

with  $E_{\theta} = 0$  and  $H_r = 0$ . The expressions for TE eigenmodes are:

$$H_z = A_{nm} \left(\frac{p_{nm}}{a}\right)^2 J_n \left(\frac{p_{nm}}{a}r\right) \sin n\theta e^{-\Gamma_{nm}z}$$
 (5.9)

$$H_r = -A_{nm} \Gamma_{nm} \frac{p_{nm}}{a} J_n \left( \frac{p_{nm}}{a} r \right) \sin n\theta e^{-\Gamma_{nm} z}$$
 (5.10)

$$H_{\theta} = -A_{nm} \Gamma_{nm} \frac{n}{r} J_n \left( \frac{p_{nm}'}{a} r \right) \cos n\theta e^{-\Gamma_{nm} z}$$
 (5.11)

$$E_r = -j\omega\mu A_{nm} \frac{n}{r} J_n \left(\frac{p_{nm}}{a}r\right) \cos n\theta e^{-\Gamma_{nm}z}$$
(5.12)

$$E_{\theta} = j\omega\mu A_{nm} \frac{p_{nm}}{a} J_n \left( \frac{p_{nm}}{a} r \right) \sin n\theta e^{-\Gamma_{nm} z}$$
 (5.13)

where  $\left(\frac{p_{nm}}{a}\right)^2 = \omega^2 \mu \varepsilon + \Gamma_{nm}^2$ . For n=0, the expressions for *TE* eigenmodes are:

$$H_z = A_{0m} \left(\frac{p_{0m}'}{a}\right)^2 J_n \left(\frac{p_{0m}'}{a}r\right) e^{-\Gamma_{0m}z}$$
 (5.14)

$$H_{r} = -A_{0m} \Gamma_{0m} \frac{p_{0m}}{a} J_{n} \left( \frac{p_{0m}}{a} r \right) e^{-\Gamma_{0m} z}$$
 (5.15)

$$E_{\theta} = j\omega \mu A_{0m} \frac{p_{0m}}{a} J_{n} \left( \frac{p_{0m}}{a} r \right) e^{-\Gamma_{0m} z}$$
 (5.16)

with  $H_{\theta} = 0$  and  $E_r = 0$ .

# 5.1.2 Eigenmodes in an Inhomogeneously Filled Waveguide

The geometry of an inhomogeneously filled waveguide is shown in Figure 5.2 which consists of two sub-regions having the same central axis. The central sub-region is a homogeneous material sample and the outer sub-region is empty space. It is noted that if the material sample has an irregular shape or is heterogeneous, the eigenmodes in such an inhomogeneously filled waveguides will be difficult, if not impossible, to be determined. Therefore, we only deal with the homogeneous material samples with simple cylindrical geometries which are placed in the cavity in this chapter.



Figure 5.2 Geometry of the inhomogeneously filled waveguide

The normal eigenmodes in this inhomogeneously filled waveguide are not, in general, either TE or TM modes, but a combination of an TE and an TM mode, a hybrid eigenmode. An exception is the case of n=0 modes which will be shown later.

In Figure 5.2, the dielectric parameters of sub-region 1 are: relative permittivity  $\varepsilon_1$ , permeability  $\mu_1$  and conductivity  $\sigma_1$ , and its radius is b. The parameters of sub-region 2 are: relative permittivity  $\varepsilon_2$ , permeability  $\mu_2$  and conductivity  $\sigma_2$  with radius a. Based on the relations between the longitudinal and the transverse components of the electromagnetic fields given in [10], we obtain the electromagnetic eigenmodes in these two sub-regions when  $n \neq 0$  as follows:

In sub-region 1, the electromagnetic eigenmodes can be expressed as

$$E_{z1} = A_{nm} k_{c1}^2 J_n(k_{c1} r) \cos n\theta e^{-\Gamma_{nm} z}$$
 (5.17)

$$H_{z1} = B_{nm} k_{c1}^2 J_n(k_{c1} r) \sin n\theta e^{-\Gamma_{nm} z}$$
 (5.18)

$$E_{r1} = \left[ -j\omega\mu_{1}B_{nm}\frac{n}{r}J_{n}(k_{c1}r) - A_{nm}\Gamma_{nm}k_{c1}J_{n}'(k_{c1}r) \right] \cos n\theta e^{-\Gamma_{nm}z}$$
 (5.19)

$$E_{\theta 1} = \left[ j \omega \mu_1 B_{nm} k_{c1} J_n'(k_{c1}r) + A_{nm} \Gamma_{nm} \frac{n}{r} J_n(k_{c1}r) \right] \sin n\theta e^{-\Gamma_{nm}z}$$
 (5.20)

$$H_{r1} = \left[ -B_{nm} \Gamma_{nm} k_{c1} J_{n}'(k_{c1}r) - j\omega \epsilon_{c1} A_{nm} \frac{n}{r} J_{n}(k_{c1}r) \right] \sin n\theta e^{-\Gamma_{nm}z}$$
 (5.21)

$$H_{\theta 1} = \left[ -B_{nm} \Gamma_{nm} \frac{n}{r} J_n(k_{c1}r) - j\omega \varepsilon_{c1} A_{nm} k_{c1} J_n'(k_{c1}r) \right] \cos n\theta e^{-\Gamma_{nm}z}$$
 (5.22)

In sub-region 2, the electromagnetic eigenmodes can be expressed as

$$E_{z2} = \left[ C_{nm} J_n(k_{c2}r) + D_{nm} Y_n(k_{c2}r) \right] k_{c2}^2 \cos n\theta e^{-\Gamma_{nm}z}$$
 (5.23)

$$H_{z2} = [E_{nm}J_n(k_{c2}r) + F_{nm}Y_n(k_{c2}r)]k_{c2}^2 \sin n\theta e^{-\Gamma_{nc}z}$$
(5.24)

$$E_{r2} = \left\{ -j\omega\mu_{2} \frac{n}{r} [E_{nm} J_{n}(k_{c2}r) + F_{nm} Y_{n}(k_{c2}r)] - \Gamma_{nm} k_{c2} \right\}$$

$$[C_{nm} J_{n}'(k_{c2}r) + D_{nm} Y_{n}'(k_{c2}r)] \left\{ \cos n\theta e^{-\Gamma_{nm}z} \right\}$$
(5.25)

$$E_{\theta 2} = \left\{ j \omega \mu_2 k_{c2} [E_{nm} J_n'(k_{c2} r) + F_{nm} Y_n'(k_{c2} r)] + \Gamma_{nm} \frac{n}{r} \right\}$$

$$[C_{nm} J_n(k_{c2} r) + D_{nm} Y_n(k_{c2} r)] \left\{ \sin n\theta e^{-\Gamma_{nm} z} \right\}$$
(5.26)

$$H_{r2} = \left\{ -\Gamma_{nm} k_{c2} [E_{nm} J_n'(k_{c2}r) + F_{nm} Y_n'(k_{c2}r)] - j\omega \varepsilon_{c2} \frac{n}{r} \right\}$$

$$[C_{nm} J_n(k_{c2}r) + D_{nm} Y_n(k_{c2}r)] \left\{ \sin n\theta e^{-\Gamma_{nm}z} \right\}$$
(5.27)

$$H_{\theta 2} = \left\{ -\Gamma_{nm} \frac{n}{r} [E_{nm} J_n(k_{c2}r) + F_{nm} Y_n(k_{c2}r)] - j\omega \varepsilon_{c2} k_{c2} \right\}$$

$$[C_{nm} J_n'(k_{c2}r) + D_{nm} Y_n'(k_{c2}r)] \cos n\theta e^{-\Gamma_{nm}z}$$
(5.28)

where

$$k_{c1}^2 = \omega^2 \mu_1 \varepsilon_{c1} + \Gamma_{nm}^2 \tag{5.29}$$

$$k_{c2}^2 = \omega^2 \mu_2 \varepsilon_{c2} + \Gamma_{nm}^2$$
 (5.30)

and 
$$\varepsilon_{ci} = \varepsilon_0 \left( \varepsilon_i + \frac{\sigma_i}{j\omega\varepsilon_0} \right), i=1,2.$$

Applying the boundary conditions to these eigenmodes, we can determine the unknown coefficients  $A_{nm}$ ,  $B_{nm}$ ,  $C_{nm}$ ,  $D_{nm}$ ,  $E_{nm}$  and  $F_{nm}$  in eqs. (5.17) to (5.28). The boundary conditions are as follows:

(1) 
$$E_{z2}(r=a)=0$$

$$C_{nm}J_n(k_{c2}a) + D_{nm}Y_n(k_{c2}a) = 0 (5.31)$$

$$(2) E_{\theta 2}(r=a)=0$$

$$\Gamma_{nm} \frac{n}{a} [C_{nm} J_n(k_{c2}a) + D_{nm} Y_n(k_{c2}a)] +$$

$$j \omega \mu_2 k_{c2} [E_{nm} J_n'(k_{c2}a) + F_{nm} Y_n'(k_{c2}a)] = 0$$
(5.32)

Based on eq. (5.31), eq. (5.32) can be rewritten as

$$E_{nm}J_{n}'(k_{c2}a) + F_{nm}Y_{n}'(k_{c2}a) = 0 (5.33)$$

(3) 
$$E_{\theta 1}(r=b^{-}) = E_{\theta 2}(r=b^{+})$$

$$j\omega\mu_{1}B_{nm}k_{c1}J_{n}'(k_{c1}b) + A_{nm}\Gamma_{nm}\frac{n}{b}J_{n}(k_{c1}b) = j\omega\mu_{2}k_{c2}[E_{nm}J_{n}'(k_{c2}b) + F_{nm}Y_{n}'(k_{c2}b)] + \Gamma_{nm}\frac{n}{b}[C_{nm}J_{n}(k_{c2}b) + D_{nm}Y_{n}(k_{c2}b)]$$
(5.34)

(4) 
$$E_{z1}(r=b^{-}) = E_{z2}(r=b^{+})$$

$$A_{nm}k_{c1}^2J_n(k_{c1}b) = \left[C_{nm}J_n(k_{c2}b) + D_{nm}Y_n(k_{c2}b)\right]k_{c2}^2$$
 (5.35)

(5) 
$$H_{\theta 1}(r=b^{-}) = H_{\theta 2}(r=b^{+})$$

$$-B_{nm}\Gamma_{nm}\frac{n}{b}J_{n}(k_{c1}b)-j\omega\varepsilon_{c1}A_{nm}k_{c1}J_{n}'(k_{c1}b) = -\Gamma_{nm}\frac{n}{b}[E_{nm}J_{n}(k_{c2}b) + F_{nm}Y_{n}(k_{c2}b)] - j\omega\varepsilon_{c2}k_{c2}[C_{nm}J_{n}'(k_{c2}b) + D_{nm}Y_{n}'(k_{c2}b)]$$
(5.36)

(6) 
$$H_{z1}(r=b^{-}) = H_{z2}(r=b^{+})$$

$$B_{nm}k_{c1}^2J_n(k_{c1}b) = [E_{nm}J_n(k_{c2}b) + F_{nm}Y_n(k_{c2}b)]k_{c2}^2$$
 (5.37)

Combining eqs. (5.31) and (5.35), we can express  $C_{nm}$  and  $D_{nm}$  in terms of  $A_{nm}$  as:

$$C_{nm} = -\frac{\frac{k_{c1}^2}{k_{c2}^2} J_n(k_{c1}b) Y_n(k_{c2}a)}{Y_n(k_{c2}b) J_n(k_{c2}a) - Y_n(k_{c2}a) J_n(k_{c2}b)} A_{nm}$$
 (5.38)

$$D_{nm} = \frac{\frac{k_{c1}^2}{k_{c2}^2} J_n(k_{c1}b) J_n(k_{c2}a)}{Y_n(k_{c2}b) J_n(k_{c2}a) - Y_n(k_{c2}a) J_n(k_{c2}b)} A_{nm}$$
(5.39)

Let's denote

$$C_{CDA} = \frac{\frac{k_{c1}^2}{k_{c2}^2} J_n(k_{c1}b)}{Y_n(k_{c2}b) J_n(k_{c2}a) - Y_n(k_{c2}a) J_n(k_{c2}b)}$$
(5.40)

Equations (5.38) and (5.39) can then be rewritten as

$$C_{nm} = -C_{CDA}Y_n(k_{c2}a)A_{nm} (5.41)$$

$$D_{nm} = C_{CDA} J_n(k_{c2} a) A_{nm} (5.42)$$

Using eqs. (5.33) and (5.37), we can express  $E_{nm}$  and  $F_{nm}$  in terms of  $B_{nm}$  as:

$$E_{nm} = -C_{EFB}Y_n'(k_{c2}a)B_{nm} (5.43)$$

$$F_{nm} = C_{EFB} J_n'(k_{c2} a) B_{nm} (5.44)$$

where  $C_{EFB}$  is denoted as

$$C_{EFB} = \frac{\frac{k_{c1}^2}{k_{c2}^2} J_n(k_{c1}b)}{Y_n(k_{c2}b) J_n'(k_{c2}a) - Y_n'(k_{c2}a) J_n(k_{c2}b)}$$
(5.45)

Substituting eqs. (5.41) to (5.44) into eqs. (5.34) and (5.36), respectively, we have

$$j\omega\mu_{1}B_{nm}k_{c1}J_{n}'(k_{c1}b) + A_{nm}\Gamma_{nm}\frac{n}{b}J_{n}(k_{c1}b) = j\omega\mu_{2}k_{c2}[C_{EFB}J_{n}'(k_{c2}a)$$

$$Y_{n}'(k_{c2}b) - C_{EFB}Y_{n}'(k_{c2}a)J_{n}'(k_{c2}b)]B_{nm} + \Gamma_{nm}\frac{n}{b}A_{nm}\frac{k_{c1}^{2}}{k_{c2}^{2}}J_{n}(k_{c1}b)$$
(5.46)

$$-B_{nm}\Gamma_{nm}\frac{n}{b}J_{n}(k_{c1}b)-j\omega\varepsilon_{c1}A_{nm}k_{c1}J_{n}'(k_{c1}b) = -\Gamma_{nm}\frac{n}{b}B_{nm}\frac{k_{c1}^{2}}{k_{c2}^{2}}J_{n}(k_{c1}b)$$

$$-j\omega\varepsilon_{c2}k_{c2}(-C_{CDA}Y_{n}(k_{c2}a)J_{n}'(k_{c2}b) + C_{CDA}J_{n}(k_{c2}a)Y_{n}'(k_{c2}b))A_{nm}$$
(5.47)

Equations (5.46) and (5.47) can be rearranged as

$$A_{nm}\Gamma_{nm}\frac{n}{b}J_{n}(k_{c1}b)\left(1-\frac{k_{c1}^{2}}{k_{c2}^{2}}\right) = j\omega\{\mu_{2}k_{c2}C_{EFB}[-Y_{n}'(k_{c2}a)J_{n}'(k_{c2}b) + J_{n}'(k_{c2}a)Y_{n}'(k_{c2}b)] - \mu_{1}k_{c1}J_{n}'(k_{c1}b)\}B_{nm}$$
(5.48)

$$-B_{nm}\Gamma_{nm}\frac{n}{b}J_{n}(k_{c1}b)\left(1-\frac{k_{c1}^{2}}{k_{c2}^{2}}\right) = j\omega\{\varepsilon_{c1}k_{c1}J_{n}'(k_{c1}b)$$

$$-\varepsilon_{c2}k_{c2}C_{CDA}[J_{n}(k_{c2}a)Y_{n}'(k_{c2}b) - Y_{n}(k_{c2}a)J_{n}'(k_{c2}b)]\}A_{nm}$$
(5.49)

Equations (5.48) and (5.49) can then be rewritten in a matrix form as

$$\begin{bmatrix} M_{11} & M_{12} \\ M_{21} & M_{22} \end{bmatrix} \begin{bmatrix} A_{nm} \\ B_{nm} \end{bmatrix} = \begin{bmatrix} 0 \\ 0 \end{bmatrix}$$
 (5.50)

where

$$M_{11} = M_{22} = -\Gamma_{nm} \frac{n}{b} J_n(k_{c1}b) \left(1 - \frac{k_{c1}^2}{k_{c2}^2}\right)$$
 (5.51)

$$M_{12} = j\omega\mu_{2}k_{c2}C_{EFB}[-Y_{n}'(k_{c2}a)J_{n}'(k_{c2}b) + J_{n}'(k_{c2}a)Y_{n}'(k_{c2}b)] - j\omega\mu_{1}k_{c1}J_{n}'(k_{c1}b)$$
(5.52)

$$M_{21} = j\omega \varepsilon_{c2} k_{c2} C_{CDA} [-Y_n(k_{c2}a) J_n'(k_{c2}b) + J_n(k_{c2}a) Y_n'(k_{c2}b)] - j\omega \varepsilon_{c1} k_{c1} J_n'(k_{c1}b)$$
(5.53)

To have non-trivial solutions for  $A_{nm}$  and  $B_{nm}$ , it is necessary that

$$M_{11}M_{22} - M_{12}M_{21} = 0 (5.54)$$

i.e. the determinant of the matrix in eq. (5.50) is zero. Therefore, we obtain the characteristic equation for the eigenmodes as

$$\left(\Gamma_{nm}\frac{n}{b}J_{n}(k_{c1}b)\left(1-\frac{k_{c1}^{2}}{k_{c2}^{2}}\right)\right)^{2} = \omega^{2}\{\mu_{2}k_{c2}C_{EFB}[Y_{n}'(k_{c2}a)J_{n}'(k_{c2}b)] - J_{n}'(k_{c2}a)Y_{n}'(k_{c2}b)] + \mu_{1}k_{c1}J_{n}'(k_{c1}b)\}\{\varepsilon_{c2}k_{c2}C_{CDA}[J_{n}(k_{c2}a)Y_{n}'(k_{c2}b)] - Y_{n}(k_{c2}a)J_{n}'(k_{c2}b)] - \varepsilon_{c1}k_{c1}J_{n}'(k_{c1}b)\}$$
(5.55)

Substituting eqs. (5.40) and (5.45) into eq. (5.55) and using the relations between  $k_{c1}$ ,  $k_{c2}$  and  $\Gamma_{nm}$  given in eqs. (5.29) and (5.30), we can numerically obtain the propagation constant  $\Gamma_{nm}$  for each eigenmode and then determine the corresponding eigenvalues  $k_{c1}$  and  $k_{c2}$ . After that, based on eqs. (5.41) to (5.44) and (5.48) we can express the other five coefficients in terms of  $A_{nm}$  as

$$B_{nm} = \frac{-\Gamma_{nm} \frac{n}{b} J_n(k_{c1}b) \left(1 - \frac{k_{c1}^2}{k_{c2}^2}\right)}{j \omega k_{c1} \left\{ \mu_1 \frac{k_{c1}}{k_{c2}} C_{BA} J_n(k_{c1}b) - \mu_2 J_n'(k_{c1}b) \right\}} A_{nm}$$
 (5.56)

where

$$C_{BA} = \left[ \frac{J_n'(k_{c2}a)Y_n'(k_{c2}b) - Y_n'(k_{c2}a)J_n'(k_{c2}b)}{Y_n(k_{c2}b)J_n'(k_{c2}a) - Y_n'(k_{c2}a)J_n(k_{c2}b)} \right]$$
(5.57)

and

$$C_{nm} = -\frac{J_n(k_{c1}b)Y_n(k_{c2}a)}{Y_n(k_{c2}b)J_n(k_{c2}a) - Y_n(k_{c2}a)J_n(k_{c2}b)} \frac{k_{c1}^2}{k_{c2}^2} A_{nm}$$
 (5.58)

$$D_{nm} = \frac{J_n(k_{c1}b)J_n(k_{c2}a)}{Y_n(k_{c2}b)J_n(k_{c2}a) - Y_n(k_{c2}a)J_n(k_{c2}b)} \frac{k_{c1}^2}{k_{c2}^2} A_{nm}$$
 (5.59)

$$E_{nm} = -\frac{J_n(k_{c1}b)Y_n'(k_{c2}a)}{Y_n(k_{c2}b)J_n'(k_{c2}a) - Y_n'(k_{c2}a)J_n(k_{c2}b)} \frac{k_{c1}^2}{k_{c2}^2} B_{nm}$$
 (5.60)

$$F_{nm} = \frac{J_n(k_{c1}b)J_n'(k_{c2}a)}{Y_n(k_{c2}b)J_n'(k_{c2}a) - Y_n'(k_{c2}a)J_n(k_{c2}b)\frac{k_{c1}^2}{k_{c2}^2}}B_{nm}$$
 (5.61)

Therefore, we can derive the expressions for all the eigenmodes in the inhomogeneously filled waveguide if we can find the coefficient  $A_{nm}$  in region II.

When n=0, the eigenmodes in region II can be either TM or TE modes. For TM modes, the eigenmodes in sub-region 1 can be expressed as

$$E_{z1} = A_{0m} k_{c1}^2 J_0(k_{c1} r) e^{-\Gamma_{0m} z}$$
 (5.62)

$$E_{r1} = -A_{0m} \Gamma_{0m} k_{c1} J_0'(k_{c1} r) e^{-\Gamma_{0m} z}$$
(5.63)

$$H_{\theta 1} = -j\omega \epsilon_{c1} A_{0m} k_{c1} J_0'(k_{c1} r) e^{-\Gamma_{0m} z}$$
(5.64)

The eigenmodes in sub-region 2 can be expressed as

$$E_{z2} = [C_{0m}J_0(k_{c2}r) + D_{0m}Y_0(k_{c2}r)]k_{c2}^2 e^{-\Gamma_{0m}z}$$
(5.65)

$$E_{r2} = -\Gamma_{0m} k_{c2} [C_{0m} J_0'(k_{c2} r) + D_{0m} Y_0'(k_{c2} r)] e^{-\Gamma_{0m} z}$$
(5.66)

$$H_{\theta 2} = -j\omega \varepsilon_{c2} k_{c2} [C_{0m} J_0'(k_{c2}r) + D_{0m} Y_0'(k_{c2}r)] e^{-\Gamma_{0m} z}$$
(5.67)

Applying boundary conditions to eqs. (5.62) to (5.67), we have

$$C_{0m}J_0(k_{c2}a) + D_{0m}Y_0(k_{c2}a) = 0 (5.68)$$

$$A_{0m}k_{c1}^2J_0(k_{c1}b) = \left[C_{0m}J_0(k_{c2}b) + D_{0m}Y_0(k_{c2}b)\right]k_{c2}^2$$
 (5.69)

$$\varepsilon_{c1} A_{0m} k_{c1} J_0'(k_{c1}b) = \varepsilon_{c2} k_{c2} [C_{0m} J_0'(k_{c2}b) + D_{0m} Y_0'(k_{c2}b)]$$
 (5.70)

Combining eqs. (5.69) and (5.70), we have the following relation of

$$C_{0m} \frac{k_{c2}^2 J_0(k_{c2}b)}{k_{c1}^2 J_0(k_{c1}b)} + D_{0m} \frac{k_{c2}^2 Y_0(k_{c2}b)}{k_{c1}^2 J_0(k_{c1}b)}$$

$$= C_{0m} \frac{\varepsilon_{c2} k_{c2} J_0'(k_{c2}b)}{\varepsilon_{c1} k_{c1}} + D_{0m} \frac{\varepsilon_{c2} k_{c2} Y_0'(k_{c2}b)}{\varepsilon_{c1} k_{c1}}$$

$$= C_{0m} \frac{\varepsilon_{c2} k_{c2} J_0'(k_{c2}b)}{\varepsilon_{c1} k_{c1} J_0'(k_{c1}b)} + D_{0m} \frac{\varepsilon_{c2} k_{c2} Y_0'(k_{c2}b)}{\varepsilon_{c1} k_{c1} J_0'(k_{c1}b)}$$
(5.71)

or

$$C_{0m} \left[ \frac{k_{c2} J_0(k_{c2}b)}{k_{c1} J_0(k_{c1}b)} - \frac{\varepsilon_{c2} J_0'(k_{c2}b)}{\varepsilon_{c1} J_0'(k_{c1}b)} \right] + D_{0m} \left[ \frac{k_{c2} Y_0(k_{c2}b)}{k_{c1} J_0(k_{c1}b)} - \frac{\varepsilon_{c2} Y_0'(k_{c2}b)}{\varepsilon_{c1} J_0'(k_{c1}b)} \right] = 0 \quad (5.72)$$

Combining eqs. (5.68) and (5.72), we obtain the following characteristic equation for the

TM modes as

$$J_{0}(k_{c2}a) \left[ \frac{k_{c2}}{k_{c1}} \frac{Y_{0}(k_{c2}b)}{J_{0}(k_{c1}b)} - \frac{\varepsilon_{c2}}{\varepsilon_{c1}} \frac{Y_{0}'(k_{c2}b)}{J_{0}'(k_{c1}b)} \right]$$

$$-Y_{0}(k_{c2}a) \left[ \frac{k_{c2}}{k_{c1}} \frac{J_{0}(k_{c2}b)}{J_{0}(k_{c1}b)} - \frac{\varepsilon_{c2}}{\varepsilon_{c1}} \frac{J_{0}'(k_{c2}b)}{J_{0}'(k_{c1}b)} \right] = 0$$
(5.73)

and the unknown coefficients can be expressed in terms of  $C_{0m}$  as

$$D_{0m} = -\frac{J_0(k_{c2}a)}{Y_0(k_{c2}a)}C_{0m}$$
 (5.74)

$$A_{0m} = C_{0m} \frac{k_{c2}^2}{k_{c1}^2} \left[ \frac{J_0(k_{c2}b)}{J_0(k_{c1}b)} - \frac{J_0(k_{c2}a)}{Y_0(k_{c2}a)} \frac{Y_0(k_{c2}b)}{J_0(k_{c1}b)} \right]$$
 (5.75)

For TE modes, the eigenmodes in sub-region 1 can be expressed as

$$H_{z1} = B_{0m} k_{c1}^2 J_0(k_{c1} r) e^{-\Gamma_{0m} z}$$
 (5.76)

$$H_{r1} = -B_{0m} \Gamma_{0m} k_{c1} J_0'(k_{c1} r) e^{-\Gamma_{0m} z}$$
(5.77)

$$E_{\theta 1} = j\omega \mu_1 B_{0m} k_{c1} J_0'(k_{c1} r) e^{-\Gamma_{0m} z}$$
 (5.78)

The eigenmodes in sub-region 2 can be expressed as

$$H_{z2} = [E_{0m}J_0(k_{c2}r) + F_{0m}Y_0(k_{c2}r)]k_{c2}^2 e^{-\Gamma_{0m}z}$$
(5.79)

$$H_{r2} = -\Gamma_{0m} k_{c2} [E_{0m} J_0'(k_{c2}r) + F_{0m} Y_0'(k_{c2}r)] e^{-\Gamma_{0m}z}$$
(5.80)

$$E_{\theta 2} = j\omega \mu_2 k_{c2} [E_{0m} J_0'(k_{c2}r) + F_{0m} Y_0'(k_{c2}r)] e^{-\Gamma_{0m}z}$$
(5.81)

Applying boundary conditions to eqs. (5.76) to (5.81), we have

$$E_{0m}J_0'(k_c,a) + F_{0m}Y_0'(k_c,a) = 0 (5.82)$$

$$\mu_1 B_{0m} k_{c1} J_0'(k_{c1}b) = \mu_2 k_{c2} [E_{0m} J_0'(k_{c2}b) + F_{0m} Y_0'(k_{c2}b)]$$
 (5.83)

$$B_{0m}k_{c1}^2J_0(k_{c1}b) = [E_{0m}J_0(k_{c2}b) + F_{0m}Y_0(k_{c2}b)]k_{c2}^2$$
(5.84)

Using eqs. (5.83) and (5.84) we have the following relation of

$$E_{0m} \frac{\mu_2 k_{c2}}{\mu_1 k_{c1}} \frac{J_0'(k_{c2}b)}{J_0'(k_{c1}b)} + F_{0m} \frac{\mu_2 k_{c2}}{\mu_1 k_{c1}} \frac{Y_0'(k_{c2}b)}{J_0'(k_{c1}r)} = E_{0m} \frac{k_{c2}^2}{k_{c1}^2} \frac{J_0(k_{c2}b)}{J_0(k_{c1}b)} + F_{0m} \frac{k_{c2}^2}{k_{c1}^2} \frac{Y_0(k_{c2}b)}{J_0(k_{c1}b)}$$
(5.85)

or

$$E_{0m} \left[ \frac{\mu_2 J_0'(k_{c2}b)}{\mu_1 J_0'(k_{c1}b)} - \frac{k_{c2} J_0(k_{c2}b)}{k_{c1} J_0(k_{c1}b)} \right] + F_{0m} \left[ \frac{\mu_2 Y_0'(k_{c2}b)}{\mu_1 J_0'(k_{c1}b)} - \frac{k_{c2} Y_0(k_{c2}b)}{k_{c1} J_0(k_{c1}b)} \right] = 0$$
 (5.86)

Combining eqs. (5.82) and (5.86), we obtain the characteristic equation for the *TE* modes as

$$J_{0}'(k_{c2}a) \left[ \frac{\mu_{2} Y_{0}'(k_{c2}b)}{J_{0}'(k_{c1}b)} - \frac{k_{c2} Y_{0}(k_{c2}b)}{k_{c1} J_{0}(k_{c1}b)} \right]$$

$$-Y_{0}'(k_{c2}a) \left[ \frac{\mu_{2} J_{0}'(k_{c2}b)}{\mu_{1} J_{0}'(k_{c1}b)} - \frac{k_{c2} J_{0}(k_{c2}b)}{k_{c1} J_{0}(k_{c1}b)} \right] = 0$$

$$(5.87)$$

and the unknown coefficients can be expressed in terms of  $E_{0m}$  as

$$F_{0m} = -\frac{J_0'(k_{c2}a)}{Y_0'(k_{c2}a)}E_{0m}$$
 (5.88)

$$B_{0m} = E_{0m} \frac{k_{c2}^2}{k_{c1}^2} \left[ \frac{J_0(k_{c2}b)}{J_0(k_{c1}b)} - \frac{J_0'(k_{c2}a)}{Y_0'(k_{c2}a)} \frac{Y_0(k_{c2}b)}{J_0(k_{c1}b)} \right]$$
 (5.89)

## 5.1.3 Normalization of Homogeneously filled Waveguide Eigenmodes

The normalization of the homogeneously filled waveguide eigenmodes can be realized by the relation of

$$\int_{CS} \dot{\hat{e}}_{n1} \cdot \dot{\hat{e}}_{n1} dS = 1 \tag{5.90}$$

where  $\dot{e}_{n1}(r,\theta)$  is the transverse component of the eigenmode in region I or III and the integration region is over the cross section of the waveguide.

For TE mode, using eqs. (5.12) and (5.13) the normalization leads to

$$-(\omega\mu A_{nm})^2 \int_{0}^{a2\pi} \left\{ \left[ \frac{n}{r} J_n \left( \frac{p_{nm}}{a} r \right) \cos n\theta \right]^2 + \left[ \frac{p_{nm}}{a} J_n \left( \frac{p_{nm}}{a} r \right) \sin n\theta \right]^2 \right\} r dr d\theta = 1 \quad (5.91)$$

when  $n \neq 0$ . Equation (4.65) gives us the integration of

$$\int_{0}^{p_{nm}} \left[ \frac{n^{2}}{r} J_{n}^{2}(r) + J_{n}^{2}(r) r \right] dr = \frac{1}{2} (p_{nm}^{2} - n^{2}) J_{n}^{2}(p_{nm})$$
 (5.92)

After integrating over the variable  $\theta$  and changing the integration variable r, eq. (5.91) can be rewritten as

$$-(\omega \mu A_{nm})^2 \pi \int_{0}^{p_{nm}'} \left[ \frac{n^2}{r} J_n^2(r) + (J_n'(r))^2 r \right] dr = 1$$
 (5.93)

Using eq. (5.92), we have

$$A_{nm} = j \sqrt{\frac{2}{\pi}} \frac{1}{\omega \mu J_n(p_{nm}') \sqrt{p_{nm}'^2 - n^2}}$$
 (5.94)

When n = 0, the normalization is given by eq. (5.16) as

$$-(\omega \mu A_{0m})^2 2\pi \int_0^a \left[ \frac{p_{0m}}{a} J_0 \left( \frac{p_{0m}}{a} r \right) \right]^2 r dr = 1$$
 (5.95)

Equations (4.70) and (4.72) give us the integration of

$$\int_{0}^{p_{0m'}} J_0^{'2}(r) r dr = \frac{p_{0m'}^{'2}}{2} J_0^2(p_{0m'})$$
 (5.96)

Therefore, the normalization constant is given by

$$A_{0m} = j \sqrt{\frac{1}{\pi}} \frac{1}{\omega \mu J_0(p_{0m}) p_{0m}}$$
 (5.97)

Combining eqs. (5.94) and (5.97), we have

$$A_{nm} = j \sqrt{\frac{\varepsilon_{0n}}{\pi}} \frac{1}{\omega \mu J_n(p_{nm}) \sqrt{p_{nm}^2 - n^2}}$$
 (5.98)

where  $\varepsilon_{0n}$  is defined in eq. (2.63).

For TM mode, using eqs. (5.2) and (5.3) the normalization leads to

$$(A_{nm}\Gamma_{nm})^2 \int_{0}^{a} \int_{0}^{2\pi} \left\{ \left[ \frac{p_{nm}}{a} J_n \left( \frac{p_{nm}}{a} r \right) \cos n\theta \right]^2 + \left[ \frac{n}{r} J_n \left( \frac{p_{nm}}{a} r \right) \sin n\theta \right]^2 \right\} r dr d\theta = 1 \quad (5.99)$$

when  $n \neq 0$ . Equation (4.80) gives us the integration of

$$\int_{0}^{p_{nm}} \left[ \frac{n^2}{r} J_n^2(r) + J_n^{2}(r) r \right] dr = \frac{p_{nm}}{2} J_n^{2}(p_{nm})$$
 (5.100)

After integrating over the variable  $\theta$ , changing the integration variable r and using eq.

(5.100), we obtain the normalization constant  $A_{nm}$  as

$$A_{nm} = \sqrt{\frac{\varepsilon_{0n}}{\pi}} \frac{1}{\Gamma_{nm} p_{nm} J_n'(p_{nm})}$$
 (5.101)

#### 5.2 Electromagnetic Fields in Three Regions

Up to now we have obtained the eigenmodes in each region shown in Figure 5.1. The electromagnetic fields in each region can then be expressed as the infinite summations of the eigenmodes in the corresponding region.

Because we assume that there is an excitation probe in region I, the electric field in region I for  $0 \le z \le z_1$  can be expressed as

$$\vec{E}_1(\vec{r}) = \int_{V} \vec{J}(\vec{r}_0) \bullet \vec{G}(\vec{r}_0, \vec{r}) dV_0$$
 (5.102)

where the dyadic Green's function is given by [10]

$$\overline{G}(\dot{r}_0, \dot{r}) = \sum_{n=1}^{N_1} \frac{-\dot{e}_{n1}(r_0, \theta_0)}{2(1 - R_{1n}R_{2n})} (1 + R_{1n}) Z_n(\dot{E}_{n1}^+(\dot{r}) + R_{2n}\dot{E}_{n1}^-(\dot{r}))$$
(5.103)

for  $z \ge 0$ .  $\hat{e}_{n1}(r_0, \theta_0)$  is the transverse component of the eigenmode in region I which is normalized by eq. (5.90).  $\hat{E}_{n1}^{\pm}(\hat{r})$  is the eigenmode propagating in  $\pm z$  direction as

$$\vec{E}_{n1}^{+}(\dot{r}) = [\dot{e}_{n1}(r,\theta) + \hat{z}e_{zn1}(r,\theta)]e^{-\Gamma_{n}z}$$
(5.104)

$$\dot{\overline{E}}_{n1}(\dot{r}) = [\dot{e}_{n1}(r,\theta) - \hat{z}e_{zn1}(r,\theta)]e^{\Gamma_n z}$$
(5.105)

 $R_{1n}$  and  $R_{2n}$  are the reflection coefficients of the *nth* mode due to the short-circuit

termination at  $z=-z_0$  and the discontinuity at  $z=z_1$  in region I, respectively. Therefore,  $R_{1n}=-e^{-2\Gamma_n z_0}$  and  $R_{2n}$  is unknown. The wave impedances for the *TE* and *TM* modes are expressed as

$$Z_{nTE} = \frac{j\omega\mu}{\Gamma_n} \tag{5.106}$$

$$Z_{nTM} = \frac{\Gamma_n}{j\omega\varepsilon} \tag{5.107}$$

where  $\Gamma_n$  is the wave propagation constant of the *nth* mode and is given by  $\Gamma_n^2 = k_{c1}^2 - \omega^2 \mu_1 \varepsilon_1 \text{ with } k_{c1} \text{ as the eigenvalue of the eigenmode, } \mu_1 \text{ and } \varepsilon_1 \text{ are the dielectric parameters of the medium in region I. The upper summation limit <math>N_I$  is set to assure a convergent result. The current density on the excitation probe is assumed to have a sinusoidal distribution as

$$\hat{J}(\hat{r}) = \hat{r}I_m \frac{\sin\beta(l-a+r)}{\sin\beta l} \delta(\theta)\delta(z)$$
 (5.108)

where  $\beta$  is the wave number in the medium of region I, l is the length of the excitation probe.

Rewriting the dyadic Green's function (5.103) as

$$\overline{G}(\dot{r}_{0}, \dot{r}) = \sum_{n=1}^{N_{1}} \frac{-\dot{e}_{n1}(r_{0}, \theta_{0})}{2} (1 + R_{1n}) Z_{n} \ \dot{\overline{E}}_{n1}^{+}(\dot{r}) 
+ \sum_{n=1}^{N} \frac{-\dot{e}_{n1}(r_{0}, \theta_{0})}{2(1 - R_{1n}R_{2n})} (1 + R_{1n}) R_{2n} Z_{n} [R_{1n} \ \dot{\overline{E}}_{n1}^{+}(\dot{r}) + \dot{\overline{E}}_{n1}^{-}(\dot{r})]$$
(5.109)

and substituting eq. (5.109) into eq. (5.102), we can obtain the electric field in region I as:

$$\vec{E}_{1}(\vec{r}) = \sum_{n=1}^{N_{1}} V_{n} e^{\Gamma_{n} z_{1}} \vec{E}_{n1}^{+}(\vec{r}) + \sum_{n=1}^{N_{1}} A_{n} e^{-\Gamma_{n} z_{1}} [R_{1n} \vec{E}_{n1}^{+}(\vec{r}) + \vec{E}_{n1}(\vec{r})]$$
 (5.110)

where

$$V_n = -\frac{1 + R_{1n}}{2} Z_n e^{-\Gamma_n z_1} \int [\dot{\hat{e}}_{n1}(r_0, \theta_0) \cdot \dot{\hat{J}}(\dot{\hat{r}}_0)] dV_0$$
 (5.111)

is known and

$$A_{n} = -\frac{1 + R_{1n}}{2(1 - R_{1n}R_{2n})} R_{2n} Z_{n} e^{\Gamma_{n} z_{1}} \int [\dot{e}_{n1}(r_{0}, \theta_{0}) \cdot \dot{\vec{J}}(\dot{r}_{0})] dV_{0}$$
 (5.112)

is unknown due to the unknown reflection coefficient  $R_{2n}$ . The magnetic field in region I can also be expressed as

$$\vec{H}_{1}(\hat{r}) = \sum_{n=1}^{N_{1}} V_{n} e^{\Gamma_{n} z_{1}} \vec{H}_{n1}^{+}(\hat{r}) + \sum_{n=1}^{N_{1}} A_{n} e^{-\Gamma_{n} z_{1}} (R_{1n} \vec{H}_{n1}^{+}(\hat{r}) + \vec{H}_{n1}^{-}(\hat{r}))$$
 (5.113)

where

$$\vec{H}_{n1}^{+}(\hat{r}) = [\hat{h}_{n1}(r,\theta) + \hat{z}h_{2n1}(r,\theta)]e^{-\Gamma_{n}z}$$
(5.114)

$$\vec{H}_{n1}(\hat{r}) = [-\hat{h}_{n1}(r,\theta) + \hat{z}h_{zn1}(r,\theta)]e^{\Gamma_n z}$$
(5.115)

In region II,  $z_1 \le z \le z_2$ , the electromagnetic fields can be represented as

$$\vec{E}_{2}(\vec{r}) = \sum_{m=1}^{M} \left[ B_{m} e^{\Gamma_{m} z_{1}} \vec{E}_{m2}^{+}(\vec{r}) + C_{m} e^{-\Gamma_{m} z_{2}} \vec{E}_{m2}^{-}(\vec{r}) \right]$$
 (5.116)

$$\vec{H}_{2}(\vec{r}) = \sum_{m=1}^{M} \left[ B_{m} e^{\Gamma_{m} z_{1}} \ \vec{H}_{m2}^{+}(\vec{r}) + C_{m} e^{-\Gamma_{m} z_{2}} \vec{H}_{m2}^{-}(\vec{r}) \right]$$
 (5.117)

where  $\vec{E}_{m2}^{\pm}(\hat{r})$  and  $\vec{H}_{m2}^{\pm}(\hat{r})$  denote the electromagnetic eigenmodes propagating in  $\pm z$  direction derived in Section 5.1.2.

In region III,  $z_2 \le z \le z_3$ , the electromagnetic fields can be represented as

$$\vec{E}_{3}(\vec{r}) = \sum_{n=1}^{N_{2}} D_{n} e^{\Gamma_{n} z_{2}} [\vec{E}_{n1}^{+}(\vec{r}) + R_{n} \vec{E}_{n1}^{-}(\vec{r})]$$
 (5.118)

$$\vec{H}_{3}(\vec{r}) = \sum_{n=1}^{N_{2}} D_{n} e^{\Gamma_{n} z_{2}} [\vec{H}_{n1}^{+}(\vec{r}) + R_{n} \vec{H}_{n1}^{-}(\vec{r})]$$
 (5.119)

where  $R_n = -e^{-2\Gamma_n c}$  is the reflection coefficient at the termination of  $z = z_3$ .

After the total electromagnetic fields in the three regions are found, we can express the transverse components of the electromagnetic fields in each region as:

$$\dot{\vec{E}}_{1t}(\dot{r}) = \sum_{n=1}^{N_1} V_n e^{-\Gamma_n(z-z_1)} \dot{\vec{e}}_{n1}(r,\theta) + \sum_{n=1}^{N_1} A_n (-e^{-\Gamma_n(z_1+2z_0+z)} + e^{\Gamma_n(z-z_1)}) \dot{\vec{e}}_{n1}(r,\theta)$$
(5.120)

$$\vec{H}_{1t}(\vec{r}) = \sum_{n=1}^{N_1} V_n e^{-\Gamma_n(z-z_1)} \hat{h}_{nl}(r,\theta) + \sum_{n=1}^{N_1} A_n (-e^{-\Gamma_n(z_1+2z_0+z)} - e^{\Gamma_n(z-z_1)}) \hat{h}_{nl}(r,\theta)$$
(5.121)

$$\vec{E}_{2t}(\hat{r}) = \sum_{m=1}^{M} \left[ B_m e^{-\Gamma_m (z - z_1)} + C_m e^{\Gamma_m (z - z_2)} \right] \dot{e}_{m2}(r, \theta)$$
 (5.122)

$$\vec{H}_{2t}(\vec{r}) = \sum_{m=1}^{M} \left[ B_m e^{-\Gamma_m (z-z_1)} - C_m e^{\Gamma_m (z-z_2)} \right] \hat{h}_{m2}(r,\theta)$$
 (5.123)

$$\vec{E}_{3t}(\hat{r}) = \sum_{n=1}^{N_2} D_n [e^{-\Gamma_n(z-z_2)} - e^{\Gamma_n(z+z_2-2z_3)}] \dot{e}_{n1}(r,\theta)$$
 (5.124)

$$\vec{H}_{3l}(\vec{r}) = \sum_{n=1}^{N_2} D_n \left[ e^{-\Gamma_n(z-z_2)} + e^{\Gamma_n(z+z_2-2z_3)} \right] \vec{h}_{n1}(r,\theta)$$
 (5.125)

The boundary conditions at the junctions of the different regions are the continuity of the transverse components of the electric and magnetic fields. Therefore, at  $z=z_1$ , we have

$$\sum_{n=1}^{N_1} V_n \dot{\tilde{e}}_{n1}(r,\theta) + \sum_{n=1}^{N_1} A_n (-e^{-2\Gamma_n(z_1 + z_0)} + 1) \dot{\tilde{e}}_{n1}(r,\theta)$$

$$= \sum_{m=1}^{M} [B_m + C_m e^{\Gamma_m(z_1 - z_2)}] \dot{\tilde{e}}_{m2}(r,\theta)$$
(5.126)

$$\sum_{n=1}^{N_1} V_n \dot{h}_{n1}(r,\theta) + \sum_{n=1}^{N_1} A_n (-e^{-2\Gamma_n(z_1 + z_0)} - 1) \dot{h}_{n1}(r,\theta)$$

$$= \sum_{m=1}^{M} [B_m - C_m e^{\Gamma_m(z_1 - z_2)}] \dot{h}_{m2}(r,\theta)$$
(5.127)

At  $z = z_2$ , the boundary conditions can be expressed as

$$\sum_{m=1}^{M} \left[ B_m e^{-\Gamma_m (z_2 - z_1)} + C_m \right] \dot{\hat{e}}_{m2}(r, \theta) = \sum_{n=1}^{N_2} D_n \left[ 1 - e^{2\Gamma_n (z_2 - z_3)} \right] \dot{\hat{e}}_{n1}(r, \theta)$$
 (5.128)

$$\sum_{m=1}^{M} \left[ B_m e^{-\Gamma_m (z_2 - z_1)} - C_m \right] \hat{h}_{m2}(r, \theta) = \sum_{n=1}^{N_2} D_n \left[ 1 + e^{2\Gamma_n (z_2 - z_3)} \right] \hat{h}_{n1}(r, \theta)$$
 (5.129)

Since the electric eigenmodes in the homogeneously filled waveguide are orthonormal, that is, they satisfy

$$\int_{CS} \dot{\hat{e}}_{n1} \cdot \dot{\hat{e}}_{m1} dS = \begin{cases} 1 & \text{if } n = m \\ 0 & \text{if } n \neq m \end{cases}$$
 (5.130)

$$\int_{CS} \vec{h}_{n1} \cdot \vec{h}_{m1} dS = \begin{cases} \frac{1}{Z_n^2} & \text{if } n = m \\ 0 & \text{if } n \neq m \end{cases}$$

$$(5.131)$$

Thus, eqs. (5.126) to (5.129) can be changed to

$$A_{n} = -\frac{V_{n}}{1 - e^{-2\Gamma_{n}(z_{1} + z_{0})}} + \frac{\sum_{m=1}^{M} [B_{m} + C_{m}e^{\Gamma_{m}(z_{1} - z_{2})}] \int_{CS} \dot{e}_{n1} \cdot \dot{e}_{m2} dS}{1 - e^{-2\Gamma_{n}(z_{1} + z_{0})}}$$
(5.132)

$$A_{n} = \frac{V_{n}}{1 + e^{-2\Gamma_{n}(z_{1} + z_{0})}} - \frac{Z_{n}^{2}}{1 + e^{-2\Gamma_{n}(z_{1} + z_{0})}} \sum_{m=1}^{M} \left[B_{m} - C_{m}e^{\Gamma_{m}(z_{1} - z_{2})}\right] \int_{CS} \hat{h}_{n1} \cdot \hat{h}_{m2} dS \quad (5.133)$$

$$D_{n} = \frac{\sum_{m=1}^{M} \left[B_{m}e^{-\Gamma_{m}(z_{2}-z_{1})} + C_{m}\right] \int_{CS} \dot{e}_{n1} \cdot \dot{e}_{m2} dS}{1 - e^{2\Gamma_{n}(z_{2}-z_{3})}}$$
(5.134)

$$Z_{n}^{2} \sum_{m=1}^{M} \left[ B_{m} e^{-\Gamma_{m}(z_{2}-z_{1})} - C_{m} \right]$$

$$D_{n} = \frac{m=1}{1 + e^{2\Gamma_{n}(z_{2}-z_{3})}} \int_{CS} \vec{h}_{n1} \cdot \vec{h}_{m2} dS$$
(5.135)

Equations (5.132) and (5.133) are valid for  $n = 1, 2, ..., N_1$  and eqs. (5.134) and (5.135) are valid for  $n = 1, 2, ..., N_2$ . Let's denote

$$e_{mn} = \int_{CS} \dot{\hat{e}}_{n1} \cdot \dot{\hat{e}}_{m2} dS \tag{5.136}$$

$$h_{mn} = \int_{CS} \dot{h}_{n1} \cdot \dot{h}_{m2} dS \tag{5.137}$$

then based on eqs. (5.132) and (5.133), we have

$$\sum_{m=1}^{M} \left( \left[ \frac{e_{mn}}{1 - e^{-2\Gamma_n(z_1 + z_0)}} + \frac{Z_n^2 h_{mn}}{1 + e^{-2\Gamma_n(z_1 + z_0)}} \right] B_m + \left[ \frac{e^{\Gamma_m(z_1 - z_2)} e_{mn}}{1 - e^{-2\Gamma_n(z_1 + z_0)}} \right] - \frac{Z_n^2 e^{\Gamma_m(z_1 - z_2)} h_{mn}}{1 + e^{-2\Gamma_n(z_1 + z_0)}} \right] C_m = \frac{2V_n}{1 - e^{-4\Gamma_n(z_1 + z_0)}}$$
(5.138)

for  $n = 1, 2, ..., N_1$ . Based on eqs. (5.134) and (5.135), we have

$$\sum_{m=1}^{M} \left[ \left[ \frac{e_{mn}}{1 - e^{2\Gamma_n(z_2 - z_3)}} - \frac{Z_n^2 h_{mn}}{1 + e^{2\Gamma_n(z_2 - z_3)}} \right] e^{-\Gamma_m(z_2 - z_1)} B_m + \left[ \frac{e_{mn}}{1 - e^{2\Gamma_n(z_2 - z_3)}} + \frac{Z_n^2 h_{mn}}{1 + e^{2\Gamma_n(z_2 - z_3)}} \right] C_m \right] = 0$$
(5.139)

for  $n = 1, 2, \dots, N_2$ . Equations (5.138) and (5.139) are expressed in a matrix form as

$$[BM_1]_{N_1 \times M}[B]_{M \times 1} + [CM_1]_{N_1 \times M}[C]_{M \times 1} = [VS]_{N_1 \times 1}$$
 (5.140)

$$[BM_2]_{N,\times M}[B]_{M\times 1} + [CM_2]_{N,\times M}[C]_{M\times 1} = [0]_{N_2\times 1}$$
 (5.141)

where the elements in each matrix defined in eqs. (5.140) and (5.141) are expressed as

$$BM_{1nm} = \frac{e_{mn}}{1 - e^{-2\Gamma_n(z_1 + z_0)}} + \frac{Z_n^2 h_{mn}}{1 + e^{-2\Gamma_n(z_1 + z_0)}}$$
(5.142)

$$CM_{1nm} = \frac{e^{\Gamma_m(z_1 - z_2)} e_{mn}}{1 - e^{-2\Gamma_n(z_1 + z_0)}} - \frac{Z_n^2 e^{\Gamma_m(z_1 - z_2)} h_{mn}}{1 + e^{-2\Gamma_n(z_1 + z_0)}}$$
(5.143)

$$VS_n = \frac{2V_n}{1 - e^{-4\Gamma_n(z_1 + z_0)}}$$
 (5.144)

for  $n = 1, 2, ..., N_1$  and m = 1, 2, ..., M.

$$BM_{2nm} = \left[ \frac{e_{mn}}{1 - e^{2\Gamma_n(z_2 - z_3)}} - \frac{Z_n^2 h_{mn}}{1 + e^{2\Gamma_n(z_2 - z_3)}} \right] e^{-\Gamma_m(z_2 - z_1)}$$
(5.145)

$$CM_{2nm} = \frac{e_{mn}}{1 - e^{2\Gamma_n(z_2 - z_3)}} + \frac{Z_n^2 h_{mn}}{1 + e^{2\Gamma_n(z_2 - z_3)}}$$
(5.146)

for  $n = 1, 2, ..., N_2$  and m = 1, 2, ..., M. The unknown coefficients can be expressed as

$$[B]_{M \times 1} = [B_1, B_2, \dots, B_M]^T$$
 (5.147)

$$[C]_{M \times 1} = [C_1, C_2, \dots, C_M]^T$$
 (5.148)

If we choose  $N_1 = N_2 = M$ , the matrices  $[BM_1]$ ,  $[CM_1]$ ,  $[BM_2]$ , and  $[CM_2]$  in eqs. (5.140) and (5.141) are square matrix and the solutions for  $B_m$  and  $C_m$  can be expressed as

$$[B]_{M\times 1} = [[BM_1] - [CM_1][CM_2]^{-1}[BM_2]]^{-1}[VS]$$
 (5.149)

$$[C]_{M\times 1} = [[CM_1] - [BM_1][BM_2]^{-1}[CM_2]]^{-1}[VS]$$
 (5.150)

Therefore, we can determine the electromagnetic fields in region II after the unknown coefficients  $B_m$  and  $C_m$  are obtained from eqs. (5.149) and (5.150). Substituting the solutions for  $B_m$  and  $C_m$  into eqs. (5.132) or (5.133) and (5.134) or (5.135), the solutions for the unknown coefficients  $A_n$  and  $D_n$  can be found and then the electromagnetic fields

in region I and III can be determined.

## 5.3 Numerical Example

In this section, the numerical results based on the mode-matching method will be demonstrated. As stated before, we restrict the material samples which are placed in a cylindrical waveguide to be of simple cylindrical shapes and homogeneous. The numerical results obtained in this chapter will be compared with the corresponding results shown in Section 4.4 in Chapter 4.

In the numerical computation, the eigenmodes in region II are derived first after the dimensions and the dielectric parameters of the material sample are selected. The integrations of product of the eigenmodes in regions I and II (given in eqs. (5.136) and (5.137)) are then calculated. After that the unknown coefficients needed in eqs. (5.110), (5.113) and (5.116) to (5.119) are obtained from eqs. (5.149), (5.150), (5.132) and (5.134). Equations (5.133) and (5.135) can be employed to check the validity of the numerical solutions for these coefficients. After the total electromagnetic fields are obtained and their numerical results can be checked further by the boundary conditions at the perfectly conducting walls and at the junctions of the different regions.

Examining the matrix eqs. (5.140) and (5.141), we find that when  $VS_n = 0$  for some indices n, the solutions for  $B_m$  and  $C_m$  become zero also. Thus, we can select the eigenmodes based on both the values of  $VS_n$  and the convergence property of the summation for the electromagnetic fields in each region.

In the following numerical computations, we assume the dimensions of the cylindrical waveguide shown in Figure 5.1 to be: the radius a=0.0762m and the length

c=0.15458m. A cylindrical material sample with the dimensions of radius  $r_0$  and length  $h_0$  is placed in the center of the waveguide. The position of the excitation probe is at c/4 from the bottom of the waveguide, that is,  $z_0=\frac{c}{4}$  and  $z_3=\frac{3\times c}{4}$ . The values of b,  $z_1$  and  $z_2$  are determined by the dimensions of the material sample to be  $b=r_0$ ,  $z_1=\frac{c}{2}-\frac{h_0}{2}-z_0$  and  $z_2=\frac{c}{2}+\frac{h_0}{2}-z_0$ . The length of the excitation probe is chosen as the half of the radius of the waveguide, a/2, and the operating frequency is 2.45 GHz. The relative permittivity of the material sample is assumed to be  $\varepsilon_r=2.5$  and it is lossless.

Several numerical calculations are carried out for the material sample with selected shapes and dimensions.

#### 1. Cubic material sample

A cubic material sample, having the diameter equal to the length, is placed in the center of the cylindrical waveguide. The dimensions of the material sample are chosen as: radius  $r_0=0.004m$  and length  $h_0=0.008m$ .

In the numerical computation, the number of modes to be summed is set to be 62 based on the non zero values of the right hand side of the eq. (5.140). However, observing the numerical results for the solutions of the unknown coefficients  $A_n$  and  $D_n$  in regions I and III, we find that there only exist several waveguide modes with significant magnitudes which are shown in Table 5.1, and the  $TM_{01}$  mode appears as the dominant mode. This result is expected because of the choice of the dimensions of the cylindrical waveguide and the operating frequency of the excitation probe. The computational results show that

Table 5.1 Significant modes in the mode-matching method when the dimensions of the cavity are: a=0.0762m, c=0.15458m and that of the material sample are:  $r_0=0.004$ m and  $h_0=0.008m$ . The operating frequency is 2.45 GHz, and the excitation probe is located at c/4 from the bottom.

Mode	A <sub>n</sub> (real, imaginary)	D <sub>n</sub> (real, imaginary)
TM <sub>01</sub>	-79.1583, 11.9465	78.8164, -14.0405
TM <sub>02</sub>	0, -0.5485	0, 0.3906
TM <sub>03</sub>	0, 0.8847	0, -0.8946
TM <sub>04</sub>	0, -1.1825	0, 1.1827
TM <sub>05</sub>	0, 1.4291	0, -1.4276
TM <sub>06</sub>	0, -1.6162	0, 1.6144
TM <sub>07</sub>	0, 1.7506	0, -1.7483
TM <sub>II</sub>	-0.1651, 0.1809	0.1798, 0.1671
TE <sub>12</sub>	-3.8618, 2.3057	4.4303, 0.7882

the electromagnetic fields in each region do not vary significantly with respect to the variable  $\theta$  and the z component of the induced electric field dominates the other two components of the electric field near the center of the waveguide.

The validity of the numerical results are checked by the continuity of the tangential components of the electromagnetic field at the junctions of the different regions and the boundary conditions at the cavity walls.

Figure 5.3 demonstrates the ratio of the z component of the induced electric field in the material sample to that of the electric field near the material sample in the empty region of the waveguide as a function of z at r=0.0004m. The ratios are around 0.69 to 0.72 which are close to 0.667 given by the electrostatic estimation of  $E_y/E_y^i = \frac{3}{2+\epsilon_r}$ , and they are consistent with the results found in Chapter 4.

For a larger cubic material sample with the dimensions:  $r_0$ =0.01m and  $h_0$ =0.02m, the number of the modes is set to be 76. The most significant values for the unknown coefficients  $A_n$  and  $D_n$  in regions I and III still belong to the  $TM_{01}$  waveguide mode. Therefore, the z component of the induced electric field dominates near the center of the waveguide, and Figure 5.4 shows the ratio of the z component of the induced electric field in the material sample to that of the electric field in the empty waveguide near the material sample varying as a function of r at the different locations of z. Due to the symmetric property of the numerical solutions, we only plot the ratios in the lower half of the material sample in Figure 5.4. Comparing the results of Figure 5.4 with that of Figure 4.9 in Chapter 4, we can see a good agreement between these two sets of numerical results generated by two different methods.

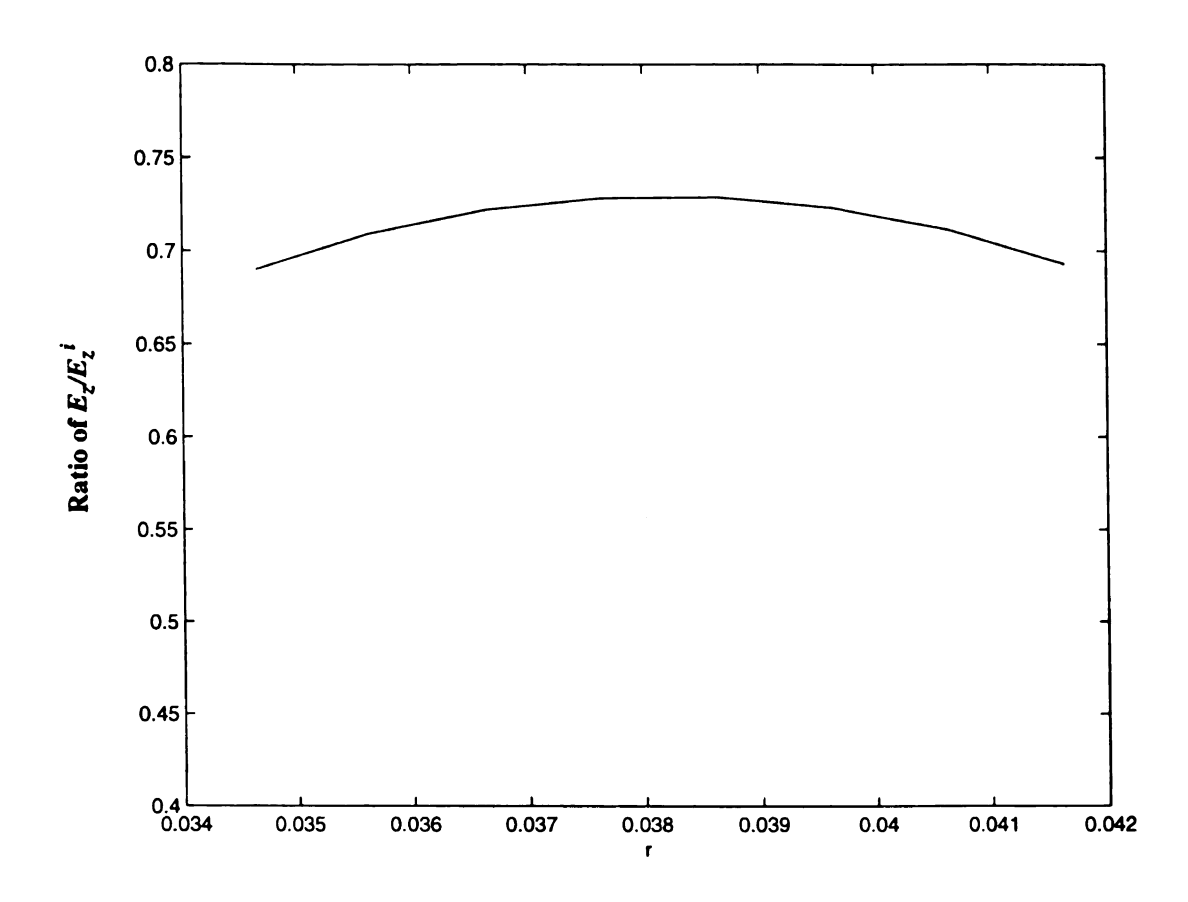


Figure 5.3 Ratio of  $E_z/E_z^i$  varies in the z direction at r=0.0004m. The dimensions of the material sample are  $r_0=0.004m$  and  $h_0=0.008m$  with the relative permittivity of  $\epsilon_r=2.5$ . The dimensions of the cylindrical waveguide are: a=0.0762m and c=0.15458m. The operating frequency is 2.45 GHz.

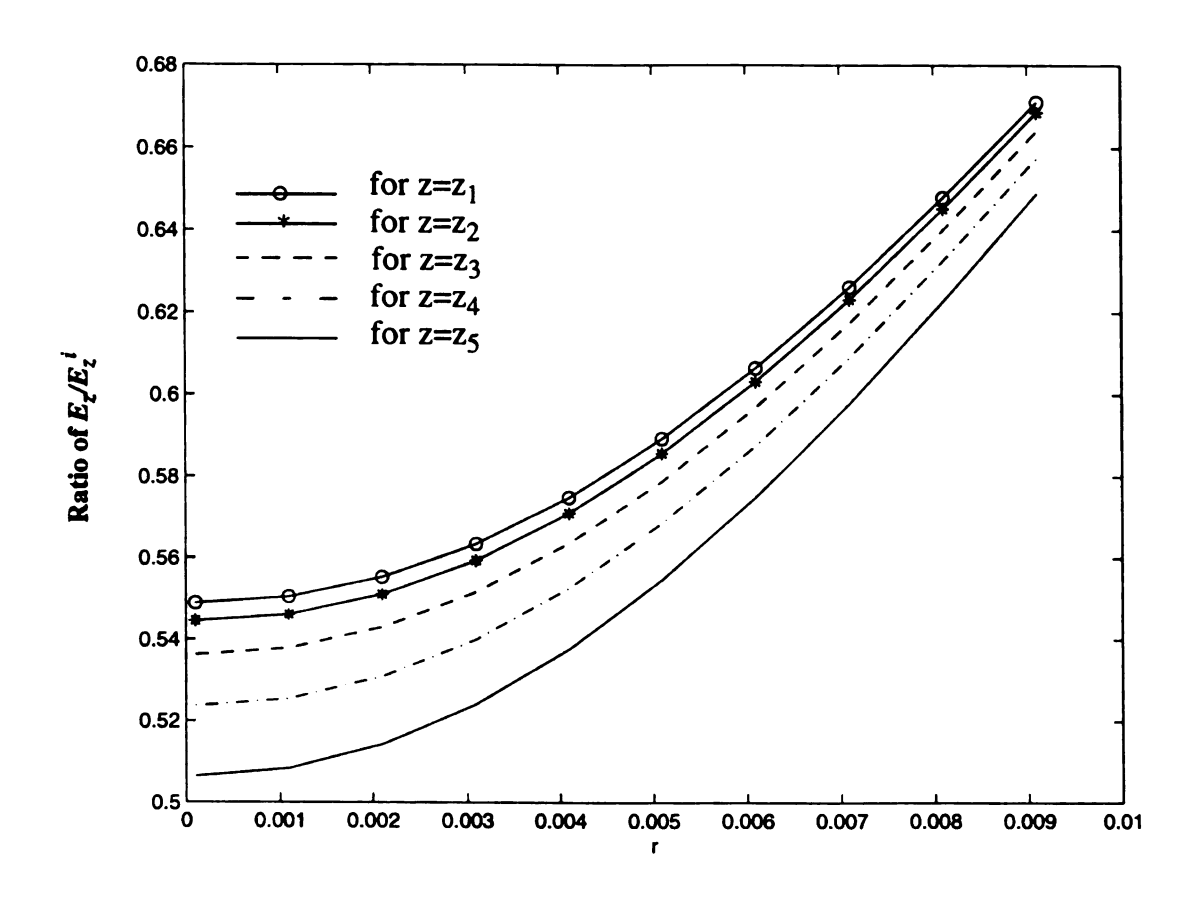


Figure 5.4 Ratio of  $E_z/E_z^i$  varies in the r direction at the different locations of z. The dimensions of the material sample are  $r_0$ =0.01m and  $h_0$ =0.02m with the relative permittivity of  $\epsilon_r = 2.5$ . The dimensions of the cylindrical waveguide are: a=0.0762m and c=0.15458m The operating frequency is 2.45 GHz.

#### 2. Thin chip case

A material sample with the shape of a thin chip, having its length much smaller than its diameter, is placed in the center of the cylindrical waveguide. The dimensions of the material sample are  $h_0=0.001m$  and  $r_0=0.02m$  and the number of the modes which are involved in the computation is 55. The numerical results are shown in Figure 5.5.

Since the z component of the induced electric field dominates near the center of the waveguide, the ratios of the z component of the induced electric field to that of the electric field near the material sample in the empty region of the waveguide are plotted as a function of the radial distance, r, in Figure 5.5. We observe that the numerical results are close to the theoretical estimation given by the boundary condition of  $E = (1/\epsilon_r)E^i = 0.4E^i$ .

#### 3. Thin pipe case

A material sample with the dimensions: the length  $h_0$ =0.044m and the radius  $r_0$ =0.004m, is placed in the center of the cylindrical waveguide. The number of the modes involved in the computation is 129 and the numerical result is shown in Figure 5.6.

Examining the numerical results for the solutions of the unknown coefficients  $A_n$  and  $D_n$  in regions I and III, we find that those with the most significant values belong to the  $TM_{01}$  waveguide mode, that is, the  $TM_{01}$  waveguide mode dominates in the empty region of the waveguide. For this case, the induced electric field inside the material sample should be approximately equal to the electric field in the empty region near the material sample because the electric field in the empty region near the material sample or near the center of the waveguide is dominated by the z component and it is tangential to the major

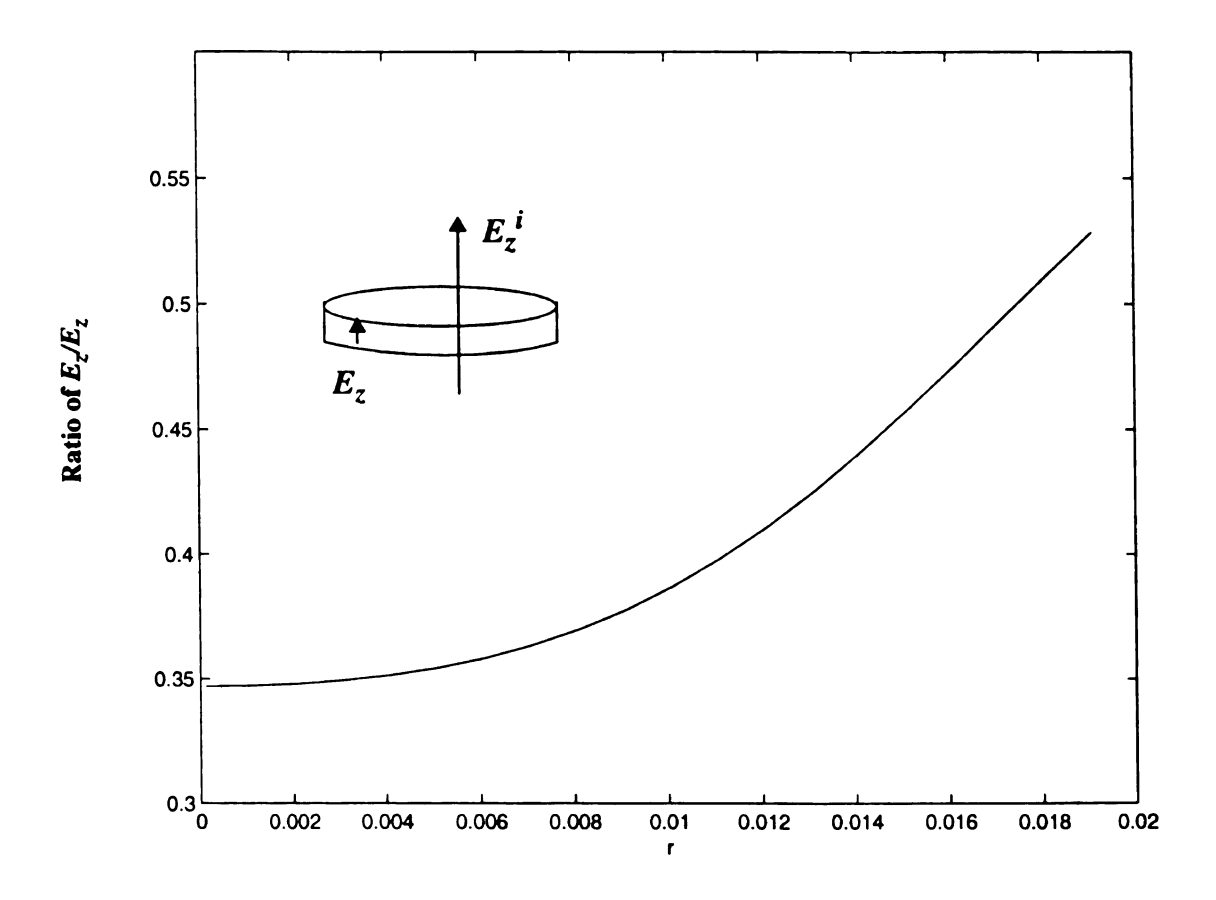


Figure 5.5 Ratio of  $E_z/E_z^i$  varies in the r direction. The dimensions of the material sample are  $r_0$ =0.02m and  $h_0$ =0.001m with the relative permittivity of  $\epsilon_r = 2.5$ . The dimensions of the cylindrical waveguide are: a=0.0762m and c=0.15458m. The operating frequency is 2.45 GHz.

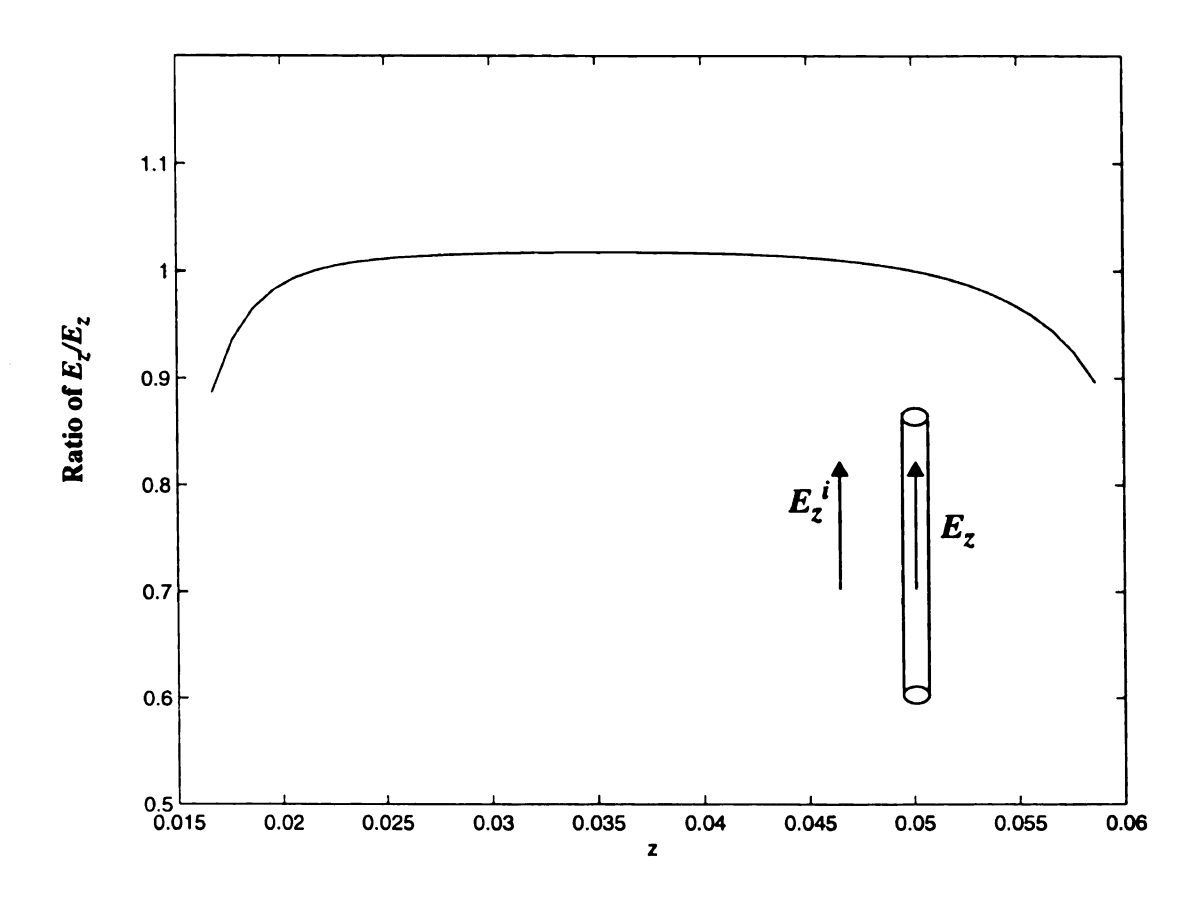


Figure 5.6 Ratio of  $E_z/E_z^i$  varies in the z direction at r=0.0004m. The dimensions of the material sample are  $r_0=0.004m$  and  $h_0=0.044m$  with the relative permittivity of  $\epsilon_r=2.5$ . The dimensions of the cylindrical waveguide are: a=0.0762m and c=0.15458m. The operating frequency is 2.45 GHz.

part of the material sample surface, also the continuity of the tangential component of the electric field at the material sample surface requires this estimation.

In Figure 5.6, we plot the ratios of the z component of the induced electric field to that of the electric field near the material sample in the empty region of the waveguide varying as a function of z at r=0.0004m. Most of the ratios are very close to 1 which is in agreement with the theoretical estimation.

Considering the numerical accuracy and the computation time, we find that in the mode-matching method the number of the modes to be summed can be reduced a great deal when compared with the integral equation method. The most important reason for this finding is that the eigenmodes used in the mode-matching method satisfy the boundary conditions on the material sample and the cavity wall. (On the other hand, the vector wave functions used in the integral equation method only satisfy the boundary conditions at the cavity wall.)

The other reason for this finding is that in the mode-matching method, the angular dependence of the eigenmodes,  $\dot{e}_{n1}$ ,  $\dot{e}_{m2}$ ,  $\dot{h}_{n1}$  and  $\dot{h}_{m2}$ , on  $\theta$  is  $\sin n\theta$  or  $\cos n\theta$ , and many of the integrations of the scalar products of these eigenmodes given in eqs. (5.136) and (5.137) become zero due to the orthogonality of the sinusoidal functions. Therefore, the matrices  $[BM_1]$ ,  $[CM_1]$ ,  $[BM_2]$ , and  $[CM_2]$  given in eqs. (5.140) and (5.141) are sparse and the computation time can be saved greatly. In spite of this advantage for the mode-matching method, it is not a very general technique because it can not be used to solve the problem involving material samples with arbitrary shapes or heterogeneous compositions.

Table 5.2 lists the number of eigenmodes used in the mode-matching method for

Table 5.2 Number of eigenmodes used in the mode-matching method for material samples of different geometries

Geometry of material sample	Number of modes
8-mm cubic material sample	62
2-cm cubic material sample	76
Thin chip case	55
Thin pipe case	129

the material samples of different geometries. From this table, we find that this number is the largest for the thin pipe case. This confirms our finding that much more summation terms are needed for the narrow strip case in Chapter 3 and the thin pipe case in Chapter 4 to secure accurate results. To overcome this shortcoming, we suggest the scheme of separating the material sample into the boundary layer and interior regions to save computation time while obtain better results.

#### CHAPTER 6

## **CONCLUSIONS**

In this dissertation, both the integral equation method and the mode-matching method are investigated to quantify the induced electric field in a material sample placed in an EM cavity. It has been demonstrated that the integral equation method is more powerful than the mode-matching method because the integral equation method can be employed to solve the problem involving the material sample with any arbitrary shape or heterogeneity while the mode-matching method can only handle the case of the homogeneous material sample with a simple geometry. The only disadvantage of the integral equation method is its slow numerical convergence and a large computation time while the mode-matching method is more computational effectiveness. To our best knowledge, this is the first attempt to solve this type of problem using the integral equation method.

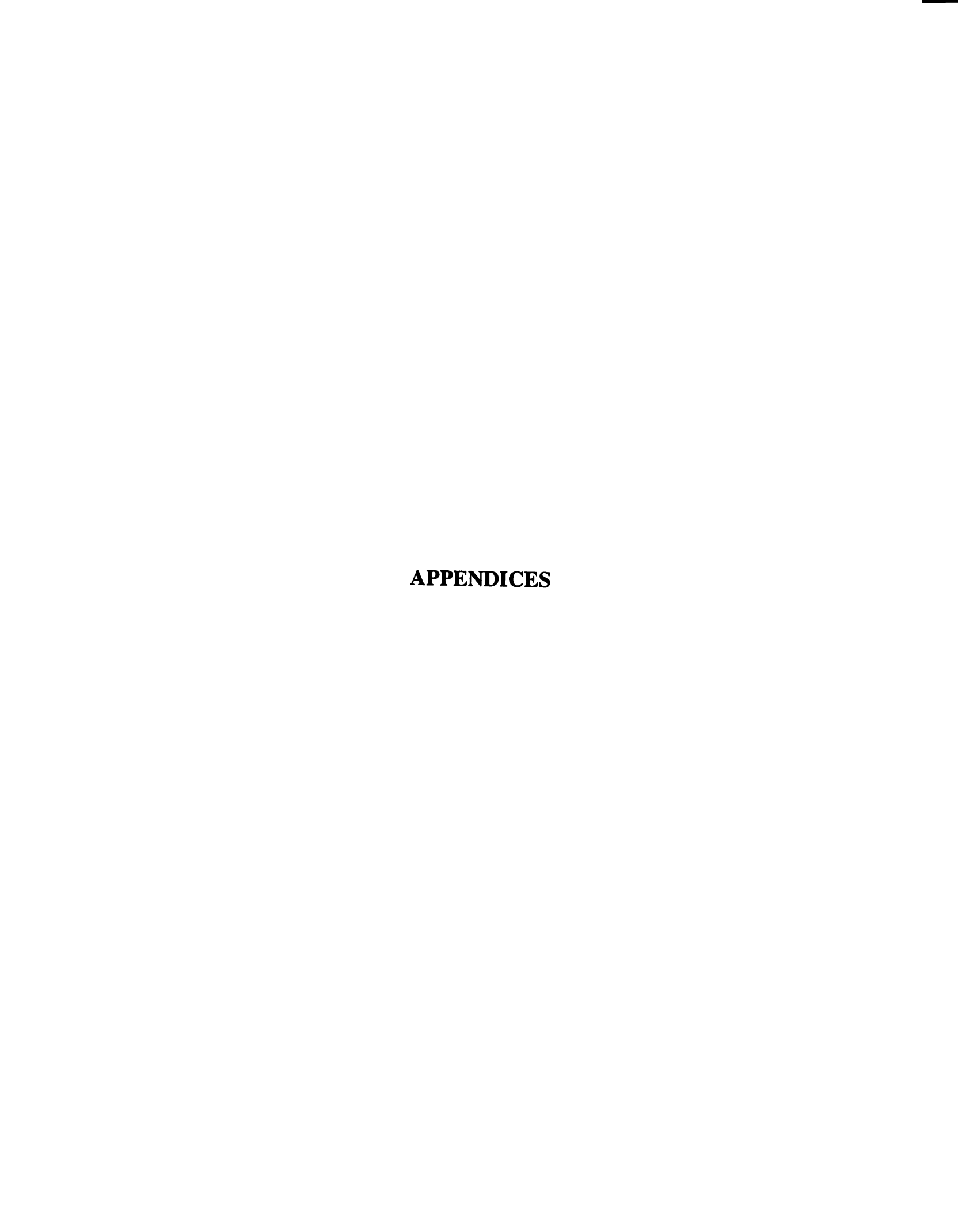
In the integral equation method, a complete set of vector wave functions  $\vec{L}_{nml}$ ,  $\vec{M}_{nml}$  and  $\vec{N}_{nml}$  which include both solenoidal and irrotational functions are employed to expand the unknown electric field in the material sample placed within an energized cavity. After the electric and magnetic dyadic Green's functions are obtained both EFIE

and MFIE are derived and they are shown to be equivalent.

Increasing the convergence rate of the dyadic Green's function is a main concern in solving the EFIE in order to obtain the electromagnetic field distribution in the material sample. To achieve this goal, the infinite triple summations over the cavity eigenmodes are reduced to the infinite double summations using the relations given in Collin [2]. The infinite double summation is further divided into a finite double summation and an infinite single summation using the well-known Poisson summation formula. However, this division is only possible for the rectangular cavity case while the infinite double summation is still used for the cylindrical cavity case because it is difficult to apply the same division technique in the cylindrical cavity case due to mathematical complexity.

As numerical results demonstrated, the electromagnetic fields in the material sample are strong functions of the geometry and the dielectric parameters of the material sample. When the initial cavity electric field is tangential to the major part of the material sample surface, the induced electric field in the material sample may be close to the initial cavity electric field as required by the boundary conditions. For this case, the convergence property of the dyadic Green's function is very poor. To overcome this difficulty, the scheme of separating the material sample into the boundary layer and the interior regions are proposed for this special case. Satisfactory numerical results can be produced with this scheme at a reduced computation time.

In this dissertation, the mode-matching method is also applied to the case of the homogeneous material sample with a simple geometry and it is found that the mode-matching method can save a great deal of computation time attributed to the use of the well-defined eigenmodes and sparse resultant matrices.





#### APPENDIX A

# COMPUTATION OF DYADIC GREEN'S FUNC-TION IN CAVITIES BY Y. RAHMAT-SAMII [11]

In [11] Y. Rahmat-Samii first obtained the magnetic dyadic Green's function, then he used the relation between electric and magnetic dyadic Green's functions of

$$k^2 \overline{G}_e(\mathring{r}_0, \mathring{r}) = \nabla \times \overline{G}_m(\mathring{r}_0, \mathring{r}) - \overline{I}\delta(\mathring{r} - \mathring{r}_0)$$
(A.1)

to derive the electric dyadic Green's function. In order to obtain the magnetic dyadic Green's function  $\overline{G}_m(r_0, r)$ , he introduced another Green's function based on the following definition:

$$(\nabla^2 + k^2) \bar{g}_m(\dot{r}_0, \dot{r}) = -\bar{l}\delta(\dot{r} - \dot{r}_0)$$
 (A.2)

and the boundary conditions for this Green's function are expressed as

$$\hat{n} \cdot \bar{g}_m(\hat{r}_0, \hat{r}) = \hat{0} \tag{A.3}$$

$$\hat{n} \times \nabla \times \bar{g}_m(\hat{r}_0, \hat{r}) = \hat{0} \tag{A.4}$$

on the perfectly conducting walls of a cavity. After applying Green's theorem, he obtained the magnetic dyadic Green's function as

$$\overline{G}_m(\mathring{r}_0,\mathring{r}) = \int_{v} \overline{g}_m(\mathring{r},\mathring{r}'') \cdot \nabla'' \times \overline{I}\delta(\mathring{r}_0 - \mathring{r}'') dv''$$
(A.5)

Therefore, in order to derive the expression for the Green's function  $\bar{g}_m(\hat{r}_0, \hat{r})$ , we should first solve eq. (A.2) with the boundary conditions (A.3) and (A.4) or eq. (11) of [3]. Equation (A.2) can be rewritten as

$$(\nabla^2 + k^2) \begin{cases} g_m^{xx} \\ g_m^{yy} \\ g_m^{zz} \end{cases} = - \begin{cases} 1 \\ 1 \\ 1 \end{cases} \delta(\mathring{r} - \mathring{r}_0)$$
(A.6)

1. The expression for  $g_m^{xx}$  is derived as follows:

Based on eq. (A.6), the equation for  $g_m^{xx}$  can be expressed as

$$(\nabla^2 + k^2)g_m^{xx} = -\delta(\hat{r} - \hat{r}_0)$$
 (A.7)

with the boundary conditions of

$$g_{m}^{xx} = 0 when x = 0, a$$

$$\frac{\partial g_{m}^{xx}}{\partial z} = \frac{\partial g_{m}^{xx}}{\partial y} = 0 when x = 0, a$$

$$\frac{\partial g_{m}^{xx}}{\partial y} = 0 when y = 0, b$$

$$\frac{\partial g_{m}^{xx}}{\partial z} = 0 when z = 0, c$$
(A.8)

In order to derive the expression for  $g_m^{xx}$ , we may obtain the eigenmodes  $H_{nx}(\hat{r})$  which satisfies the equation,

$$(\nabla^2 + k_n^2) H_{nx}(\hat{r}) = 0 (A.9)$$

and also satisfies the same boundary conditions as  $g_m^{xx}$  does.

Using the variables separation method and applying the boundary conditions (A.8), the expression for  $H_{nx}(r)$  can be found as

$$H_{nmlx}(r) = A_{nml} \sin\left(\frac{n\pi}{a}x\right) \cos\left(\frac{m\pi}{b}y\right) \cos\left(\frac{l\pi}{c}z\right)$$
 (A.10)

while the normalization factor is given by

$$A_{nml} = \sqrt{\frac{\varepsilon_{0n}\varepsilon_{0m}\varepsilon_{0l}}{abc}}$$
 (A.11)

and the eigenvalues are expressed as

$$k_{nml}^2 = \left(\frac{n\pi}{a}\right)^2 + \left(\frac{m\pi}{b}\right)^2 + \left(\frac{l\pi}{c}\right)^2 \tag{A.12}$$

That is, we have obtained a set of orthonormal eigenmodes  $H_{nmlx}(\hat{r})$  and  $g_m^{xx}$  can be represented by the linear combination of these eigenmodes  $H_{nmlx}(\hat{r})$  as:

$$g_m^{xx}(\mathring{r} - \mathring{r}_0) = \sum_n \sum_m \sum_m a_{nml} H_{nmlx}(\mathring{r})$$
 (A.13)

Substituting eq. (A.13) into eq. (A.7), we have

$$(\nabla^2 + k^2) \sum_{n} \sum_{m} \sum_{m} a_{nml} H_{nmlx}(\hat{r}) = -\delta(\hat{r} - \hat{r}_0)$$
 (A.14)

or

$$\sum_{n} \sum_{m} \sum_{m} a_{nml} (k^2 - k_{nml}^2) H_{nmlx}(\mathring{r}) = -\delta(\mathring{r} - \mathring{r}_0)$$
 (A.15)

Multiplying  $H_{pqrx}(\hat{r})$  on both sides, integrating over the cavity volume and using the orthogonality of  $H_{pqrx}(\hat{r})$ , we obtain the expression for the unknown expansion coefficient  $a_{nml}$  in eq. (A.13) as

$$a_{nml} = \frac{-1}{k^2 - k_{nml}^2} \int \delta(\mathring{r} - \mathring{r}_0) H_{nmlx}(\mathring{r}) d\nu = \frac{-1}{k^2 - k_{nml}^2} H_{nmlx}(\mathring{r}_0)$$
 (A.16)

Substituting eq. (A.16) into eq. (A.13), we obtain the expression for  $g_m^{xx}$  as

$$g_{m}^{xx}(\mathring{r} - \mathring{r}_{0}) = \sum_{n} \sum_{m} \sum_{l} \frac{-1}{k^{2} - k_{nml}^{2}} H_{nmlx}(\mathring{r}_{0}) H_{nmlx}(\mathring{r})$$

$$= \sum_{n} \sum_{l} \sum_{l} \frac{-1}{k^{2} - k_{nml}^{2}} \frac{\varepsilon_{0n} \varepsilon_{0m} \varepsilon_{0l}}{abc} \sin\left(\frac{n\pi}{a}x\right) \sin\left(\frac{n\pi}{a}x_{0}\right)$$

$$\cos\left(\frac{m\pi}{b}y\right) \cos\left(\frac{m\pi}{b}y_{0}\right) \cos\left(\frac{l\pi}{c}z\right) \cos\left(\frac{l\pi}{c}z_{0}\right)$$
(A.17)

2. The same procedure can be employed to obtain the expressions for  $g_m^{yy}$  and  $g_m^{zz}$ . They are expressed as

$$g_{m}^{yy} = \sum_{n} \sum_{m} \sum_{l} \frac{-1}{k^{2} - k_{nml}^{2}} \frac{\varepsilon_{0n} \varepsilon_{0m} \varepsilon_{0l}}{abc} \cos\left(\frac{n\pi}{a}x\right) \cos\left(\frac{n\pi}{a}x_{0}\right)$$

$$\sin\left(\frac{m\pi}{b}y\right) \sin\left(\frac{m\pi}{b}y_{0}\right) \cos\left(\frac{l\pi}{c}z\right) \cos\left(\frac{l\pi}{c}z_{0}\right)$$
(A.18)

$$g_{m}^{zz} = \sum_{n} \sum_{m} \sum_{l} \frac{-1}{k^{2} - k_{nml}^{2}} \frac{\varepsilon_{0n} \varepsilon_{0m} \varepsilon_{0l}}{abc} \cos\left(\frac{n\pi}{a}x\right) \cos\left(\frac{n\pi}{a}x_{0}\right)$$

$$\cos\left(\frac{m\pi}{b}y\right) \cos\left(\frac{m\pi}{b}y_{0}\right) \sin\left(\frac{l\pi}{c}z\right) \sin\left(\frac{l\pi}{c}z_{0}\right)$$
(A.19)

Comparing eqs. (A.17) to (A.19) with eq. (26) in [11], we find that there is a minus

sign missing in eq. (26) of [11]. Therefore, we can explain the discrepancy of the expression for  $\overline{G}_{eo}(\overset{\star}{r}_0,\overset{\star}{r})$  which is specified in Section 2.2.5.



## APPENDIX B

## THE IDENTITY OF

$$\sum_{n}\sum_{m}\sum_{l}\left[\vec{L}_{nml}(\vec{r}_{0})\vec{L}_{nml}(\vec{r}_{1})+\vec{N}_{nml}(\vec{r}_{0})\vec{N}_{nml}(\vec{r}_{1})+\vec{M}_{nml}(\vec{r}_{0})\vec{M}_{nml}(\vec{r}_{1})\right]=\bar{I}\delta(\vec{r}_{1}-\vec{r}_{0})$$
 IN

## RECTANGUALR CAVITIES

The identity which we need to prove is

$$\sum_{n}\sum_{m}\sum_{l}\left[\vec{L}_{nml}(\vec{r}_{0})\vec{L}_{nml}(\vec{r})+\vec{N}_{nml}(\vec{r}_{0})\vec{N}_{nml}(\vec{r})+\vec{M}_{nml}(\vec{r}_{0})\vec{M}_{nml}(\vec{r})\right]=\bar{I}\delta(\vec{r}-\vec{r}_{0})~(\mathrm{B}.1)$$

In Chapter2, we have derived the expressions for  $\vec{L}_{nml}$ ,  $\vec{M}_{nml}$  and  $\vec{N}_{nml}$  which are expressed in eqs. (2.17), (2.24) and (2.32) as:

$$\hat{L}_{nml} = \frac{A_{nml}}{k_{nml}} \left[ \hat{x} \frac{n\pi}{a} \cos\left(\frac{n\pi}{a}x\right) \sin\left(\frac{m\pi}{b}y\right) \sin\left(\frac{l\pi}{c}z\right) \right. \\
+ \hat{y} \frac{m\pi}{b} \sin\left(\frac{n\pi}{a}x\right) \cos\left(\frac{m\pi}{b}y\right) \sin\left(\frac{l\pi}{c}z\right) \\
+ \hat{z} \frac{l\pi}{c} \sin\left(\frac{n\pi}{a}x\right) \sin\left(\frac{m\pi}{b}y\right) \cos\left(\frac{l\pi}{c}z\right) \right]$$
(B.2)

$$\vec{M}_{nml} = B_{nml} \left[ -\hat{x} \frac{m\pi}{b} \cos\left(\frac{n\pi}{a}x\right) \sin\left(\frac{m\pi}{b}y\right) \sin\left(\frac{l\pi}{c}z\right) + \hat{y} \frac{n\pi}{a} \sin\left(\frac{n\pi}{a}x\right) \cos\left(\frac{m\pi}{b}y\right) \sin\left(\frac{l\pi}{c}z\right) \right]$$
(B.3)

$$\vec{N}_{nml} = \frac{C_{nml}}{k_{nml}} \left[ (-\hat{x}) \frac{n\pi l\pi}{a} \cos\left(\frac{n\pi}{a}x\right) \sin\left(\frac{m\pi}{b}y\right) \sin\left(\frac{l\pi}{c}z\right) \right. \\
\left. - \hat{y} \frac{m\pi l\pi}{b} \sin\left(\frac{n\pi}{a}x\right) \cos\left(\frac{m\pi}{b}y\right) \sin\left(\frac{l\pi}{c}z\right) \\
+ \hat{z} \left(\left(\frac{n\pi}{a}\right)^2 + \left(\frac{m\pi}{b}\right)^2\right) \sin\left(\frac{n\pi}{a}x\right) \sin\left(\frac{m\pi}{b}y\right) \cos\left(\frac{l\pi}{c}z\right) \right]$$
(B.4)

where the normalization constants are given by eqs. (2.60), (2.62) and (2.65) as

$$A_{nml} = \sqrt{\frac{\varepsilon_{0n}\varepsilon_{0m}\varepsilon_{0l}}{abc}}$$
 (B.5)

and

$$B_{nml} = C_{nml} = \sqrt{\frac{\varepsilon_{0n} \varepsilon_{0m} \varepsilon_{0l}}{abc}} \sqrt{\frac{1}{\left(\frac{n\pi}{a}\right)^2 + \left(\frac{m\pi}{b}\right)^2}} = A_{nml} \sqrt{\frac{1}{\left(\frac{n\pi}{a}\right)^2 + \left(\frac{m\pi}{b}\right)^2}}$$
(B.6)

Substituting eqs. (B.2) to (B.4) into the left hand side (LHS) of eq. (B.1), we can obtain its nine components as follows:

#### 1. Coefficient for $\hat{x}\hat{x}$ component is expressed as

$$\left(\frac{A_{nml}}{k_{nml}}\right)^{2} \left(\frac{n\pi}{a}\right)^{2} + B_{nml}^{2} \left(\frac{m\pi}{b}\right)^{2} + \left(\frac{C_{nml}}{k_{nml}}\right)^{2} \left(\frac{n\pi l\pi}{ac}\right)^{2}$$

$$= A_{nml}^{2} \left[\frac{\left(\frac{n\pi}{a}\right)^{2}}{k_{nml}^{2}} + \frac{\left(\frac{m\pi}{b}\right)^{2}}{\left(\frac{n\pi}{a}\right)^{2} + \left(\frac{m\pi}{b}\right)^{2}} + \frac{\left(\frac{n\pi l\pi}{ac}\right)^{2}}{k_{nml}^{2} \left(\left(\frac{n\pi}{a}\right)^{2} + \left(\frac{m\pi}{b}\right)^{2}\right)}\right]$$

$$= A_{nml}^{2} \frac{\left(\frac{n\pi}{a}\right)^{2} \left(\left(\frac{n\pi}{a}\right)^{2} + \left(\frac{m\pi}{b}\right)^{2}\right) + k_{nml}^{2} \left(\frac{m\pi}{b}\right)^{2} + \left(\frac{n\pi l\pi}{ac}\right)^{2}}{k_{nml}^{2} \left(\left(\frac{n\pi}{a}\right)^{2} + \left(\frac{m\pi}{b}\right)^{2}\right)}$$

$$= A_{nml}^{2}$$

$$= A_{nml}^{2}$$

$$= A_{nml}^{2}$$
(B.7)

Thus, the  $\hat{x}\hat{x}$  component of the LHS of the eq. (B.1) is given by

$$\sum_{n} \sum_{m} \sum_{l} A_{nml}^{2} \cos\left(\frac{n\pi}{a}x\right) \cos\left(\frac{n\pi}{a}x_{0}\right) \sin\left(\frac{m\pi}{b}y\right) \sin\left(\frac{m\pi}{b}y_{0}\right) \sin\left(\frac{l\pi}{c}z\right) \sin\left(\frac{l\pi}{c}z_{0}\right)$$

$$= \delta(\mathring{r} - \mathring{r}_{0})$$
(B.8)

based on eq. (19) of [11].

2. Coefficients for  $\hat{x}\hat{y}$  and  $\hat{y}\hat{x}$  components are expressed as

$$\left(\frac{A_{nml}}{k_{nml}}\right)^{2} \left(\frac{n\pi}{a}\right) \left(\frac{m\pi}{b}\right) - B_{nml}^{2} \left(\frac{n\pi}{a}\right) \left(\frac{m\pi}{b}\right) + \left(\frac{C_{nml}}{k_{nml}}\right)^{2} \left(\frac{n\pi}{a}\right) \left(\frac{m\pi}{b}\right) \left(\frac{l\pi}{c}\right)^{2}$$

$$= A_{nml}^{2} \left(\frac{n\pi}{a}\right) \left(\frac{m\pi}{b}\right) \left[\frac{1}{k_{nml}^{2}} - \frac{1}{\left(\frac{n\pi}{a}\right)^{2} + \left(\frac{m\pi}{b}\right)^{2}} + \frac{\left(\frac{l\pi}{c}\right)^{2}}{k_{nml}^{2} \left(\left(\frac{n\pi}{a}\right)^{2} + \left(\frac{m\pi}{b}\right)^{2}\right)}\right]$$

$$= A_{nml}^{2} \left(\frac{n\pi}{a}\right) \left(\frac{m\pi}{b}\right) \frac{\left(\frac{n\pi}{a}\right)^{2} + \left(\frac{m\pi}{b}\right)^{2} - k_{nml}^{2} + \left(\frac{l\pi}{c}\right)^{2}}{k_{nml}^{2} \left(\left(\frac{n\pi}{a}\right)^{2} + \left(\frac{m\pi}{b}\right)^{2}\right)} = 0$$
(B.9)

Thus, the  $\hat{x}\hat{y}$  and  $\hat{y}\hat{x}$  components of the LHS of eq. (B.1) are zero.

3. Coefficients for  $\hat{x}\hat{z}$  and  $\hat{z}\hat{x}$  components are expressed as

$$\left(\frac{A_{nml}}{k_{nml}}\right)^{2} \frac{n\pi l\pi}{a} \frac{l\pi}{c} - \left(\frac{C_{nml}}{k_{nml}}\right)^{2} \left(\frac{n\pi}{a}\right) \frac{l\pi}{c} \left(\left(\frac{n\pi}{a}\right)^{2} + \left(\frac{m\pi}{b}\right)^{2}\right)$$

$$= \left(\frac{A_{nml}}{k_{nml}}\right)^{2} \frac{n\pi l\pi}{a} \frac{l\pi}{c} \left[1 - \frac{\left(\frac{n\pi}{a}\right)^{2} + \left(\frac{m\pi}{b}\right)^{2}}{\left(\frac{n\pi}{a}\right)^{2} + \left(\frac{m\pi}{b}\right)^{2}}\right] = 0$$
(B.10)

Thus, the  $\hat{x}\hat{z}$  and  $\hat{z}\hat{x}$  components of the LHS of eq. (B.1) are zero.

4. Coefficients for  $\hat{y}\hat{z}$  and  $\hat{z}\hat{y}$  components are expressed as

$$\left(\frac{A_{nml}}{k_{nml}}\right)^2 \frac{m\pi l\pi}{b} \frac{l\pi}{c} - \left(\frac{C_{nml}}{k_{nml}}\right)^2 \frac{m\pi l\pi}{b} \frac{l\pi}{c} \left(\left(\frac{n\pi}{a}\right)^2 + \left(\frac{m\pi}{b}\right)^2\right) \\
= \left(\frac{A_{nml}}{k_{nml}}\right)^2 \frac{m\pi l\pi}{b} \frac{l\pi}{c} \left[1 - \frac{\left(\frac{n\pi}{a}\right)^2 + \left(\frac{m\pi}{b}\right)^2}{\left(\frac{n\pi}{a}\right)^2 + \left(\frac{m\pi}{b}\right)^2}\right] = 0$$
(B.11)

Thus, the  $\hat{y}\hat{z}$  and  $\hat{z}\hat{y}$  components of the left hand side of eq. (B.1) are zero.

5. Coefficient for  $\hat{y}\hat{y}$  component is expressed as

$$\left(\frac{A_{nml}}{k_{nml}}\right)^{2} \left(\frac{m\pi}{b}\right)^{2} + B_{nml}^{2} \left(\frac{n\pi}{a}\right)^{2} + \left(\frac{C_{nml}}{k_{nml}}\right)^{2} \left(\frac{m\pi}{b}\right)^{2} \left(\frac{l\pi}{c}\right)^{2} \\
= A_{nml}^{2} \left[\frac{\left(\frac{m\pi}{b}\right)^{2}}{k_{nml}^{2}} + \frac{\left(\frac{n\pi}{a}\right)^{2}}{\left(\frac{n\pi}{a}\right)^{2} + \left(\frac{m\pi}{b}\right)^{2}} + \frac{\left(\frac{m\pi}{b}\right)^{2} \left(\frac{l\pi}{c}\right)^{2}}{k_{nml}^{2} \left(\left(\frac{n\pi}{a}\right)^{2} + \left(\frac{m\pi}{b}\right)^{2}\right)}\right] \\
= A_{nml}^{2} \frac{\left(\frac{m\pi}{b}\right)^{2} \left(\left(\frac{n\pi}{a}\right)^{2} + \left(\frac{m\pi}{b}\right)^{2}\right) + k_{nml}^{2} \left(\frac{n\pi}{a}\right)^{2} + \left(\frac{m\pi}{b}\right)^{2} \left(\frac{l\pi}{c}\right)^{2}}{k_{nml}^{2} \left(\left(\frac{n\pi}{a}\right)^{2} + \left(\frac{m\pi}{b}\right)^{2}\right)} \\
= A_{nml}^{2} = A_{nml}^{2}$$
(B.12)

Thus, based on eq. (19) of [11], the  $\hat{y}\hat{y}$  component of the LHS of eq.(B.1) is expressed as

$$\sum_{n} \sum_{m} \sum_{l} A_{nml}^{2} \sin\left(\frac{n\pi}{a}x\right) \sin\left(\frac{n\pi}{a}x_{0}\right) \cos\left(\frac{m\pi}{b}y\right) \cos\left(\frac{m\pi}{b}y_{0}\right) \sin\left(\frac{l\pi}{c}z\right) \sin\left(\frac{l\pi}{c}z_{0}\right)$$

$$= \delta(\mathring{r} - \mathring{r}_{0})$$
(B.13)

6. Coefficient for  $\hat{z}\hat{z}$  component is expressed as

$$\left(\frac{A_{nml}}{k_{nml}}\right)^{2} \left(\frac{l\pi}{c}\right)^{2} + \left(\frac{C_{nml}}{k_{nml}}\right)^{2} \left(\left(\frac{n\pi}{a}\right)^{2} + \left(\frac{m\pi}{b}\right)^{2}\right)^{2}$$

$$= \left(\frac{A_{nml}}{k_{nml}}\right)^{2} \left[\left(\frac{l\pi}{c}\right)^{2} + \frac{\left(\left(\frac{n\pi}{a}\right)^{2} + \left(\frac{m\pi}{b}\right)^{2}\right)^{2}}{\left(\frac{n\pi}{a}\right)^{2} + \left(\frac{m\pi}{b}\right)^{2}}\right]$$

$$= A_{nml}^{2}$$
(B.14)

Thus, the  $\hat{z}\hat{z}$  component of the LHS of eq.(B.1) is

$$\sum_{n} \sum_{m} \sum_{l} A_{nml}^{2} \sin\left(\frac{n\pi}{a}x\right) \sin\left(\frac{n\pi}{a}x_{0}\right) \sin\left(\frac{m\pi}{b}y\right) \sin\left(\frac{m\pi}{b}y_{0}\right) \cos\left(\frac{l\pi}{c}z\right) \cos\left(\frac{l\pi}{c}z_{0}\right)$$

$$= \delta(\mathring{r} - \mathring{r}_{0})$$
(B.15)

Therefore, the identity given by eq. (B.1) has been proved after combining eqs. (B.8), (B.9), (B.10), (B.11), (B.13) and (B.15).

A DDENIDIV C
APPENDIX C

#### APPENDIX C

## AN ALTERNATIVE REPRESENTATION OF THE ELECTRIC DYADIC GREEN'S FUNCTION

In Chapter 2, we have obtained the electric dyadic Green's function (2.100)as

$$\overline{G}_e(\overset{\triangleright}{r}_0,\overset{\triangleright}{r}) = \overline{G}_{eo}(\overset{\triangleright}{r}_0,\overset{\triangleright}{r}) - \frac{\overline{I}\delta(\overset{\triangleright}{r}-\overset{\triangleright}{r}_0)}{k_0^2}$$
 (C.1)

where the detailed expression for  $\overline{G}_{eo}(r, r)$  is given in Section 2.2.5 as

$$\begin{split} \overline{G}_{eo}(\hat{r}_0,\hat{r}) &= \frac{1}{k_0^2} \sum_{n=0}^{\infty} \sum_{m=0}^{\infty} \sum_{l=0}^{\infty} \frac{\varepsilon_{0n} \varepsilon_{0m} \varepsilon_{0l}}{abc(k_n^2 - k_0^2)} \Big[ \Big( \Big( \frac{m\pi}{b} \Big)^2 + \Big( \frac{l\pi}{c} \Big)^2 \Big) \cos \frac{n\pi}{a} x \cos \frac{n\pi}{a} x_0 \\ & \sin \frac{m\pi}{b} y \sin \frac{m\pi}{b} y_0 \sin \frac{l\pi}{c} z \sin \frac{l\pi}{c} z_0 \hat{x} \hat{x} + \Big( \Big( \frac{n\pi}{a} \Big)^2 + \Big( \frac{l\pi}{c} \Big)^2 \Big) \sin \frac{n\pi}{a} x \sin \frac{n\pi}{a} x_0 \\ & \cos \frac{m\pi}{b} y \cos \frac{m\pi}{b} y_0 \sin \frac{l\pi}{c} z \sin \frac{l\pi}{c} z_0 \hat{y} \hat{y} + \Big( \Big( \frac{n\pi}{a} \Big)^2 + \Big( \frac{m\pi}{b} \Big)^2 \Big) \sin \frac{n\pi}{a} x \\ & \sin \frac{n\pi}{a} x_0 \sin \frac{m\pi}{b} y \sin \frac{m\pi}{b} y_0 \cos \frac{l\pi}{c} z \cos \frac{l\pi}{c} z_0 \hat{z} \hat{z} - \frac{n\pi}{a} \frac{m\pi}{b} \cos \frac{n\pi}{a} x \sin \frac{n\pi}{a} x_0 \\ & \sin \frac{m\pi}{b} y \cos \frac{m\pi}{b} y_0 \sin \frac{l\pi}{c} z \sin \frac{l\pi}{c} z \sin \frac{l\pi}{c} z_0 \hat{x} \hat{y} - \frac{n\pi}{a} \frac{m\pi}{b} \sin \frac{n\pi}{a} x \cos \frac{n\pi}{a} x_0 \cos \frac{m\pi}{b} y \sin \frac{m\pi}{b} y_0 \\ & \sin \frac{m\pi}{b} y_0 \sin \frac{l\pi}{c} z \sin \frac{l\pi}{c} z_0 \hat{y} \hat{x} - \frac{m\pi}{b} \frac{l\pi}{c} \sin \frac{n\pi}{a} x \sin \frac{n\pi}{a} x_0 \cos \frac{m\pi}{b} y \sin \frac{m\pi}{b} y_0 \\ & \sin \frac{l\pi}{c} z \cos \frac{l\pi}{c} z_0 \hat{y} \hat{z} - \frac{m\pi}{b} \frac{l\pi}{c} \sin \frac{n\pi}{a} x \sin \frac{n\pi}{a} x_0 \sin \frac{m\pi}{b} y \cos \frac{l\pi}{c} z \sin \frac{l\pi}{c} z_0 \hat{z} \hat{x} \\ & \sin \frac{l\pi}{c} z_0 \hat{z} \hat{y} - \frac{n\pi}{a} \frac{l\pi}{c} \sin \frac{n\pi}{a} x \cos \frac{n\pi}{a} x \cos \frac{n\pi}{b} y \sin \frac{m\pi}{b} y_0 \cos \frac{l\pi}{c} z \sin \frac{l\pi}{c} z_0 \hat{z} \hat{x} \\ & - \frac{n\pi}{a} \frac{l\pi}{c} \cos \frac{n\pi}{a} x \sin \frac{n\pi}{a} x_0 \sin \frac{m\pi}{b} y \sin \frac{m\pi}{b} y \sin \frac{l\pi}{c} z \cos \frac{l\pi}{c} z_0 \hat{x} \hat{z} \Big] \end{split}$$

and  $\varepsilon_{0n}$  is defined by eq. (2.63).

In Chapter 3, we have demonstrated that this series converges extremely slow. As a general rule, if one series representation converges very slowly an alternative series representation usually converges more rapidly.

We know the following relation which is given in [1] as

$$\sum_{n=1}^{\infty} \frac{\cos(nx)}{n^2 - a^2} = \frac{1}{2a^2} - \frac{\pi}{2a} \frac{\cos((x - \pi)a)}{\sin(\pi a)} \qquad 0 < x < 2\pi$$
 (C.3)

If we evaluate the summations of  $\sum_{l=1}^{\infty} \frac{\sin\left(\frac{l\pi}{c}z\right)\sin\left(\frac{l\pi}{c}z_0\right)}{k_n^2 - k_0^2} \text{ and } \sum_{l=1}^{\infty} \frac{\cos\left(\frac{l\pi}{c}z\right)\cos\left(\frac{l\pi}{c}z_0\right)}{k_n^2 - k_0^2}$ 

into closed form expressions, then the triple summations in eq. (C.2) can be reduced to double summations to increase the series convergence.

1. Evaluation of 
$$\sum_{l=1}^{\infty} \frac{\sin\left(\frac{l\pi}{c}z\right)\sin\left(\frac{l\pi}{c}z_0\right)}{k_n^2 - k_0^2}$$
:

$$\sum_{n=1}^{\infty} \frac{\sin\left(\frac{l\pi}{c}z\right)\sin\left(\frac{l\pi}{c}z_0\right)}{k_n^2 - k_0^2} = \frac{1}{2} \left[ \sum_{l=1}^{\infty} \frac{\cos\left(\frac{l\pi}{c}(z - z_0)\right)}{\left(\frac{l\pi}{c}\right)^2 - k_g^2} - \sum_{l=1}^{\infty} \frac{\cos\left(\frac{l\pi}{c}(z + z_0)\right)}{\left(\frac{l\pi}{c}\right)^2 - k_g^2} \right]$$
(C.4)

where

$$k_g^2 = k_0^2 - \left(\frac{n\pi}{a}\right)^2 - \left(\frac{m\pi}{b}\right)^2$$
 (C.5)

When  $z > z_0$ , the summations in the right hand side of eq. (C.4) are given by

$$\frac{1}{2} \sum_{l=1}^{\infty} \frac{\cos\left(\frac{l\pi}{c}(z-z_0)\right)}{\left(\frac{l\pi}{c}\right)^2 - k_g^2} = \frac{1}{2} \left(\frac{c}{\pi}\right)^2 \sum_{l=1}^{\infty} \frac{\cos\left(\frac{l\pi}{c}(z-z_0)\right)}{l^2 - \left(\frac{c}{\pi}k_g\right)^2}$$

$$= \frac{1}{2} \left(\frac{c}{\pi}\right)^2 \left[ \frac{1}{2\left(\frac{c}{\pi}k_g\right)^2} - \frac{\pi}{2\frac{c}{\pi}k_g} \frac{\cos\left(\left(\frac{\pi}{c}(z-z_0) - \pi\right)\frac{c}{\pi}k_g\right)}{\sin\left(\frac{c}{\pi}k_g\right)} \right]$$

$$= \frac{1}{4k_g^2} - \frac{c}{4k_g} \frac{\cos((z-z_0-c)k_g)}{\sin(ck_g)}$$
(C.6)

$$\frac{1}{2} \sum_{l=1}^{\infty} \frac{\cos\left(\frac{l\pi}{c}(z+z_0)\right)}{\left(\frac{l\pi}{c}\right)^2 - k_g^2} = \frac{1}{2} \left(\frac{c}{\pi}\right)^2 \sum_{l=1}^{\infty} \frac{\cos\left(\frac{l\pi}{c}(z+z_0)\right)}{l^2 - \left(\frac{c}{\pi}k_g\right)^2}$$

$$= \frac{1}{4k_g^2} - \frac{c}{4k_g} \frac{\cos((z+z_0-c)k_g)}{\sin(ck_g)}$$
(C.7)

Substituting eqs. (C.6) and (C.7) into eq. (C.4), we evaluate  $\sum_{l=1}^{\infty} \frac{\sin(\frac{l\pi}{c}z)\sin(\frac{l\pi}{c}z_0)}{k_n^2 - k_0^2}$  as

$$\sum_{l=1}^{\infty} \frac{\sin\left(\frac{l\pi}{c}z\right) \sin\left(\frac{l\pi}{c}z_{0}\right)}{k_{n}^{2} - k_{0}^{2}}$$

$$= \frac{1}{4k_{g}^{2}} - \frac{c}{4k_{g}} \frac{\cos((z - z_{0} - c)k_{g})}{\sin(ck_{g})} - \left(\frac{1}{4k_{g}^{2}} - \frac{c}{4k_{g}} \frac{\cos((z + z_{0} - c)k_{g})}{\sin(ck_{g})}\right)$$

$$= \frac{c}{4k_{g}\sin(ck_{g})} \left[\cos((z + z_{0} - c)k_{g}) - \cos((z - z_{0} - c)k_{g})\right]$$

$$= \frac{c}{2k_{g}\sin(ck_{g})} \sin(k_{g}(c - z))\sin(k_{g}z_{0})$$
(C.8)

When  $z < z_0'$ , the first summation in the right hand side of eq. (C.4) is given by

$$\frac{1}{2} \sum_{l=1}^{\infty} \frac{\cos\left(\frac{l\pi}{c}(z-z_0)\right)}{\left(\frac{l\pi}{c}\right)^2 - k_g^2} = \frac{1}{2} \left(\frac{c}{\pi}\right)^2 \sum_{l=1}^{\infty} \frac{\cos\left(\frac{l\pi}{c}(z_0-z)\right)}{l^2 - \left(\frac{c}{\pi}k_g\right)^2}$$

$$= \frac{1}{2} \left(\frac{c}{\pi}\right)^2 \left[\frac{1}{2\left(\frac{c}{\pi}k_g\right)^2} - \frac{\pi}{2\frac{c}{\pi}k_g} \frac{\cos\left(\left(\frac{\pi}{c}(z_0-z) - \pi\right)\frac{c}{\pi}k_g\right)}{\sin\left(\frac{c}{\pi}k_g\pi\right)}\right]$$

$$= \frac{1}{4k_g^2} - \frac{c}{4k_g} \frac{\cos((z_0-z-c)k_g)}{\sin(ck_g)}$$
(C.9)

and the evaluation of  $\sum_{l=1}^{\infty} \frac{\sin\left(\frac{l\pi}{c}z\right)\sin\left(\frac{l\pi}{c}z_0\right)}{k_n^2 - k_0^2}$  leads to

$$\sum_{l=1}^{\infty} \frac{\sin\left(\frac{l\pi}{c}z\right) \sin\left(\frac{l\pi}{c}z_{0}\right)}{k_{n}^{2} - k_{0}^{2}}$$

$$= \frac{1}{4k_{g}^{2}} - \frac{c}{4k_{g}} \frac{\cos((z_{0} - z - c)k_{g})}{\sin(ck_{g})} - \left(\frac{1}{4k_{g}^{2}} - \frac{c}{4k_{g}} \frac{\cos((z + z_{0} - c)k_{g})}{\sin(ck_{g})}\right)$$

$$= \frac{c}{4k_{g}\sin(ck_{g})} [\cos((z + z_{0} - c)k_{g}) - \cos((z_{0} - z - c)k_{g})]$$

$$= \frac{c}{2k_{g}\sin(ck_{g})} \sin(k_{g}z)\sin(k_{g}(c - z_{0}))$$
(C.10)

Combining eqs. (C.8) and (C.10), we obtain the closed form expression of

$$\sum_{l=1}^{\infty} \frac{\sin\left(\frac{l\pi}{c}z\right) \sin\left(\frac{l\pi}{c}z_0\right)}{k_n^2 - k_0^2} = \frac{c}{2k_g \sin(k_g c)} \begin{cases} \sin(k_g (c-z)) \sin(k_g z_0) & z > z_0 \\ \sin(k_g z) \sin(k_g (c-z_0)) & z < z_0 \end{cases}$$
(C.11)

If we define

$$f_{mn}(z, z_0) = \begin{cases} \sin(k_g(c-z))\sin(k_g z_0) & z > z_0\\ \sin(k_g z)\sin(k_g(c-z_0)) & z < z_0 \end{cases}$$
(C.12)

then eq. (C.11) can be rewritten as

$$\sum_{l=1}^{\infty} \frac{\sin(\frac{l\pi}{c}z)\sin(\frac{l\pi}{c}z_0)}{k_n^2 - k_0^2} = \frac{c}{2k_g \sin(k_g c)} f_{mn}(z, z_0)$$
 (C.13)

2. Evaluation of 
$$\sum_{l=1}^{\infty} \frac{\cos\left(\frac{l\pi}{c}z\right)\cos\left(\frac{l\pi}{c}z_0\right)}{k_n^2 - k_0^2}$$

$$\sum_{l=1}^{\infty} \frac{\cos\left(\frac{l\pi}{c}z\right)\cos\left(\frac{l\pi}{c}z_{0}\right)}{k_{n}^{2} - k_{0}^{2}} = \frac{1}{2} \left[ \sum_{l=1}^{\infty} \frac{\cos\left(\frac{l\pi}{c}(z - z_{0})\right)}{\left(\frac{l\pi}{c}\right)^{2} - k_{g}^{2}} + \sum_{l=1}^{\infty} \frac{\cos\left(\frac{l\pi}{c}(z + z_{0})\right)}{\left(\frac{l\pi}{c}\right)^{2} - k_{g}^{2}} \right]$$
(C.14)

where  $k_g^2$  is given by eq. (C.5). Based on eqs. (C.6), (C.7) and (C.9), we have

$$\sum_{l=1}^{\infty} \frac{\cos\left(\frac{l\pi}{c}z\right)\cos\left(\frac{l\pi}{c}z_{0}\right)}{k_{n}^{2}-k_{0}^{2}}$$

$$=\begin{cases} \frac{1}{4k_{g}^{2}} - \frac{c}{4k_{g}} \frac{\cos((z-z_{0}-c)k_{g})}{\sin(ck_{g})} \\ \frac{1}{4k_{g}^{2}} - \frac{c}{4k_{g}} \frac{\cos((z_{0}-z-c)k_{g})}{\sin(ck_{g})} + \frac{1}{4k_{g}^{2}} - \frac{c}{4k_{g}} \frac{\cos((z+z_{0}-c)k_{g})}{\sin(ck_{g})} \end{cases}$$

$$=\begin{cases} \frac{1}{2k_{g}^{2}} - \frac{c}{2k_{g}} \frac{\cos((ck_{g}-c)k_{g})}{\sin(ck_{g})} & (C.15) \end{cases}$$

$$=\begin{cases} \frac{1}{2k_{g}^{2}} - \frac{c}{2k_{g}} \frac{\cos(ck_{g}-c)\cos(k_{g}(c-z))\cos(k_{g}z_{0})}{\cos(k_{g}z_{0})} & z > z_{0} \\ \frac{1}{2k_{g}^{2}} - \frac{c}{2k_{g}} \frac{\cos(ck_{g}-c)\cos(k_{g}z_{0})}{\cos(k_{g}z_{0})} & z < z_{0} \end{cases}$$

That is,

$$\sum_{l=1}^{\infty} \frac{\cos\left(\frac{l\pi}{c}z\right)\cos\left(\frac{l\pi}{c}z_{0}\right)}{k_{n}^{2} - k_{0}^{2}} - \frac{1}{2k_{g}^{2}} = -\frac{c}{2k_{g}\sin(ck_{g})}g_{mn}$$
 (C.16)

where

$$g_{mn} = \begin{cases} \cos(k_g(c-z))\cos(k_g z_0) & z > z_0 \\ \cos(k_g z)\cos(k_g(c-z_0)) & z < z_0 \end{cases}$$
 (C.17)

Therefore,

$$\sum_{l=0}^{\infty} \frac{\varepsilon_{0n} \cos\left(\frac{l\pi}{c}z\right) \cos\left(\frac{l\pi}{c}z_0\right)}{2(k_n^2 - k_0^2)} = -\frac{c}{2k_g \sin(ck_g)} g_{mn}$$
 (C.18)

After we derived these two closed form expressions (eqs. (C.13) and (C.18)) of the series summation, we can apply them to the electric dyadic Green's function to obtain an alternative representation.

In order to derive the alternative expressions for the electric dyadic Green's function based on eqs. (C.13) and (C.18), we can evaluate the summation over any one of the three indices n, m, and l. However, there are different numerators for the different components in eq. (C.2). Therefore, to derive the simplest expression for the dyadic Green's function, we may evaluate the summation over index n for  $\hat{x}\hat{x}$ ,  $\hat{y}\hat{z}$ , and  $\hat{z}\hat{y}$  components, the summation over index m for  $\hat{y}\hat{y}$ ,  $\hat{x}\hat{z}$ , and  $\hat{z}\hat{x}$  components and the summation over index l for  $\hat{z}\hat{z}$ ,  $\hat{x}\hat{y}$ , and  $\hat{y}\hat{x}$  components using eqs. (C.13) and (C.18). The expression for  $\overline{G}_{eo}$  (D.2) can then be rewritten as

$$\begin{split} \overline{G}_{eo}(\hat{r}_0,\hat{r}) &= -\frac{1}{k_0^2} \Biggl\{ \sum_{m=1}^{\infty} \sum_{l=1}^{\infty} \frac{4}{bck_{gml} \sin(ak_{gml})} \Biggl[ \Biggl( \left( \frac{m\pi}{b} \right)^2 + \left( \frac{l\pi}{c} \right)^2 \Biggr) g_{ml}(x,x_0) \\ &\sin \frac{m\pi}{b} y \sin \frac{m\pi}{b} y_0 \sin \frac{l\pi}{c} z \sin \frac{l\pi}{c} z_0 \hat{x} \hat{x} + \frac{m\pi l\pi}{b} \frac{l\pi}{c} f_{ml}(x,x_0) \Biggl( \cos \frac{m\pi}{b} y \right) \\ &\sin \frac{m\pi}{b} y_0 \sin \frac{l\pi}{c} z \cos \frac{l\pi}{c} z_0 \hat{y} \hat{z} + \sin \frac{m\pi}{b} y \cos \frac{m\pi}{b} y_0 \cos \frac{l\pi}{c} z \sin \frac{l\pi}{c} z_0 \hat{z} \hat{y} \Biggr) \Biggr] \\ &+ \sum_{n=1}^{\infty} \sum_{l=1}^{\infty} \frac{4}{ack_{gnl} \sin(bk_{gnl})} \Biggl[ \Biggl( \left( \frac{n\pi}{a} \right)^2 + \left( \frac{l\pi}{c} \right)^2 \Biggr) g_{nl}(y,y_0) \sin \frac{n\pi}{a} x \Biggr] \\ &\sin \frac{n\pi}{a} x_0 \sin \frac{l\pi}{c} z \sin \frac{l\pi}{c} z_0 \hat{y} \hat{y} + \frac{n\pi l\pi}{a} \frac{l\pi}{c} f_{nl}(y,y_0) \Biggl( \sin \frac{n\pi}{a} x \cos \frac{n\pi}{a} x_0 \cos \frac{l\pi}{c} z \cos \frac{l\pi}{c} z \Biggr) \Biggr] \\ &+ \sum_{n=1}^{\infty} \sum_{m=1}^{\infty} \frac{4}{abk_{gnm} \sin(ck_{gnm})} \Biggl[ \Biggl( \Biggl( \frac{n\pi}{a} \Biggr)^2 + \Biggl( \frac{m\pi}{b} \Biggr)^2 \Biggr) g_{nm}(z,z_0) \sin \frac{n\pi}{a} x \Biggr] \\ &\sin \frac{n\pi}{a} x_0 \sin \frac{m\pi}{b} y \sin \frac{m\pi}{b} y_0 \hat{z} \hat{z} + \frac{n\pi m\pi}{a} \frac{m\pi}{b} f_{nm}(z,z_0) \Biggl( \cos \frac{n\pi}{a} x \sin \frac{n\pi}{a} x_0 \Biggr] \Biggr\} \\ &\sin \frac{m\pi}{b} y \cos \frac{m\pi}{b} y_0 \hat{x} \hat{y} + \sin \frac{n\pi}{a} x \cos \frac{n\pi}{a} x_0 \cos \frac{m\pi}{b} y \sin \frac{m\pi}{b} y_0 \hat{y} \hat{x} \Biggr) \Biggr] \Biggr\} \end{split}$$

where the parameters

$$k_{gml} = \sqrt{k_0^2 - \left(\left(\frac{m\pi}{b}\right)^2 + \left(\frac{l\pi}{c}\right)^2\right)}$$
 (C.20)

$$k_{gnl} = \sqrt{k_0^2 - \left(\left(\frac{n\pi}{a}\right)^2 + \left(\frac{l\pi}{c}\right)^2\right)}$$
 (C.21)

$$k_{gnm} = \sqrt{k_0^2 - \left(\left(\frac{n\pi}{a}\right)^2 + \left(\frac{m\pi}{b}\right)^2\right)}$$
 (C.22)

$$g_{ml}(x, x_0) = \begin{cases} \cos(k_{gml}(a - x))\cos(k_{gml}x_0) & x > x_0 \\ \cos(k_{gml}x)\cos(k_{gml}(a - x_0)) & x < x_0 \end{cases}$$
 (C.23)

$$g_{nl}(y, y_0) = \begin{cases} \cos(k_{gnl}(b-y))\cos(k_{gnl}y_0) & y > y_0\\ \cos(k_{gnl}y)\cos(k_{gnl}(b-y_0)) & y < y_0 \end{cases}$$
(C.24)

$$g_{nm}(z, z_0) = \begin{cases} \cos(k_{gnm}(c - z))\cos(k_{gnm}z_0) & z > z_0\\ \cos(k_{gnm}z)\cos(k_{gnm}(c - z_0)) & z < z_0 \end{cases}$$
 (C.25)

$$f_{nm}(z, z_0) = \begin{cases} \sin(k_{gnm}(c - z))\sin(k_{gnm}z_0) & z > z_0\\ \sin(k_{gnm}z)\sin(k_{gnm}(c - z_0)) & z < z_0 \end{cases}$$
 (C.26)

$$f_{ml}(x, x_0) = \begin{cases} \sin(k_{gml}(a - x))\sin(k_{gml}x_0) & x > x_0\\ \sin(k_{gml}x)\sin(k_{gml}(a - x_0)) & x < x_0 \end{cases}$$
 (C.27)

$$f_{nl}(y, y_0) = \begin{cases} \sin(k_{gnl}(b-y))\sin(k_{gnl}y_0) & y > y_0\\ \sin(k_{gnl}y)\sin(k_{gnl}(b-y_0)) & y < y_0 \end{cases}$$
(C.28)

That is, we have obtained the double summation representation instead of the triple summation representation for the electric dyadic Green's function.

So far we have not considered the singularity of the closed-form evaluation. Since there exists  $k_{gml}\sin(ak_{gml})$  in the denominator of the evaluation (for  $\hat{x}\hat{x}$ ,  $\hat{y}\hat{z}$ , and  $\hat{z}\hat{y}$  components of  $\overline{G}_{eo}(\hat{r}_0,\hat{r})$ ), the singularity occurs when  $k_{gml}=0$  or  $ak_{gml}=p\pi$ , where p is an integer. Since the three sides of the rectangular cavity (a,b,andc) are not in integer proportion in order to avoid more degenerated modes, the singularity occurs only when one of the summation modes is exactly equal to the initial mode, that is

$$k_0^2 = k_n^2 (C.29)$$

for some indices m and l. For this case, we can not use the above closed-form evaluations to obtain the alternative expressions for the electric dyadic Green's function. However,

based on the analysis given in Chapter 3, we know that the initial resonant frequency will shift slightly after a material sample is placed within the cavity. Therefore, when the singularity occurs, we can make the estimation of

$$k_n^2 - k_0^2 \cong -sk_0^2 \tag{C.30}$$

where s is the shift rate of the resonant eigenvalue and the summation over any one of the three indices can be obtained as follows. For brevity, we only show the derivation for the  $\hat{x}\hat{x}$  component of  $\overline{G}_{eo}(\hat{r}_0, \hat{r})$  when there exists singularity.

When we evaluate the  $\hat{x}\hat{x}$  component of  $\overline{G}_{eo}(\hat{r}_0,\hat{r})$ , we obtain a closed form expression for the summation over index n of

$$\sum_{n=0}^{\infty} \frac{\varepsilon_{0n}}{a} \frac{1}{k_n^2 - k_0^2} \cos \frac{n\pi}{a} x \cos \frac{n\pi}{a} x_0$$
 (C.31)

and  $k_g = \sqrt{k_0^2 - \left(\left(\frac{m\pi}{b}\right)^2 + \left(\frac{l\pi}{c}\right)^2\right)}$ . At the singularity points of  $k_g$ , we find that they occur when

$$k_n^2 - k_0^2 = \left(\frac{n\pi}{a}\right)^2 - \left(\frac{n_0\pi}{a}\right)^2$$
 (C.32)

where  $n_0$  denotes one of the three indices of the initial mode (we assume that the three sides a, b, and c of the rectangular cavity are not in integer proportion). The summation in eq. (C.31) can be written as

$$\sum_{n=0}^{\infty} \frac{\varepsilon_{0n}}{a} \frac{1}{\left(\frac{n\pi}{a}\right)^2 - \left(\frac{n_0\pi}{a}\right)^2} \cos\frac{n\pi}{a} x \cos\frac{n\pi}{a} x_0 \tag{C.33}$$

There are formulas for summations of [2]

$$\sum_{n=1}^{\infty} \frac{\cos nx}{n^2 - a^2} = \frac{1}{2a^2} - \frac{\pi}{2a} \frac{\cos(x - \pi)a}{\sin(\pi a)} \qquad 0 < x < 2\pi$$
 (C.34)

$$\sum_{n=1}^{\infty} \frac{\cos nx}{n^2 (n^2 - a^2)} = \frac{\pi x}{2a^2} - \frac{\pi^2}{6a^2} - \frac{x^2}{4a^2} - \frac{\pi \cos(x - \pi)a}{2a^3 \sin(\pi a)} + \frac{1}{2a^4} \qquad 0 < x < 2\pi$$
 (C.35)

Using eqs. (C.34) and (C.35), we can obtain the following summation as

$$\sum_{n=1}^{\infty} \frac{\cos nx}{n^2} = \frac{x^2}{4} + \frac{\pi^2}{6} - \frac{\pi x}{2}$$
 (C.36)

and based on eq. (C.36), we can obtain the following summation of

$$\sum_{n=1}^{\infty} \frac{2}{a} \frac{\cos \frac{n\pi}{a} x \cos \frac{n\pi}{a} x_0}{\left(\frac{n\pi}{a}\right)^2} = \frac{1}{a} \sum_{n=1}^{\infty} \frac{\cos \frac{n\pi}{a} (x + x_0) + \cos \frac{n\pi}{a} |x - x_0|}{\left(\frac{n\pi}{a}\right)^2}$$

$$= \frac{1}{2a} (x^2 + x_0^2) + \frac{a}{3} - x_b$$
(C.37)

where  $x_b$  is the greater one of x and  $x_0$ . In general  $n_0$  is not very large because we assume a lower order mode as the initial mode.

When  $n_0 = 0$ , based on eq. (C.37) the summation (C.31) or (C.33) is given by

$$-\frac{1}{a}\frac{1}{sk_0^2} + \sum_{n=1}^{\infty} \frac{2}{a} \frac{\cos\frac{n\pi}{a}x\cos\frac{n\pi}{a}x_0}{\left(\frac{n\pi}{a}\right)^2} = -\frac{1}{a}\frac{1}{sk_0^2} + \frac{1}{2a}(x^2 + x_0^2) + \frac{a}{3} - x_b$$
 (C.38)

When  $n_0 \neq 0$ , based on eq. (C.37) the summation (C.33) can be expressed as

$$\sum_{n=0}^{\infty} \frac{\varepsilon_{0n}}{a} \frac{1}{\left(\frac{n\pi}{a}\right)^{2} - \left(\frac{n_{0}\pi}{a}\right)^{2}} \cos\frac{n\pi}{a}x \cos\frac{n\pi}{a}x_{0}$$

$$= \sum_{\substack{n=0\\n\neq n_{0}\\n\neq n_{0}}}^{n_{0n}} \frac{\varepsilon_{0n}}{a} \frac{1}{\left(\frac{n\pi}{a}\right)^{2} - \left(\frac{n_{0}\pi}{a}\right)^{2}} \cos\frac{n\pi}{a}x \cos\frac{n\pi}{a}x_{0} + \sum_{n=1}^{\infty} \frac{2}{a} \frac{1}{\left(\frac{n\pi}{a}\right)^{2}} \cos\frac{n\pi}{a}x \cos\frac{n\pi}{a}x_{0}$$

$$- \sum_{n=1}^{n_{0n}} \frac{2}{a} \frac{1}{\left(\frac{n\pi}{a}\right)^{2}} \cos\frac{n\pi}{a}x \cos\frac{n\pi}{a}x_{0} - \frac{2}{a} \frac{1}{sk_{0}^{2}} \cos\frac{n_{0}\pi}{a}x \cos\frac{n_{0}\pi}{a}x_{0}$$

$$= \sum_{n=1}^{n_{0n}} \frac{2}{a} \frac{\left(\frac{n_{0}\pi}{a}\right)^{2}}{\left(\frac{n\pi}{a}\right)^{2} + \left(\frac{n_{0}\pi}{a}\right)^{2}} \cos\frac{n\pi}{a}x \cos\frac{n\pi}{a}x_{0} - \frac{1}{a} \left(\frac{a}{n_{0}\pi}\right)^{2}$$

$$+ \frac{1}{2a} (x^{2} + x_{0}^{2}) + \frac{a}{3} - x_{b} - \frac{2}{a} \left(\frac{1}{\left(\frac{n_{0}\pi}{a}\right)^{2}} + \frac{1}{sk_{0}^{2}}\right) \cos\frac{n_{0}\pi}{a}x \cos\frac{n_{0}\pi}{a}x_{0}$$
(C.39)

where  $n_{0i}$  is chosen in such a way that when  $n > n_{0i}$  the following approximation is valid

$$\left(\frac{n\pi}{a}\right)^2 - \left(\frac{n_0\pi}{a}\right)^2 \cong \left(\frac{n\pi}{a}\right)^2 \tag{C.40}$$

Equation (C.38) or (C.39) is another alternative representation for the  $\hat{x}\hat{x}$  component of  $\overline{G}_{eo}(\hat{r}_0, \hat{r})$  when there exists singularity. The same procedure can be applied to obtain the alternative expressions for the other components of the dyadic Green's function when there exist singularties.



#### APPENDIX D

# INHOMOGENEOUS DIELECTRIC SPHERE IN UNIFORMELY APPLIED STATIC FIELD

In this appendix, the electric field in an inhomogeneous dielectric sphere which includes two regions of different dielectric materials induced by a uniform static electric field is determined. The geometry of this inhomogeneous dielectric sphere is shown in Figure D.1.

We select the polar axis ( $\theta = 0$  or z-axis) to be in parallel with  $\vec{E}_0$ . Using the spherical coordinate system, the induced electric field inside the dielectric sphere will be independent of  $\phi$  [14]. Therefore,

$$\vec{E} = \vec{E}(r, \theta) \tag{D.1}$$

inside the dielectric sphere.

In the absence of the sphere, the primary electric field is given by

$$\vec{E}^P = E_0 \hat{z} \tag{D.2}$$

in rectangular coordinate system. The primary potential is given by

$$V^P = -E_0 z \tag{D.3}$$

in rectangular coordinates. In spherical coordinates, we have

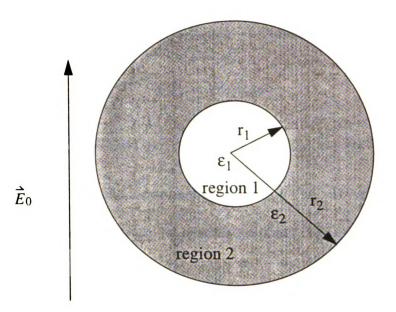


Figure D.1 Geometry of an inhomogeneous dielectric sphere

$$z = r\cos\theta \tag{D.4}$$

$$\hat{z} = \cos\theta \hat{r} - \sin\theta \hat{\theta} \tag{D.5}$$

So the primary electric field and potential can be expressed in the spherical coordinates as

$$\vec{E}^{p}(r,\theta) = E_0 \cos \theta \hat{r} - E_0 \sin \theta \hat{\theta}$$
 (D.6)

$$V^{p}(r,\theta) = -E_0 r \cos\theta \tag{D.7}$$

This  $V^p(r, \theta)$  also satisfies the Laplace equation  $\nabla^2 V^p(r, \theta) = 0$ .

The next step is to find the secondary potentials  $V^s(r, \theta)$  which are maintained by the equivalent induced charges on the spherical surfaces. The total potentials in region 1 and 2 are expressed as:

$$V_1(r, \theta) = V^p(r, \theta) + V_1^s(r, \theta)$$
 (D.8)

$$V_{\gamma}(r,\theta) = V^{p}(r,\theta) + V_{\gamma}^{s}(r,\theta)$$
 (D.9)

All the potentials satisfy the Laplace equation  $\nabla^2 V(r, \theta) = 0$ .

To determine  $V^s(r, \theta)$ , we need to employ the variables separation method to solve a Laplace equation. The solution of this Laplace equation is given by [14]:

$$V^{s}(r,\theta) = \sum_{n=0}^{\infty} [G_{n}r^{n} + H_{n}r^{-(n+1)}]P_{n}(\cos\theta)$$
 (D.10)

where  $P_n(\cos\theta)$  denotes the Legendre function of order n and degree 0.

The secondary potentials  $V^{s}(r, \theta)$  in regions 1 and 2 can be expressed as

$$V_1^s(r,\theta) = \sum_{n=0}^{\infty} A_n r^n P_n(\cos\theta)$$
 for  $0 \le r < r_1$  (D.11)

$$V_2^s(r,\theta) = \sum_{n=0}^{\infty} [B_n r^n + C_n r^{-(n+1)}] P_n(\cos\theta) \qquad \text{for } r_1 \le r < r_2$$
 (D.12)

and the secondary potential  $V^{s}(r, \theta)$  outside the sphere can be expressed as

$$V_0^s(r,\theta) = \sum_{n=0}^{\infty} D_n r^{-(n+1)} P_n(\cos\theta) \qquad \text{for } r \ge r_2$$
 (D.13)

The total potentials in the three regions are then given as:

(1) for  $0 \le r < r_1$ 

$$V_1(r,\theta) = -E_0 r \cos \theta + \sum_{n=0}^{\infty} A_n r^n P_n(\cos \theta)$$
 (D.14)

(2) for  $r_1 \le r < r_2$ 

$$V_2(r,\theta) = -E_0 r \cos \theta + \sum_{n=0}^{\infty} [B_n r^n + C_n r^{-(n+1)}] P_n(\cos \theta)$$
 (D.15)

(3) for  $r \ge r_2$ 

$$V_0(r,\theta) = -E_0 r \cos \theta + \sum_{n=0}^{\infty} D_n r^{-(n+1)} P_n(\cos \theta)$$
 (D.16)

The unknown coefficients  $A_n$ ,  $B_n$ ,  $C_n$  and  $D_n$  will be determined by the boundary conditions on  $r = r_1$  and  $r = r_2$  as:

$$V_1(r_1, \theta) = V_2(r_1, \theta)$$
 (D.17)

$$V_2(r_2, \theta) = V_0(r_2, \theta)$$
 (D.18)

$$D_{1r}(r_1, \theta) = D_{2r}(r_1, \theta)$$
 (D.19)

$$D_{2r}(r_2, \theta) = D_{0r}(r_2, \theta)$$
 (D.20)

Equation (D.17) leads to

$$\sum_{n=0}^{\infty} A_n r_1^n P_n(\cos \theta) = \sum_{n=0}^{\infty} [B_n r_1^n + C_n r_1^{-(n+1)}] P_n(\cos \theta)$$
 (D.21)

Since  $P_n(\cos\theta)$  are a set of orthogonal functions [14], we have

$$A_n = B_n + C_n r_1^{-(2n+1)} (D.22)$$

Equation (D.18) leads to

$$\sum_{n=0}^{\infty} [B_n r_2^n + C_n r_2^{-(n+1)}] P_n(\cos \theta) = \sum_{n=0}^{\infty} D_n r_2^{-(n+1)} P_n(\cos \theta)$$
 (D.23)

and

$$D_n = B_n r_2^{2n+1} + C_n (D.24)$$

Equation (D.19) leads to

$$\epsilon_{1} \left\{ -E_{0} \cos \theta + \sum_{n=0}^{\infty} n A_{n} r_{1}^{n-1} P_{n}(\cos \theta) \right\}$$

$$= \epsilon_{2} \left\{ -E_{0} \cos \theta + \sum_{n=0}^{\infty} [n B_{n} r_{1}^{n-1} - (n+1) C_{n} r_{1}^{-(n+2)}] P_{n}(\cos \theta) \right\}$$
(D.25)

or

$$\sum_{n=0}^{\infty} \left[ \varepsilon_2 (nB_n r_1^{n-1} - (n+1)C_n r_1^{-(n+2)}) - \varepsilon_1 nA_n r_1^{n-1} \right] P_n(\cos \theta)$$

$$= (\varepsilon_2 - \varepsilon_1) E_0 \cos \theta$$
(D.26)

Equation (D.20) leads to

$$\epsilon_{2} \left\{ -E_{0} \cos \theta + \sum_{n=0}^{\infty} [nB_{n} r_{2}^{n-1} - (n+1)C_{n} r_{2}^{-(n+2)}] P_{n}(\cos \theta) \right\} \\
= \epsilon_{0} \left\{ -E_{0} \cos \theta - \sum_{n=0}^{\infty} (n+1)D_{n} r_{2}^{-(n+2)} P_{n}(\cos \theta) \right\} \tag{D.27}$$

or

$$\sum_{n=0}^{\infty} \left[ \varepsilon_2 (nB_n r_2^{n-1} - (n+1)C_n r_2^{-(n+2)}) + \varepsilon_0 (n+1)D_n r_2^{-(n+2)} \right] P_n(\cos \theta)$$

$$= (\varepsilon_2 - \varepsilon_0) E_0 \cos \theta$$
(D.28)

Using eqs. (D.26) and (D.28), we have

$$\varepsilon_2[nB_nr_1^{n-1} - (n+1)C_nr_1^{-(n+2)}] - \varepsilon_1nA_nr_1^{n-1} = 0$$
 (D.29)

$$\varepsilon_2[nB_nr_2^{n-1} - (n+1)C_nr_2^{-(n+2)}] + \varepsilon_0(n+1)D_nr_2^{-(n+2)} = 0$$
 (D.30)

for  $n \neq 1$  and

$$\varepsilon_2(B_1 - 2C_1r_1^{-3}) - \varepsilon_1A_1 = (\varepsilon_2 - \varepsilon_1)E_0$$
 (D.31)

$$\varepsilon_2(B_1 - 2C_1r_2^{-2}) + 2\varepsilon_0D_1r_2^{-3} = (\varepsilon_2 - \varepsilon_0)E_0$$
 (D.32)

Substituting eqs. (D.22) and (D.24) into eqs. (D.29) and (D.30), we have

$$(\varepsilon_2 - \varepsilon_1) n r_1^{n-1} B_n - [\varepsilon_1 n + \varepsilon_2 (n+1)] r_1^{-(n+2)} C_n = 0$$
 (D.33)

$$[\varepsilon_2 n + \varepsilon_0 (n+1)] r_2^{n-1} B_n - (\varepsilon_2 - \varepsilon_0) (n+1) r_2^{-(n+2)} C_n = 0$$
 (D.34)

For non-trivial solutions for  $B_n$  and  $C_n$ , coefficient matrix needs to be zero. That is, the determinant of the following matrix is zero.

$$\begin{bmatrix} (\varepsilon_{2} - \varepsilon_{1})nr_{1}^{n-1} & -[\varepsilon_{1}n + \varepsilon_{2}(n+1)]r_{1}^{-(n+2)} \\ [\varepsilon_{2}n + \varepsilon_{0}(n+1)]r_{2}^{n-1} & -(\varepsilon_{2} - \varepsilon_{0})(n+1)r_{2}^{-(n+2)} \end{bmatrix}$$
(D.35)

However, the matrix in eq. (D.35) is a function of  $r_1$ ,  $r_2$ ,  $\varepsilon_0$ ,  $\varepsilon_1$ , and  $\varepsilon_2$ , and it is obvious that the determinant of this matrix can not be zero. Therefore, the unknown coefficients  $B_n$  and  $C_n$  are all equal to zero for  $n \ne 1$  and the unknown coefficients  $A_n$  and  $D_n$  are also equal to zero based on eqs. (D.22) and (D.24).

For n = 1, the unknown coefficients  $A_1$ ,  $B_1$ ,  $C_1$  and  $D_1$  are to be obtained as follows:

Substituting eqs. (D.22) and (D.24) into eqs.(D.31) and (D.32), we have

$$(\varepsilon_1 - \varepsilon_2)B_1 + (\varepsilon_1 + 2\varepsilon_2)r_1^{-3}C_1 = (\varepsilon_1 - \varepsilon_2)E_0$$
 (D.36)

$$(\varepsilon_2 + 2\varepsilon_0)B_1 - 2(\varepsilon_2 - \varepsilon_0)r_2^{-3}C_1 = (\varepsilon_2 - \varepsilon_0)E_0$$
 (D.37)

Then the solutions for  $A_1$ ,  $B_1$ ,  $C_1$  and  $D_1$  can be expressed as

$$B_{1} = \frac{[(\varepsilon_{1} + 2\varepsilon_{2})r_{1}^{-3} + 2(\varepsilon_{1} - \varepsilon_{2})r_{2}^{-3}](\varepsilon_{2} - \varepsilon_{0})E_{0}}{(\varepsilon_{1} + 2\varepsilon_{2})(\varepsilon_{2} + 2\varepsilon_{0})r_{1}^{-3} + 2(\varepsilon_{1} - \varepsilon_{2})(\varepsilon_{2} - \varepsilon_{0})r_{2}^{-3}}$$
(D.38)

$$C_1 = \frac{3\varepsilon_0(\varepsilon_1 - \varepsilon_2)E_0}{(\varepsilon_1 + 2\varepsilon_2)(\varepsilon_2 + 2\varepsilon_0)r_1^{-3} + 2(\varepsilon_1 - \varepsilon_2)(\varepsilon_2 - \varepsilon_0)r_2^{-3}}$$
(D.39)

$$A_{1} = \frac{(2\varepsilon_{0}\varepsilon_{1} - 5\varepsilon_{0}\varepsilon_{2} + \varepsilon_{1}\varepsilon_{2} + 2\varepsilon_{2}^{2})r_{1}^{-3} + 2(\varepsilon_{2} - \varepsilon_{0})(\varepsilon_{1} - \varepsilon_{2})r_{2}^{-3}}{(\varepsilon_{1} + 2\varepsilon_{2})(\varepsilon_{2} + 2\varepsilon_{0})r_{1}^{-3} + 2(\varepsilon_{1} - \varepsilon_{2})(\varepsilon_{2} - \varepsilon_{0})r_{2}^{-3}}E_{0}$$
(D.40)

$$D_1 = \frac{(\varepsilon_1 + 2\varepsilon_2)(\varepsilon_2 - \varepsilon_0)r_1^{-3}r_2^3 + (\varepsilon_1 - \varepsilon_2)(\varepsilon_0 + 2\varepsilon_2)}{(\varepsilon_1 + 2\varepsilon_2)(\varepsilon_2 + 2\varepsilon_0)r_1^{-3} + 2(\varepsilon_1 - \varepsilon_2)(\varepsilon_2 - \varepsilon_0)r_2^{-3}}E_0$$
 (D.41)

Therefore, the potentials in the three regions are given as

$$V_1(r,\theta) = \frac{-9\varepsilon_0\varepsilon_2r_1^{-3}E_0}{(\varepsilon_1 + 2\varepsilon_2)(\varepsilon_2 + 2\varepsilon_0)r_1^{-3} + 2(\varepsilon_1 - \varepsilon_2)(\varepsilon_2 - \varepsilon_0)r_2^{-3}}r\cos\theta$$
 (D.42)

$$V_{2}(r,\theta) = \frac{-3\varepsilon_{0}(\varepsilon_{1} + 2\varepsilon_{2})r_{1}^{-3}E_{0}}{(\varepsilon_{1} + 2\varepsilon_{2})(\varepsilon_{2} + 2\varepsilon_{0})r_{1}^{-3} + 2(\varepsilon_{1} - \varepsilon_{2})(\varepsilon_{2} - \varepsilon_{0})r_{2}^{-3}}r\cos\theta + \frac{3\varepsilon_{0}(\varepsilon_{1} - \varepsilon_{2})E_{0}}{(\varepsilon_{1} + 2\varepsilon_{2})(\varepsilon_{2} + 2\varepsilon_{0})r_{1}^{-3} + 2(\varepsilon_{1} - \varepsilon_{2})(\varepsilon_{2} - \varepsilon_{0})r_{2}^{-3}}\frac{\cos\theta}{r^{2}}$$
(D.43)

$$V_0(r,\theta) = -E_0 r \cos \theta + \frac{(\varepsilon_1 + 2\varepsilon_2)(\varepsilon_2 - \varepsilon_0)r_1^{-3}r_2^3 + (\varepsilon_1 - \varepsilon_2)(\varepsilon_0 + 2\varepsilon_2)}{(\varepsilon_1 + 2\varepsilon_2)(\varepsilon_2 + 2\varepsilon_0)r_1^{-3} + 2(\varepsilon_1 - \varepsilon_2)(\varepsilon_2 - \varepsilon_0)r_2^{-3}} \frac{E_0 \cos \theta}{r^2} (D.44)$$

and the electric field in region 1 is given as

$$\vec{E}_1 = \frac{-9\varepsilon_0 \varepsilon_2 r_1^{-3} E_0}{(\varepsilon_1 + 2\varepsilon_2)(\varepsilon_2 + 2\varepsilon_0) r_1^{-3} + 2(\varepsilon_1 - \varepsilon_2)(\varepsilon_2 - \varepsilon_0) r_2^{-3}} \hat{z}$$
 (D.45)

The ratio of  $E_1/E_0$  is a constant within region 1 of this inhomogeneous sphere. The electric field in region 2 is given as

$$\dot{\vec{E}}_{2} = 3\varepsilon_{0}E_{0} \left\{ \frac{(\varepsilon_{1} - \varepsilon_{2})r^{-3} - (\varepsilon_{1} + 2\varepsilon_{2})r_{1}^{-3}}{(\varepsilon_{1} + 2\varepsilon_{2})(\varepsilon_{2} + 2\varepsilon_{0})r_{1}^{-3} + 2(\varepsilon_{1} - \varepsilon_{2})(\varepsilon_{2} - \varepsilon_{0})r_{2}^{-3}} \hat{z} + \frac{(\varepsilon_{1} - \varepsilon_{2})r^{-3}}{(\varepsilon_{1} + 2\varepsilon_{2})(\varepsilon_{2} + 2\varepsilon_{0})r_{1}^{-3} + 2(\varepsilon_{1} - \varepsilon_{2})(\varepsilon_{2} - \varepsilon_{0})r_{2}^{-3}} 3\cos\theta\hat{r} \right\}$$
(D.46)

The z component of the electric field in region 2 can be expressed as

$$E_{2z} = 3\varepsilon_0 \frac{(\varepsilon_1 - \varepsilon_2)r^{-3} - (\varepsilon_1 + 2\varepsilon_2)r_1^{-3}}{(\varepsilon_1 + 2\varepsilon_2)(\varepsilon_2 + 2\varepsilon_0)r_1^{-3} + 2(\varepsilon_1 - \varepsilon_2)(\varepsilon_2 - \varepsilon_0)r_2^{-3}} E_0$$
 (D.47)

It is noted that there are other smaller components of the electric field in region 2.

For the special case of  $r_1 = r_2$  and  $\varepsilon_1 = \varepsilon_2$ , i.e. a homogeneous sphere, based on eq. (D.42) the potential in this region is given by

$$V_1(r,\theta) = \frac{-3\varepsilon_0 E_0}{\varepsilon_1 + 2\varepsilon_0} r \cos\theta$$
 (D.48)

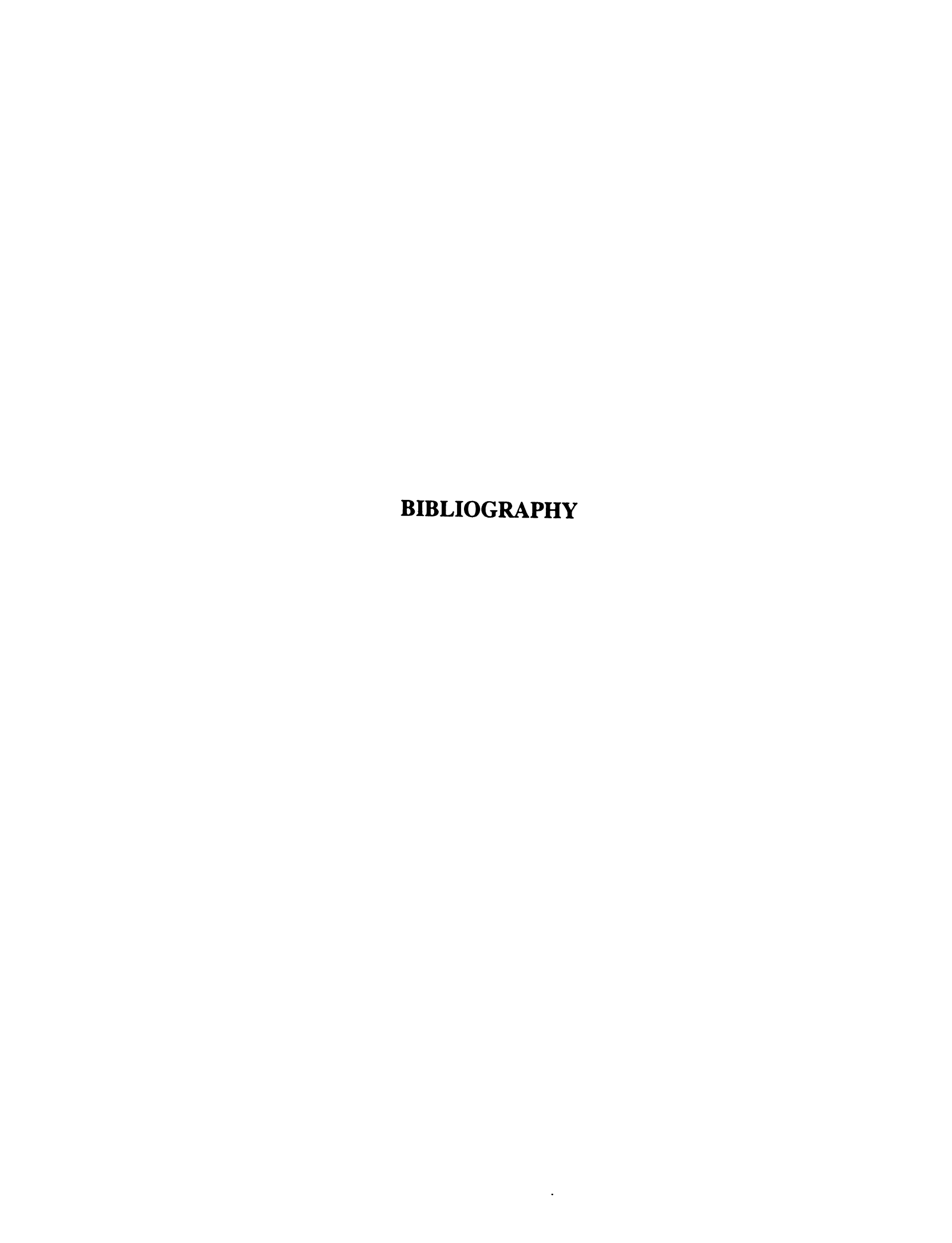
and the electric field is obtained as

$$\vec{E}_1 = \frac{-3\varepsilon_0 E_0}{\varepsilon_1 + 2\varepsilon_0} \hat{z} \tag{D.49}$$

This is the result given in [14]. For another special case of  $r_1 \rightarrow 0$ , which is also a homogeneous sphere, based on eq. (D.43) the potential in this region is given by

$$V_2(r,\theta) = \frac{-3\varepsilon_0 E_0}{\varepsilon_2 + 2\varepsilon_0} r \cos\theta$$
 (D.50)

and the electric field in this region have the same expression as eq. (D.49).



### **BIBLIOGRAPHY**

- [1] A. C. Metaxas and R. Meredith, *Industrial Microwave Heating*, Peter Peregrinus, Ltd. London, England, 1983.
- [2] R. E. Collin, Field Theory of Guided Waves, second edition, IEEE Press, 1991.
- [3] K. G. Ayappa, H.T. Davis, E.A. Davis and J. Gordon, "Two-dimensional finite element analysis of microwave heating," *AIChE Journal*, Vol. 38, pp1577-1592, Oct. 1992
- [4] X. Jia and P. Jolly, "Simulation of microwave field and power distribution in a cavity by a three-dimensional finite element method," *Journal of Microwave Power and Electromagnetic Energy*, Vol. 27, No.1, pp11-22, 1992
- [5] F. Liu, I. Turner, and M. Bialkowski, "A finite-difference time-domain simulation of power density distribution in a dielectric loaded microwave cavity," *Journal of Microwave Power and Electromagnetic Energy*, Vol. 29, pp138-148, 1994.
- [6] H. Zhao, I. Turner, and F. W. Liu, "Numerical simulation of the power density distribution generated in a multimode cavity by using the method of lines technique to solve directly for the electric field," *IEEE Trans. Microwave Theory Tech.*, Vol. MTT-44, pp2185-2194, 1996.
- [7] F. Torres and B. Jecko, "Complete FDTD analysis of microwave heating processing in frequency-dependent and temperature-dependent media," *IEEE Trans. Microwave Theory Tech.*, Vol. MTT-45, pp108-117, 1997.
- [8] W. Fu and A. Metaxas, "Numerical prediction of three-dimensional power density distribution in a multi-mode cavity," *Journal of Microwave Power and Electromagnetic Energy*, Vol. 29, pp67-75, 1994.
- [9] C. T. Tai, *Dyadic Green's Functions in Electromagnetic Theory*, Scranton, International Textbook Educational Publishers, 1971.
- [10] K.M. Chen, *Notes for EE 836*, Michigan State University.
- [11] Y. Rahmat-Samii, "On the question of computation of the dyadic Green's Function at the source region in waveguides and cavities," *IEEE Trans. Microwave Theory Tech.*, Vol. MTT-23, pp762-765,1975

- [12] K. Kurokawa, "The expansions of electromagnetic fields in cavities," *IRE Trans. Microwave Theory Tech.* vol. MTT-6,pp178-187,1958.
- [13] M. Kisliuk, "The dyadic Green's functions for cylindrical waveguides and cavities," *IEEE Trans. Microwave Theory Tech.*, Vol. MTT-28, pp894-898,1980.
- [14] K. M. Chen, *Notes for EE 835*, Michigan State University.
- [15] W. A. Johnson, A. Q. Howard, and D. G. Dudley, "On the irrotational component of the electric Green's function," *Radio Science*, Vol. 14, pp961-967, 1979.
- [16] J. C. Slater, *Microwave Electronics*, D. Van Nostrand Co., Inc. New York, N.Y. 1950.
- [17] R. E. Collin, "On the incompleteness of E and H modes in waveguides," Can. J. Phys., Vol. 51, pp1135-1140, 1973.
- [18] A. Q. Howard, "On the longitudinal component of the Green's function dyadic," *Proc. IEEE*, vol. 62, pp1704-1705,1974.
- [19] V. Bladel, J. "Some remarks on Green's dyadic for infinite space," *IEEE Trans. Antenna Propagation.*, Vol. AP-9, pp563-566,1961.
- [20] C. T. Tai, "Equivalent layers of surface charge, current sheet, and polarization in the eigenfunction expansions of Green's functions in electromagnetic theory," *IEEE Trans. Antennas and Propagation*, vol. AP-29, pp733-739,1981.
- [21] C. T. Tai and P. Rozenfeld, "Different representations of dyadic Green's functions for a rectangular cavity," *IEEE Trans. Microwave Theory Tech.*, Vol. MTT-24, pp597-601,1976.
- [22] R. F. Harrington, Field Computation by Moment Methods, New York,: Macmillan, 1968.
- [23] J. A. Stratton, *Electromagnetic Theory*, New York, NY: McGraw-Hill Book Company, Inc., 1941.
- [24] A. D. Yaghjian, "Electric dyadic Green's functions in the source region," *Proc. IEEE*, Vol. 68 pp248-263,Feb. 1980.
- [25] L. W. Pearson, "On the spectral expansion of the electric and magnetic dyadic Green's functions in cylindrical harmonics," *Radio Science*, Vol.18, pp166-174, 1983.
- [26] R. Lampe, P. Klock, and P. Mayes, "Integral transforms useful for the accelerated summation of periodic, free-space Green's functions,", *IEEE Trans. Microwave Theory Tech.*, Vol. MTT-33, pp734-736,1985.

- [27] K. M. Chen, "A simple physical picture of tensor Green's function in source region," *Proc. IEEE*, Vol. 65 pp1202-1204, August 1977.
- [28] C. T. Tai, "On the eigenfunction expansion of dyadic Green's functions," *Proc. IEEE*, Vol. 61 pp480-481, Apr. 1973.
- [29] J. Xu, "Fast Convergent dyadic Green's function in a rectangular waveguide," *International Journal of Infrared and Millimeter Waves*, Vol. 14 No.9 pp1789-1800, 1993.
- [30] D. E. Livesay and K. M. Chen, "Electromagnetic fields induced inside arbitrarily shaped biological bodies," *IEEE Trans. Microwave Theory Tech.*, Vol. MTT-22, pp1273-1280,1974.
- [31] B. S. Guru and K. M. Chen, "Experimental and theoretical studies on electromagnetic fields induced inside finite biological bodies," *IEEE Trans. Microwave Theory Tech.*, Vol. MTT-24, pp433-440,1976.
- [32] A. Ittipiboon and L. Shafai, "Probe mutual impedance in a rectangular waveguide," *IEEE Trans. Microwave Theory Tech.*, Vol. MTT-33, pp327-335, 1985.
- [33] L. W. Li, P. S. Kooi, M. S. Leong, T. S. Yeo, and S. L. Ho, "On the eigenfunction expansion of electromagnetic dyadic Green's functions in rectangular cavities and waveguides," *IEEE Trans. Microwave Theory Tech.*, Vol. MTT-43, pp700-702,1995.
- [34] S. Hashemi-Yeganeh, "On the summation of double infinite series field computations inside rectangular cavities," *IEEE Trans. Microwave Theory Tech.*, Vol. MTT-43, pp641-646,1995.
- [35] A. S. Omar, E. Jensen, and S. Lutgert, "On the modal expansion of resonator field in the source region," *IEEE Trans. Microwave Theory Tech.*, Vol. MTT-40, pp1730-1732,1992.
- [36] R. M. Shubair and Y. L. Chow, "Efficient computation of the periodic Green's function in layered dielectric media," *IEEE Trans. Microwave Theory Tech.*, Vol. NiTT-41 pp498-502,1993.
- [37] E. B. Manring and J. Asmussen, "Useful Bessel function identities and integrals," *IEEE Trans. Microwave Theory Tech.*, Vol. MTT-41, pp1468-1471,1993.
- [38] R. F. Harrington, *Time-Harmonic Electromagnetic Fields*, New York: McGraw-Hill, 1961.
- [39] C. A. Balanis, Advanced Engineering Electromagnetics, New York: Wiley, 1989.
- [40] J. M. Jarem, "A multifilament method-of moments solution for the input impedance of a probe-excited semi-infinite waveguide," *IEEE Trans. Microwave Theory Tech.*,

- Vol. MTT-35, pp14-19, 1987.
- [41] K. Ishibashi and E. Sawadom "A method for the rapidly convergent representation of electromagnetic fields in a rectangular waveguide," *IEEE Trans. Microwave Theory Tech.*, Vol. MTT-39, pp1796-1799, 1991.
- [42] P. M. Morse and H. Feshbach, *Methods of Theoretical Physics*, New York: McGraw-Hill, New York, N. Y. Vol. 1, 1953.
- [43] R. Courant and D. Hilbert, *Methods of Mathematical Physics*, Interscience Publishers, New York, N. Y. Vol. 1, 1953.
- [44] M. N. O. Sadiku, Numerical Techniques in Electromagnetics, CRC Press, 199.
- [45] A. D. Wheelon, "On the summation of infinite series in closed form," *Journal of applied physics*, Vol. 25, pp113-118, January 1954
- [46] L. A. Pipes, "The summation of Fourier series by operational methods," *Journal of applied physics*, Vol. 21, pp298-301, April 1950
- [47] Y. Leviatan, P. G. Li, A. T. Adams, and J. Perini, "Single-post inductive obstacle in rectangular waveguide," *IEEE Trans. Microwave Theory Tech.*, Vol. MTT-31, pp806-811, 1983.
- [48] R. H. MacPhie, and K. L. Wu, "Scattering at the junction of a rectangular waveguide and a larger circular waveguide," *IEEE Trans. Microwave Theory Tech.*, Vol. MTT-43, pp2041-2045, 1995.
- [49] A. W. Mathis and A. F. Peterson, "A comparison of Acceleration procedure for the two-dimensional periodic Green's function," *IEEE Trans. Microwave Theory Tech.*, Vol. MTT-44, pp567-571, 1996.
- [50] M. J. Park, J. Park, and S. Nam, "Efficient calculation of the Green's function for the rectangular cavity," *IEEE Microwave and Guided Wave Letter*, Vol. 8, pp124-126, 1998.
- [51] A. W. Mathis and A. F. Peterson, "Efficient electromagnetic analysis of a doubly infinite array of rectangular apertures," *IEEE Trans. Microwave Theory Tech.*, Vol. MTT-46, pp46-54, 1998.
- [52] R. E. Jorgenson and R. Mittra, "Efficient calculation of the free-space periodic Green's function," *IEEE Trans. Antenna and Propagation*, Vol. AP-38, pp633-642, 1990.
- [53] K. M. Chen, "A mathematical formulation of the equivalence principle," *IEEE Trans. Microwave Theory Tech.*, Vol. MTT-37, pp1576-1581, 1989.
- [54] S. Singh and R. Singh, "On the use of Levin's T-transform in acceleration the

- summation of series representing the free-space periodic Green's functions," *IEEE Trans. Microwave Theory Tech.*, Vol. MTT-41, pp884-886, 1993.
- [55] S. Singh and R. singh, "Efficient computation of the free-space periodic Green's function," *IEEE Trans. Microwave Theory Tech.*, Vol. MTT-39, pp1226-1229, 1991.
- [56] S. Singh and R. Singh, "A convergence acceleration procedure for computing slowly converging series," *IEEE Trans. Microwave Theory Tech.*, Vol. MTT-40, pp168-171, 1992.
- [57] S. Singh and R. Singh, "On the use of Chebyschev-Toeplitz algorithm in accelerating the numerical convergence of infinite series," *IEEE Trans. Microwave Theory Tech.*, Vol. MTT-40, pp171-173, 1992.
- [58] S. Singh and R. Singh, "Application of transform to accelerate the summation of periodic free-space Green's functions," *IEEE Trans. Microwave Theory Tech.*, Vol. MTT-38, pp1746-1748, 1990.
- [59] M. I. Aksum and R. Mittra, "Choices of expansion and testing functions for the method of moments applied to a class of electromagnetic problem," *IEEE Trans. Microwave Theory Tech.*, Vol. MTT-41, pp503-508, 1993.
- [60] W. W. Hansen, "A new type of expansion in radiation problems," *Physics Review*, Vol. 47, pp139-143, 1935.
- [61] W. W. Hansen, "Directional characteristic of and antenna over a plane earth," *Journal of Applied Physics*, Vol. 7, pp460-465,1936.
- [62] W. W. Hansen, "Transformations useful in certain antenna calculation," *Journal of Applied Physics*, Vol.8, pp282-286,1937.
- [63] J. B. Wei, T. Shidaker and M. C. Hawley, "Recent progress in microwave processing of polymers and composites," Polymer Science, Jan. 1996, Vol. 4 No. 1
- [64] N. W. McLachlan, Bessel Functions for Engineers, Oxford at the Clarendon Press, 1934.
- [65] C. J. Tranter, Bessel Functions with Some Physical Applications, Hart Publishing Company, Inc., New York City, 1968.
- [66] J. M. Osepchuk, "A history of microwave heating applications," *IEEE Trans. Microwave Theory Tech.*, Vol. MTT-32, pp1200-1223, 1984.
- [67] R. J. Spiegel, "A review of numerical models for predicting the energy deposition and resultant thermal response of humans exposed to electromagnetic fields," *IEEE Trans. Microwave Theory Tech.*, Vol. MTT-32, pp730-746, 1984.

- [68] E. B. Manring, Electromagnetic field solutions for the natural modes of a cylindrical cavity loaded with lossy materials, Dissertation for the Degree of Ph. D., Michigan State University, 1992
- [69] Y. Kobayashi, and T. Senju, "Resonant modes in shielded uniaxial-anisotropic dielectric rod resonantors," *IEEE Trans. Microwave Theory Tech.*, Vol. MTT-41, pp2198-2205, 1993.
- [70] R. E. Collin, Foundation for Microwave Engineering, New York: McGraw\_Hill, 1966.
- [71] J. R. Reitz, F. J. Milford, and R. W. Christy, *Foundations of Electromagnetic Theory*, 3d edition, Reading, Mass.: Addison-Wesley, 1979.
- [72] A. S. Omar, and K. F. Schunemann, "Complex and backward wave modes in inhomogeneously and anisotropically filled waveguides," *IEEE Trans. Microwave Theory Tech.*, Vol. MTT-35, pp268-275, 1987.

MICHIGAN STATE UNIV. LIBRARIES
31293017665138